ABSTRACT

| | |
|---|---|
| Title: | DISTINGUISHING MODES OF EUKARYTIC GRADIENT SENSING |
| | Ron Skupsky, Ph.D., 2005 |
| Directed By: | Professor Wolfgang Losert and Dr. Ralph Nossal |

The behaviors of biological systems depend on complex networks of interactions between large numbers of components. The network of interactions that allows biological cells to detect and respond to external gradients of small molecules with directed movement is an example where many of the relevant components have been identified. This behavior, called chemotaxis, is essential for biological functions ranging from immune response in higher animals to the food gathering and social behavior of ameboid cells. Gradient sensing is the component of this behavior whereby cells transduce the spatio-temporal information in the external stimulus into an internal distribution of molecules that mediate the mechanical and morphological changes necessary for movement. Signaling by membrane lipids, in particular 3' phosphoinositides (3'PIs), is thought to play an important role in this transduction. Key features of the network of interactions that regulates the dynamics of these lipids are coupled positive feedbacks that might lead to response bifurcations and the involvement of molecules that translocate from the cytosol to the membrane, coupling responses at distant point on the cell surface. Both are likely to play important roles in amplifying cellular responses and shaping their qualitative features.

To better understand the network of interactions that regulates 3'PI dynamics in gradient sensing, we develop a computational model at an intermediate level of detail. To investigate how the qualitative features of cellular response depend on the structure of this network, we define four variants of our model by adjusting the effectiveness of the included feedback loops and the importance of translocating molecules in response amplification. Simulations of characteristic responses suggest that differences between our model variants are most evident at transitions between efficient gradient detection and failure. Based on these results, we propose criteria to distinguish between possible modes of gradient sensing in real cells, where many biochemical parameters may be unknown. We also identify constraints on parameters required for efficient gradient detection. Finally, our analysis suggests how a cell might transition between responsiveness and non-responsiveness, and between different modes of gradient sensing, by adjusting its biochemical parameters.

DISTINGUISHING MODES OF EUKARYTIC GRADIENT SENSING


By


Ron Skupsky




Dissertation submitted to the Faculty of the Graduate School of the
University of Maryland, College Park, in partial fulfillment
of the requirements for the degree of
Doctor of Philosophy
2005

Advisory Committee:
Professor Wolfgang Losert, Chair
Adjunct Professor Ralph Nossal, Co-Chair
Professor David C Levermore
Professor Victor Yakovenko
Professor James A Yorke

# Preface

Modern molecular and cellular biology are continually identifying cellular components and interactions that are important for regulating cellular behaviors, such as gradient sensing. In this dissertation, we ask, how do the identified components and interactions work together to regulate cellular responses to chemical gradients? Several models of cellular gradient sensing have recently been published, and it has become apparent that multiple gradient sensing mechanisms are consistent with experimental observations of characteristic behaviors. Further, different cell types might make use of different mechanisms.

For these reasons, we have developed a model of eukaryotic gradient sensing, and used it to explore a range of possible mechanisms, or 'Modes', of gradient sensing. Our model includes cellular components whose dynamics can be visualized in live cells, and is based on proposed biochemical mechanisms. Thus, our model can be used to investigate how cellular behaviors depend on particular biochemical mechanisms, and how these behaviors might be observed experimentally. In particular, we find that different Modes of gradient sensing are characterized by differences in transitions in cellular response between efficient gradient sensing and failure. We use these differences to suggest criteria for distinguishing between different Modes of gradient sensing in real cells. These are some of the features that make our model unique.

This model was primarily developed at the NIH. The longer I remained there, the more I became interested in the cell biological aspects of this project. This dissertation is directed towards researchers with varying backgrounds in both biology

and physics. Each chapter is broken into many subsections. I have tried to indicate which might contain more mathematical or biochemical detail, and which contain more qualitative discussions. Each chapter also includes overview and summary sections. These should allow the reader to choose those sections that are most appropriate to his/her interests and background. In addition, important and cell biological terms are highlighted in bold and generally discussed the first time that they are mentioned. The glossary found in 'Molecular Biology of the Cell', which cited as reference 28, might be helpful for further definitions.

# Acknowledgements

This project was initiated based on a presentation given by my advisor at the NIH, Dr. Ralph Nossal, a bit over four years ago. Then, he suggested that the feedback regulation involved in phosphoinositide signaling might act as a trigger for endocytotic vesicle formation. While this dissertation focuses on the roles of phosphoinosides in gradient sensing, I expect that many of the ideas developed will be applicable as well to understanding cellular vesicle formation processes. I would particularly like to thank Ralph for very much patience and encouragement, allowing me to develop my own research project, many good suggestions for its development, and essential guidance in writing and presenting it. Working in his lab was a wonderful opportunity to be part of a dynamic scientific community, explore exciting areas of cell biology, and develop physics and engineering approaches to ask biologically interesting questions.

When my advisor at the University of Maryland, Dr. Wolfgang Losert, became involved in this project, it really began to develop into the form presented in this dissertation. I need to thank him as well for a great deal of patience and encouragement, and for many good suggestions for developing and presenting this work. His energy and enthusiasm were often contagious, as he began to develop new cell biology related projects in his lab, many of which might extend and complement the work in this dissertation. It is truly an amazing thing the way that he can jump into a new area and make things happen.

A wonderful thing about the NIH is that one can find world experts in most areas of biology, who are excited to share their knowledge. I was particularly fortunate that

# Table of Contents

# List of Tables

# List of Figures

# Chapter 1: Introduction and Background

## 1.1     Overview

Many biological cells move directionally in response to external gradients of small molecules at some time during their development.  This behavior, called chemotaxis, is important in functions ranging from immune response in higher animals to the food gathering and social behavior of ameboid cells.

Successful chemotaxis requires that the cell's experience of chemotactic stimuli be relayed to the biochemical machinery that controls its movements and generates forces. This transduction processes, referred to as gradient sensing, depends on the spatio-temporal dynamics of many types of molecules, on multiple length and time scales, in a closed and irregular geometry.  These dynamics demonstrate high gain in response to external stimuli, at the same time as adaptation and plasticity, and are regulated by complex networks of biochemical interactions having multiple levels of organization. The relevant interactions often involve supramolecular structures, such as cytoskeletal filaments and various cellular membranes, and may couple biochemical reactions to mechanical deformations.  Modern molecular and cellular biology have identified many cellular constituents that are important for this regulation, but detailed mechanisms remain to be elucidated.

Computational modeling has become an essential tool for understanding how complex networks of interactions regulate cellular behaviors.  The complexity involved, as well as the many unknowns, presents an exciting opportunity to employ and develop a wide range of theoretical and experimental approaches.  The model of eukaryotic gradient

sensing that we develop in this dissertation represents only one such approach to modeling cellular behaviors. It focuses on a particular subset of the features and interactions that are involved. Further investigations based on alternative approaches undoubtedly will yield new insights.

This first chapter gives a broad background as well as a general introduction to our model of eukaryotic gradient sensing. In Chapter 2, we will develop a set of model equations to describe the network of regulatory interactions that are thought to be relevant. We will then define four variants of our model that illustrate the qualitatively different gradient sensing possibilities that are suggested by the generic features of this network. Our model and its variants are further characterized in Chapter 3. In Chapter 4, the responses to typical chemotactic stimuli are simulated and the results are used to define criteria that distinguish between our model variants. These criteria are then applied to characterize the behaviors of our model as several parameters are systematically varied. We conclude with a discussion of implications for real cells.

This chapter begins by introducing eukaryotic gradient sensing in its larger biological context and highlighting several related aspects of cellular behavior whose understanding would benefit from further theoretical modeling (Sec. 1.2). The types of cells to which our model applies, in particular Dictyostelium and neutrophils, are discussed in Sec. 1.2.2; characteristic behaviors in these cells, which our model will capture, are discussed Sec. 1.2.6.

Phosphoinositide (PI) signaling will provide the biochemical basis for our model, and is introduced in Sec. 1.3. In particular, Sec. 1.3.3 discusses the important features of spatial localization and feedback regulation that make PI signaling particularly well

suited to mediate cellular behaviors that, like gradient sensing, are highly regulated in space and time.

General considerations for modeling cellular signal transduction processes are discussed in Sec. 1.4; our approach, which includes an intermediate level of detail, is discussed in Sec. 1.5.4. Section 1.5 discusses recent models of eukaryotic gradient sensing, focusing on their differences. This discussion serves to motivate our focus on regulatory elements that might lead to qualitatively different gradient sensing mechanisms (Secs. 1.5.4 and 1.5.5). Our model is further introduced in Sec. 1.6.

## 1.2 Eukaryotic chemotaxis and spatial gradient sensing

**Cellular chemotaxis** is the process whereby cells respond to gradients of small molecules, which are often ligands for cell surface **receptors**, with directional movement. Chemotactic ligands that induce cellular movement towards higher concentrations are referred to as **chemoattractants**. **Eukaryotic** cells are defined by a nucleus that contains genetic material, as well as other spatially organized internal compartments. Eukaryotic chemotactic response depends directly on the spatial as well as the temporal features of chemotactic stimuli[#] (4-6). In this section, we will place eukaryotic gradient sensing in the larger context of cellular chemotactic behavior.

### 1.2.1 Importance of chemotaxis

Cellular chemotaxis is important in phenomena as diverse as the immune response of

---

[#] Spatial sensing in eukaryotic chemotaxis is often contrasted with bacterial chemotaxis, which relies on a 'run and tumble' mechanism. Bacterial chemotaxis is generally thought to directly involve only responses to temporal gradients; spatial sensing in bacterial cells is achieved by movement, which transduces an external spatial gradient of chemottractant into an experienced temporal gradient in receptor activation. This, in turn, affects the bacterial tumbling frequency (1-3).

higher animals (7, 8), wound healing (9, 10), neuronal patterning (11, 12), vascular (13)

and embryonic (14) development, as well as the food gathering and social behavior of

some amoeboid cells (15).  Its disregulation can have deleterious effects, including

immune disease (16), aberrant angiogenesis (17), and cancer metastasis (18-20) in multi-

cellular organisms, and aggregation defects in ameboid cells (15).

1.2.2.  Cell types and experimental systems – Neutrophils and Dictyostelium

In this dissertation, we will be primarily concerned with the chemotactic behavior of

highly motile eukaryotic cells.  Most of the data that we consider will be derived from

experiments in **neutrophils**, which are a type of immune cell (white blood cell), and the

ameboid cell, **Dictyostelium discoidium** in its early aggregation stage (we will simply

refer to these cells as Dictyostelium).  When fully extended, these types of cells might be

of order 20 $\mu m$ in length.  Their chemotactic behavior can be characterized as a biased

random walk (21-23), generally involving velocities of order 10 $\mu m$/min. (~1/2 cell

length per minute) and highly polarized morphologies.  Cells adapt to the average ligand

concentration presented in solution, and detect and respond to changing gradients of a

few percent across their length, within seconds to tens of seconds, over several orders of

magnitude in absolute concentration (6, 24, 25).  The adaptive yet highly amplified and

persistent nature of this response has inspired a great deal of mathematical modeling over

the past several decades (26, 27).

   Neutrophils are part of the body's **innate immune system** which is constantly active

and responds to generic features of typical infectious agents.  Neutrophils are one of the

first types of immune cells recruited to a new site of infection.  They generally have short

4

life times (hours to days) and their production rate from **progenitor cells** increases in response to an infection.

An example of a neutrophil's response to an infection and associated inflammation might be as follows:  If the neutrophil is circulating in the blood stream, it will recognize **chemokines** (a particular class of small molecule ligands, for which neutrophils have receptors) released by other immune cells (such as **macrophage**) and by the **endothelial cells** that line the **capillaries** near a site of infection.  Adhesion receptors on the surface of the neutrophil will then become activated and bind proteins on the surface of the endothelial cells (the **expression** of these endothelial proteins is increased as part of the inflammatory response).  The neutrophil will then crawl from the blood stream to the infected tissue by either passing through spaces in the capillary walls (also created as part of the inflammatory response) or by being **transcytosed** through the endothelial cells.  Chemotaxis towards the source of infection will continue, both in response to chemokines released by other body cells near the infection and in response to molecules released by the pathogen (such as **metabolites)**.  The neutrophil might then either engulf the pathogen (via **phagocytosis**) or release toxic enzymes to attack it (28).

The role of neutrophils in immune response involves many cellular behaviors, including responses to multiple chemotactic ligands and a coordinated population dynamics with other immune and body cells.  However, neutrophils can also be isolated, and their chemotactic responses to different ligands studied under controlled conditions (29, 30).  Further, **cell lines** have been developed that share with neutrophils many qualitative features, as well as many specific **biochemical pathways** important in chemotactic response (31, 32).  These cell lines, often referred to as **neutrophil-like**

**cells**, can be grown in the lab and are easier to manipulate than neutrophils (neutrophils need to be harvested from animals and have short lifetimes). A typical experiment might involve allowing an initial distribution of cells to adhere to a coverslip, generating a pattern of chemoattractant by using a **micropipette**, and imaging the cellular response. If molecules inside of the cell are **fluorescently labeled**, their distribution can be imaged as well (33, 34).

Dictyostelium is a model organism often used to study chemotaxis. Dictyostelium cells act as single celled organisms under conditions when food is plentiful. Under conditions of starvation, a development program begins, involving changes in gene expression. Among other things, the cells begin to periodically secrete and chemotax in response to the cyclic nucleotide, **cAMP**. As a result, streaming patterns and spirals with well defined centers spontaneously form. The cells aggregate towards these centers and form a multi-cellular slug, finally developing into a **fruiting body** composed of a narrow stalk with a collection of spores at the top. This structure is stable without food or water over long periods of time (15, 35-38). Patterning during Dictyostelium aggregation is an area which has been fruitful for mathematical modeling (39-45).

The experiments that will be discussed in this dissertation generally refer to Dictyostelium cells in the early stages of aggregation/starvation. Starvation can be initiated in the lab by, for example, plating cells at an appropriate density on agar in the absence of nutrients. After approximately 5 hours, the cells will have reached an appropriate stage of development where they can be studied individually and where chemotaxis in response to gradients of cAMP is robust (25, 46). In a typical experiment,

the cells might be dispersed and plated on a glass coverslip, stimulated with different patterns of cAMP, and their responses imaged under a microscope.

A major advantage of performing experiments with Dictyostelium is that they are genetically much simpler than mammalian cells (such as neutrophils or neutrophil-like cells). Many of the molecules involved in Dictyostelium chemotaxis and gradient sensing have been fluorescently labeled, **mutated**, and/or **knocked out**. The relevant **signaling pathways** and interactions inside of the cell are generally simpler as well. For example, there are fewer known chemoattractants and generally fewer **isoforms** (variants) of a given protein in Dictyostelium than in neutrophils. Despite these differences, many of the mechanisms and molecules involved in chemotaxis are similar enough between these two cell types that results in one can generally be applied to generate new understanding in the other (15, 47, 48).

In developing our model, we will be using data taken from both Dictyostelium and neutrophils. We expect the general features of our analysis to apply to both. Other cellular systems in which chemotaxis has been studied, such as **neurons** (nerve cells) or **fibroblasts** (connective tissue cells), respond on time scales that are slower by at least an order of magnitude than responses in Dictyostelium and neutrophils (on the order of hours to days) (11, 49, 50). These cells might not demonstrate the characteristic behaviors that we will enumerate below (Sec. 1.2.6). In particular, there is evidence to suggest that fibroblasts do not adapt to the spatial average of the stimulus that they experience (49, 51, 52). Thus, the ideas developed in this dissertation would have to be modified for applications to these types of cells.

### 1.2.3 Cellular processes involved in chemotaxis

Chemotaxis results from the integration of several distinct and complex processes, each involving multiple proteins and assembly or disassembly of **supramolecular** structures (26). The cell adopts a polarized morphology with a distinct **leading edge** (front) and **uropod** (back). **Organelles**, such as the **nucleus** and **endosomal system** (53), become polarized with respect to the axis of the cell. The **microtubule** network (54), together with intracellular functions such as **membrane** and **protein trafficking** (55), becomes polarized as well. **Actin** rich protrusions, such as a **lamellipodium** and **filopodia**, are extended preferentially at the leading edge of the cell (29, 56) and become attached to the substrate upon which the cell crawls (57-59). Contractile polymer bundles, including **motor proteins** of the **Myosin** family, maintain tension in the uropod. The uropod is detached from the substrate and pulled forward as the cell moves (60).

In order for the above processes to result in directed movement with respect to an external gradient of chemoattractant ligand, the cell must transduce the external pattern of ligand into an internal distribution of **signaling molecules**, which mediate the necessary mechanical and morphological changes. We refer to this transduction as **gradient sensing**. Figure 1.1 depicts the above-discussed cellular processes and structures.


### 1.2.4 Chemotaxis as an integrated cellular behavior

To produce the cellular behavior of chemotaxis, each of the processes discussed in Sec. 1.2.3 is integrated and involved in complex feedback regulation with the others. For example, in the process of gradient sensing, the cell might localize one set of molecules which will define a leading edge – these molecules will take part in nucleating the actin-

**Branched, dendritic actin structures** drive protrusion of the leading edge, possibly via a Brownian ratchet mechanism. Actin forms flexible filaments on cellular length scales, which are cross-linked and bundled for stability.

**Cross-linked actin structures** contract to pull the uropod forward. Associated motor proteins maintain tension and prevent protrusions away from the leading edge.

**Microtubules**, which help define intracellular polarity and provide 'tracks' for trafficking vesicles, become oriented. These are stiff polymers on cellular length scales, and have an intrinsic polarity (the two ends have different properties).

**Endosomes** form a network of membrane compartments that becomes oriented with respect to the axis of a chemotaxing cell; other intracellular compartments become oriented as well. Endosomes receive vesicles from the plasma membrane and other internal membrane compartments. Material is sorted, repackage into vesicles, and delivered to appropriate compartments.

**Membrane vesicles** exchange material between intracellular compartments. This trafficking becomes oriented with respect to the axis of a chemotaxing cell.

**Adhesions to the surface** upon which the cell crawls are formed as the leading edge is extended and are released as the uropod is pulled forward. These are dynamic and often include specialized proteins (for example, integrins in neutrophils).

**Leading edge** – The front of a chemotaxing cell, characterized by **protrusive** actin-based structures.
**Lamellapod** – Wide flat extension at the leading edge, characterized by a **dendritic actin network**.
**Filopodia** – Narrow extensions that 'explore' the environment, characterized by **parallel actin bundles**.
**Cytosol** – Fluid component of the cell interior.
**Plasma membrane** – Fluid lipid bilayer that acts as an interface between the cell and its environment.
**Nucleus** – Contains genetic material. Positioned with respect to the axis of the cell.
**Uropod** – Rear of the cell, characterized by a **contractile** actin network.

**Fig. 1.1 Cellular processes involved in chemotaxis**. Structures and processes discussed in the text are represented schematically. The schematic is only meant to be illustrative; it is not to scale, the depicted structures appear at much higher densities in real cells, and details differ from cell to cell. In particular, a typical cell contains many internal membrane-bound compartments and a dense polymer network that gives it structure (the **cytoskeleton**). In addition, the cytosol contains a high concentration of macromolecules (typically 50-400 mg/ml, or up to 40% of the fluid volume (61, 62)).

based structures that drive cellular protrusions (56, 63-65).  Another set of molecules will be localized at the rear – these will regulate the contractile network that defines the uropod (66).  The structures at the front and back of the cell are thought to be mutually exclusive; cellular polarization might thus be interpreted as a kind of self organization that is initiated by the external stimulus (67).  The discussed structures can further act as scaffolds, themselves localizing the molecules that regulate their production (68, 69).

In addition, the morphological and mechanical changes at the leading edge and uropod will affect the positioning of internal membrane compartments, as well as the microtubule network.  This internal reorganization and polarization will affect the membrane and protein trafficking patterns inside of the cell (70-72).  Membrane trafficking is thought to play a role in extending the leading edge and retracting the uropod by delivering material from the back to the front of the cell (72-74).  Protein trafficking (often involving **membrane vesicles**) directs signaling molecules to specific locations inside of the cell.  The positioning of microtubules is also thought to play a role in controlling the stability of cellular adhesions to the substrate upon which it crawls (possibly by modulating protein trafficking patterns) (75, 76).  Cellular adhesions localize signaling molecules that mediate many cellular processes (58).  This localization is thought to depend on the forces exerted on the adhesion (77).

Modeling each of the above processes in the complex environment of the cell is a separate and unique challenge.  How to integrate them into a more complete model of chemotaxis is still very much an open question (26, 78).

1.2.5   Gradient sensing decoupled from motility

Recent experiments have suggested that aspects of eukaryotic gradient sensing can be decoupled from other major processes in chemotactic response.  Cells treated with actin depolymerizing agents, such as **Latrunculin A** or **B**, still localize certain signaling molecules with spatio-temporal dynamics similar to those of untreated cells.  These cells are round, immobile, and cannot form protrusions that depend on actin polymerization. Nevertheless, in these drug treated cells, markers for 3' phosphorylated **phosphoinositides** (3'PIs, which are signaling lipids to be discussed in Sec. 1.3.2) still translocate from the **cytosol** to the **plasma membrane** in a pattern that parallels the spatio-temporal dynamics of actin polymerization in untreated cells (29, 32, 79).

Motivated by these observations, we will develop a model of 3'PI-mediated gradient sensing decoupled from motility.  Integrating this model with models of other processes involved in chemotaxis will be the subject of future work.


1.2.6   Characteristic behaviors of gradient sensing

Gradient sensing responses in cells such as neutrophils and Dictyostelium are generally characterized by three types of behaviors.  These characteristic behaviors are reflected in the dynamics of actin polymerization and in the localization of specific signaling molecules in response to chemotactic stimuli.  In particular, these behaviors are still seen in the dynamics of markers for 3'PIs on the plasma membrane in the above-mentioned cells where actin has been depolymerized (illustrated in Fig. 1.2 below).

i) Cells adapt to the average concentration of chemotactic ligand in solution.  This allows sensitivity to relative gradients over many orders of magnitude in absolute concentration

**i) Transient response and adaptation to a uniform stimulus (PH-GFP label).**
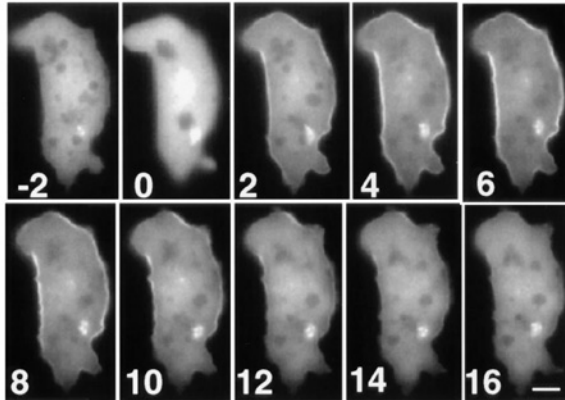
**ii) Highly polarized response to a static gradient (PH-GFP label).**
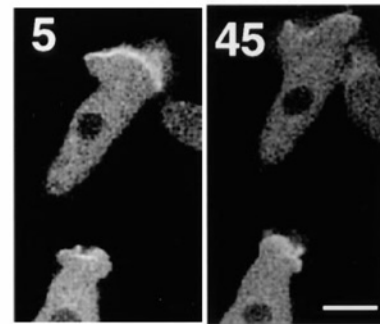
**ii, iii) Highly polarized and persistent response to a static gradient and plasticity in response to a changing gradient (actin labeled with Coronin-GFP).**
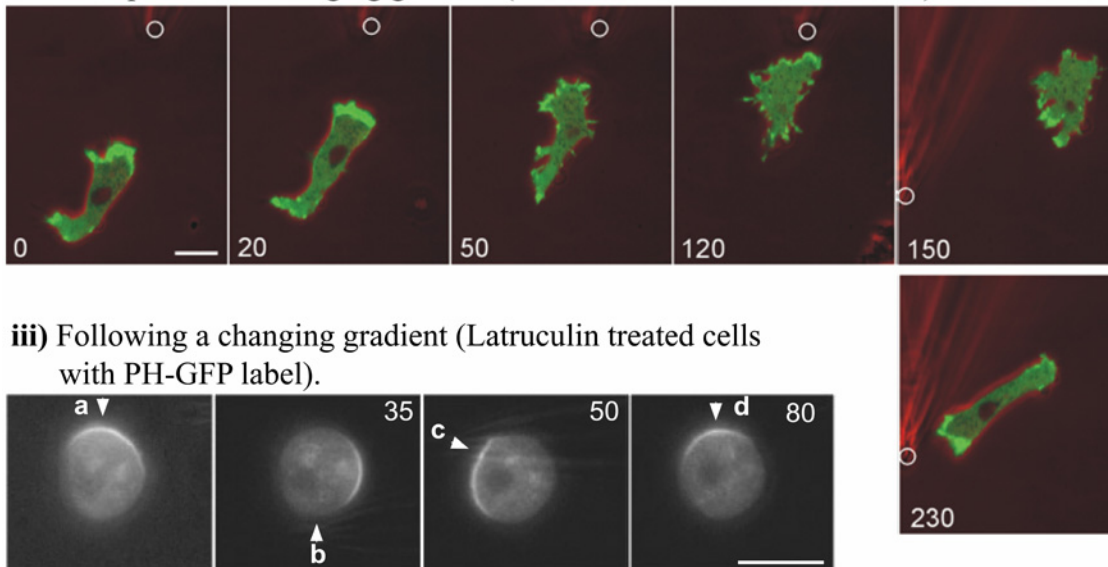
**iii) Following a changing gradient (Latruculin treated cells with PH-GFP label).**
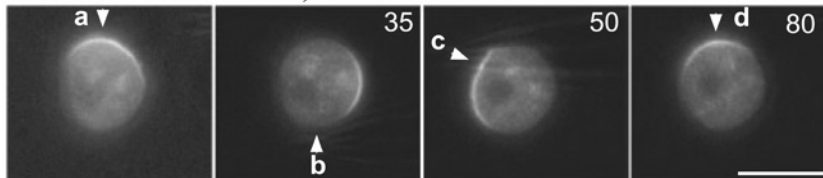
**Fig. 1.2. Characteristic behaviors of gradient sensing.** The characteristic gradient sensing behaviors discussed in the text are illustrated by microscopy images of Dictyostelium cells expressing fluorescently tagged marker for 3'PI (PH-GFP) (**i**, **ii**, **iii**) or a fluorescent marker for polymerized actin (Coronin-GFP) (**ii/iii**). Images are labeled by the characteristic behavior that they illustrate. **i)** A transient response to a uniform increase in extra-cellular cAMP. Numbers indicate the time in seconds relative to when the cAMP was added. The scale bar represents 6 *μm* (reproduced with permission from reference 79). **ii)** Persistent polarization in response to a static gradient. A micropipette, positioned to the top right of the figure, generates a gradient of cAMP. Time is labeled and the scale bar represents 5.6 *μm* (reproduced with permission from reference 79). **ii,iii)** Persistent polarization in response to a static gradient and reorientation when the gradient changes. Actin is labeled. Notice that the pattern of fluorescence is similar to the 3'PI label in **ii**. A circle marks the position of a pipette that leaks cAMP. The scale bar represents 10 *μm* (reproduced with permission from reference 80). **iii)** Cells are treated with laruculin to depolymerized actin. Time is labeled in seconds and an arrow indicates the position of the micropipette. The scale bar represents 10 *μm* (reproduced with permission from reference 81).

12

(25, 82). In particular, Disctyostelium cells can respond to gradients of cAMP whose absolute concentration ranges from picomolar to miromolar concentration (25). If a uniform dose of ligand is applied suddenly, the cellular response, which includes production of 3'PIs, is transient and returns to baseline (79), as illustrated in Fig. 1.2.i.

ii) When exposed to a shallow and static gradient of chemotactic ligand, the cell responds with a sharp and persistent internal gradient of signaling molecules, including 3'PIs (32), as illustrated in Fig. 1.2.ii and 1.2.ii/iii. Cells have been observed to respond to gradients of a few percent across their length (25), corresponding to a difference in ligand binding between the front and back of the cell that is on the order of what might be expected form thermal fluctuations under some conditions (21, 83). This permits immune cells to migrate towards a source of infection and amoeboid cells to move towards a food source over long distances.

iii) If the gradient of ligand changes direction, the distribution of signaling molecules (including 3'PIs) will follow with some fidelity (81), as illustrated in Fig. 1.2.iii. A neutrophil thereby can capture a moving bacterium, and Dictyostelium cells can form dynamic patterns during development in response to changing gradients of cAMP.

## 1.3    Signal transduction and 3'PIs

Gradient sensing is an example of signal transduction in cells. In this section we discuss general features of this transduction. The above mentioned 3'PIs are further introduced. The dynamics of 3'PIs on the plasma membrane in response to external stimuli will be a primary output of our model.

### 1.3.1 General features of cellular signal transduction

All biological cells experience their environment and modify their behavior based on that experience. The complex network of interactions that relays the information from the cell's experience of its environment to the structures that actuate its responses is generally referred to as cellular signal transduction (28, 84, 85). Gradient sensing is an example of such a transduction, where a pattern of ligand-mediated receptor activation at the cell surface represents its experience of the environment and its response is actuated via cytoskeletal rearrangements that lead to mechanical and morphological changes. The lipid signaling that we will discuss below is thought to be an important component of the network of interactions that mediates the relevant information relay.

### 1.3.2 Phosphoinositide signaling

Phosphoinositides (PIs) are signaling lipids in the membranes of eukaryotic cells, generally accounting for only a minor fraction of total membrane lipid (on the order of a few percent) (86, 87). They help regulate processes as diverse as cytoskeletal rearrangement, vesicle formation, gene regulation, cell survival and proliferation (88-93), as well as cell migration and gradient sensing (6, 32, 94).

PIs are composed of two **fatty acids** (hydro-carbon chains) **esterified** to two adjacent carbons of a **glycerol** backbone (a 3-carbon structure). An **inositol** sugar (6 carbon ring) is attached to the third carbon of the glycerol via a **phosphate** group. The fatty acid chains are **hydrophobic** and insert into one side of the bilayer of biological membranes. The inositol ring, which is exposed at the surface of the bilayer, can be **phosphorylated** at various positions. PIs are thus named according to which carbons on the inositol ring

14
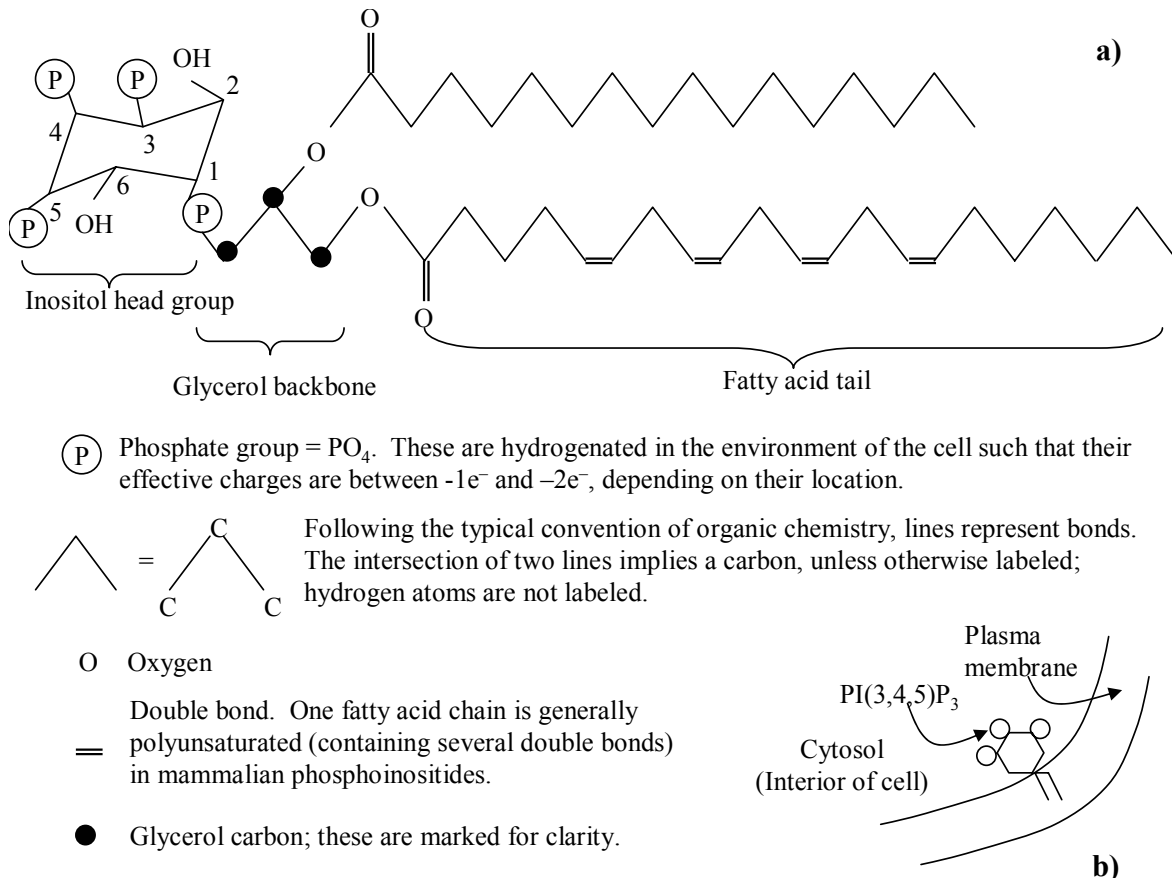
**Fig. 1.3. Anatomy of a phosphoinositide. a)** A typical chemical structure of a phosphoinositide. Structures discussed in the text are labeled, as well as the numbering scheme for carbons of the inositol head group. PI(3,4,5)P$_3$ is depicted. Note, that the number of carbons and double bonds in the fatty acid tails are variable, and any double bonds will result in kinks in the fatty acid chain (not depicted). **b)** Cartoon of PI(3,4,5)P$_3$ in the inner leaflet of the plasma membrane. The bilayer is fluid and lipids such as PIs can thus diffuse laterally. The drawings are not to scale.

are phosphorylated. For example, 3'PIs are phosphorylated in the 3' position and PI(3,4,5)P$_3$ specifies a PI with three additional phosphates, which are located the 3', 4' and 5' positions (86), as illustrated in Fig. 1.3.

The primary function of PIs, with which we will be concerned, is to recruit to the membrane specific subsets of cytosolic molecules that are involved in various cellular behaviors. These molecules often bind, via various binding domains (91, 95, 96), to

specifically phosphorylated PIs.  Thus, the phosphorylation state and localization of PIs are highly regulated (87, 91).

Particular PIs are phosphorylated at specific positions by various families of **kinases** and dephosphorylated at specific positions by various families of **phosphatases**.  The activities of these kinases and phosphatases often depend on extracellular signals.  In this way, the concentrations and spatial localizations of the various PIs in the cell will be modulated in response to external stimuli.  This modulation will alter the properties of any given cellular membrane, as well as the activities of the combinations of molecules that are recruited to that membrane, and effect particular cellular responses (87).


1.3.3   Ubiquitous features of PI signaling: Spatial localization and feedback regulation

Biological membranes, which are multi-component fluid bilayers with well regulated compositions, form the interface between eukaryotic cells and their environment (as well as between the various intracellular compartments).  Membrane viscosity is generally significantly higher than cytosolic viscosity.  Thus, reactions such as interconversions of PIs, whose kinetics would generate relatively uniform distributions if they took place in the cytosol, can lead to spatial patterns because they occur on a membrane (97).  Further, molecules that translocate from the cytosol to the membrane will couple dynamics on different length and time scales.

PIs recruit many molecules to the membrane, including proteins that regulate cytoskeletal dynamics (98), as well as proteins implicated in vesicle formation (99) and trafficking (89).  In particular, **enzymes** directly affecting membrane composition and PI interconversion are recruited (100).  Thus, molecules affecting various cellular functions

are recruited to the membrane in combination, interacting with each other and themselves localizing other proteins and lipids. Such feedback regulation is a common feature of PI signaling in cells (101, 102).

As a result of the above-mentioned feedback regulation and spatial localization, a relatively small signal on the cell surface might be amplified in a highly regulated and localized way via PI interconversion. Such a mechanism is particularly well suited to affect functions that include morphological changes at the cell surface, such as chemotaxis. The mentioned ubiquitous features of PI signaling in cells are depicted schematically in Fig. 1.4.
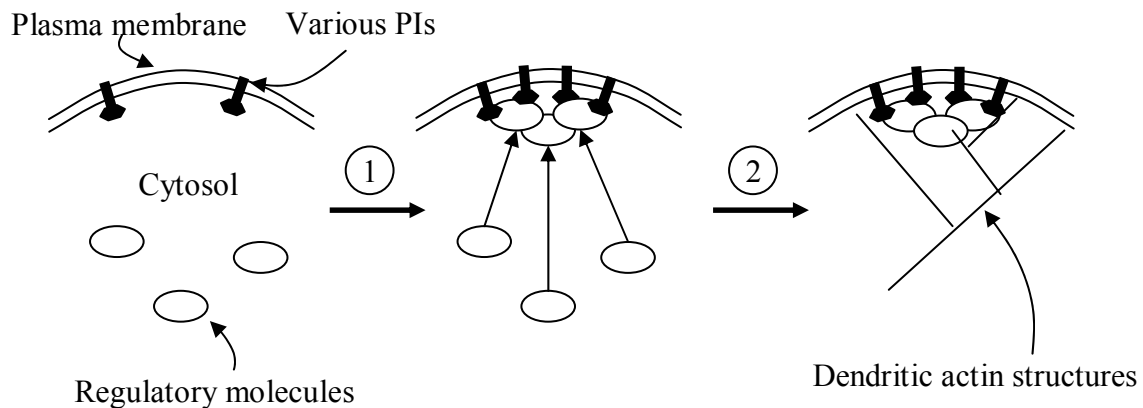


**Fig. 1.4**. **Ubiquitous features of PI signaling in cells**. ① A small signal changes the local distribution of PIs on the membrane, causing regulatory molecules to **translocate** from the cytosol to the membrane. Some of these molecules further affect the distribution of PIs on the membrane, recruiting more molecules. This is **feedback** regulation. Molecules on the membrane can form **local patterns**, while those in the cytosol are generally diffuse. Thus, translocation couples dynamics with different characteristic length scales. ② As a result, highly localized signals in space and time can be generated on the membrane to regulate cellular processes. Nucleation of dendritic actin structures, such as those at the leading edge of chemotaxing cells, is depicted as an example.

## 1.3.4  3' PIs in gradient sensing

The PIs that we will focus on, which are thought to play important roles in eukaryotic gradient sensing, are the 3' PIs, PI(3,4,5)$P_3$ and PI(3,4)$P_2$.  Together they comprise on the order of 0.02% of total plasma membrane lipid in resting cells and specifically act to recruit a similar set of cytosolic molecules to the membrane (66, 87, 103).  PI(4,5)$P_2$ is also important in many cellular functions, including cytoskeletal regulation; these will not be discussed in this dissertation.

The following picture has emerged concerning the potential role of 3'PIs in gradient sensing (schematized in Fig. 1.5).  Chemotactic ligand binding activates receptors on the cell surface, which activate the **heterotrimeric G-proteins** (HTGs) to which they are coupled.  This combination of activated receptors and HTGs on the inner surface of the plasma membrane will activate many intercellular proteins, both on the membrane and in the cytosol.  In particular, PI3' Kinases (PI3Ks, which are enzymes that phosphorylate PIs in the 3' position) will be recruited to the membrane and activated.  The newly generated 3'PIs will recruit other regulatory molecules to the membrane and the 3'PI signal will be amplified via feedback regulation, as discussed in the previous subsection. Among the molecules recruited to the membrane will be those that nucleate and regulate the actin-based structures at the leading edge of chemotaxing cells – this accounts for the coincidence of markers for 3'PIs and actin polymerization, which was noted in Sec. 1.2.6 (4, 48, 66, 104).  As mentioned, a qualitatively similar dynamic of 3'PIs is observed in response to chemotactic stimuli in rounded and immobile cells where actin polymerization has been poisoned.  It is the 3'PI dynamics in these rounded cells that our model will aim to capture.
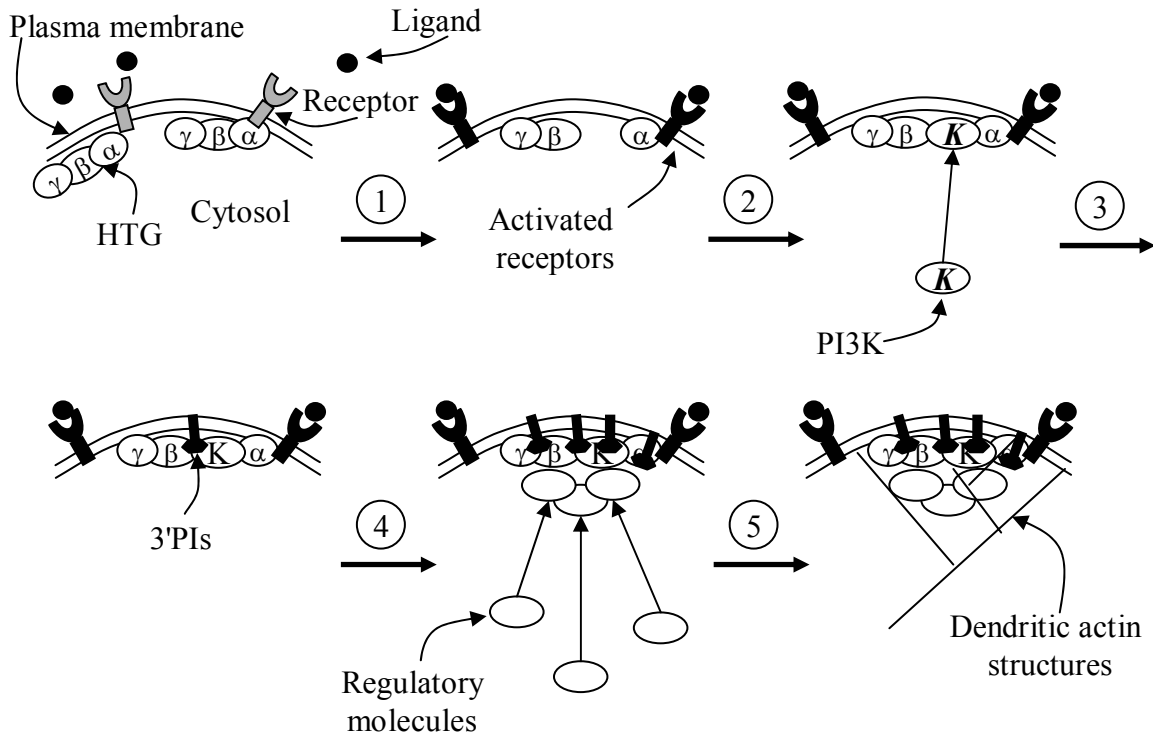
**Fig. 1.5. 3'PIs in gradient sensing**. ① Chemotactic ligand in solution binds to chemotactic receptors on the cell surface. These become activated, together with the heterotrimeric G-proteins (HTGs) to which they are coupled (causing dissociation of their β and γ subunit from the α subunit). ② Activated receptors and HTGs recruit PI3K to the membrane. ③ 3'PIs are generated on the membrane. ④ Regulatory molecules are recruited to the membrane and feedback regulation amplifies the 3'PI signal. ⑤ Localization of regulatory proteins and 3'PIs leads to production of the structures that define the leading edge of a chemotaxing cell. For example, dendritic actin structures are nucleated.

## 1.4 Modeling cellular signal transduction

Biological systems are complex and approaches to modeling their behavior are constantly developing. In this section, we discuss several general considerations that motivate our approach to modeling eukaryotic gradient sensing.

## 1.4.1 Systems/computational biology

The behaviors of biological systems depend on complex networks of interactions

between large numbers of components.  Even a small number of biological components studied in isolation, such as membrane lipids or cytoskeletal proteins, can demonstrate a wide range of behaviors.  As modern molecular biology continues to identify more of these parts and their interactions, it becomes less intuitive how the network of interactions in a biological system functions to regulate its observed behaviors.  Thus, there is an increasing trend in modern biology, and in particular in studies of signal transduction, to develop 'systems' types of approaches (85, 105-110).  These approaches are often motivated by ideas from the more quantitative sciences, such as physics and engineering.  However, it is often unclear how to apply these ideas to biological systems. Thus, there is tremendous need and opportunity in biology to develop new approaches to better understand and to experimentally probe the network of interactions that regulates the systems-level behaviors of cells.

1.4.2   Modularity in signaling networks

One approach to analyzing the complex networks of interactions that regulate cellular behaviors is to break them down into smaller functional blocks, often referred to as 'modules' (111, 112).  There have been attempts to formalize the definition of a module, such that it can be applied to a complex network of interactions whose function might not be known (113, 114).  However, when a known function is investigated, a partitioning of the relevant network into modules is often done empirically as a simplifying tool.  This breakdown is generally not unique.

For the purposes of this dissertation, we might roughly define a module as a subset of interactions that regulate a given response, and that may be coupled loosely or in a well

defined way to the rest of the network under investigation.  For example, gradient sensing might be considered a functional module involved in chemotactic response and the network of interactions for 3'PI regulation, from which we will develop our model, might be considered a functional module involved in gradient sensing.  In Secs. 1.2.5 and 1.2.6, we have noted that actin depolymerization can decouple aspects of 3'PI-meidated gradient sensing from the other processes involved in chemotaxis.

When we develop our model, we will further interpret the network of interactions regulating 3'PIs in gradient sensing as being composed of an amplification and adaptation module; their coupling accounts for the characteristic behaviors of gradient sensing (discussed further in Sec. Sec. 1.5.2).  Thus, the breakdown of a given network into functional modules is often hierarchical, as illustrated schematically in Fig. 1.6. Integration of the modules under consideration into the larger network of relevant interactions is a difficult and important problem.
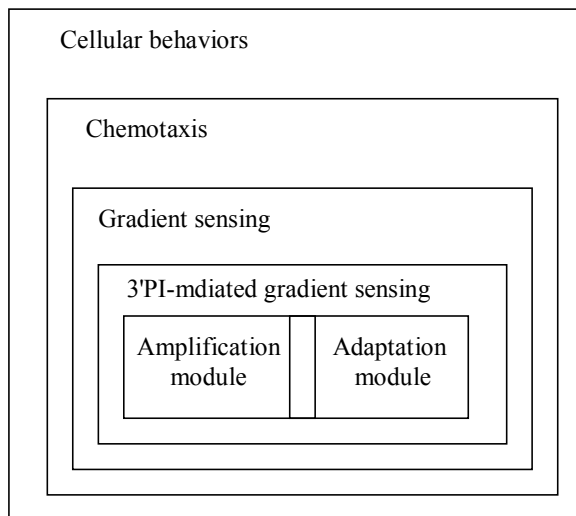


**Fig. 1.6**. **Hierarchical organization of cellular behavior modules.** Chemotaxis is a type of cellular behavior; gradient sensing is a process involved in chemotaxis; 3'PI regulation can account for characteristic gradient sensing behaviors, though other regulation is probably important as well.  We will choose a subset of the interactions involved in 3'PI regulation to develop our model of gradient sensing, and break this network down into an amplification and adaptation module.  These are drawn as overlapping to indicate that they may share components and interact.  Processes at each level are integrated with other processes on that level, which are not depicted.

### 1.4.3   Reaction-diffusion models

Measurements of gradient sensing responses in rounded and immobile cells (see Secs. 1.2.5 and 1.2.6) suggest that aspects of gradient sensing are regulated by a network of biochemical interactions (as opposed to, for example, long range mechanical interactions), and that simple geometries might be considered.  Further, fluorescent labeling techniques have allowed experimental observations of the spatio-temporal dynamics of 3'PIs on the plasma membrane in response to chemotactic stimuli, as well as observations of several key enzymes that regulate their production/degradation (discussed further in Sec. 2.3.1).  These observations motivate our choice of reaction-diffusion equations to model the dynamics of 3'PIs and of the enzymes that regulate their interconversion.


### 1.4.4   Level of detail

The level of detail included in models of cellular processes such as gradient sensing can vary over a wide range.  For example, Turing-type activator/inhibitor models with only a few components have been used to explain aspects of patterning and morphogenesis during development of multi-cellular organisms (115, 116).  Minimal models of this sort are useful for understanding general features of cellular behavior.  In particular, they can be used to capture characteristic gradient sensing behaviors.  However, they can be difficult to map onto the more complex regulatory networks that are often thought to be important in real cells.  Further, the application of these types of models to predict cellular responses under a given set of conditions is generally unclear.

At the other extreme, models have been developed that include most known components of particular signaling pathways. These types of models might include hundreds of components and thousands of parameters, a large fraction of which will be either unknown or poorly constrained (110, 117-119). Due to their large size, however, it is often unclear how to interpret these models and extract useful information

In general, the appropriate level of detail to be included in a model will depend on the available data and on the questions that one would like to address.


1.4.5   Our approach

The molecular mechanisms involved in eukaryotic gradient sensing are continuously being uncovered. Nevertheless, many details remain unknown and many regulatory mechanisms are not fully understood. Thus, in developing our model, we will focus on regulatory elements that affect the qualitative features of gradient sensing responses. We will make simplifications concerning elements that are not well understood in such a way that preserves the qualitative features under consideration. We will further be interested in how these qualitative features depend on cellular biochemical parameters and particular regulatory mechanisms. Thus, our model will not be a minimal model consisting of unnamed activators and inhibitors. Rather, we will include those molecules that are directly relevant to 3'PI-mediated gradient sensing, whose spatio-temporal dynamics in response to chemotactic stimuli have been studied experimentally. The structure of the regulatory network that controls their dynamics will be derived directly from cellular biochemical data whenever possible, and our equations will be derived

directly from an interpretation of this network. In this way, we will develop our model at an intermediate level of detail.

## 1.5    Recent models of eukaryotic gradient sensing

Several models directly relating to PI-mediated gradient sensing were published by other groups as we were developing our own. These models include several features that are present in our model, though our approach and the questions that we address differ significantly. In this section, we introduce a conceptual framework for understanding many of the essential features of eukaryotic gradient sensing, as well as models thereof. We then briefly discuss several recent models, focusing on their differences. This serves to motivate the development of our model, which takes a comparative approach and focuses on elements affecting the qualitative features of gradient sensing mechanisms.

### 1.5.1   Local activation, global inhibition

The gradient sensing response that we wish to model involves a highly amplified response restricted to the up-gradient side of a cell in a shallow gradient of chemoattractant (characteristic behavior 'ii' in Sec. 1.2.6). This suggests that localized amplification mechanisms are involved in regulating responses to chemotactic stimuli. On the other hand, cellular responses adapt to the average value of the external stimulus (characteristic behavior 'i'), which is a global quantity. This suggests that global inhibitory mechanisms, which integrate the information in the pattern of receptor activation around the perimeter of the cell, regulate responses as well. Thus, it has been suggested that gradient sensing results from the combination of local activation and
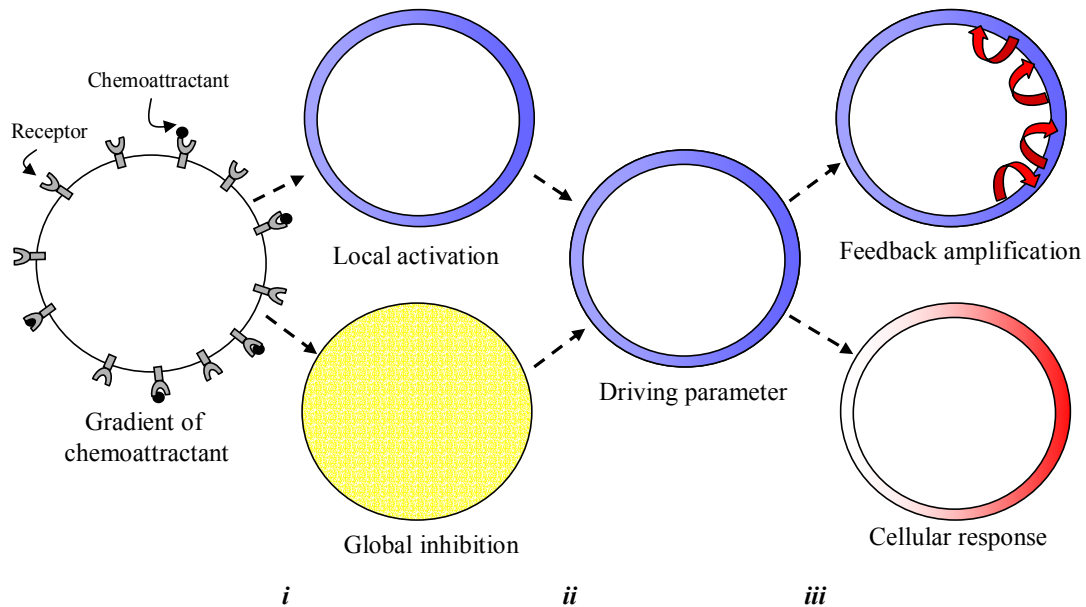
**Fig. 1.7**. **Conceptual framework for understanding eukaryotic gradient sensing**. Receptor activation leads to fast production of locally acting activator molecules and slower production of globally acting inhibitor molecules. Their balance drives an amplification module, a component of which is recorded as the cellular response. If the stimulus is uniform, then at long times the production of activator and inhibitor balance each other everywhere on the membrane. The result is a transient response followed by response adaptation, as was illustrated in Fig. 1.2.i. If a gradient of stimulus is applied, the entire cell experiences the same level of inhibitor (which acts globally), while the production of activator molecules (which is local) reflects the slight gradient of stimulus (*i*). Their balance results in a slightly higher value of the driving parameter at the front of the cell then at the back (*ii*), driving the amplification module at the front of the cell. The result is a highly amplified response at the front of the cell (*iii*).

global inhibition (6, 120), as depicted schematically in Fig. 1.7 and discussed further in

the next subsection.

## 1.5.2 Amplification and adaptation modules

In order to apply the ideas of Sec. 1.5.1 to analyze the network of biochemical interaction

that is thought to be involved in eukaryotic gradient sensing, we suggest a modular

interpretation. The network of interactions that regulates response amplification might be

considered to constitute an **amplification module**. In the simplest case, we might

25

identify a single **driving parameter**, which controls the response of this amplification module at each point on the membrane. This driving parameter will include a combination of concentrations and activities of various signaling molecules, and should be coupled directly to the outside stimulus. In order to reproduce the characteristic responses of gradient sensing, this driving parameter must further be controlled by an **adaptation module**, such that the response of the cell always adapts to the spatial average of the outside stimulus around the membrane. This can be accomplished if the driving parameter reflects a balance between local activation and global inhibition, as discussed in Sec. 1.5.1 and depicted schematically in Fig. 1.7. If this regulation of the driving parameter approximates an **integral feedback**, then perfect adaptation will be ensured (121). Variants of this modular structure can be found in several of the recent models of gradient sensing (discussed below), as well as our own.

### 1.5.3   Recent models relating to phosphoinositide-mediated gradient sensing

The suggestion that gradient sensing can be decoupled from motility, and that it is mediated by a feedback scheme such as those implicated in PI signaling, has inspired several recent mathematical models. Each accounts for characteristic behaviors in a different way.

Levchenko and Iglesias (122) have analyzed a general model (which we will refer to as the LI model) that maps onto a scheme of receptor-mediated production of $PI(3,4,5)P_3$ with feedback through **small GTPases** (molecules that **hydrolize** GTP); feedback involving small GTPases will be an important component of our model as well. The ratio of PI3K (a kinase that produces 3'PIs) and PTEN (a phosphatase that depohsphorylates

3'PIs) can be interpreted as a driving parameter in the LI model, and adaptation occurs because receptor activation stimulates both of these molecules.

Narang, Subramanian and Lauffenburger (123) have analyzed a model (henceforth, NSL model) abstracted from a scheme of receptor-mediated regulation of PI(4,5)P$_2$ levels, modulated by Phospholipase C activity (PLC, which is an enzyme that cleaves the inositol head group from PIs) and feedback through substrate delivery from other membrane compartments. Receptor activity can be interpreted as a driving parameter in this model and adaptation occurs through receptor desensitization.

Postma and Van Haastert (97) have analyzed a general model (PvH model) in which a cytosolic **effector** molecule (a molecule that 'effects' a cellular response) enhances receptor-mediated production of a lipid **second messenger** (that is, a signaling lipid). In turn, the lipid recruits the effector molecule from the cytosol to the membrane. Positive feedback of this sort, involving translocating molecules, will be an important feature of our model as well. The PvH model does not include adaptation.

The above mentioned models share important features with our model. Other recent models relating to PI-mediated gradient sensing that take substantially different approaches have been developed as well (see, for example, 19 and 20).


1.5.4   Differences between the models

In addition to being based on different biochemical mechanisms, the models mentioned in Sec. 1.5.3 demonstrate qualitative differences in behavior, suggesting that they represent different modes of gradient sensing. For example, in the LI model the steady-state response of the cell always reflects the current stimulus, while in the NSL model,

once elicited by an above-threshold stimulus, a cellular response can persist. The PvH model requires a high baseline concentration of translocating molecule on the membrane for efficient gradient sensing. Qualitative comparisons of these models, addressing some of their differences, have been published in several recent reviews (5, 78).

### 1.5.5   Coupled positive feedbacks and translocation

Which elements in the above mentioned models lead to their noted differences? If the gradient sensing machinery of the cell is modeled as a reaction-diffusion system, we expect to find qualitative differences in systems that include different spatial couplings and/or exhibit different types of bifurcations.

The general picture of PI signaling presented in Secs. 1.3.2 and 1.3.3 suggests that regulation by coupled positive feedbacks and/or cooperative interactions is ubiquitous. Variations in the strengths of these feedbacks might lead to response bifurcations. Another ubiquitous feature of PI signaling is regulation by molecules that translocate to the membrane from a shared pool in the cytosol. Including these molecules might lead to a global coupling of responses at all points on the membrane. Using our model, we will investigate how variations in these features lead to qualitative differences in gradient sensing behavior such as those noted above. To our knowledge, ours is the first quantitative and systematic analysis of this sort.

### 1.6   Our model

Our model aims to capture the spatio-temporal dynamics of 3'PIs in gradient sensing. We will focus on the qualitatively different gradient sensing mechanisms that result

depending on how coupled positive feedbacks and translocating molecules are included. The possibilities that we will analyze derive directly from the generic features of PI regulation, as discussed above.

Here we give a brief overview of our model. The approach that we take and the kinds of simplifications that we will make are further discussed as our model is developed in Chapter 2.

### 1.6.1 Questions to be addressed

We have suggested that qualitatively different gradient sensing mechanisms might be possible, depending on how coupled positive feedbacks and translocating molecules are included. What are these qualitatively different possibilities (which we will refer to as 'Modes' of gradient sensing) and how can they be distinguished experimentally? How do the qualitative features of gradient sensing response depend on biochemical parameters and proposed regulatory mechanisms? Why might a given cell type make use of one Mode vs. another, and how might it adjust its biochemical parameters to make use of a given Mode or transition from one type of behavior to another? These are the types of questions that we will address with our model.

### 1.6.2 Overview of the model

To address the above questions, we will develop a mathematical model of PI-mediated gradient sensing at an intermediate level of detail, assuming a highly simplified geometry. Our model will consist of a set of reaction-diffusion equations for the spatio-temporal patterns of 3'PIs on the plasma membrane, as well as for the kinase that

generates them and the phosphatase that deactivates them. Our equations will be developed from proposed regulatory network, based on observation in several different types of cells. Because many relevant details remain unknown, simplifications will be made that preserve the topological features of this regulatory network and effectively include the feedbacks and translocation that we would like to study. Most of our model parameters will be unknown and we will set them empirically to reproduce characteristic responses in Dictyostelium cells. We will be particularly interested in identifying those parameters that are most important in shaping the qualitative features of our model's responses, and in the behavior of our model as a function of those parameters.

### 1.6.3   Model variants – a comparative approach

To analyze the qualitatively different gradient sensing possibilities that depend on how coupled positive feedbacks and translocating molecules are included in our model, we will develop four model variants by appropriately adjusting parameters. Thus, we will take a comparative approach to understand possible gradient sensing mechanisms, rather than analyzing a single version of our model.

### 1.6.4   Main results

We will show that each of our model variants demonstrates the characteristic gradient sensing behaviors enumerated in Sec. 1.2.6. These behaviors are generally elicited by strong stimuli in experiments whose aim is to observe a clear response. Differences between our model variants will become evident in responses to weaker stimuli. These differences are seen most clearly in simulated dose-response experiments, which

highlight transitions between efficient and inefficient gradient sensing. We will use these results to define criteria that distinguish between the Modes of gradient sensing illustrated by our model variants. Applying these criteria to analyze the parameter space of our model suggests that boundaries between different types of behavior can be sharp and regions that display a given behavior can be narrow with respect to variations of some combinations of parameters. Thus, efficient gradient sensing might require homeostatic mechanisms, which regulate combinations of parameters to be within specified ranges. Further, because cells in a given population will have a distribution of biochemical parameters, we expect that subpopulations might function in different regions of parameter space, making use of different Modes of gradient sensing. Finally, because biochemical parameters can vary during the course of development (e.g. through changes in gene expression), any given cell might transition between efficient and inefficient gradient sensing, and between different modes of gradient sensing, to suite its needs.

## 1.6.5 Distinctive features of our approach to modeling gradient sensing

Several features of our model are particularly important in distinguishing it from other recent models of gradient sensing. First, we have developed our model under the premise that several qualitative possibilities are consistent with current experimental observations, and that different cell types under different sets of conditions might demonstrate a range of gradient sensing behaviors. We have developed our model variants to investigate some of these possibilities. Second, we have focused on transitions that occur under non-ideal conditions, when gradient sensing responses begin to fail. All of our model variants reproduce characteristic gradient sensing behaviors under ideal conditions, and it is only

by analyzing these transitions that the qualitative behaviors demonstrated by our model variants can be distinguished. Finally, our model includes molecules whose dynamics can be visualized, and is developed from real biochemical mechanisms. Thus, our criteria to differentiate between Modes of gradient sensing can be applied to real cells, and our model can be used to investigate how the qualitative features of cellular response depend on proposed biochemical mechanisms.

## 1.7    Summary

Cellular **chemotaxis** is the process whereby biological cells respond with directed movement to gradients of small molecules, which are often ligands for cell surface receptors. To accomplish this behavior, these cells must transduce the external distribution of ligand into an internal distribution of molecules that mediate the mechanical and morphological changes necessary for movement. This transduction, referred to as **gradient sensing**, is an example of cellular **signal transduction** whereby cells modulate the activities and spatial localizations of subsets of molecules that affect cellular behaviors in response to external cues.

Gradient sensing in eukaryotic cells involves responses to both the spatial and the temporal features of chemotactic stimuli. In this dissertation, we will focus on gradient sensing in highly motile eukaryotic cells, such as **neutrophils** (which are immune cells) and **Dictyostelium** (an aggregating ameboid cell). Both of these types of cells respond to relative gradients of a few percent across their length over several orders of magnitude in absolute concentration with cellular velocities of order 10 $\mu m$/min. (about 1/2 cell length/min.).

**Phosphoinositides** (PIs) are signaling lipids in the membranes of eukaryotic cells. They are named according to the positions on their inositol head group that are phosphorylated.  Depending on how they are phosphorylated, PIs specifically recruit to the membrane cytosolic molecules that participate in a wide range of cellular functions, including those that regulate the phosphorylation state of PIs.  This **feedback regulation**, as well as the **spatial localization** of PIs on biological membranes, makes them well suited to mediate cellular processes that are highly regulated in space and time, such as chemotaxis.  In particular, PIs phosphorylated in the 3' position (**3'PI**s) have been found to be important for gradient sensing.

3'PIs are thought to function in gradient sensing by recruiting molecules to the membrane  that regulate the actin-based structures that drive protrusion at the leading edge of chemotaxing cells.  Recent experiments in cells that are round and immobile, due to drug induced disruption of actin structures, have demonstrated that the patterns of 3'PIs on the membrane in response to chemotactic stimuli in these cells are qualitatively similar to the patterns observed in normal cells.  These experiments suggest that aspects of **gradient sensing can be decoupled from motility**.  Our model aims to capture the dynamics of 3'PI on the plasma membrane in response to chemotactic stimuli, as well as of the molecules that regulate their production, in the absence of motility.

Our model will capture **three characteristic behaviors of gradient sensing**.
i) Cells adapt to the average stimulus.  In particular, if the stimulus is uniform, the response is transient and the state of the cell returns to baseline.
ii) In response to a small static gradient, the response is highly polarized and persistent.
iii) If the gradient of stimulus changes direction, the direction of response polarization

follows with some fidelity.

These behaviors can be observed in the dynamics of markers for 3'PIs on the plasma membrane, both in rounded and in motile cells.

Many details of the mechanisms regulating eukaryotic gradient sensing are still being discovered. For this reason, we will develop our model at an **intermediate level of detail** and focus on elements that affect the qualitative features of cellular response. Differences between recent models relating to PI-mediated gradient sensing, as well as the general features of PI regulation, suggest that qualitative different gradient sensing mechanisms might result depending on whether **coupled positive feedbacks lead to response bifurcations**, and on the way in which **molecules that translocate from the cytosol to the membrane affect spatial couplings**. We will generate four variants of our model to explore and characterize several such possibilities, and use simulations to suggest experiments that distinguish between them.

# Chapter 2: Model Development

## 2.1    Overview

In Chapter 1, we introduced eukaryotic gradient sensing as a cellular signal transduction process involved in chemotaxis. Data were discussed suggesting that aspects of gradient sensing may be decoupled from the morphological and mechanical changes necessary for motility and that signaling by 3' phosphoinositides (3'PIs) might mediate this transduction. We further suggested that regulation by coupled positive feedbacks and translocating molecules, both of which are generic features of PI signaling in cells, might lead to a range of gradient sensing possibilities. In this Chapter, we develop a reaction-diffusion model of 3'PI-mediated gradient sensing and define four variants of our model to investigate the qualitative possibilities that result.

Biological cells are complex entities and many approaches are possible to model their behaviors. Because many biochemical details and interactions that are relevant to eukaryotic gradient sensing remain unknown, we have suggested developing our model at an intermediate level of detail. Thus, we begin this chapter with a discussion of the general features of our model and the simplifications that are made (Sec. 2.2). These simplifications concern model elements or mechanisms that are either poorly understood or that do not seem essential to capture the characteristic behaviors and qualitative features that we will investigate.

Our model is derived directly from a suggested biochemical schematic that represents the network of interactions thought to regulate 3'PIs in gradient sensing cells. This schematic is developed on multiple levels in Sec. 2.3 and the qualitative features of our

35

biochemical scheme are highlighted in Figs. 2.3 and 2.4. In Sec. 2.5, we write a set of model equations based this schematic (summarized in Table 2.3). A qualitative discussion of our model's response to typical chemotactic stimuli is given in Sec. 2.5.5. Our model parameters are set empirically to reproduce characteristic gradient sensing behaviors and noted biochemical observations (Sec. 2.6 and Table 2.4).

In Sec. 2.7, parameters controlling the strengths of coupled positive feedbacks and the degree to which translocating molecules are depleted upon cellular stimulation are adjusted to define four variants of our model. The qualitative features of our model variants are illustrated schematically in Fig. 2.14 and are summarized in Table 2.7. These variants are further characterized in Chapter 3 and their responses to chemotactic stimuli are simulated in Chapter 4.

## 2.2    General features of the model

### 2.2.1    Geometry

We treat the cell as a disk with the cytosol as its interior and the plasma membrane as its perimeter, reflecting the geometry of a rounded cell where actin has been depolymerized. '$X$' marks the position along the membrane and is normalized so that the circumference of the cell is 1. Cytosolic molecules translocate to this boundary, along which 3'PIs diffuse, as depicted in Fig. 2.1.

Clearly, more pattern forming possibilities would be available if we treated the membrane as two-dimensional and considered cellular deformations. However the simplified geometry chosen adequately accounts for the gradient sensing possibilities that
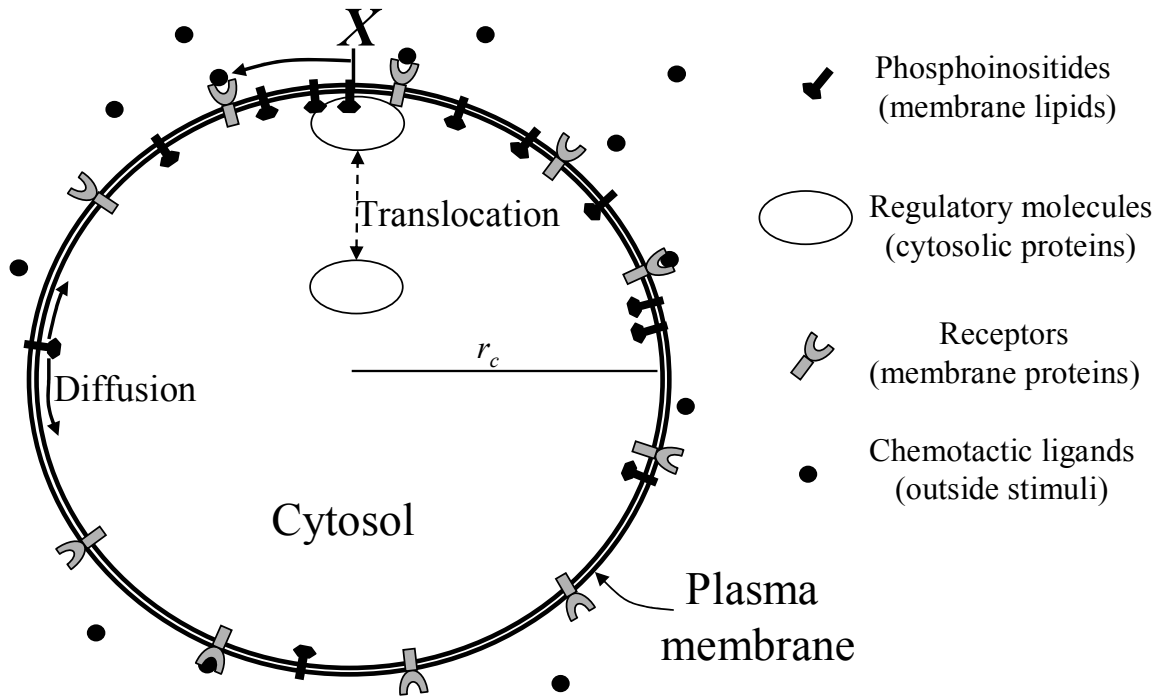
**Fig. 2.1. Model geometry**. The normalized coordinate, $X$, is periodic. Lipid diffusion along the membrane, and protein translocation from the cytosol to the membrane, are indicated. The cell radius, $r_c$, is equal to $1/2\pi$ in units where the circumference of the cell is 1. The labeled model components are discussed further in Secs. 2.2.2 and 2.2.4.

we will investigate. Extending our model to include a 2-d treatment of the membrane and possible deformations is a subject of current work.

### 2.2.2 Space/time scales

A rounded Dictyostelium cell might have a radius ($r_c$) of 4 $\mu m$, and the fastest cellular responses occur on time scales of seconds (81, 124). Diffusion coefficients for cytosolic proteins, membrane bound proteins, and membrane lipids, might be of order 20 $\mu m^2/s$, 0.03 $\mu m^2/s$ and 0.5 $\mu m^2/s$, respectively (52, 125, 126). On cellular length scales, these estimates result in diffusion times of order 100 $ms$, 100 $s$ and 1 $s$ ($t \sim r_c^2/2dD$, where 'd' is the dimension of the space and $D$ is the relevant diffusion coefficient).

Because of the noted differences in time scales, we simplify our model by treating cytosolic molecules as being uniformly distributed and membrane bound proteins as fixed. Lipid diffusion, however, occurs on the same time scale as cellular response and is explicitly calculated. Thus, in our model, cytosolic molecules act globally, coupling reactions at all points on the membrane, proteins act locally, and the spatial characteristics of lipids are context dependent. The discussed characteristic space/time scales and model simplifications are summarized in Table 2.1.

**Table 2.1. Characteristic space/time scales**

| Cellular component | Typical diffusion coefficient $D$ ($\mu m^2/s$) | Characteristic time scale $t = r_c^2/2dD$ (s) | Model treatment |
|---|---|---|---|
| Membrane proteins | 0.03 | > 100 | Fixed |
| Cytosolic proteins | 20 | < 0.1 | Uniform |
| Membrane lipids | 1 | ~ 1 | Diffusion calculated |

**Cellular response**
   Characteristic length scale ($r_c$): ~ 4 $\mu m$
   Characteristic time scale ($T$): ~ *Secs.*

The above simplifications, based on the suggested characteristic space/time scales for the types of molecules considered, are intuitive. While our simplified treatment will be sufficient to capture the gradient sensing possibilities that we will analyze, other authors have proposed that dynamics on faster time scales (of order $10 - 100$ *ms*) might be important for gradient sensing (127). These authors have suggested gradient sensing mechanisms that explicitly depend on the dynamics of cytosolic diffusion and on geometric constraints, though experimental evidence to support such a hypothesis does not yet exist.

In addition to the possible importance of such fast cellular processes, diffusion of large molecules through the cross-linked cytoskeletal network at the cell periphery might be significantly slower than our above estimate (125, 128-130).  Further, bulk diffusion can play an essential role in controlling surface instabilities when moving boundaries are considered (131).  Thus, explicitly considering cytosolic diffusion will be important for possible extensions of our model.

### 2.2.3    Coupling to outside stimuli

In both Dictyostelium and neutrophils, ligand binding activates receptors, which activate the heterotrimeric G-proteins (HTGs) to which they are coupled (see Fig. 1.5) in a pattern that closely reflects that of ligand in solution  (31, 81, 126).  Both receptor and HTG activation lead to recruitment and activation of PI3' kinases (PI3Ks), which are enzymes that phosphorylate PIs in the 3' position.  Many details of this activation remain unknown (132, 133).  For these reasons and because, at least in Dictyostelium, receptor and HTG desensitization do not seem to drive adaptation on time scales considered[#] (136), we let a single variable, $\mathcal{R}$, represent ligand-mediated receptor and HTG activation, which together drive PI3K recruitment and activation.  In our model, this defines the external stimulus at each point on the membrane.

### 2.2.4    Model Components

Our model will include the dynamics on the membrane of the 3'PIs thought to be relevant for gradient sensing.  The enzyme that produces them (a PI3K) and an enzyme that

---

[#] Receptor and HTG desensitization might play a more significant role for adaptation in neutrophil chemotaxis (134).  Such desensitization is also thought to affect receptor affinity in Dictyostelium, allowing sensitivity over many orders of magnitude in ligand concentration (25, 135).

dephosphorylates them (a PTEN phosphatase) will be included as well. We will calculate the dynamics at each point on the membrane for these enzymes, as well as the dynamics of a cytosolic inactive fraction (discussed further in Sec. 2.3).

The spatio-temporal dynamics of 3'PIs have been observed experimentally in Dictyostelium cells expressing fluorescently tagged protein domains that bind them specifically (such as particular **PH domains**). Several PI3Ks, and the single known PTEN, have also been fluorescently labeled in Dictyostelium as well. Sample data from the literature concerning these molecules are illustrated in Fig. 2.2.

### 2.2.5 Steady-state assumptions and intermediate level of detail

The dynamics of the molecules that regulate the above-discussed components of our model are generally less well characterized (in several cases the molecules have not yet been identified experimentally). Further, we are not aware of any observed delays in cellular response, which are specifically associated with activation of these regulatory molecules. Thus, we will introduce simplifications to effectively include them in our model. Concentrations of regulatory molecules whose dynamics are not thought to be directly relevant to the role of 3'PIs in gradient sensing will be treated as fixed. Concerning regulatory molecules whose dynamics are likely to be an integral part of 3'PI regulation in gradient sensing, we introduce the following simplifying procedure: kinetic equations are written for the dynamics of these molecules; time derivatives are set to zero; the resulting steady-state equations are used to express the concentrations of these molecules in terms of our model variables. This procedure will be illustrated when we derive our scaled model equations in Secs. 2.5.2 and 2.5.3.

**a)** Responses to uniform stimuli

PTEN labeled in Dictyostelium
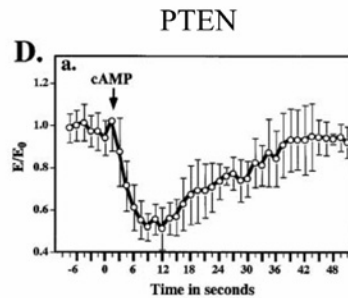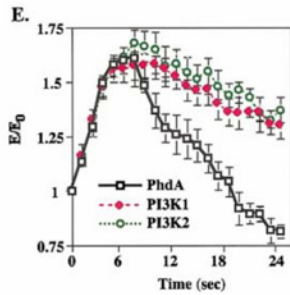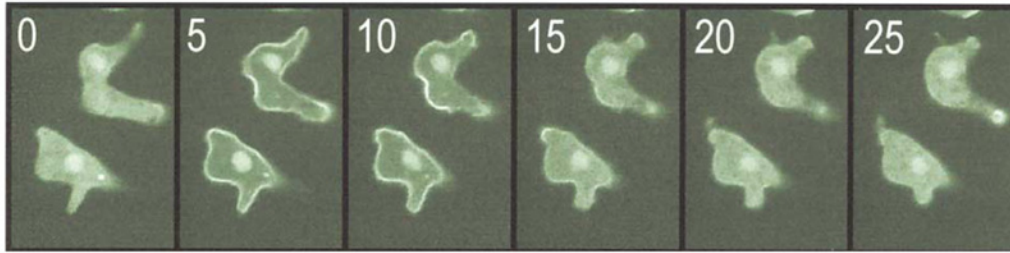




Time courses in response
to uniform stimuli

**b)** SPatial distribution of signaling molecules in response to a gradient

3'PI label
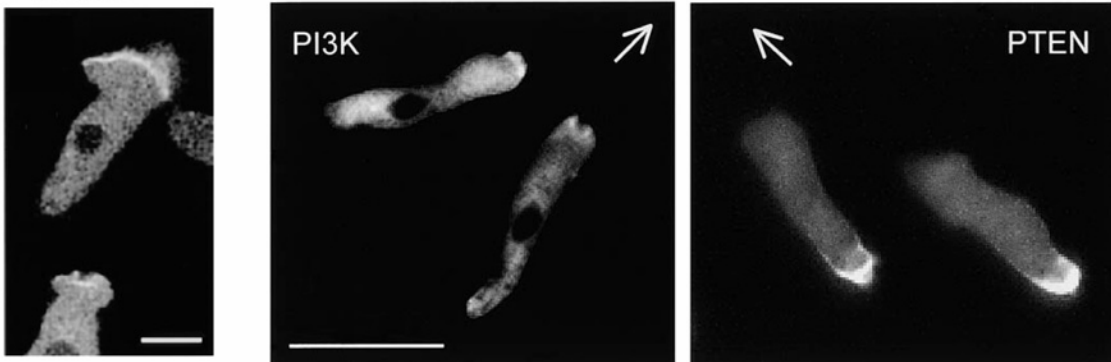


**Fig. 2.2. Sample images of fluorescently labeled cells.** All images are of
Dictyostelium cells responding to cAMP. 3' PIs are visualized in cells that have been
stably transfected to express domains of proteins that are thought to specifically bind
3'PIs, and which are tagged with GFP or a variant thereof (33). PI3K and PTEN
dynamics are visualized in cells that stably express chimeras of those proteins, also
tagged with GFP variants as well. **a)** In response to a uniform increase in cAMP, 3'PIs
are produced transiently on the membrane, PI3K translocates to the membrane, and
PTEN is removed. The depicted microscopy images are taken from a movie of PTEN
translocation from the membrane (reproduced with permission from reference 137).
Time courses which attempt to quantify the change in fluorescence on the membrane are

41

also illustrated; PhdA is a protein domain the binds specifically to 3'PIs; PI3K1 and PI3K2 are isoforms of PI3K in Dictyostelium that are thought to be relevant for gradient sensing (reproduced with permission from reference 132). **b)** Spatial localization of signaling molecules in response to a gradient of cAMP generated by a micropipette. 3'PIs are produced and PI3K is recruited to the leading edge of the cell, while PTEN is removed. For the image with 3'PIs labeled, the pipette is located to the top right and the scale bar represents 5.6 $\mu m$ (reproduced with permission from reference 79). For the images of PI3K and PTEN distributions, the pipette location is indicated by the arrow and the scale bar corresponds to 15 $\mu m$ (reproduced with permission from reference 4). (**Fig. 2.2.** caption, cont.)

The above procedure has the virtues of preserving steady-state solutions, as well as many effects of translocation; i.e. it preserves the qualitative features that we wish to investigate (see Secs. 1.5.5 and 1.6.1; also Sec. 2.7.4). Many uncertain biochemical details will no longer appear explicitly in our equations; further, our equations will often be consistent with alternate biochemical mechanisms that give rise to similar qualitative behaviors. On the other hand, our equations will be directly developed from a biochemical scheme thought to be relevant for 3'PI-mediated gradient sensing, and our model parameters will be related to real cellular biochemical parameters. Thus, we will be able to investigate how qualitative behaviors depend on biochemical parameters. In this way, our model will be developed at an intermediate level of detail (levels of detail in models of cellular signal transduction were discussed in Secs. 1.4.4 and 1.4.5).

## 2.3    Biochemical scheme

Our biochemical scheme for 3'PI regulation in gradient sensing is developed in several stages. First, biochemical observations that motivate our choice of model variables, and suggest a topology for the network of interactions that regulates their dynamics, are discussed in Sec. 2.3.1; a modular interpretation of this network is given in Sec. 2.3.2.

We then propose biochemical mechanisms that account for the suggested regulatory loops. Where the relevant mechanisms have not been identified in gradient sensing cells, we suggest regulatory mechanisms based on interactions that have been studied in the context of other cellular behaviors.

The figures in this section will schematize the biochemical interactions included in our model at various levels of detail, as is appropriate to the discussion in each subsection. The interactions associated with regulation of each of our model variables will be represented in more detail in Sec. 2.5, when our model equations are developed.

### 2.3.1  Biochemical observation, model variables and network topology

Our model variables and the topological features of the network of interactions that regulates them are summarized in Fig. 2.3 at the end of this subsection. First, we discuss regulation of each of our model components separately.

*2.3.1a  3'PIs*

The 3'PIs thought to be relevant in gradient sensing are $PI(3,4,5)P_3$ and $PI(3,4)P_2$. Both specifically act to recruit a similar set of cytosolic molecules to the membrane (66, 87, 103). Production of $PI(3,4,5)P_3$ via phosphorylation of $PI(4,5)P_2$ by a PI3K , and of $PI(3,4)P_2$ via dephosphorylation of $PI(3,4,5)P_3$ by a PI 3' phosphatase such as SHIP (138), are thought to be the relevant production pathways (87, 138).

$PI(3,4)P_2$ dynamics generally follows $PI(3,4,5)P_3$ dynamics with a slight lag (139). However, there is evidence in Dictyostelium cells suggesting that disruption of a phosphatase which acts on both (PTEN, discussed below) affects their dynamics differently (140). Thus, we will model $PI(3,4,5)P_3$ and $PI(3,4)P_2$ separately and use the

scaled variables, $P_3$ and $P_2$, to represent their concentrations. Their sum, which we denote $P_n$, is a primary output of our model.

There is evidence in neutrophil-like cell lines for a positive feedback from 3'PIs to delivery of PI(4,5)P$_2$ to PI3K, involving small GTPases of the Arf and Rho family (102, 141, 142). This feedback, which enhances substrate delivery for production of PI(3,4,5)P$_3$, is highlighted by **Loop I** in Fig. 2.3.

### 2.3.1b  Membrane-bound PI3K/PTEN

The enzyme that generates 3'PIs – a PI3K – and an enzyme that dephosphorylates 3'PIs in the 3' position – the PTEN phosphatase – are also essential components of our model. As mentioned, PI3K localization and activation are thought to be coupled to outside stimuli (see Sec. 2.2.3). Further, in Dictyostelium, PI3K localization has been observed to parallel 3'PI localization upon cellular stimulation (132), and PTEN translocation to the membrane has been observed to occur in an inverse pattern (132, 137); these observations were illustrated in the sample data of Fig. 2.2. If we consider 3'PIs to be the primary signal that localizes other molecules in gradient sensing, this suggests a positive feedback from 3'PIs to the enzymes that produce and degrade them, represented by **Loop II** in Fig. 2.3. In our model, the variables $K_m$ and $T_m$ will represent scaled concentrations on the membrane of PI3K and PTEN, respectively.

### 2.3.1c  Phosphorylated/inactive PI3K and PTEN in the cytosol

Because cellular response eventually adapts to the average stimulus, as do PI3K and PTEN activities (132, 137), there must be some form of integral feedback regulating cellular responses (121). We represent this negative feedback for adaptation by **Loop III**

in Fig. 2.3. The mechanism of this feedback is currently unknown, though several

possibilities have been suggested (48). Both PI3K and PTEN activity are known to be

controlled by phosphorylation in some cell types (143, 144), and we will suggest this as a

mechanism for global inhibition in Sec. 2.3.3d. We use the scaled variables $K_c{}^*$ and $T_c{}^*$

represent the fractional concentrations of PI3K and PTEN, respectively, which are

cytoplasmic and phosphorylated; these are catalytically inactive in our model.

## 2.3.2   Modular interpretation

The topology of the regulatory network, suggested by the observations noted in Sec. 2.3.1

and illustrated in Fig. 2.3 maps easily onto the modular scheme suggested for
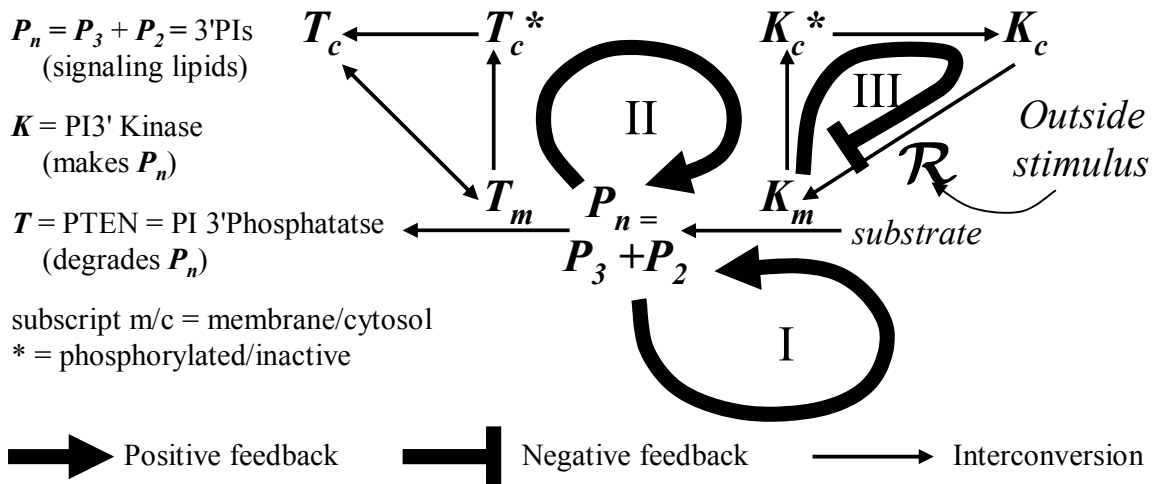


**Fig. 2.3.  Model variables and network topology.**  Regulatory loops are represented by bold arrows and labeled with Roman numerals. Variables drawn along arrows represent enzymes that are necessary for the depicted interconversion (e.g. $\mathcal{R}$ is required for PI3K translocation to the membrane).  Details of biochemical mechanisms are discussed in Sec. 2.3.3. Negative feedback **Loop III** is drawn as regulating PI3K translocation in anticipation of our proposed adaptation mechanism (see Sec. 2.3.3d).

gradient sensing in Sec. 1.5.2. We will consider positive feedback **Loops I** and **II** to

constitute an amplification module. These feedbacks are driven by receptor and HTG

activation (represented by the scaled variable, $\mathcal{R}$, as discussed in Sec. 2.2.3), which drive

cytosolic unphosphorylated PI3K ($K_c$) to the membrane. Their product will be

interpreted as a driving parameter for our model. Negative feedback **Loop III** will be

treated as an adaptation module. This modular interpretation, which is illustrated

schematically in Fig. 2.4, will be important to develop a more intuitive understanding of

our model and its variants (discussed further in Secs. 2.5.5 and 2.7, as well as Chapter 3).

### 2.3.3 Proposed biochemical mechanisms

The biochemical mechanisms that might account for the above noted observations and

suggested regulatory loops are still not well understood. Possible mechanisms, from
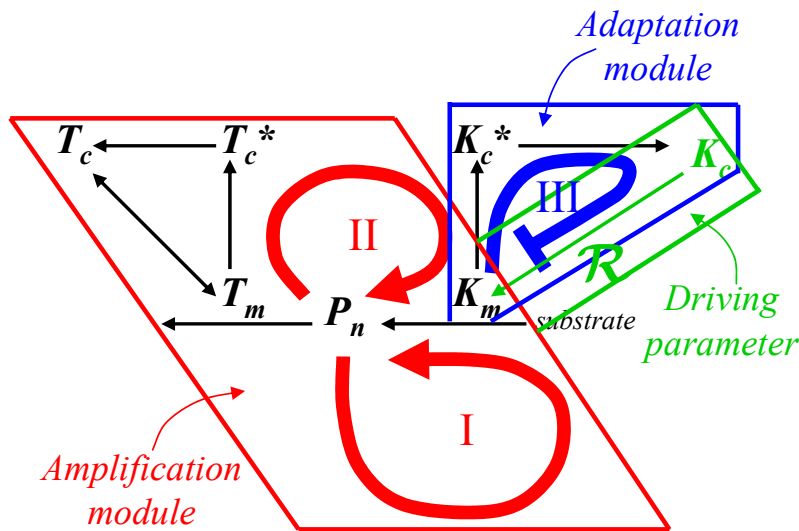


**Fig. 2.4. Modular structure.** Boxes and color-coding are used to indicate the features discussed in the text. These will be more formally defined when we develop and discuss our model equations (see, in particular, Sec. 2.5.5). Elements of the amplification module will be adjusted to define variants of our model, which demonstrate qualitative differences in gradient sensing mechanisms (Sec. 2.7). Notation is as in Fig. 2.3.

**Loops I** – Positive feedback enhancing substrate delivery to PI3K.

**Loops II** – Positive feedback regulating enzyme activity.

**Loop III** – Negative feedback for adaptation.

which we will develop our model equations, are schematized and discussed individually below; experimental observations that suggest these mechanisms are summarized as well.

The complete biochemical scheme, upon which our model is based, is schematized in Fig. 2.8 at the end of this subsection.

*2.3.3a* **Loop I** *– Positive feedback through substrate delivery*

A possible mechanism for the feedback in **Loop I**, many elements of which have been studied in neutrophils or neutrophil-like cells, is depicted in Fig. 2.5. 3'PIs recruit GTP exchange factors (GEFs) to the membrane (①), where they catalyze the exchange of GDP for GTP in specific small GTPases (gP) of the Arf and Rho family (145, 146) (②). These GTPases are then activated and stabilized on the membrane (147, 148), and play roles (together with their regulators) in remodeling the membrane and actin network (67, 149, 150). Some have been shown to stimulate PI(4)P5′ kinases (PIPKs) to make additional PI(4,5)P$_2$ (③) (141, 142).

Experimental observations do not indicate an accumulation of free PI(4,5)P$_2$ upon cellular stimulation (151, 152), suggesting that the PI(4,5)P$_2$ generated by the feedback in **Loop I** is used immediately. This observation could be explained if the generated PI(4,5)P$_2$ was bound to a transfer protein (PITP) (④) and passed directly to PI3K for conversion to PI(3,4,5)P$_3$ (⑤). The importance of PITP activity for 3'PI production has been suggested by experiments in neutrophils (153), though it has not been investigated in Dictyostelium and the role that it might play in gradient sensing is not yet clear. In our model, we assume this mechanism and do not include the dynamics of free PI(4,5)P$_2$. This simplification is consistent with the lack of clear evidence for spatial gradients of free PI(4,5)P$_2$ in chemotaxing cells (151, 154).
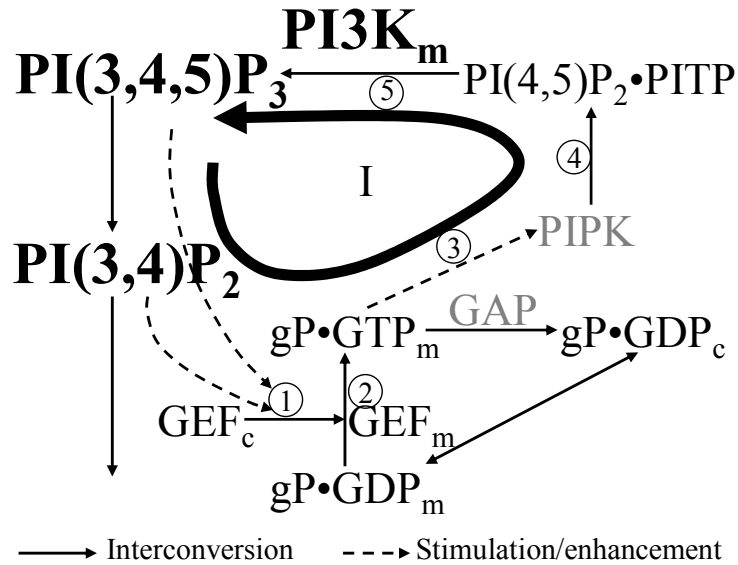
**Fig. 2.5. Mechanisms for Loop I.** Processes discussed in the text are numbered. Molecules that will be modeled directly are labeled in large bold font, those that will be included through steady-state assumptions are labeled in normal font, and those whose concentrations will be treated as fixed are labeled in grey. A GAP (GTPase Activating Protein), which is generally considered essential for hydrolysis of GTP (conversion of GTP to GDP) by the GTPase (gP), has been included in the diagram, though its regulation is not modeled (several GAPs are known to bind $PI(4,5)P_2$). Abbreviations have been given in the text, and are summarized in Fig. 2.8.

Feedback regulation by small GTPases is the most essential feature of **Loop I** that we would like to capture in our model. The action of GEFs, which often exist in the cell at low concentrations, is essential for small GTPase activation. Thus, it is possible that the relevant GEFs involved in **Loop I** may become depleted from the cytosol upon cellular stimulation, saturating its activity. Under these conditions, competition for GEF might act to couple responses over the entire membrane. We will consider this possibility when we define variants of our model.

*2.3.3b* ***Loop II*** *– Positive feedback through enzyme regulation*

The biochemical mechanisms for the suggested feedback in **Loop II** have not yet been identified experimentally. To capture the qualitative features of this feedback in our model, we propose the mechanisms depicted in Fig. 2.6. 3'PIs recruit an as yet
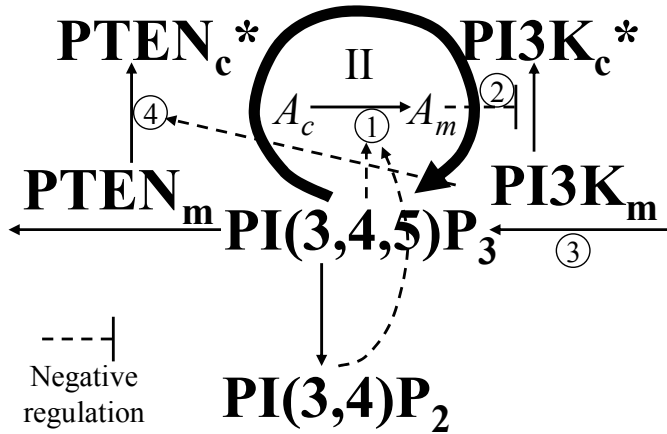
**Fig. 2.6. Mechanisms for Loop II.** '*A*' represents an unidentified molecule that stabilizes PI3K on the membrane. In our model, it will do so by forming a complex with PI3K and inhibiting PI3K phosphorylation (②). Other possibilities for this feedback are discussed in Sec. 2.5.4. Abbreviations and notation are as in the text and in Fig. 2.5.

unidentified molecule (labeled '*A*') to the membrane (①), which stabilizes membrane-bound PI3K (②). Membrane-bound PI3K then produces more $PI(3,4,5)P_3$ (③). To account for a PTEN dynamic inverse to that of PI3K, we propose that PI3K, in its capacity as a protein kinase (155), or another molecule whose dynamics parallels PI3K dynamics, phosphorylates PTEN (④). In our model, phosphorylated PTEN is cytosolic and inactive.

Our proposed mechanisms for **Loop II** are a convenient way to reproduce the PI3K and PTEN translocation dynamics observed experimentally in Dictyostelium (see Fig. 2.2 and Sec. 2.3.1b). The protein kinase activity of PI3K and regulation of PTEN activation by phosphorylation have been studied in several types of mammalian cells. However, the roles that these processes might play in chemotaxis and gradient sensing are unclear, and neither has been investigated in Dictyostelium. In addition, to our knowledge, an interaction between PI3K and PTEN has not been directly investigated experimentally in any cell type. Further investigation of the plausibility of translocation dynamics being regulated by PI3K activity is a subject of current work.

*2.3.3c* **Loop III** *– Negative feedback for adaptation*

The mechanisms of response adaptation in gradient sensing, which we have represented

by negative feedback **Loop III** in Fig. 2.3, are not yet understood experimentally. To

account for this feedback, we propose the mechanism depicted in Fig. 2.7. PI3K on the

membrane is phosphorylated by an as yet unidentified kinase[#] (labeled '*B*'), which is

constitutively active on the membrane (①). Phosphorylated PI3K is cytosolic and

inactive in our model. We will assume that the reaction that dephosphrylates PI3K in the

cytosol is saturated (②) (this assumption is discussed further in Sec. 2.5.3d); PI3K

phosphorylation acts as a mechanism of global inhibition in our model because it depletes

the cytosolic pool of active/unphosphorylated PI3K, which is a shared pool for

recruitment to the entire membrane.

   Regulation of PI3K activity by phosphorylation has been studied in several types of

mammalian cells, but not in Dictyostelium; the role that this regulatory mechanism might

play in gradient sensing is still unclear. In our model, it is a convenient mechanism that

accounts for response adaptation, but requires further experimental investigation.
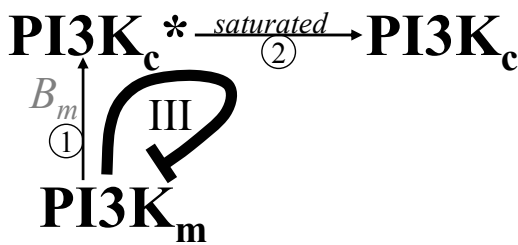


**Fig. 2.7. Mechanisms for Loop III.** '*B*' represents the unidentified kinase that phosphorylates PI3K. Abbreviations and notation are as in Fig. 2.5.

---

[#] An attractive alternative that leads to the same set of equations in our treatment without proposing an unidentified kinase, is that PI3K autophosphorylates. This has been shown to occur in some cellular systems, though the role that it plays in chemotaxis is unclear (143, 155-158). To our knowledge, PI3K autophosphorylation has not yet been directly investigated in Dictyostelium. Further, recent data in Dictyostelium cells where PI3K activity has been inhibited suggests that adaptation mechanisms independent of PI3K activity must be relevant as well. Thus, even if it plays an important role, autophosphorylation cannot be the sole mechanism for response adaptation in Dictyostelium. Investigation of cellular response under conditions of PI3K inhibition is a subject of current work.

*2.3.3d  Constitutive processes*

The above-proposed biochemical mechanisms will be used to account for the characteristic behaviors of gradient sensing, as enumerated in Sec. 1.2.6, and for the observations noted in Sec. 2.3.1.  In addition to the processes discussed above, our model will also include constitutive unregulated processes (not depicted in Figs. 2.5 – 2.8). These will be assumed to occur in parallel with the regulated processes of our model and will be represented by constant terms in our equations.

Unregulated processes are included in our model because inhibition of any of the processes whose regulation is modeled generally does not lead to complete inactivation of the signaling network.  Further, our model treatment of cellular biochemical processes is at best phenomenological, and only a subset of the interactions are included that might regulate our model variables in real cells.  Thus, our inclusion of constitutive processes might be interpreted as a lowest order attempt to include some of the other regulatory processes that undoubtedly exist.  Specific constitutive terms are discusses briefly when we develop our model equations in Sec. 2.5.

**2.4     Assessing the biochemical scheme**

The complete biochemical scheme, from which our model will be developed, is represented schematically in Fig. 2.8.  Schematics of this sort are often used to represent the networks of interactions that regulate cellular behaviors such as gradient sensing. However, there are many difficulties and subtleties involved in developing and interpreting them.  For example, many relevant interactions are often unknown, and it may be necessary to propose mechanisms to complete the schematic and to accounts for
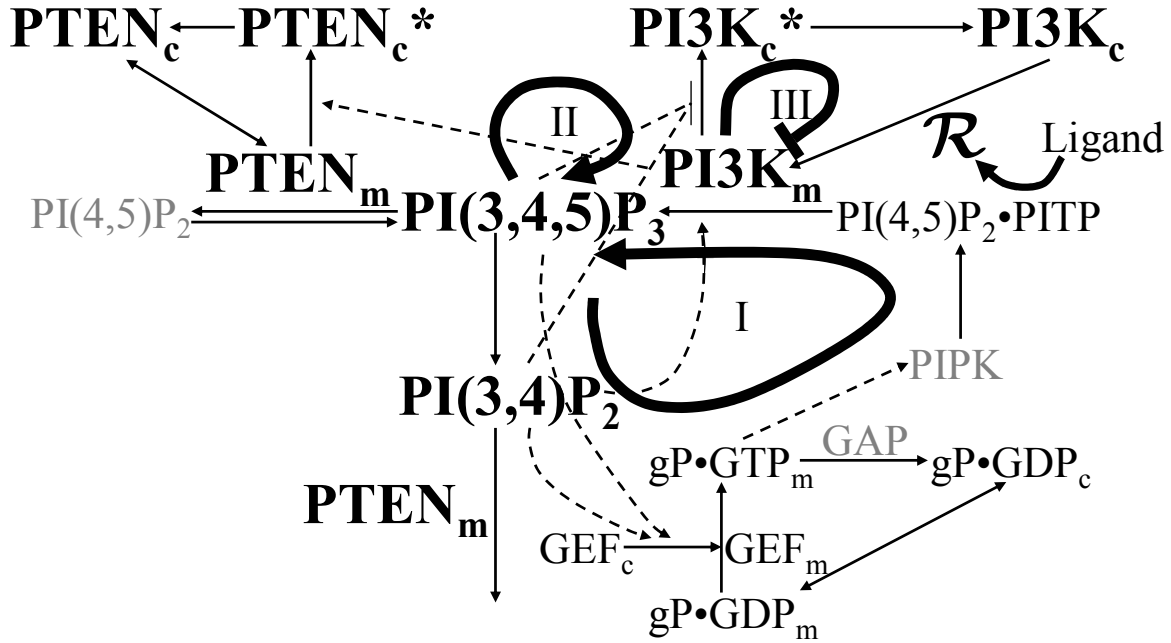
**Fig. 2.8. Complete biochemical scheme.** Notation is as in Figs. 2.5-2.7. Unidentified molecules '*A*' and '*B*' are not explicitly represented, nor are constitutive processes that act in parallel with the regulated processes of our model. Abbreviations used: $PI(3,4,5)P_3$ = PI(3,4,5) tris-phosphate; $PI(4,5)P_2$ = PI(4,5) bis-phosphate; $PI(3,4)P_2$ = PI(3,4) bis-phosphate; PI3K = PI 3'kinase; PTEN = PI 3' phosphatase (); $\mathcal{R}$ = chemotactic stimulus; gP = small GTPase; GEF = GTP exchange factor; PITP = PI transfer protein; PIPK = PI(4)P 5'Kinase; GAP = GTPase activating protein. Subscripts c/m denote cytosolic/membrane.

experimental observations. Relevant data often comes from multiple cell types, and a single cell may not employ all of the proposed regulatory mechanisms. Multiple isoforms will exist of most of the molecules involved, and they will interact with multiple partners, possibly functioning in other cellular processes that are not considered. Few rate constants and biochemical parameters have been measured directly in intact cells.

Difficulties of the sort discussed above motivate the approach that we have taken to modeling 3'PI regulation in gradient sensing. In particular, we will include an intermediate level of detail, making many simplifications and focusing on qualitative features of cellular response. We will explore a wide range of model parameters to

investigate these qualitative features and their dependence on proposed biochemical mechanisms.

Given the complexity of cellular behaviors, and the many unknowns relating to their regulation, other theoretical approaches are likely to yield further insight as well.

## 2.5    Model equations

To develop our model, we will assume linear mass-action kinetics (Sec. 2.5.1) to write a set of unscaled equations representing the biochemical processes schematized in Fig. 2.8 (Sec. 2.5.2). Steady-state assumptions are then employed, and quantities scaled (as discussed in Sec. 2.2.5) to write a set of equations for our six model variables. These are discussed term by term in Sec. 2.5.3 and parameters that are important in shaping the qualitative features of our model are emphasized. Our equations are summarized in Table 2.3 of Sec. 2.5.4 and a qualitative discussion of how our model accounts for the characteristic behaviors of gradient sensing is given in Sec. 2.5.5.

### 2.5.1   Reaction kinetics

In order to derive a set of model equations from the biochemical scheme in Fig. 2.8, we must assume functional forms to represent the depicted biochemical processes. Because we do not aim to investigate detailed reaction kinetics for biochemical processes inside of the cell, which are generally unknown, we will thus assume linear mass-action kinetics unless otherwise noted. That is, the concentrations of each molecule involved in a given reaction will appear linearly in our equations. In several instance (that will be discussed) we will assume Michaelis-Menten type kinetics.

## 2.5.2 Unscaled equations and model reduction – a worked example

As an example of how our scaled model equations are derived from a more complete set of unscaled equations, we consider the regulation of PI3K on the membrane. This includes the feedback in **Loop II** and coupling to outside stimuli. The relevant interactions are summarized in Fig. 2.9.

### 2.5.2a Symbolic representation of reactions in kinetic equations

We can symbolically represent the processes regulating PI3K dynamics on the membrane as follows:

$$\frac{\partial\left[\mathrm{PI3K_m}\right]}{\partial t} = \mathcal{P}_K\left\{\underbrace{\left(\boldsymbol{R}\|\left[\mathrm{PI3K_c}\right]\right)}_{3a},\underbrace{\left(\xi_R\|\left[\mathrm{PI3K_c}\right]\right)}_{3a'}\right\} - \mathcal{D}_K\left\{\underbrace{\left(\left[B_\mathrm{m}\right],\left[A_\mathrm{m}\right]\|\left[\mathrm{PI3K_m}\right]\right)}_{3b}\right\}. \quad (2.1)$$



**PI3K$_c$\***

$B_m$ (3b)

**PI3K$_m$**  $\boldsymbol{R}$ (3a) **PI3K$_c$**

**3'PIs**  $-A_m$•PI3K$_m$  (3a') $\xi_R$

(11a) (12a) (12b)

$A_c$  $A_m$

(11b)

$A_m$•PI3K$_m$
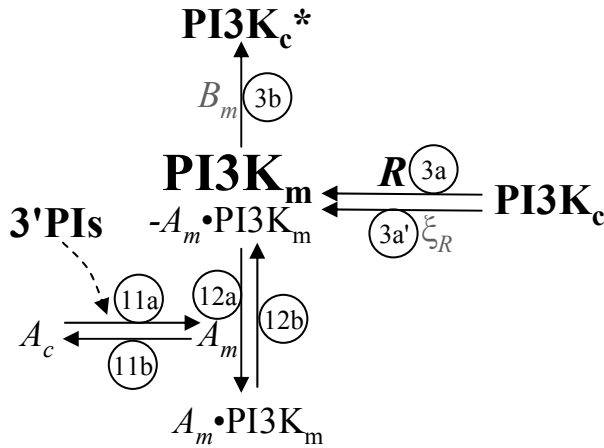
**Fig. 2.9. Regulation of membrane-bound PI3K.** In order to write kinetic equation, the depiction here is more detailed than the corresponding part of the schematic in Fig. 2.8. $\boldsymbol{R}$ is the unscaled counterpart of our model variable, $\mathcal{R}$, which represents receptor and HTG activation that drive PI3K to the membrane. Constitutive processes, occurring in parallel with the regulated processes of Fig. 2.8, are represented by the symbol '$\xi$' (e.g. $\xi_R$) and labeled with a prime (e.g. 3a'). PI3K$_m$ represents total membrane-bound PI3K (assumed to be catalytically active). PI3K bound to molecule $A$ ($A_m$•PI3K$_m$) cannot be phosphorylated in our model (see Sec. 2.3.3). PI3K$_m - A_m$•PI3K$_m$, which appears at the center of the schematic, thus represents the portion of membrane-bound PI3K can be phosphorylated. Terms in our kinetic equations below are numbered in correspondence to the labeled interactions. The model element, for which we would like to write a kinetic equation, is represented in larger font (PI3K$_m$). Notation and abbreviations are otherwise as in Fig. 2.8.

The function $\mathcal{P}_K\{\ \}$ represents processes that increase the concentration of PI3K on the membrane, and the function $\mathcal{D}_K\{\ \}$ represents processes that decrease PI3K on the membrane. Each relevant process is represented in parentheses in Eq. 2.1 and labeled below the equation in correspondence with Fig. 2.9. Concentrations are denoted by strait brackets ('[ ]'). To represent an enzyme or other molecule, $E_X$, acting on or regulating another molecule $Y$ that changes its state, we use the notation, $([E_X]\|[Y])$. Constitutive processes are generally represented by the symbol, $\xi$, and labeled with a prime (e.g. 3$a'$, see Sec. 2.3.3d for discussion).

Based on the above conventions, process 3$a$ in Eq. 2.1 represents activated receptors and HTGs, (whose concentration on the membrane is represented by the unscaled variable $R$) acting to recruit PI3K from the cytosol to the membrane (i.e. PI3K$_m$ is converted to PI3K$_c$). Process 3$a'$ represents unregulated recruitment of PI3K to the membrane. This will define the baseline state of the cell in our model, since it will drive the feedbacks of our amplification module in the absence of receptor activation (depicted in Fig. 2.4). Process 3$b$ represents removal of PI3K from the membrane due to phosphorylation by an unidentified kinase ($B_m$) that is constitutively on the membrane (**Loop III**). This phosphorylation is regulated by an unidentified molecule '$A$' that binds stochiometrically to PI3K – our model assumes that PI3K bound to molecule $A$ cannot be phosphorylated, and that molecule $A$ is recruited to the membrane by 3'PIs, as indicated. This will account for the feedback in **Loop II**, as described below. Diffusion of PI3K along the membrane is not included in our model (we assume that the on/off rates for PI3K binding to the membrane are faster than its diffusion along the membrane on cellular length scales, as discussed in Sec. 2.2.2).

55

## 2.5.2b  Writing unscaled kinetic equations

Assuming linear kinetics, we write the following equation to model the processes represented in Eq. 2.1:

$$\frac{\partial\left[\text{PI3K}_\text{m}\right]}{\partial t} = \underbrace{\kappa_K^+\left[\text{PI3K}_\text{c}\right](\underset{3a}{\underbrace{R}} + \underset{3a'}{\underbrace{\xi_R}})}_{} - \underbrace{\kappa_K^-\left[B_m\right]\left(\left[\text{PI3K}_\text{m}\right] - \left[A_m\bullet\text{PI3K}_\text{m}\right]\right)}_{3b}, \tag{2.2}$$

where $\kappa_K^+$ and $\kappa_K^-$ are forward and backwards rate constants, respectively, and the parameter $\xi_R$ may include both rate constants and concentrations of molecules whose regulation is not modeled (assumed fixed). $\left[A_m\bullet\text{PI3K}_\text{m}\right]$ represents the concentration of PI3K on that is bound by molecule $A$; the factor $\left(\left[\text{PI3K}_\text{m}\right] - \left[A_m\bullet\text{PI3K}_\text{m}\right]\right)$ represents the local unbound fraction of PI3K on the membrane, which can be phosphorylated and return to the cytosol[#].

The notation of Eq. 2.1 is used further in Appendix A to symbolically represent the biochemical processes in Fig. 2.8.  Below, we directly assume linear kinetics and write equations for the regulation of molecule $A$ and its complex with PI3K on the membrane, as in Eq. 2.2.

For the concentration of molecule $A$ on the membrane, we write the following equation:

$$\frac{\partial\left[A_m\right]}{\partial t} = \underbrace{\kappa_A^+\left[A_c\right]\left[3'\text{PI}\right]}_{11a} - \underbrace{\kappa_A^-\left[A_m\right]}_{11b}, \tag{2.3}$$

where $\left[3'\text{PI}\right] \equiv \left[\text{PIP}_3\right] + \left[\text{PI(3,4)P}_2\right]$. \hfill (2.3a)

---

[#] We assume that PI3K bound to $A$ is still catalytically active.  Total PI3K on the membrane (PI3K$_\text{m}$, which includes the portion complexed with molecule $A$) is thus the appropriate specie to consider where PI3K activity is included in our model.

Term 11*a* represents cytosolic $A$ ($A_c$) binding to 3'PIs on the membrane with rate constant $\kappa_A^+$. Term 11*b* represents spontaneous returns of $A$ to the cytosol.

To describe complex formation between PI3K and molecule $A$, we write the following equation:

$$\frac{\partial\left[A_m\bullet\text{PI3K}_m\right]}{\partial t} = \underbrace{\kappa_{AK}^+\left[A_m\right]\left(\left[\text{PI3K}_m\right]-\left[A_m\bullet\text{PI3K}_m\right]\right)}_{12a} - \underbrace{\kappa_{AK}^-\left[A_m\bullet\text{PI3K}_m\right]}_{12b}. \tag{2.4}$$

Term 12*a* describes complex formation, with rate constant, $\kappa_{AK}^+$, between molecule $A$ on the membrane ($A_m$) and the fraction of PI3K that is not already bound to $A$; we assume that the reaction is limited by the availability of PI3K[#]. Term 12*b* describes spontaneous dissociation of the complex $A_m\bullet\text{PI3K}_m$, with rate constant $\kappa_{AK}^-$.

*2.5.2c  Model reduction using steady-state assumptions*

Because the properties of molecule $A$ are unknown, we simplify our analysis by setting the LHS of Eqs. 2.3 and 2.4 to zero; the concentration of the complex, $A_m\bullet\text{PI3K}_m$, can then be expressed in terms of components of our model variables (as discussed in Sec. 2.2.5). We find:

$$\left[A_m\bullet\text{PI3K}_m\right] = \frac{\left[\text{PI3K}_m\right]\left[3'\text{PI}\right]/\kappa_{AK}}{\left[3'\text{PI}\right]/\kappa_{AK}+1}, \tag{2.5}$$

where $\kappa_{AK} = \dfrac{\kappa_A^-\kappa_{AK}^-}{\kappa_A^+\left[A_c\right]\kappa_{AK}^+}$, and we have further assumed that only a small fraction of $A$ translocates to the membrane ($A_c \sim$ constant). Thus, the fraction of PI3K on the

---

[#] PI3K generally exists in cells at low concentrations. We thus assume that molecule $A$ is relatively more abundant on the membrane than PI3K. $A_m$ will thus approximate the concentration of $A$ on the membrane that is not already complexed with PI3K.

membrane, which is not bound to molecule $A$ – this fraction is free to be phosphorylated and return to the cytosol – is given by:

$$1 - \frac{\left[A_m \cdot PI3K_m\right]}{\left[PI3K_m\right]} = \frac{1}{\left[3'PI\right]/\kappa_{AK} + 1} \,. \tag{2.6}$$

Using Eq. 2.6, we can rewrite Eq. 2.2 as:

$$\frac{\partial\left[PI3K_m\right]}{\partial t} = \kappa_K^+ \left[PI3K_c\right] (\underbrace{\boldsymbol{R}}_{3a} + \underbrace{\xi_R}_{3a'}) - \underbrace{\kappa_K^- \left[B_m\right]\left[PI3K_m\right]\frac{1}{\left[3'PI\right]/\kappa_{AK} + 1}}_{3b} \,. \tag{2.7}$$

The form obtained for term $3b$ describes phosphorylation by molecule $B$, with rate constant, $\kappa_K^-$, of the fraction of PI3K on the membrane not bound to molecule $A$. In this way, 3'PIs on the membrane prevent PI3K return to the cytosol, accounting for the feedback regulation of PI3K represented by **Loop II** in our model.

*2.5.2d  Conservation relations can be used to eliminate model variables*

In our model, PI3K can be on the membrane, and either phosphorylated or unphosphorylated in the cytosol. The following equation represents conservation of total PI3K, and can be used to eliminate $\left[PI3K_c\right]$ from Eq. 2.7 (as an alternative, $PI3K_c*$ can be eliminated, as is convenient):

$$\underbrace{\left[PI3K_0\right] A_{cell}}_{\text{Total PI3K}} = \underbrace{\left[PI3K_c\right] A_{cell}}_{\substack{\text{Total cytosolic} \\ \text{unphosphrylated PI3K}}} + \underbrace{\left[PI3K_c*\right] A_{cell}}_{\substack{\text{Total cytosolic} \\ \text{phosphrylated PI3K}}} + \underbrace{\int_0^1 \left[PI3K_m\right] dX}_{\substack{\text{Total membrane-} \\ \text{bound PI3K}}} \,. \tag{2.8}$$

[PI3K$_0$] is the total PI3K in our assumed 2-d cell, divided by the area of the cell, $A_{cell}$, where we have assumed that cytosolic molecules are uniformly distributed (discussed in Sec. 2.2.2). In units where the circumference is of the cell is 1, $A_{cell} = 1/4\pi$.

This example is continued below in Sec. 2.5.3b, where we rewrite Eqs. 2.7 and 2.8 in terms of our scaled model variables and further discuss their form.


2.5.3   Scaled equations

In Appendix A, we apply the procedure demonstrated above to write a complete set of unscaled equations describing the processes represented in Fig. 2.8.  We similarly apply simplifying steady-state assumptions to write all concentrations in terms of those represented by our scaled model variables.  This set of 'reduced' equation is then rewritten in terms of scaled model variables and parameters.  Scaled model variables are summarized in Table 2.2; definitions of scaled model parameters, in terms of unscaled parameter, are summarized in Table A.2 of Appendix A.

In our scaled model equations below, integrals over $X$ account for exchange of translocating molecules between cytosolic pools and the entire membrane.  Because our spatial variable is normalized, these integrals are equivalent to spatial averages (denoted

**Table 2.2. Model variables**

| Variable | Meaning | Scaled by[#] |
|---|---|---|
| $\mathcal{R}$ | The combination of receptor and HTG activation that drives PI3K to the membrane. | Constitutive PI3K activation ($\xi_R$, see Eq. 2.7). |
| $P_n =$ $P_3 + P_2$ | Sum of the 3'PIs thought to be important in gradient sensing – a primary model output of our model. | [3'PI] that saturates **Loop I** – results in the relationship $1/\kappa_m + 1/\kappa_c = 1$ (see Eq. 2.9a). |
| $K_m$ | PI3K on the membrane – generates $P_3$. | $A_{cell}[\text{PI3K}_0]$ |
| $K_c*$ | Inactive cytosolic PI3K. | $A_{cell}[\text{PI3K}_0]$ |
| $T_m$ | PTEN on membrane – dephosphorylates $P_n$. | $A_{cell}[\text{PTEN}_0]$ |
| $T_c*$ | Inactive cytosolic PTEN. | $A_{cell}[\text{PTEN}_0]$ |

[#] $A_{cell}$ is the area of the cell, $[\text{PI3K}_0]$ and $[\text{PTEN}_0]$ are the total concentrations of PI3K and PTEN in the cell; thus, $A_{cell}[\text{PI3K}_0]$ and $A_{cell}[\text{PTEN}_0]$ are the total PI3K and PTEN is the cell.

$\langle\ \rangle_X$ ). The parameter, $\chi$, is generally used to represent scaled forward rate constants, $\lambda$ to

represent backwards rate constants, and $\kappa$ to represent saturation concentrations and/or

concentrations at which a term becomes effective. The parameter $\zeta$ is used to represent

constitutive processes acting in parallel with the regulated processes of our model, as

discussed in Sec. 2.3.3d.

### 2.5.3a  3'PI dynamics – a primary model output

The interactions of our model that regulate the 3'PIs on the membrane, PI(3,4,5)P$_3$ ($P_3$)

and PI(3,4)P$_2$ ($P_2$) , are schematized in Fig. 2.10.

The following equations describe the dynamics of $P_3$ on the membrane:

$$\frac{\partial P_3}{\partial t} = \chi_3 K_m \left( \underbrace{\frac{\Xi}{1 + K_m/\kappa_3}}_{1a} + \underbrace{\zeta_{3/PITP}}_{1a'} \right) + \underbrace{\zeta_3}_{1a''} - \lambda_3 P_3 (\underbrace{T_m}_{1b} + \underbrace{\zeta_{3/T}}_{1b'}) + D\frac{\partial^2 P_3}{\partial X^2} , \tag{2.9}$$

$$\text{where } \Xi \equiv \underbrace{\frac{P_n}{P_n/\kappa_m + \int_0^1 P_n dX/\kappa_c + 1}}_{gP-dependent} + \underbrace{\zeta_{PITP}}_{\substack{gP-\\independent}} \tag{2.9a}$$
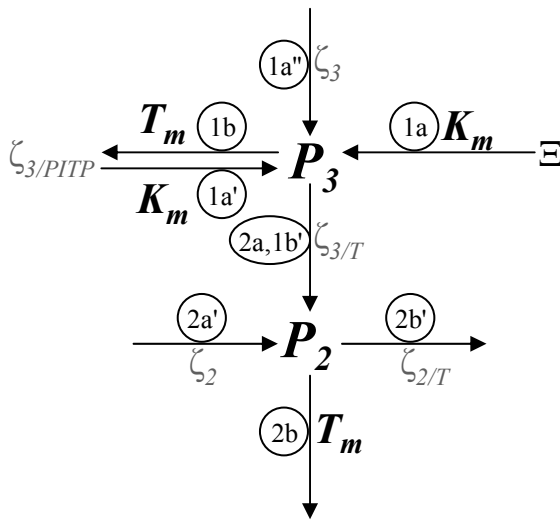


**Fig. 2.10.  $P_n$ regulation.**  The schematic is written in terms of our scaled model variables.  The symbol, $\Xi$, represents the scaled concentration of PITP-bound PI(4,5)P$_2$ that results when elements of **Loop I** are set to steady-state with respect to our model variables (derived in Appendix A and discussed below).  Numbered interactions represent terms in our scaled equations.  Constitutive terms are labeled with a prime; the molecules involved are represented by the symbol $\zeta$, which is the same parameter used to include them in our scaled equations.  Processes appearing in multiple equations are numbered twice (e.g. 2a, 1b').  Notation is otherwise as in earlier schematics.

and $P_n \equiv P_3 + P_2$; (2.9b)

Because the feedback in our model generally depends on the sum of the 3'PIs ($P_n$), which is a primary output of our model, we have made the substitution 2.9b wherever possible.

In Eq. 2.9, term 1$a$ accounts for $P_3$ production due to PI3K acting on PITP-bound PI(4,5)P$_2$. This term couples **Loops I** and **II**, and saturates at large $K_m$ (of order $\kappa_3$) because the PITP is depleted. The factor, $\Xi$, is proportional to the concentration of PITP-bound PI(4,5)P$_2$. Its form (Eq. 2.9a) is obtained in Appendix A by writing kinetic equations for the regulatory molecules in **Loop I** (depicted in Figs. 2.5 and 2.8), many of whose spatio-temporal dynamics are not well characterized; the concentrations of these regulatory molecules are set to steady-state with respect to the variables of our model, as was illustrated in the example of Sec. 2.5.2.

The denominator of the small G-protein dependent (*gP-dependent*) part of $\Xi$ includes a local term ($P_n / \kappa_m$), which accounts for saturation of **Loop I** due to depletion of membrane bound molecules, and a global term ($\int_0^1 P_n dX / \kappa_c \equiv \langle P_n \rangle_X / \kappa_c$), which accounts for saturation of this feedback due to depletion of cytosolic molecules that translocate to the membrane (in particular, the GEF in **Loop I**). If the latter term dominates, then under conditions where redistribution of translocating molecule keeps $\langle P_n \rangle_X$ fixed, $\Xi$ will vary approximately linearly with $P_n$ and hence contain a term linear in $P_3$; the degradation terms in Eq. 2.9 (1$b$ and 1$b'$) are linear in $P_3$ as well. Under these conditions, we might expect a sharp transition in $P_3$ production as $K_m$ and $T_m$ vary, and the balance between production and degradation shifts. The constitutive production terms in Eq. 2.9, $\zeta_{PITP}$, $\zeta_{3/PITP}$, and $\zeta_3$ (1$a'$, 1$a''$ and *gP-independent*), which account for

production of $P_3$ by mechanisms independent of the various molecules in **Loop I**, cushion any such sharp transitions.

The loss terms in Eq. 2.9 account for dephosphorylation of $P_3$ at the 3' position by PTEN ($T_m$, term 1*b*) and for conversion of $P_3$ to $P_2$ by a phosphatase such as SHIP (138), whose dynamics are not included in our model (represented by $\zeta_{3/T}$, term 1*b′*). The final term in Eq. 2.9 accounts for diffusion of $P_3$ along the membrane with diffusion coefficient, $D$.

In Eqs. 2.9 and 2.9a, the relative values of $\kappa_m$ and $\kappa_c$ determine the relative importance of molecules in **Loop I** that translocate from the cytosol to the membrane; both $P_3$ and $P_2$ have been scaled such that the relationship, $1/\kappa_m + 1/\kappa_c = 1$ is preserved. The ratio $\chi_3/\lambda_3$ is important in determining the strength of **Loop I**. The ratio $D/\lambda_3$ controls the effects of diffusion on spatial responses.

The following equation describes the dynamics on the membrane of $P_2$, which track $P_3$ dynamics with a slight lag:

$$\frac{\partial P_2}{\partial t} = \underbrace{\zeta_2}_{2a'} + \underbrace{\lambda_3 \zeta_{3/T} P_3}_{2a} - \lambda_2 P_2 (\underbrace{T_m}_{2b} + \underbrace{\zeta_{2/T}}_{2b'}) + D \frac{\partial^2 P_2}{\partial X^2}. \tag{2.10}$$

$P_2$ is generated from $P_3$ (2*a*), as well as from other sources (2*a′*). The loss terms account for dephosphorylation of $P_2$ at the 3' position by PTEN ($T_m$, process 2*b*) and for dephosphorylation by other phosphatases (2*b′*). The final term in Eq. 2.10 accounts for diffusion of $P_2$ along the membrane with diffusion coefficient, $D$ (assumed to be the same for $P_3$ and $P_2$). The ratio $D/\lambda_2$ controls the effects of diffusion on spatial responses.

*2.5.3b Membrane bound PI3K – coupling to outside stimuli*

Figure 2.11 represents the interactions that regulate PI3K on the membrane ($K_m$) in terms

of our scaled model variables (these interactions were represented in terms of unscaled

model variables in Fig. 2.9). Scaled equations representing these processes are obtained

by rewriting Eqs. 2.7 and 2.8 in terms of the scaled model variables (defined in Table 2.2

above) and parameters (defined in Table A.2 of Appendix A). The result is:

$$\frac{\partial K_m}{\partial t} = \lambda_K \left( \underbrace{\gamma}_{3a,a'} - \underbrace{\frac{K_m}{1 + P_n / \kappa_K}}_{3b} \right), \tag{2.11}$$

where $\gamma \equiv (\chi_K / \lambda_K)(\underbrace{\mathcal{R}}_{3a} + \underbrace{1}_{3a'}) K_c$ $\qquad$ (2.11a)

and $K_c = \left( 1 - A_{cell} K_c{}^* - \int_0^1 K_m \, dX \right) / A_{cell}.$ $\qquad$ (2.11b)

The term $\gamma$ in Eq. 2.11 represents recruitment of cytosolic PI3K ($K_c$) to the membrane

in response to receptor activation by outside stimuli ($\mathcal{R}$, term 3a in Eq. 2.11), as well as

constitutive recruitment (3a'). $\mathcal{R}$ is scaled by unregulated recruitment of PI3K to the

membrane, such that the factor $\mathcal{R}+1$ thus accounts for the sum of receptor-mediated and

unregulated recruitment. Equation 2.11b expresses conservation of total PI3K and is

used to eliminate $K_c$ from our equations (alternatively, it could be used to eliminate $K_c{}^*$);

total PI3K is scaled to 1 (see Table 2.2).

The loss term in Eq. 2.11 (3b) represents PI3K phosphorylation by molecule $B$, which

is assumed to be constitutively on the membrane; $[B_m]$ is fixed and has been absorbed by
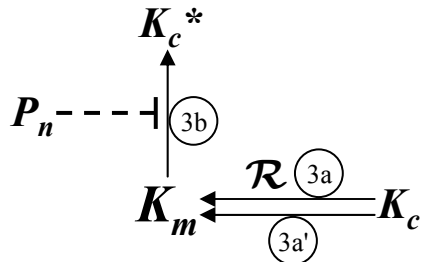


**Fig. 2.11. $K_m$ regulation**. **Loop II** interactions involving unidentified molecules $A$ and $B$, which are not explicitly included in our model, are represented schematically by $P_n$ inhibition of PI3K phosphorylation (conversion of $K_m$ to $K_c{}^*$).

the scaled rate constant, $\lambda_K$. PI3K phosphorylation is regulated by molecule $A$, which has been eliminated via steady-state assumptions, as discussed in Sec. 2.5.2. The resulting factor in the denominator, $1 + P_n / \kappa_K$, accounts for the feedback in **Loop II** by decreasing the rate of removal of PI3K from the membrane with increasing $P_n$. This factor becomes important only when $P_n \sim \kappa_K$. Thus, the magnitude of $\kappa_K$ determines the effectiveness of **Loop II** in signal amplification.

*2.5.3c. PTEN dynamics – amplifying the effects of PI3K*

The dynamics of PTEN on the membrane ($T_m$), and of the fraction of total PTEN concentration that is cytosolic and phosphorylated/inactive ($T_c*$), are schematized in Fig. 2.12 and captured by the following equations:

$$\frac{\partial T_m}{\partial t} = \underbrace{\chi_T T_c}_{4a} - \underbrace{\lambda_T T_m (\underbrace{K_m}_{4b} + \underbrace{\zeta_T}_{4b'})}_{} , \tag{2.12}$$

where $T_c = \left( 1 - A_{cell} T_c * - \int_0^1 T_m dX \right) / A_{cell}$ ; $\tag{2.12a}$

$$\frac{\partial T_c *}{\partial t} = \underbrace{\lambda_T \int_0^1 T_m K_m dX / A_{cell}}_{5a} - \underbrace{\lambda_{T*} T_c *}_{5b} . \tag{2.13}$$
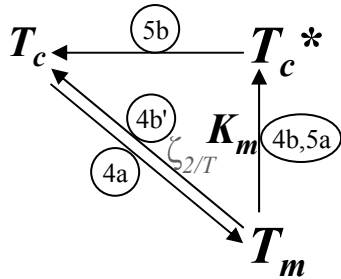


**Fig. 2.12. Regulation of $T_m$ and $T_c*$.** Notation as in previous schematics.

The first term in Eq. 2.12 (4*a*) accounts for constitutive recruitment of cytosolic PTEN ($T_c$) to the membrane with rate constant, $\chi_T$. The loss term represents PTEN removal from the membrane by PI3K-mediated phosphorylation (4*b*, as discussed in Sec. 2.3.3b), as well as constitutive removal (4*b'*); the magnitude of $\zeta_T$ determines the value

of $K_m$ where PI3K inhibition of PTEN becomes important in our model.  Equation 2.12a

expresses conservation of total PTEN and is used to eliminate $T_c$ from our equations

(alternatively, it could be used to eliminate $T_c\!*$); total PTEN is scaled to 1.

In Eq. 2.13, the first term (5a) accounts for phosphorylation of PTEN over the entire

membrane and subsequent return to the cytosol; this term is the integral of term 4b in Eq.

2.12 divided by the area of the cell.  The loss term (5b) represents dephosphorylation of

PTEN in the cytosol, which is constitutive with rate constant $\lambda_{T*}$.

Equations 2.12 and 2.13 reproduce a $T_m$ dynamics inverse to $K_m$ dynamics, enhancing

the effects of **Loop II**.


*2.5.3d. Cytosolic/inactive PI3K – adaptation*

Figure 2.13 illustrates regulation of the fractional concentration of PI3K that is cytosolic

and phosphorylated/inactive in our model ($K_c\!*$).  The following equation describes the

dynamics that result:

$$\frac{\partial K_c\!*}{\partial t} = \lambda_K (\underbrace{\int_0^1 \frac{K_m}{1+P_n/\kappa_K} \frac{dX}{A_{cell}}}_{6a} - \underbrace{\left(\frac{\lambda_{K*}}{\lambda_K}\right) \frac{K_c\!*}{\kappa_{K*}+K_c\!*}}_{6b}) \qquad (2.14)$$

The first term in Eq. 2.14 (6a) represents phosphorylation of PI3K over the entire

membrane; this term is the integral of term 3b in Eq. 2.11 divided by the area of the cell.



$$K_c\!* \xrightarrow[\underset{6b}{}]{\textit{saturated}} K_c$$

$$P_n \dashv \!\!\mid_{6a}$$

$$K_m$$
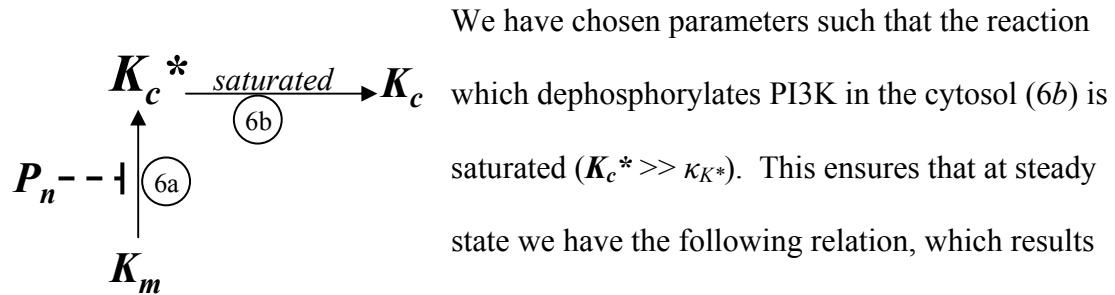
**Fig. 2.13. Regulation of $K_c\!*$.**

We have chosen parameters such that the reaction

which dephosphorylates PI3K in the cytosol (6b) is

saturated ($K_c\!* \gg \kappa_{K*}$).  This ensures that at steady

state we have the following relation, which results

from averaging Eq. 2.11 over the entire membrane,

combining with Eq. 2.14, and replacing the integral with an equivalent spatial average:

$$\langle \gamma \rangle_X \equiv (\chi_K / \lambda_K)(\langle \mathcal{R} \rangle_X + 1) K_c = \left\langle \frac{K_m}{1 + P_n / \kappa_K} \right\rangle_X \sim \frac{A_{cell} \lambda_{K*}}{\lambda_K} \equiv \gamma_0 = \text{constant.} \qquad (2.15)$$

Thus, adaptation to the average stimulus occurs in our model because PI3K is phosphorylated over the entire membrane, thus depleting the shared cytosolic pool of unphosphorylated PI3K ($K_c$) such that $\gamma$ always return to $\gamma_0$ (discussed further below).

2.5.4  Equation summary and alternative biochemical mechanisms

Our model equations are summarized below in Table 2.3 for easier reference. They are labeled with an 'M' for 'Model'; terms representing the discussed feedback loops are indicated.

Equations M.1 – M.2, which describe lipid dynamics on the membrane, are spatially dependent and include diffusion. Equations M.3 – M.4 describe the dynamics of proteins on the membrane. These are spatially dependent as well, but their diffusion is not included (see Sec. 2.2.2 and Table 2.1); the effects of diffusion in our model are thus completely tied to lipid dynamics.

Equations M5 – M.6 describe the dynamics of cytosolic proteins, which are assumed to be uniform in our treatment. Equations M.7 – M.8 account for conservation of total PI3K and PTEN in the cell. These equations are used to eliminate $K_c$ and $T_c$ from Eqs. M.3 and M.4 for our simulations. Alternatively, $K_c^*$ and $T_c^*$ could be eliminated and the auxiliary equations M.10 and M.11 could be used in place of Eqs. M.5 and M.6; this alternative is chosen in several instances where it leads to easier analysis.

The steady-state equation, M.9, defines the baseline state of the cell in the absence of receptor activity and will ensure perfect adaptation to the spatial average of the external

66

**Table 2.3. Model equations**

Primary equations:

*Membrane lipids*

$$\frac{\partial \boldsymbol{P_3}}{\partial t} = \chi_3 \boldsymbol{K_m} \left( \frac{\Xi}{1 + \boldsymbol{K_m} / \kappa_3} + \zeta_{3/PITP} \right) + \zeta_3 - \lambda_3 \boldsymbol{P_3} \left( \boldsymbol{T_m} + \zeta_{3/T} \right) + D \frac{\partial^2 \boldsymbol{P_3}}{\partial X^2} \qquad \text{M.1}$$

$$\Xi \equiv \underbrace{\frac{\boldsymbol{P_n}}{\boldsymbol{P_n} / \kappa_m + \int_0^1 \boldsymbol{P_n} dX / \kappa_c + 1}}_{Loop\ I} + \zeta_{PITP} \qquad \text{M.1a}$$

$$\boldsymbol{P_n} \equiv \boldsymbol{P_3} + \boldsymbol{P_2} \qquad \text{M.1b}$$

$$\frac{\partial \boldsymbol{P_2}}{\partial t} = \zeta_2 + \lambda_3 \zeta_{3/T} \boldsymbol{P_3} - \lambda_2 \boldsymbol{P_2} \left( \boldsymbol{T_m} + \zeta_{2/T} \right) + D \frac{\partial^2 \boldsymbol{P_2}}{\partial X^2} \qquad \text{M.2}$$

*Active proteins on the membrane*

$$\frac{\partial \boldsymbol{K_m}}{\partial t} = \lambda_K (\boldsymbol{\gamma} - \underbrace{\frac{\boldsymbol{K_m}}{1 + \boldsymbol{P_n} / \kappa_K}}_{Loop\ II}) \qquad \text{M.3}$$

$$\boldsymbol{\gamma} \equiv \left( \chi_K / \lambda_K \right) \left( \boldsymbol{\mathcal{R}} + 1 \right) \boldsymbol{K_c} \qquad \text{M.3a}$$

$$\frac{\partial \boldsymbol{T_m}}{\partial t} = \chi_T \boldsymbol{T_c} - \underbrace{\lambda_T \boldsymbol{T_m} (\boldsymbol{K_m}}_{Loop\ II} + \zeta_T ) \qquad \text{M.4}$$

*Inactive proteins in the cytosol*

$$\frac{\partial \boldsymbol{T_c}^*}{\partial t} = \lambda_T \int_0^1 \boldsymbol{T_m} \boldsymbol{K_m} dX / A_{cell} - \lambda_{T*} \boldsymbol{T_c}^* \qquad \text{M.5}$$

$$\frac{\partial \boldsymbol{K_c}^*}{\partial t} = \lambda_K \left( \int_0^1 \frac{\boldsymbol{K_m}}{1 + \boldsymbol{P_n} / \kappa_K} \frac{dX}{A_{cell}} - \left( \frac{\lambda_{K*}}{\lambda_K} \right) \frac{\boldsymbol{K_c}^*}{\kappa_{K*} + \boldsymbol{K_c}^*} \right) \sim \underbrace{\frac{\lambda_K}{A_{cell}} \left( \left\langle \frac{\boldsymbol{K_m}}{1 + \boldsymbol{P_n} / \kappa_K} \right\rangle_X - \gamma_0 \right)}_{Loop\ III} \qquad \text{M.6}$$

$$\gamma_0 \equiv \frac{A_{cell} \lambda_{K*}}{\lambda_K} \qquad \text{M.6a}$$

Conservation equations:

$$1 = \boldsymbol{K_c} A_{cell} + A_{cell} \boldsymbol{K_c}^* + \int_0^1 \boldsymbol{K_m} dX \qquad \text{M.7}$$

$$1 = \boldsymbol{T_c} A_{cell} + A_{cell} \boldsymbol{T_c}^* + \int_0^1 \boldsymbol{T_m} dX \qquad \text{M.8}$$

Steady-state equation:

$$\left\langle \boldsymbol{\gamma} \right\rangle_X \equiv \left( \chi_K / \lambda_K \right) \left( \left\langle \boldsymbol{\mathcal{R}} \right\rangle_X + 1 \right) \boldsymbol{K_c} = \left\langle \frac{\boldsymbol{K_m}}{1 + \boldsymbol{P_n} / \kappa_K} \right\rangle_X \sim \frac{A_{cell} \lambda_{K*}}{\lambda_K} \equiv \gamma_0 = \text{constant} \qquad \text{M.9}$$

at steady state.

Auxiliary equations:

$$\frac{\partial \boldsymbol{T_c}}{\partial t} = \lambda_{T*} \boldsymbol{T_c}^* - \chi_T \int_0^1 \boldsymbol{T_c} dX / A_{cell} \qquad \text{M.10}$$

$$\frac{\partial \boldsymbol{K_c}}{\partial t} = \frac{\lambda_{K*} \boldsymbol{K_c}^*}{\kappa_{K*} + \boldsymbol{K_c}^*} - \lambda_K \int_0^1 \boldsymbol{\gamma} dX / A_{cell} \sim \left( \lambda_K / A_{cell} \right) \left( \gamma_0 - \left\langle \boldsymbol{\gamma} \right\rangle_X \right) \qquad \text{M.11}$$

stimulus, when one is present. This will be discussed further in the next subsection. Definitions M.3a and M.6a can be used to simplify Eq. M.11, as indicated.

Our model equations were derived by assuming specific biochemical mechanisms for the suggested regulatory loops. To the extent that our model parameters are related to the unscaled biochemical parameters from which they were derived, our model retains connection with the details of our proposed mechanisms. However, the qualitative features of our equations are consistent with other possibilities. For example, a similar PTEN dynamics would result if PTEN were inactivated by another molecule whose dynamics parallels that of PI3K upon cellular stimulation. The form of Eqs. M.3 and M.6 would be preserved if we assumed PI3K autophosphorylation as the mechanism for PI3K removal from the membrane, rather than phosphorylation by another kinase. The feedback in **Loop II** could be effectively included in Eq. M.3 if we had assumed that 3'PIs recruit a molecule to the membrane that helped bring PI3K to the membrane, rather than one that inhibited its removal (the $P_n$ dependence would then be shifted to the production term from the denominator of the degradation term). We are currently exploring several of these possibilities.

### 2.5.5 Qualitative discussion – Defining modules and accounting for characteristic behaviors

Equations M.1 – M.5 describe positive feedback (**Loops I** and **II**) and can be considered to constitute an amplification module; Equation M.6 describes negative feedback (**Loop III**) and constitutes an adaptation module. The parameter $\gamma$ (defined Eq. M.3a) is

interpreted as a driving parameter.  It serves both to couple these modules to each other

and to couple the entire system to outside stimuli[#] (see Fig. 2.4).

The signaling network described by Eqs. M.1 – M.6 might function in gradient

sensing as follows:  Receptor activation increases the local value of $\mathcal{R}$ and hence the

local value of $\gamma$ (Eqs. M.3, M.3a), recruiting PI3K to the membrane and driving the

amplification module (Eqs. M.1 – M.5).  PI3K on the membrane is then phosphorylated

and returns to the cytosol (Eq. M.6).  The pool of PI3K that is free to return to the

membrane ($K_c$), and hence the level value of $\gamma$, drops.  If $\mathcal{R}$ is uniform, $\gamma$ returns to $\gamma_0$

everywhere, as indicated by Eq. M.9 and M.11, and the cellular response returns to

baseline.  Thus, we interpret $\gamma_0$ as setting the baseline state of the cell.  If there is a

gradient in $\mathcal{R}$, $\gamma$ will remain elevated at the front of the cell, where $\mathcal{R}$ is above its

average value, $\langle \mathcal{R} \rangle_X$.  If $\gamma_0$ is set appropriately, the amplification module will still be

driven in this region, but not at the back of the cell where $\mathcal{R}$ is below $\langle \mathcal{R} \rangle_X$ and $\gamma$ has

dropped below $\gamma_0$.

## 2.6    Setting parameters

Our model parameters are generally not known experimentally.  Thus, we have set them

empirically to capture characteristic gradient sensing behaviors and to reproduce the

qualitative features of experimental observations in Dictyostelium (discussed in Secs.

1.2.6, 2.2.4 and 2.3.3.b).  The meanings of our model parameters, as well as their values,

are summarized in Table 2.4; a range is indicated for parameters that differ between our

model variants, which will be discussed in Sec. 2.7.  Here, we briefly outline the intuitive

---

[#] The LI model is based on a similar modular structure, as is a more recent variation (159).

procedure that was used to fix their values. A more detailed discussion is given in Appendix B.

Combinations of parameters that determine the uniform steady state of values of our model variables were set first. Based on an intuitive interpretation of the roles that they play in our equations, these parameters can be qualitatively divided into the following categories: parameters that set uniform steady-state concentrations in the unstimulated cell; parameters that adjust the range of our model variables for which a given feedback is effective; parameters controlling the strengths of the feedbacks in our model; parameters controlling the importance of constitutive process in our model. The roles that many of these parameters play in our equations were discussed when they were introduced in Sec. 2.5.3.

Variations of parameters in the same category often had similar effects, and simultaneous variations of several parameters could thus compensate for each other. A specific example of parameters whose variations might compensate for each other is given in Sec. 4.5.3. Under these conditions, parameter values were chosen empirically to give a robust set of results and allow clear definitions of variants of our model, which will be introduced in Sec. 2.7.

Parameters that fix cytosolic concentrations were set next. The fraction of PI3K and PTEN that is cytosolic and phosphorylated ($K_c^*$ and $T_c^*$) in the unstimulated cell, for which we could not find experimental data in Dictyostelium, was fixed at 50%.

Finally, degradation rate constants ($\lambda$) were set to adjust the kinetics of each of our model variables. These were set such that the initial response to a uniform stimulus occurs within seconds, and response adaptation within tens of seconds with 3'PIs, PI3K

70

**Table 2.4.  Model parameters**

| Parameter | Equation | Interpretation | Value |
|---|---|---|---|
| $\chi_3$ | M.1 | Rate constant for **Loop I** regulated $P_3$ production | 120.0 |
| $\kappa_m$ | | $P_n$ which begins to saturate **Loop I** by depleting membrane molecules. | 1.18 – 5.0 |
| $\kappa_c$ | | $P_n$ which begins to saturate **Loop I** by depleting cytosolic molecules. | 1.25 – 6.7 |
| $\zeta_{PITP}$ | | Rate of g-P independent $P_3$ production/rate constant for gP dependent production. | 0.025 |
| $\kappa_3$ | | $K_m$ at which PI3K binding to PITP·PI(4,5)P$_2$ becomes saturated. | 0.05 |
| $\zeta_{3/PITP}$ | | Rate of PITP independent $P_3$ production/rate constant for PITP dependent production. | 0.025 |
| $\zeta_3$ | | Rate of unregulated $P_3$ production. | 0.3 |
| $\lambda_3$ | | Rate constant for $P_3$ removal by $T_m$. | 15.0 |
| $\zeta_{3/T}$ | | Rate of $P_3$ conversion to $P_2$/rate constant for $T_m$-mediated removal. | 0.13 |
| $\zeta_2$ | M.2 | Rate of unregulated production of $P_2$. | 0.02 |
| $\lambda_2$ | | Rate constant for $T_m$-mediated removal of $P_2$. | 8.0 |
| $\zeta_{2/T}$ | | Rate of unregulated removal of $P_2$/rate constant for $T_m$-mediated removal. | 0.05 |
| $\chi_K$ | M.3 | Rate constant for unregulated $K_c$ translocation to the membrane. | 0.0049 – 0.0076 |
| $\mathcal{R}$ | | Ligand-induced, receptor-mediated activation, which drives translocation of $K_c$. | external |
| $\lambda_K$ | | Rate constant for $K_m$ phosphorylation and removal from the membrane. | 0.73 – 4.2 |
| $\kappa_K$ | | $P_n$ at which 3'PI inhibition of $K_m$ return to the cytosol (**Loop II**) becomes effective. | 0.95 – 5.5 |
| $\chi_T$ | M.4 | Rate constant for $T_c$ translocation to the membrane. | 0.019 |
| $\lambda_T$ | | Rate constant for $T_m$ phosphorylation by $K_m$. | 30.0 |
| $\zeta_T$ | | Rate of unregulated $T_m$ return to cytosol/rate constant for $T_m$ phosphorylation by $K_m$. | 0.002 |
| $\lambda_{T*}$ | M.5 | Rate constant for $T_c^*$ dephosphorylation in the cytosol. | 0.15 – 0.21 |
| $\lambda_{K*}$ | M.6 | Rate constant for $K_c^*$ dephosphorylation in the cytosol. | 0.34 – 0.58 |
| $\kappa_{K*}$ | | $K_c^*$ for which the reaction that dephosphorylates PI3K begins to saturate. | 0.013 |
| $D$ | 1,2 | Coefficient of lipid diffusion in units where the circumference of the cell is 1. | 0.003 |
| $A_{cell}$ | M.5 – M.8 | Area of the cell in units where the circumference is 1 ($1/4\pi$). | $1/4\pi$ |

and PTEN ($P_n$, $K_m$, and $T_m$) showing similar time courses, as has been observed in Dictyostelium. The lipid diffusion coefficient, $D$ (defined in units where the circumference of the cell is 1), was set to a value corresponding to approximately twice the typical value suggested by experimental measurements (assuming a rounded cell with a radius of 4 $\mu m$). A larger value of $D$ was done because only 1-d diffusion is considered in our model.

**2.7    Model variants**

2.7.1    Qualitative possibilities

A highly non-linear response of our amplification module and the possibility of multiple steady states are expected if both **Loops I** and **II** become strongly activated upon cellular stimulation. If depletion of translocating molecules saturates either of these **Loops**, qualitative differences in responses to uniform stimuli and to gradients, where redistribution of these molecules can significantly amplify responses, will be possible. To investigate these possibilities, and the qualitatively different gradient sensing mechanisms to which they lead, we develop four variants of our model.

2.7.2    Adjusting strength of positive feedbacks and the importance of translocation

To vary whether coupled positive feedbacks lead to multiple steady-states, we adjusted the parameter $\kappa_K$ (Eq. M.3); this parameter controls the effectiveness of **Loop II** in signal amplification. To adjust the importance of redistribution of translocating molecules in amplifying responses to gradients, we varied the parameter $\kappa_c$ (Eq. M.1, M.1a); this

parameter controls the degree to which cytosolic depletion saturates **Loop I**[#]. After combinations of $\kappa_K$ and $\kappa_c$ were chosen, the baseline parameter, $\gamma_0$, was adjusted to optimize cellular responses to a small static gradient of stimulus (discussed further in Sec. 3.5.1). Larger $\gamma_0$ results in higher concentrations of PI3K and 3'PIs on the membrane in the unstimulated cell.

By varying these parameters, we generated four variants of our model that illustrate the qualitatively different 'Modes' of gradient sensing that result from varying the roles of coupled positive feedbacks and translocation in our model. We refer to these as Cases 1-4; their qualitative features are schematized in Fig. 2.14. The parameters values that define our model variants are given in Table 2.5. The steady-state values of our model variables in the uniform unstimulated cell are given in Table 2.6; these will be used to initialize our simulations.
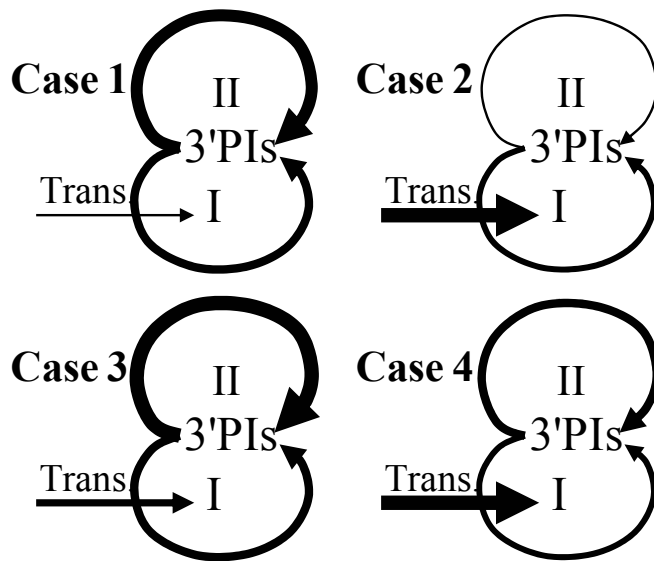


**Fig. 2.14. Model variants.** Depicted elements of the model's amplification module are adjusted by varying model parameters to define four variant of our model. The thickness of an arrow indicates the strengths of the depicted feature. When **Loops I** and **II** are sufficiently activated upon cellular stimulation, coupled positive feedbacks can result in multiple steady states (as in Cases 3, 4). If translocation ('Trans.') is important for amplification, then redistribution of molecules between the front and back of the cell can enhance responses to gradients (as in Cases 2 and 4).

---

[#] As mentioned in Sec. 2.5.3a, $1/\kappa_m$, which controls the degree to which depletion of membrane-bound molecules saturates **Loop I**, was adjusted such that the relationship $1/\kappa_c + 1/\kappa_m = 1$ was preserved.

**Table 2.5. Parameters which define the model variants**

| Parameter | Case 1 | Case 2 | Case 3 | Case 4 |
|---|---|---|---|---|
| $\kappa_K$ | 1.3 | 5.5 | 0.95 | 4.0 |
| $\kappa_c$ | 6.7 | 1.38 | 5.0 | 1.25 |
| $\gamma_0$ | 0.014 | 0.037 | 0.011 | 0.028 |

**Table 2.6. Steady-state, uniform profile for each variant at zero stimulus**

| Variable | Case 1 | Case 2 | Case 3 | Case 4 |
|---|---|---|---|---|
| $P_3$ | 0.38 | 1.16 | 0.19 | 0.85 |
| $P_2$ | 0.60 | 2.82 | 0.25 | 1.78 |
| $P_n\ (=P_3+P_2)$ | 0.98 | 4.0 | 0.44 | 2.63 |
| $K_m$ | 0.025 | 0.064 | 0.016 | 0.046 |
| $T_m$ | 0.1 | 0.054 | 0.15 | 0.071 |
| $A_{cell}K_c{}^*$ | 0.50 | 0.50 | 0.50 | 0.50 |
| $A_{cell}T_c{}^*$ | 0.50 | 0.50 | 0.50 | 0.50 |

2.7.3   Descriptions of the model variants

The characteristics of our model variants are summarized Table 2.7 at the end of this

subsection and discussed below.  As mentioned, our model shares important features with

several recently published models; these are discussed briefly as well.

Case 1: Coupled positive feedbacks do not result in multiple steady states for any

stimulus, and redistribution of signaling molecules does not significantly contribute to

responses amplification.  We expect this variant to share features with the LI model[#]

(122).

Case 2:  Multiple steady states are absent.  Upon global stimulation, the amplification

module depletes cytosolic molecules and the response saturates.  In response to gradients,

however, these molecules are redistributed from the back to the front of the cell,

---

[#] The LI model does not deplete cytosolic molecules in the amplification module, and the steady-state response of the cell is uniquely determined by the pattern of receptor activation (which determines the ratio [PI3K]/[PTEN] that acts as a driving parameter in this model) (122).

stabilizing and enhancing the polarized response. This variant's amplification module shares features with the PvH model (97).

Case 3: Coupled positive feedback in **Loops I** and **II** is sufficient to produce multiple steady states. Responses to uniform stimuli as well as to gradients are amplified, but some redistribution of translocating molecules between the front and back of the cell is necessary to stabilize polarized responses against diffusion. In a shallow gradient of stimulus, the cell can be either in a slightly or highly polarized state; switching between these states requires overcoming a threshold in stimulus. Thus, the steady-state response of the cell depends on the history of the applied stimulus, as well as on its current value. We expect this variant to share features with the NSL model (123) (as well as Meinhardt's formulation, (160)), where strong polarization requires overcoming a stimulus threshold and, under some conditions, cellular responses can persist after the stimulus is removed.

Case 4: As in Case 2, responses to uniform stimuli are weak due to depletion of cytosolic molecules. However, redistribution of translocating molecules in response to a gradient enhances amplification due to coupled positive feedbacks and results in multiple steady states. The uniform state of the cell is unstable and a slight gradient will induce a highly polarized state, which is stable and can persist when the stimulus is removed. This variant shares features with the NSL and Meinhardt models, as well (123, 160).

## 2.8    Summary

In this chapter, we have developed a model for the dynamics and regulation of 3'PIs in

**Table 2.7.  Characteristics of model variants**

| | Case 1 | Case 2 | Case 3 | Case 4 |
|---|---|---|---|---|
| **Relating to coupled positive feedbacks:** | | | | |
| Multiple steady states in response to gradients. | No | No | Yes | Yes |
| Responses to gradients depend on how the stimulus was applied. | No | No | Yes | Yes |
| Highly polarized response to small gradients requires overcoming a stimulus threshold. | No | No | Yes | No |
| Uniform state is unstable to small perturbations. | No | No | No | Yes |
| **Relating to translocation:** | | | | |
| Strong responses to uniform stimuli – comparable to responses to gradients. | Yes | No | Yes | No |
| A cytosolic factor is significantly depleted in uniform responses. | No | Yes | No | Yes |
| Redistribution of translocating molecules enhances responses to gradients. | No | Yes | Some-what | Yes |

eukaryotic gradient sensing.  Our aim was to better understand how the network of interactions that regulates 3'PIs accounts for characteristic cellular responses to chemotactic stimuli and to examine elements that might shape the qualitative features of these responses.  In particular, we focused on how coupled positive feedbacks and molecules that translocate from the cytosol to the membrane might lead to qualitatively different gradient sensing mechanisms.  Another goal of our model was to investigate how its qualitative features depend on proposed biochemical mechanisms that might change during cellular development, and that might be externally perturbed through genetic and pharmacological means.  These considerations shaped our approach to model development.

We began by making several simplifications.  A simplified geometry was suggested by experiments which noted that characteristic gradient sensing behaviors can be

observed in round and immobilized cells (Sec. 2.2.1 and Fig. 2.1). Because the time scale for bulk diffusion in the cytosol is likely to be faster than cellular response, we chose to treat the cytosol as uniform; membrane proteins, demonstrating much slower diffusion times, were treated as fixed (Sec. 2.2.2 and Table 2.1). Fluorescent labeling techniques have allowed observation of several key molecules involved in gradient sensing. These were explicitly included in our model (Sec. 2.2.4), and we made simplifying steady-state assumptions to effectively include other regulatory molecules in our model, whose dynamics are less well characterized (Sec. 2.2.5). Our model, with these simplifications, adequately captures the qualitative features of gradient sensing response that we aim to investigate. Further addressing these simplifications and extending our model to investigate other aspects of gradient sensing behaviors, is the subject of current work.

We continued by noting key biochemical observations in gradient sensing cells (Sec. 2.3.1). In particular, data using fluorescent labeling techniques in Dictyostelium indicated that in the transient response to a uniform chemotactic stimulus, 3'PIs are produced on the membrane (represented by our model variable, $P_n$), PI3K (the molecule that makes 3'PIs, represented by the scaled variable $K_m$) translocates to the membrane, and PTEN (the molecule that degrades 3'PIs, represented by the scaled variable $T_m$) leaves the membrane. In response to a gradient of chemoattractant, 3'PIs are produced at the leading edge of the cell, PI3K becomes localized at the leading edge, and PTEN is removed from the leading edge. These observations suggest that the dynamics of these molecules are coupled together and that a potential feedback exists from 3'PIs to the

molecules that produce and degrade them. Biochemical observations also suggest a second positive feedback from 3'PIs to delivery of substrate to PI3K.

We interpreted these two coupled positive feedback loops as together constituting and amplification module. We interpreted the product of activated receptors on the cell surface and PI3K in the cytosol (which is recruited to the cell surface by activated receptors) as a driving parameter for this amplification module. Some form of negative feedback is necessary to account for cellular adaptation to the average value of the applied stimulus. We considered this negative feedback to constitute an adaptation module. This suggested modular structure for our model was discussed in Sec. 2.3.2 and Figs. 2.3 – 2.4.

Many details of the biochemical mechanisms that account for the suggested topology of the network of interactions regulating gradient sensing remain unknown. Thus, to continue our model development, we proposed biochemical mechanisms for the noted feedback loops (Sec. 2.3.3). Some are based on interactions that have been observed in the context of other cellular behaviors and clearly require further experimental investigation. Theoretical investigation of the roles that these mechanisms play in our model is a subject of current research.

We then developed a set of six partial differential equations to describe the dynamics of our model variables (model variables are summarized in Table 2.2) and their regulation by our proposed biochemical scheme (Sec. 2.5). Diffusion was only included for lipid dynamics. Cytosolic molecules in our model were assumed to be uniform, and acted to couple the dynamics at all points on our model membrane; this lead to integrals in our equations. A qualitative discussion of how our model accounts for characteristic

gradient sensing behaviors was given in Sec. 2.5.5. Our model equations, to which we will continue to refer in the remainder of this dissertation, were summarized in Table 2.3.

Most of our model parameters are unknown, and were set empirically to reproduce characteristic gradient sensing behaviors (Sec. 2.6). Several parameters controlling the effectiveness of coupled positive feedbacks and the degree to which cytosolic molecules are depleted upon cellular stimulation were adjusted to define four variants of our model. These variants are designed to illustrate the qualitatively different Modes of gradient sensing that depend on the roles of these elements in our model. We will further characterize the differences between our model variants in Chapter 3. The responses of our model to different patterns of chemotactic stimuli will be investigated in Chapter 4.

# Chapter 3: Model characterization

## 3.1    Overview

In the previous chapter, we had developed a mathematical model of 3'PI-mediated gradient sensing at an intermediate level of detail. We had further suggested that qualitatively different gradient sensing mechanisms might result, depending on how coupled positive feedbacks and translocating molecules are included. These elements were thus adjusted to generate four variants of our model. The features of our model variants were summarized in Table 2.7; our model equations, to which we will make extensive reference in this chapter, are summarized in Table 2.3 of Sec. 2.5.4.

How do the qualitative features of our model variants arise from our model's structure, and what are the conditions for each to adequately reproduce characteristic gradient sensing behaviors? In Sec. 2.3.2 and 2.5.4, we had suggested that our model might be better understood based on a modular interpretation. In this chapter, we continue to make use of this interpretation and further characterize our model using several approaches.

We begin this chapter by analyzing a projection in the $P_n$, $\gamma$ plane of the phase space dynamics for our model's responses to spatially uniform shifts in its initial conditions (Sec. 3.2). This dynamics will demonstrate the coupled behaviors of our model's amplification and adaptation modules. We continue by analyzing the steady-state response of each variant's amplification module (represented by $P_n$) at fixed values of its driving parameters ($\gamma$), making several different simplifying assumptions relating to spatial couplings (Sec. 3.3). This analysis will highlight the formal features that lead to the qualitative differences between our model variants.

Steady-state solutions to our model equations are characterized in Sec. 3.4 based on a linear stability analysis. In particular, we illustrate how the stability properties of uniform steady-state solutions can be understood based on the previously-analyzed responses of our model's amplification module (Sec. 3.4.2). We then investigate the stability of polarized solutions and suggest that the shape of the slowest decaying eigenmode perturbations for these solutions may contain information relating to the turning behavior of our model in response to changing gradients (Sec. 3.4.5). Finally, we analyze necessary constraints on several model parameters for efficient gradient sensing in each of our model variants (Sec. 3.6).

## 3.2 Projected phase-space dynamics in the $\gamma$, $P_n$ plane

In Secs. 2.3.2 and 2.5.4 we had suggested that our model might be interpreted as being composed of an amplification module and an adaptation module, coupled by a driving parameter. Our model is designed such that in response to a uniform stimulus all of the variables of the amplification module respond approximately in phase, in accordance with the qualitative features of the experimental data that was illustrated in Fig. 2.2. Thus, we might consider the behavior of the model variable, $P_n$ (representing the total concentration of 3'PIs on the membrane), to be representative of the response of the entire amplification module. Our model's driving parameter, $\gamma$, controls the response of this amplification module. The dynamics of $\gamma$ are in turn controlled by the adaptation module. We might thus hope to capture the dynamics of our model's response to uniform stimuli, including the action of both its amplification and adaptation modules, by visualizing the dynamics of the variables $P_n$ and $\gamma$.

81

An equation for the dynamics of the model variable, $\boldsymbol{P_n}$, can be written by combining Eqs. M.1 and M.2 of Table 2.3. The result is

$$\frac{\partial \boldsymbol{P_n}}{\partial t} = \chi_3 \boldsymbol{K_m} \left( \frac{\Xi}{1 + \boldsymbol{K_m} / \kappa_3} + \zeta_{3/PITP} \right) + \zeta_3 + \zeta_2$$

$$- \lambda_3 \boldsymbol{T_m} \boldsymbol{P_n} + \lambda_3 \boldsymbol{T_m} \boldsymbol{P_2} - \lambda_2 \boldsymbol{P_2} \left( \boldsymbol{T_m} + \zeta_{2/T} \right) + D \frac{\partial^2 \boldsymbol{P_n}}{\partial X^2} \tag{3.1}$$

Similarly, an approximate equation for the dynamics of the driving parameter, $\gamma$, can be written based on Eq. M.11, using definition M.3a, and assuming that the outside stimulus is constant. The result is

$$\frac{\partial \gamma}{\partial t} \sim \left( \mathcal{R} + 1 \right) \left( \chi_K / A_{cell} \right) \left( \gamma_0 - \langle \gamma \rangle_X \right). \tag{3.2}$$

As before, $\mathcal{R}$ represents the external stimulus in our model, $\gamma \equiv \left( \chi_K / \lambda_K \right) \left( \mathcal{R} + 1 \right) \boldsymbol{K_c}$ (Eq. M.3a), and the spatial variable, $X$, is normalized such that the average in Eq. 3.2 is equivalent to an integral over the entire membrane.

Figure 3.1 depicts the phase space dynamics, projected into the $\gamma$, $\boldsymbol{P_n}$ plane, of the uniform response of our model to shifts in its initial conditions that mimic application of a uniform stimulus (long-dashed curves). The bold circle represents the uniform steady-state solution for each of our model variants, which is unique and specified by the values in Table 2.6 of Sec. 2.7.2. Our model variables were first initialized to these values, with $\mathcal{R} = 0$. The value of $\gamma$ was then shifted by changing the variable $\boldsymbol{K_c}^{\#}$, which represents the concentration of cytosolic PI3K that is available to translocate to the membrane in our model. These initial conditions are marked by the non-bold circles.

---

[#] Similar results were observed by uniformly changing $\mathcal{R}$, after first initializing with $\mathcal{R} \neq 0$, to directly simulate our model's response to a uniform step stimulus (see Sec. 4.3.1).
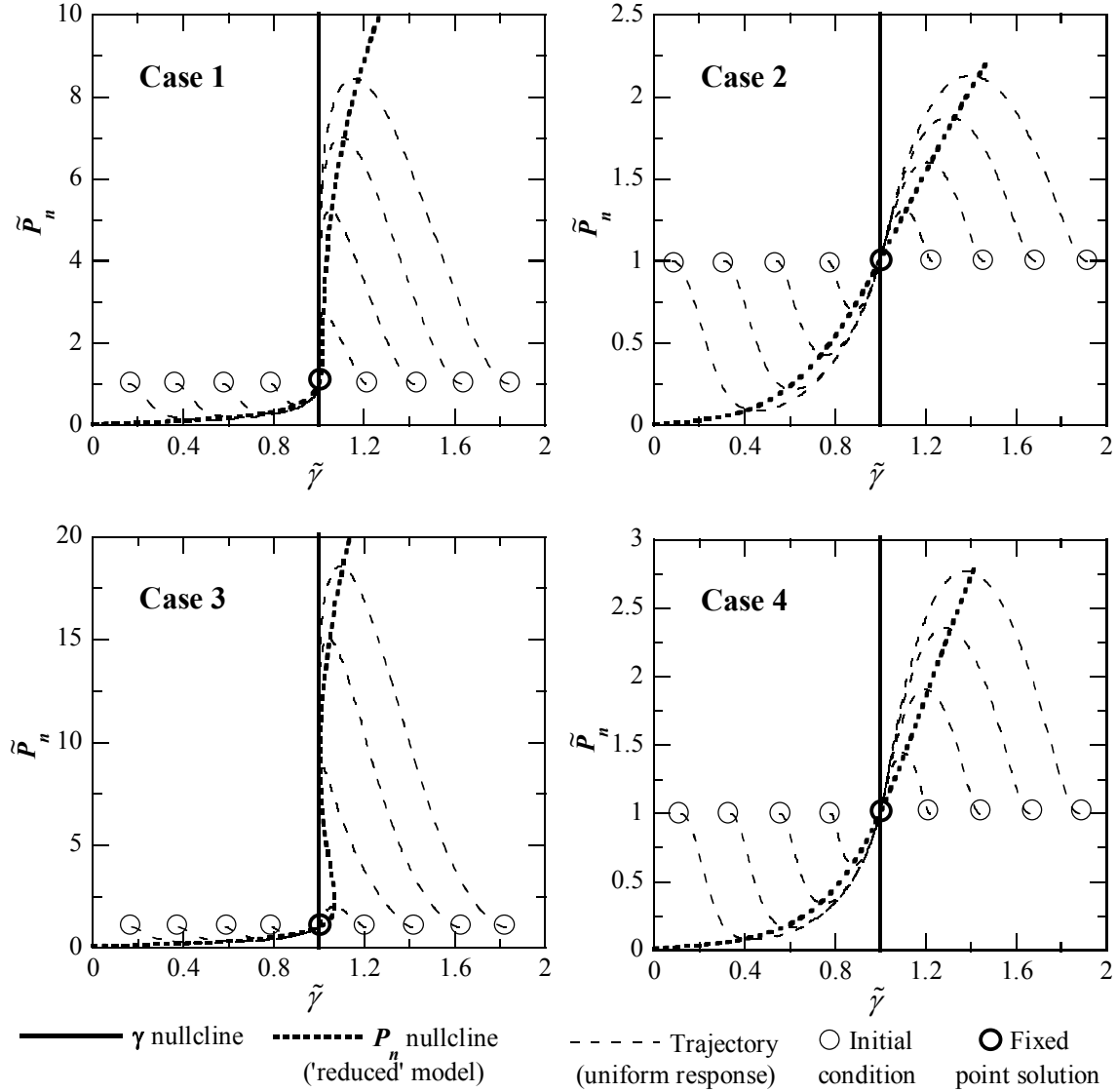
**Figure 3.1. Phase space dynamics for uniform solutions, projected in the $\gamma$, $P_n$ plane.** $\tilde{P}_n = P_n / \bar{P}_n$ is plotted against $\tilde{\gamma} = \gamma / \gamma_0$ to illustrate the dynamics of our model's amplification and adaptation modules. $\bar{P}_n$ is the uniform steady-state value of $P_n$ in the unstimulated cell (at $\tilde{\gamma} = 1$) and $\gamma_0$ is the steady-state value of $\gamma$, which sets the baseline state of the cell (see Eq. 3.2 and discussion in Secs. 2.5.4 – 2.5.5). The long-dashed curves represent projections in the $\gamma$, $P_n$ plane of trajectories for a spatially uniform system. The non-bold circles denote initial conditions for these trajectories. The bold solid line represents the nullcline of the equation describing the dynamics of the driving parameter, $\gamma$ (Eq. 3.2). The bold short-dashed curve represents the nullcline of the equation describing $P_n$ dynamics (Eq. 3.1) in the 'reduced' model described in the text. The uniform steady-state solution for each model variant, to which all uniform trajectories evolve, is marked by a bold circle at the intersection of these nullclines.

The bold vertical line in each plot of Fig. 3.1 represents the projection of the nullcline

of Eq. 3.2 onto the $\gamma$, $P_n$ plane.  This projection is possible because Eq. 3.2 only depends

on $\gamma$.  Uniform solutions to our model equations evolve towards this line from the right

and the left.  The bold short-dashed curve in each plot represents the nullcline of Eq. 3.1

in the $\gamma$, $P_n$ plane, for what we will refer to as a 'reduced' model.  That is, to generate this

curve, we have assumed that our other variables are set to uniform steady-state values

with respect to $P_n$ and $\gamma$.  Solutions in Fig. 3.1 evolve towards this 'reduced' nullcline

from above and below.  A similar kind of reduction was used to effectively include

regulation in our model by molecules whose dynamics are not known (see Secs. 2.2.5 and

2.5.2).  We will see in Secs. 3.3 and 3.4 how consideration of such a 'reduced' model (i.e.

where other model variables are set to steady-state values with  respect to $P_n$ and $\gamma$) can

lead to a more intuitive understanding of the formal features of our model.  The

intersection of the two depicted nullclines in each plot of Fig. 3.1, which is marked by the

bold circle, represents a fixed point solution for our model under conditions where its

spatial profile remains uniform.

The trajectories in Fig. 3.1 represent time courses similar to those depicted in the

sample experimental data of Fig. 2.2 in Sec. 2.2.4, and to the simulation results for

responses to uniform stimuli that will be discussed in Fig. 4.1 of Chapter 4.  If $\gamma$ is

increased, then PI3K is recruited to the membrane, PTEN is removed, and 3'PIs are

produced.  This is the response of the amplification module, which is represented by an

initial increase of $P_n$ in Fig. 3.1.  Subsequently, PI3K becomes phosphorylated, the pool

of PI3K that is free to return to the membrane is depleted, and $\gamma$ returns to its baseline

value ($\tilde{\gamma} = 1$) with the other variables of our amplification module following.  This

illustrates the action of our model's adaptation module, which returns $P_n$ and $\gamma$ to their

uniform steady-state values in the phase space plot. The dynamics are inverted for the depicted trajectories where $\gamma$ is initially decreased.

We see that all of the trajectories in Fig. 3.1.return to the uniform steady-state solution, marked by the bold circle for each Case, suggesting that this fixed point solution is stable if the system is forced to remain uniform (we will see that this is true for all Cases, though for Case 4 the uniform steady-state solution is unstable towards non-uniform perturbations). Further, the trajectories generally cross the bold short-dashed curve approximately horizontally, suggesting that points on this 'reduced' nullcline approximate well the projected position where the true nullcline of the $P_n$ equation is crossed by the illustrated phase-space trajectories. The value of $P_n$ on this 'reduced' nullcline for a given initial value of $\gamma$ correlates with the peak value of $P_n$ along that trajectory. This peak value increases sharply for trajectories as the initial value of $\gamma$ is increased for Cases 1 and 3, indicating a strong uniform response of our model's amplification module for these Cases. In contrast, Cases 2 and 4 require redistribution of translocating molecules to produce a highly amplified response, and thus demonstrate a weaker uniform response to increases in $\gamma$. Finally, the projected trajectories do not cross, supporting our suggestion that the dynamics of uniform solutions to our model can be captured by projection onto the $\gamma$, $P_n$ plane.

### 3.3 Response of the amplification module ($P_n$ vs. $\gamma$)

Our model equations describe the dynamics of six model variables, four of which are spatially dependent. However, our analysis above suggested that many features of our model might be understood in the $\gamma$, $P_n$ plane. Further, the responses of our model's

amplification module (represented by the value of $P_n$) at fixed values of the driving

parameter ($\gamma$) might contain important information about the features that distinguish our

model variants (the differences between our model variants are in their respective

amplification modules, see Sec. 2.7).

In this section, we analyze the steady-state responses of our model's amplification

module at fixed values of its driving parameter, making different simplifying assumptions

concerning the spatial dependences in our equations. By interpreting these responses as

nullclines of the equation for $P_n$ dynamics in an appropriate 'reduced' model, we will

propose simple criteria for the stability of uniform steady-state solutions of our model.

This will be explored further in the next section.


### 3.3.1    Simplifying assumptions concerning spatial dependences

In our model, fixing $\gamma$ is equivalent to decoupling the amplification and adaptation

modules. Thus, the steady-state value of $P_n$ at fixed $\gamma$ represents the steady-state

response of the amplification module. We will calculate this response by setting the LHS

of Eqs. M.1 – M.5 (Table 2.3) to zero and solving for $P_n$ in terms of $\gamma$.

Our model equations contain spatial couplings consisting of diffusion terms and

integrals (these integrals are equivalent to spatial averages and account for exchange of

molecules between cytosolic pools and the entire membrane, see Secs. 2.2.2 and 2.5.3).

In order to calculate the steady-state response of our amplification module, we will make

three kinds of simplifying assumptions concerning these spatial couplings.

First, we will consider the situation where the cell remains spatially uniform. Then the spatial average of a quantity is equal to its value anywhere on the membrane. We will refer to these solutions as the 'uniform' response of the amplification module.

Second, we will consider the situation where diffusion is neglected and all averages are fixed at the values they obtain in the uniform cell at steady-state. This might be appropriate if we wish to consider the response at a single point on the membrane (neglecting diffusion), which would not affect averages and cytosolic concentrations. We will refer to this second set of solutions as the 'fixed average' response of the amplification module. Comparison to the 'uniform' response will highlight the relative importance of translocating molecules in each model variant's amplification module.

We note that the 'uniform' response of the amplification module is, by definition, the nullcline for the $P_n$ equation in the $\gamma$, $P_n$ plane for the 'reduced' model, where all concentrations are set to steady-state values with respect to $P_n$ and $\gamma$ for a uniform system. This was discussed in Sec. 3.2 and depicted by the bold short-dashed curves in Fig. 3.1. The 'fixed average' response', however, does not have a useful interpretation as a nullcline for non-uniform solutions because it neglects diffusion.

The final situation that we will consider is a lowest order attempt to include the effects of diffusion on non-uniform responses of our amplification module, without formally calculating spatially dependent solutions. Averages and cytosolic concentrations are fixed, as for the 'fixed average' response. However, instead of neglecting diffusion, we will replace diffusion terms by $'-D(2\pi)^2 \left( P_i - \bar{P}_i \right)'$, where the subscript, $i$, takes the values *2*, *3* or *n*, depending on if Eq. M.1, M.2, or 3.1 is being considered, and $\bar{P}_i$ is the uniform steady-state value of $P_i$. This transformation preserves the value of $P_i$ that will

be calculated for $\gamma = \gamma_0$ (i.e. $\boldsymbol{P_i} = \overline{\boldsymbol{P_i}}$ for the baseline state of the cell), while including the effects of diffusion for a solution of the form $\left(\boldsymbol{P_i} - \overline{\boldsymbol{P_i}}\right)\cos\left(2\pi jX - \varphi\right)$ with $j = 1$, where $\varphi$ is an arbitrary phase. We will thus refer to these solutions as the '1st mode' response of the amplification module.

A spatially linear gradient in the outside stimulus results in a pattern of $\boldsymbol{\gamma}$ with a spatial dependence of the form $\cos\left(2\pi X - \varphi\right)$, where $\varphi$ specifies the direction of the gradient with respect to the $X = 0$ direction (this will be discussed further in Sec. 4.2.3). If the steady-state response of the cell to gradients varies continuously, then for small gradients, all of the spatially dependent model variables will be altered from their uniform steady-state distributions by a component with this same spatial dependence; our model equations can also be linearized under these conditions, as discussed further in Sec. 3.4. If we cancel this spatial dependence from our equations, then the resulting diffusion terms will be of the form suggested for our '1st mode' response of the amplification module and spatial averages will remain fixed. Thus, the '1st mode' response gives the amplitude of the steady-state polarized response to small gradients in $\boldsymbol{\gamma}$ about $\gamma = \gamma_0$. The resulting relationship between $\boldsymbol{P_n}$ and $\boldsymbol{\gamma}$ gives the nullcline, near $\gamma = \gamma_0$ in the $\boldsymbol{\gamma}$, $\boldsymbol{P_n}$ plane, of the equation describing the amplitude of this response in the variable $\boldsymbol{P_n}$, for the 'reduced' model, with the above '1st mode' assumption made concerning its spatial dependences.

### 3.3.2   Responses of the amplification module – General features and those that distinguish the model variants

The steady-state responses of our model's amplification module are plotted in Fig. 3.2.
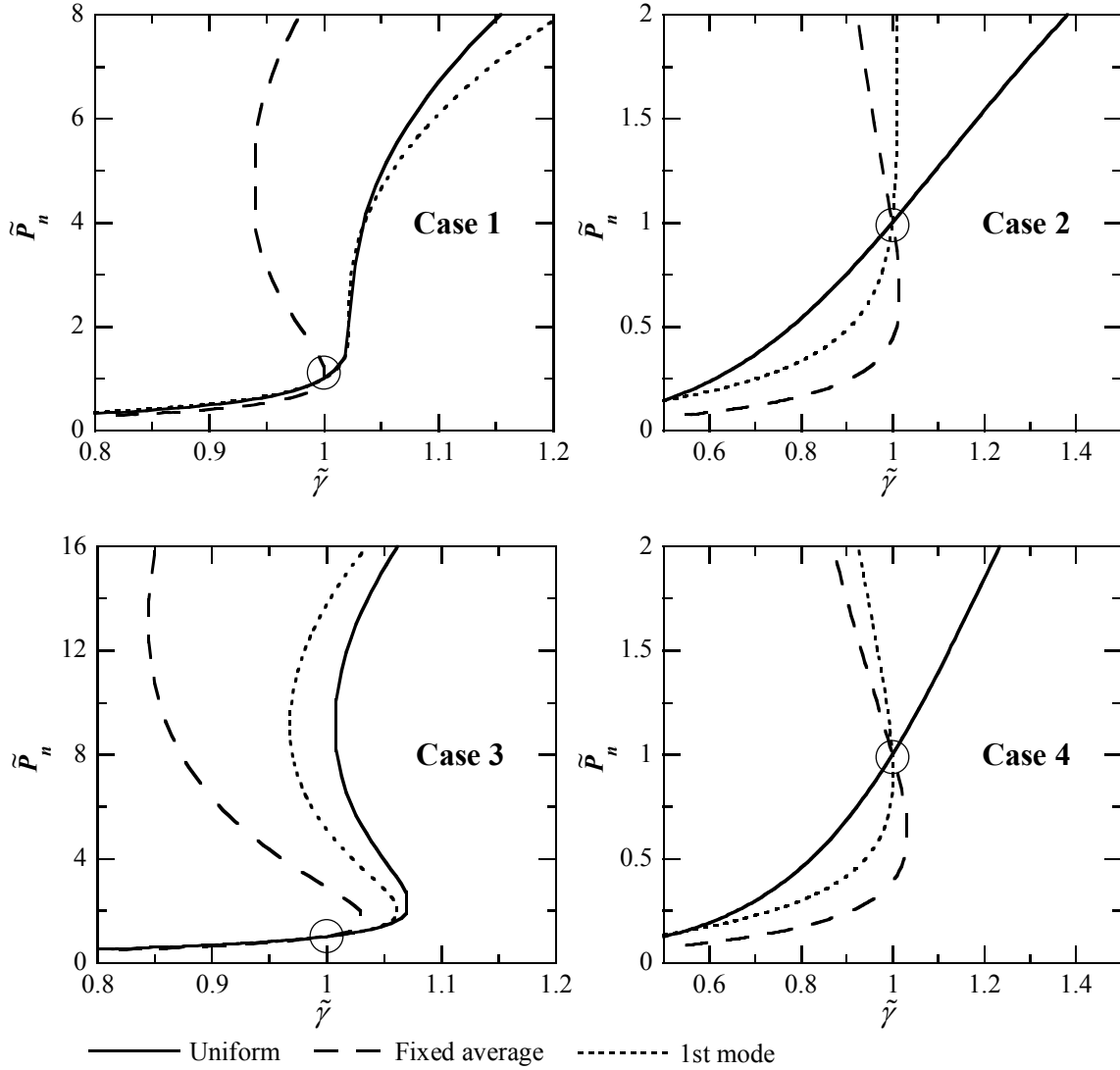
**Figure 3.2. Steady-state response of the amplification module: isoclines in $P_n$, $\gamma$ plane.** Steady-state solutions to our model equations are calculated at fixed $\gamma$ for each variant, under the simplifying conditions described in Sec. 3.3.1. These solutions represent the 'uniform' response, the 'fixed average' response, and the '1st mode' response of our model's amplification module. $\tilde{P}_n = P_n / \bar{P}_n$ is plotted against $\tilde{\gamma} = \gamma / \gamma_0$, where $\bar{P}_n$ is the uniform steady-state value of $P_n$ in the unstimulated cell (at $\tilde{\gamma} = 1$) and $\gamma_0$ is the steady-state value of $\gamma$, which sets the baseline state of the cell (defined in Eq. M.6a of Table 2.3, and discussed in Secs. 2.5.3 – 2.5.5). A circle marks the uniform steady-state solution for each variant.

The curves that result from our three simplifying assumptions concerning spatial

dependences intersect at the uniform steady-state solution for each Case, marked by a

circle at $\tilde{\gamma} = 1$. We note several general features of these curves, which exist for a large range of parameter values about those that were considered. At $\tilde{\gamma} = 0$, $\tilde{P}_n$ is small and increases slowly with $\tilde{\gamma}$ for all curves. In this regime, $P_n$ production is controlled by the constitutive processes that have been included in our model. As $\tilde{\gamma}$ becomes of order 1, i.e. as it approaches the baseline value for each model variant, positive feedbacks in the amplification module become effective and $\tilde{P}_n$ increases more sharply. This increase is further sharpened if parameters are adjusted such that coupled positive feedbacks become more effective and constitutive processes become less significant.

Some of the curves depicted in Fig. 3.2 double back on themselves. For these curves, positive feedbacks are sufficiently strong to induce multiple steady-state responses of our amplification module at fixed $\gamma$ (under the appropriate simplifying assumption). On the other hand, a single value of $P_n$ always uniquely specifies a value of $\gamma$ for each curve. Thus, we can write

$$\gamma = f\left(P_n\right), \tag{3.3}$$

for some function, $f$. When multiple steady-state responses do exist for a particular $\gamma$, the following relationships hold: $\partial P_n / \partial \gamma \equiv 1/\left(\partial f / \partial P_n\right) > 0$ for the solution with smallest $P_n$; the sign of $\partial P_n / \partial \gamma$ alternates for successive solutions, assuming that it remains finite; in general, no more than three solutions were found for a given $\gamma$.

For the 'uniform' responses of the amplification module depicted in Fig. 3.2, we find that the value of $P_n$ is always uniquely determined at $\tilde{\gamma} = 1$, i.e. the uniform steady state in the unstimulated cell is uniquely determined by $\gamma_0$ for each variant. At $\tilde{\gamma} = 1$, the 'fixed average' response and the '1st mode' response always increase more sharply with $\gamma$ than

the 'uniform' response. This is because averages and cytosolic quantities are held fixed for the 'fixed average' and the '1st mode' responses, while these terms act to saturate the 'uniform' response as $\gamma$ is increased.

The curves in Fig. 3.2 highlight the differences between our model variants, which are essentially found in their respective amplification modules. Cases 1 and 3 demonstrate high gain in the 'uniform' response of their amplification modules. For these Cases, cytosolic molecules are not significantly depleted as $\gamma$ is increased about $\tilde{\gamma} = 1$. In addition, because positive feedbacks are more effective for Case 3, multiple uniform steady-states at fixed $\gamma$ are possible for a range of $\gamma$. The depicted uniform response is weaker for Cases 2 and 4 because cytosolic molecules are more significantly depleted as $\gamma$ is increased. On the other hand, the 'fixed average' and '1st mode' responses, for which cytosolic concentrations are held fixed, are sharp for all Cases. The greater difference between the 'uniform' response and the 'fixed average' response, for Cases 2 and 4 near their circled intersections, indicates that redistribution of translocating molecules plays a more important role in amplifying responses to non-uniform stimuli for these Cases than for the others.

For all Cases, the 'fixed average' response eventually doubles back on itself, suggesting that multiple steady-states may be possible for patterns of stimuli that lead to non-uniform steady-state patterns of $\gamma$ on the membrane. On the other hand, the '1st mode' response, which includes some effects of diffusion, only doubles back on its self for Cases 3 and 4. This suggests that when diffusion is included, multiple steady-states may only be possible for these Cases. This will be confirmed later with simulations of our model's responses to spatial gradients of stimulus (see Sec. 4.3.2).

### 3.3.3 Interpretation as nullclines – stability criteria for uniform steady-state solutions, based on the reduced model

In Sec. 3.3.1, we had suggested that the 'uniform' and '1st mode' responses of our model's amplification module (depicted in Fig. 3.2) can be interpreted as nullclines of the $P_n$ equation for a 'reduced' model where other variables are set to steady-state with respect to $P_n$ and $\gamma$ and appropriate assumptions are made concerning spatial dependences. In particular, the 'uniform' response describes the nullcline of the $P_n$ equation in the 'reduced' model, assuming uniform solutions, and the '1st mode' response describes the nullcline if the spatial dependence is of the form that would result in response to a '1st mode' harmonic perturbation. Here we further develop these ideas.

For small perturbations, the equations describing the dynamics of the reduced model can be linearized about the uniform steady-state solution defined by $\gamma = \gamma_0$ and $P_n = \bar{P}_n$. The resulting linearized equation describing the dynamics of $\gamma$ can be written in the form

$$\frac{\partial \gamma}{\partial t} = \lambda_\gamma \left( \gamma_0 - \gamma \right). \tag{3.4}$$

For a uniform system, $\lambda_\gamma > 0$ is given by Eq. 3.2. For a system with fixed averages (such as the '1st mode' response), $\lambda_\gamma = 0$ in the absence of external stimuli since $\gamma$ depends only on the cytosolic variable, $K_c$, which has no spatial dependence.

The linearized equation describing $P_n$ dynamics can be written in the form

$$\frac{\partial P_n}{\partial t} = \lambda_{P_n} \left( \left( \gamma - \gamma_0 \right) - \left. \frac{\partial f \left( P_n \right)}{\partial P_n} \right|_{\bar{P}_n} \left( P_n - \bar{P}_n \right) \right). \tag{3.5}$$

The function $f$, defined in Eq. 3.3, describes the nullcline of the $P_n$ equation in the reduced model under the appropriate simplifying assumption, as described in the previous subsection. If the nullcline derived from the 'uniform' response of the amplification

92

module is used, then Eqs. 3.4 and 3.5 describe the dynamics of small uniform

perturbations. If the nullcline derived from the '1st mode' response is used, then these

equations describe the dynamics of small 1st mode harmonic perturbations. From Eqs.

M.3 and M.1 of Table 2.3, it is clear that increasing $\gamma$ above its uniform steady-state

value will increase $K_m$ and produce more $P_n$. Thus, $\lambda_{P_n} > 0$ in Eq. 3.5 for both

interpretations.

If eigenmode solutions for Eqs. 3.4 and 3.5 are calculated, it can be shown that the

condition for linear growth of perturbations is $\partial f\left(P_n\right)/\partial P_n\big|_{\bar{P}_n} \equiv 1/\left(\partial P_n/\partial\gamma\big|_{isocline,\gamma=\gamma_0}\right) < 0$.

We see in Fig. 3.2 that for the uniform responses of the amplification module,

$\partial P_n/\partial\gamma > 0$ at $\tilde{\gamma} = 1$ for all Cases. We thus conclude that in the 'reduced' model, the

uniform steady-state solution is stable to uniform perturbations for all Cases. Only for

Case 4 is $\partial P_n/\partial\gamma < 0$ for the '1st mode' response at $\tilde{\gamma} = 1$. We thus conclude that the

uniform steady state is unstable towards 1st mode perturbations for Case 4, while the

uniform steady-state solutions for the other Cases are stable towards '1st mode'

perturbations. Because higher mode harmonic perturbations are dissipated mode quickly

by the diffusion terms in our equations, the other Cases will be stable to those

perturbations as well; they are thus linearly stable to all perturbations in the 'reduced'

model. In the next section, we will show that the criteria for uniform steady-state

solutions to be linearly stable in the 'full' model are equivalent to these simpler stability

criteria in the 'reduced' model.


## 3.4  Linear stability analysis

We now explore stability properties of solutions to our model equations. We begin by

formally writing linearized equations for small perturbations about uniform steady-state solutions and inserting normal-mode test solutions (Sec. 3.4.1). Analyzing these linearized equations will further elucidate the structure of our model and identify parameters that qualitatively shape its responses. We will then argue that the criteria for stability of uniform steady-state solutions to our full set of model equations are equivalent to the more intuitive stability criteria suggested in Sec. 2.3.3, based on the discussed 'reduced' model (Sec. 3.4.2). This equivalence is confirmed numerically when we explicitly calculate linear growth rates for the fastest growing eigenmode perturbations about our model's uniform steady-state solutions (Sec. 3.4.3). We conclude this section by discussing bifurcations in the response of our model at zero stimulus (Sec. 3.4.4), and by extending our numerical analysis to investigate the stability of polarized steady-state solutions (Sec. 3.4.5).

3.4.1    Linearized equations for analyzing responses to small perturbations

To explore the stability properties of our model, we linearize our six model equations (M.1 – M.6 in Table 2.3) about their steady-state solutions, and insert trial solutions that describe the dynamics of small normal-mode perturbations. The analysis is clearer if we make several changes of variables. Perturbations in $P_3$ are eliminated in favor of perturbations in the variable $P_n$ – we consider Eq. 3.1 in place of Eq. M.1. Perturbations in the variable $K_c{}^*$ are eliminated in favor of perturbations in the driving parameter, $\gamma$ – we consider Eq. 3.2 in place of Eq. M.6. Perturbations in the variable $T_c{}^*$ are eliminated in favor of $T_c$ – we consider Eq. M.10 in place of Eq. M.5.

We begin by inserting trial solution of the form

$$U(X,t) = U_0(X) + \delta U(X,t) \tag{3.6}$$

in our model equations, making the above-mentioned substitutions and linearizing with respect to $\delta U(X,t)$. Here, $U$ represents any model variable, $U_0(X)$ describes the initial spatial distribution of that variable, and $\delta U(X,t)$ describes the dynamics of perturbations in that variable.

If outside stimuli are absent or constant in time, then our system contains no explicit time dependence. Thus, we can introduce trial solutions of the form

$$\delta U(X,t) = \varepsilon \tilde{U}_j(X) \exp(\sigma_j t), \tag{3.7}$$

where $\varepsilon$ is small. Here, '$j$' designates an anticipated normal-mode solution with spatial distribution given by $\tilde{U}_j(X)$ and linear growth rate, $\sigma_j$ (both of which might be complex). If, in addition, we are considering perturbations about uniform steady-state solutions, then our equations will not include any explicit spatial dependence. We may then introduce a harmonic spatial dependence as

$$\tilde{U}_j(X) = \hat{U}_j \exp(i2\pi jX). \tag{3.8}$$

Here, $i$ is the imaginary unit and $j$ must be an integer for solutions that vary smoothly about $X = 0$. $\hat{U}_j$ is the component of the perturbation in the 'direction' of the variable '$U$' in the space of our six model variables. We note that for cytosolic variables no subscript is necessary, as only uniform perturbations with $j = 0$ are considered.

For perturbations about uniform steady-state solutions, we thus use the forms in Eqs. 3.7 and 3.8 in our linearized equations, keeping only lowest order terms in $\varepsilon$. After multiplying by a complex conjugate solution, integrating over the membrane, and making

95

the appropriate changes of variables, we arrive at the following system of linear equations in our perturbation components:

$$\sigma_j \hat{\boldsymbol{P}}_{n,j} = \frac{\chi_3 \boldsymbol{K}_m}{\left(1 + \boldsymbol{K}_m / \kappa_3\right)} \tilde{\Xi}_j \hat{\boldsymbol{P}}_{n,j} + \chi_3 \left(\frac{\Xi}{\left(1 + \boldsymbol{K}_m / \kappa_3\right)^2} + \zeta_{3/PITP}\right) \hat{\boldsymbol{K}}_{m,j} - \left(\lambda_3 \boldsymbol{P}_3 + \lambda_2 \boldsymbol{P}_2\right) \hat{\boldsymbol{T}}_{m,j}$$
$$- \lambda_3 \boldsymbol{T}_m \hat{\boldsymbol{P}}_{n,j} + \left(\lambda_3 \boldsymbol{T}_m - \lambda_2 \left(\boldsymbol{T}_m + \zeta_{2/T}\right)\right) \hat{\boldsymbol{P}}_{2,j} - D\left(2\pi j\right)^2 \hat{\boldsymbol{P}}_{n,j} \tag{3.9}$$

where, $\tilde{\Xi}_j = \dfrac{1 + \left(1 - \delta_{0,j}\right) \langle \boldsymbol{P}_n \rangle_X / \kappa_c}{\left(\boldsymbol{P}_n / \kappa_m + \langle \boldsymbol{P}_n \rangle_X / \kappa_c + 1\right)^2}$, \hfill (3.9a)

and $\Xi$ is defined in Eq. M.1a.

$$\sigma_j \hat{\boldsymbol{P}}_{2,j} = \lambda_3 \zeta_{3/T} \hat{\boldsymbol{P}}_{n,j} - \lambda_2 \boldsymbol{P}_2 \hat{\boldsymbol{T}}_{m,j} - \left(\lambda_3 \zeta_{3/T} + \lambda_2 \left(\boldsymbol{T}_m + \zeta_{2/T}\right) + D\left(2\pi j\right)^2\right) \hat{\boldsymbol{P}}_{2,j} \tag{3.10}$$

$$\sigma_j \hat{\boldsymbol{K}}_{m,j} = \delta_{0,j} \lambda_K \hat{\gamma} + \frac{\lambda_K \boldsymbol{K}_m / \kappa_K}{\left(1 + \boldsymbol{P}_n / \kappa_K\right)^2} \hat{\boldsymbol{P}}_{n,j} - \frac{\lambda_K}{1 + \boldsymbol{P}_n / \kappa_K} \hat{\boldsymbol{K}}_{m,j}, \tag{3.11}$$

$$\sigma_j \hat{\boldsymbol{T}}_{m,j} = \chi_T \delta_{0,j} \hat{\boldsymbol{T}}_c - \lambda_T \boldsymbol{T}_m \hat{\boldsymbol{K}}_{m,j} - \lambda_T \left(\boldsymbol{K}_m + \zeta_T\right) \hat{\boldsymbol{T}}_{m,j} \tag{3.12}$$

$$\sigma_0 \hat{\boldsymbol{T}}_c = -\left(\lambda_{T^*} - \lambda_T \zeta_T\right) \hat{\boldsymbol{T}}_{m,0} / A_{cell} - \left(\chi_T / A_{cell} + \lambda_{T^*}\right) \hat{\boldsymbol{T}}_c. \tag{3.13}$$

$$\sigma_0 \hat{\gamma} \sim -\left(\chi_K / A_{cell}\right)\left(\mathcal{R} + 1\right)\hat{\gamma} \tag{3.14}$$

Here, variables with no '^' represent the steady-state solutions about which we perturb, and we have replaced integrals by spatial averages to make a more compact notation. Terms involving $\delta_{0,j}$ arise because the average value of our perturbation around the membrane is 0 unless $j = 0$, and because perturbations in cytosolic quantities have no spatial dependence. Our model variables are defined with subscripts that are fixed (e.g. 2, 3, n, c, m). Thus, we have introduced a ',' before the subscript, $j$, whose range includes all integers.

Equations. 3.9 – 3.14 can be written in matrix form as

$$\sigma_j \bar{U}_j = \ddot{A}_j \bar{U}_j,$$  (3.15)

where $\ddot{A}_j$ is a 6X6 matrix and the vector $\bar{U}_j$ is the vector of components, $\hat{U}_j$, of the perturbation in our six model variables. For each $j$, Eq. 3.15 is an eigenvalue problem. We will be particularly interested in the sign of the growth rate, $\sigma_j$, for the fastest growing solution. A positive growth rate indicates that our steady-state solution is unstable to the corresponding perturbation. Before solving Eq. 3.15, we discuss some of the important terms and parameters that will determine when instability might result.

As noted in Sec. 3.2, our model has been designed such that the variables $P_3$, $P_2$ and $K_m$ generally display a similar dynamic, while $T_m$ displays an inverse dynamic. These variables are all constituents of our model's amplification module. Consistent with this observation, we can conclude from Eq. 3.9 that the growth rate of a perturbation in $P_n$ is increased if $\hat{P}_{2,j}$ and $\hat{K}_{m,j}$ have the same sign as $\hat{P}_{n,j}$ (parameters are set such that $\left( \lambda_3 T_m - \lambda_2 \left( T_m + \zeta_{2/T} \right) \right) > 0$), while $\hat{T}_{m,j}$ has the opposite sign. The growth rate in Eq. 3.9 is further enhanced if the feedback in **Loop I** is strong. Thus, increased $\chi_3$, $K_m$ and $P_n$ (which result in increased $\Xi$ and $\Xi_j$) will all increase the possibility of a positive growth rate and could potentially lead to instability.

We further see from Eq. 3.9 that, though diffusion results in greater dissipation for higher $j$, $\tilde{\Xi}_j$ is larger for non-uniform perturbations $( j \neq 0)$. This increase in $\Xi_j$ is more significant for smaller $\kappa_c$, i.e. if depletion of translocating molecules in our model is more significant. Thus, if depletion of translocating molecules in our amplification module is significant, a non-uniform perturbation might grow more quickly than a uniform one

97

because it redistributes translocating molecules rather than further depleting them from the cytosol. As mentioned in Sec. 2.7.2, the value of $\kappa_c$ was adjusted to control the role of translocating molecules in our model and to specify our model variants.

From Eq. 3.10, we see that the growth rate of a perturbation in $P_2$ is increased if $\hat{P}_{2,j}$ and $\hat{P}_{n,j}$ have the same sign, while $\hat{T}_{m,j}$ has opposite sign.

The possibility of instability also requires **Loop II** to be effective, as this feedback will control $\hat{K}_{m,j}$ and $\hat{T}_{m,j}$. Equation 3.11, which describes the primary feedback in **Loop II**, says that perturbations grow more quickly if $\hat{P}_{n,j}$ and $\hat{K}_{m,j}$ have the same sign. The growth rate is further enhanced if $\kappa_K$ is small, which makes the feedback in **Loop II** more effective; the parameter $\kappa_K$ was adjusted to control the role of coupled positive feedbacks in our model and to specify our model variants (as discussed in Sec. 2.7.2). The growth rate for $j = 0$ involves $\hat{y}$ as well. However we will see below that $\hat{y} \sim 0$ is required for positive $\sigma_0$. Thus, we can conclude from Eq. 3.11 for all $j$, that positive $\sigma_j$ requires $\hat{P}_{n,j}$ and $\hat{K}_{m,j}$ have the same sign.

Similarly, Eq. 3.12, which also describes **Loop II** regulation, indicates that perturbations grow more quickly if $\hat{T}_{m,j}$ and $\hat{K}_{m,j}$ have opposite sign. Equation 3.13 requires that $\hat{T}_{m,0}$ and $\hat{T}_c$ have opposite sign for positive $\sigma_0$ (parameters were set such that $\lambda_{T*} - \lambda_T \zeta_T > 0$). Thus, we can conclude from Eq. 3.12 and 3.13 that for any $j$, if $\sigma_j$ is to be positive, $\hat{T}_{m,j}$ and $\hat{K}_{m,j}$ must have opposite sign.

Finally, Eq. 3.14 describes the dynamics of small perturbations in our driving parameter, as controlled by our adaptation module (**Loop III**). These perturbations

always decay.  We thus conclude that a positive growth rate requires

$$\hat{\gamma} \sim 0 . \tag{3.14'}$$

### 3.4.2.  Stability criteria based in the reduced model ($P_n$ and γ)

To clarify the conditions for linear instability of uniform solutions, we regroup terms in

our linearized equations:

$$\left(\sigma_j + \lambda_3\left(T_m + \zeta_{3/T}\right) + D\left(2\pi j\right)^2\right)\hat{P}_{n,j} =$$

$$\frac{\chi_3 K_m}{\left(1 + K_m / \kappa_3\right)}\tilde{\Xi}_j\hat{P}_{n,j} + \left(\lambda_3\left(T_m + \zeta_{3/T}\right) - \lambda_2\left(T_m + \zeta_{2/T}\right)\right)\hat{P}_{2,j} \tag{3.9'}$$

$$+\chi_3\left(\frac{\Xi}{\left(1 + K_m / \kappa_3\right)^2} + \zeta_{3/PITP}\right)\hat{K}_{m,j} - \left(\lambda_3 P_3 + \lambda_2 P_2\right)\hat{T}_{m,j}$$

where
$$\tilde{\Xi}_j = \frac{1 + \left(1 - \delta_{0,j}\right)\langle P_n\rangle_X / \kappa_c}{\left(P_n / \kappa_m + \langle P_n\rangle_X / \kappa_c + 1\right)^2} \tag{3.9a'}$$

$$\left(\sigma_j + \lambda_3\zeta_{3/T} + \lambda_2\left(T_m + \zeta_{2/T}\right) + D\left(2\pi j\right)^2\right)\hat{P}_{2,j} = \lambda_3\zeta_{3/T}\hat{P}_{n,j} - \lambda_2 P_2\hat{T}_{m,j} \tag{3.10'}$$

$$\left(\sigma_j + \frac{\lambda_K}{1 + P_n / \kappa_K}\right)\hat{K}_{m,j} = \frac{\lambda_K K_m / \kappa_K}{\left(1 + P_n / \kappa_K\right)^2}\hat{P}_{n,j} \tag{3.11'}$$

$$\left(\sigma_j + \lambda_T\left(K_m + \zeta_T\right)\right)\hat{T}_{m,j} = \chi_T\delta_{0,j}\hat{T}_c - \lambda_T T_m\hat{K}_{m,j} \tag{3.12'}$$

$$\left(\sigma_0 + \chi_T / A_{cell} + \lambda_{T*}\right)\hat{T}_c = -\left(\lambda_{T*} - \lambda_T\zeta_T\right)\hat{T}_{m,0} / A_{cell}$$
$$\tag{3.13'}$$

$$\hat{\gamma} \sim 0 \tag{3.14'}$$

These equations have been renumbered with primes in correspondence to the equations in

Sec. 3.4.1.

As noted in Sec. 3.4.1, for positive σ, Eq. 3.13' requires $\hat{T}_c \propto -\hat{T}_{m,0}$. Similarly, Eq. 3.12' requires $\hat{T}_{m,j} \propto -\hat{K}_{m,j}$ and Eq. 3.11' requires $\hat{K}_{m,j} \propto \hat{P}_{n,j}$. Then Eq. 3.10' requires $\hat{P}_{2,j} \propto \hat{P}_{n,j}$. These conditions hold as well, with the same sign, if σ is set to 0 in Eqs. 3.10' – 3.13'. This is equivalent to setting our other model variables to steady-state values with respect to $P_n$ and γ. The resulting system of linearized equations describes the dynamics of perturbations in the 'reduced' model introduced earlier in this chapter, under the appropriate simplifying assumptions concerning spatial dependences ($j = 0$ corresponds to the assumption that the system remains 'uniform' and $j = 1$ corresponds to the assumption of a '1st mode' spatial dependence, as discussed in Sec. 3.3.1 and 3.3.3).

In fact, we show in Appendix C that the conditions for stability of uniform solutions to perturbations in our full model are precisely the same as conditions for stability in the 'reduced' model. Thus, if we are only concerned with whether a solution is stable (i.e. we are concerned with the sign of the growth rate for the fastest growing perturbation), the result can be obtained intuitively by noting the slope of the nullcline for the $P_n$ equation in the reduced model, considering 'uniform' and '1st mode' spatial dependences, as discussed in Sec. 3.3.3. As noted in Sec. 3.3.2, this is equivalent to analyzing the slopes of the 'uniform' and '1st mode' responses of our model's amplification module as, the driving parameter is increased about its baseline value. In practice, such 'reduced' criteria were generally used to qualitatively characterize the stability properties of our model as parameters were varied. Obtaining the actual growth rate for the fastest growing perturbation of wave number $j$, however, requires explicitly solving the eigenvalue problem represented by Eq. 3.15.

### 3.4.3    Growth rates of perturbations about uniform steady-state solutions

To confirm the suggested simplified stability criteria of Sec. 3.4.2, and to investigate in more detail the growth rates of perturbations about uniform steady-state solutions, we explicitly solved the eigenvalue problem, represent by Eqs. 3.9 – 3.14, for fastest growing eigenmode perturbation for each $j$. If the steady-state solution was found to be stable, the fastest growing mode was the one that decayed most slowly.

The components of the fastest growing mode, $\vec{U}_j$, and its corresponding growth rate, $\sigma_j$, were calculated from Eq. 3.15 using the following iterative algorithm. The matrix $\vec{\vec{A}}_j$ was first shifted according to the transformation

$$\vec{\vec{A}}_j{}' = \vec{\vec{A}}_j + \alpha_j \vec{\vec{I}} , \tag{3.16}$$

where $\vec{\vec{I}}$ is the identity matrix with '1's on the diagonal and all other elements 0 and $\alpha_j$ is a constant large enough that $\left( \vec{\vec{A}}_j' \vec{U}_j \right) \cdot \vec{U}_j > 0$ for any vector, $\vec{U}_j$. Thus, all of the eigenvalues of $\vec{\vec{A}}_j{}'$ are positive; the eigenvalues of $\vec{\vec{A}}_j$, representing the linear growth rates of eigenmode perturbations in our linearized equations, can be obtained from those of $\vec{\vec{A}}_j{}'$ by subtracting $\alpha_j$. Starting with a set of basis vectors for the 6-d space of our model variables as initial guesses, we applied the matrix $\vec{\vec{A}}_j{}'$ and then normalized the result. This procedure was iterated until the normalization factor became constant; the direction of the resulting normalized vector became constant as well, indicating that the solution had in fact converged on an eigenvector.

The results of applying the above algorithm to find the fastest growing perturbations about uniform steady-state solutions are given in Fig. 3.3. For each $j$, applying our

iteration to a complete basis of initial guesses always converged on a unique solution and the components of the calculated eigenvector were always found in a relationship consistent with our discussion in Sec. 3.4.2.

In Fig. 3.3, we see that the 'fastest growing' perturbations generally decay more quickly for larger $j$ due to increased diffusive dissipation. However, for Cases 2 and 4, the growth rate is larger for $j = 1$ than for $j = 0$. This occurs because perturbations for $j \neq 0$ do not affect averages and cytosolic concentrations in our linearized equations, while perturbations with $j = 0$ (uniform perturbations) deplete cytosolic molecules, causing the positive feedbacks in our model to saturate. The slower decay rate for non-uniform perturbations highlights the importance of redistribution of translocating molecules for amplifying responses to gradients in Cases 2 and 4. A positive growth rate is found only for Case 4 at $j = 1$. Thus, for Case 4, the uniform steady-state solution is unstable towards polarization, while the uniform steady-state solutions for the other
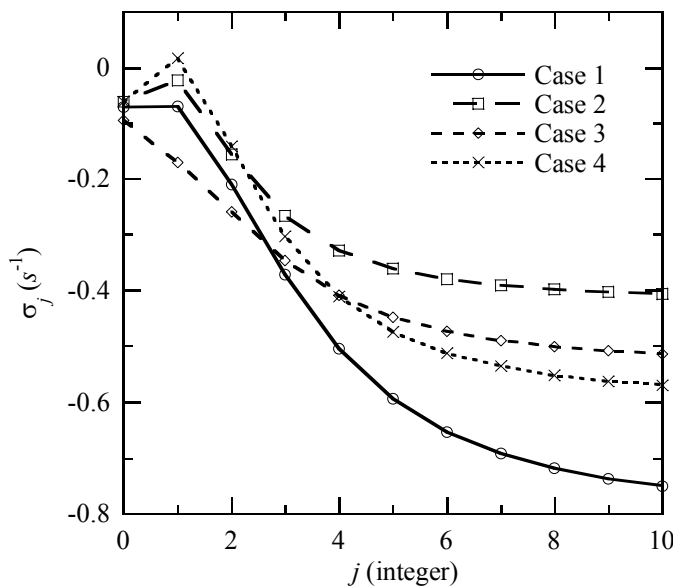


**Figure 3.3. Linear growth rates of perturbations about uniform steady-state solutions**. The largest linear growth rate for a small perturbation of mode number $j$ is calculated for each Case by using the iterative procedure outlined in the text. Symbols represent calculated growth rates, while lines are meant as a guide to the eye (only integer values of $j$ represent perturbations with correct periodic boundary conditions). Notice, that the largest growth rates are all negative, except for $j = 1$ for Case 4.

Cases are stable to all perturbations. These stability properties are consistent with the intuitive criteria suggested in Secs. 3.3.3 and 3.4.2.

The calculations of this subsection have further been confirmed by explicitly diagonalizing the linearized matrix to obtain the full spectrum of eigenmodes for each $j$ (not shown).

### 3.4.4    Bifurcations in parameter space ($\kappa_K$ and $\kappa_c$)

We have noted in the above discussion that our model variants have different linear stability properties. The characteristics our model variants were adjusted by varying the parameter $\kappa_K$, which controls the effectiveness of **Loop II**, and the parameter $\kappa_c$, which controls the degree to which depletion of translocating molecules saturates **Loop I** (the baseline parameter, $\gamma_0$, was also adjusted; this will be discussed further in the next section).

To further characterize the stability properties of our model, we calculate the linear growth rates for the fastest growing perturbations as $\kappa_K$ and $1/\kappa_c$ are systematically varied. Other parameters are set as in Case 4. Only $j = 0$ and $j = 1$ are considered, as these are always the fastest growing spatial modes.

We see in Fig 3.4 that as $\kappa_K$ is varied the uniform steady state always remains stable to uniform perturbations (i.e., with $j = 0$). However, it becomes unstable towards perturbations with $j = 1$ (i.e. '1st mode' perturbations) at intermediate values of $\kappa_K$. Decreasing $\kappa_K$ increases the effectiveness of **Loop II** and initially drives instability. On the other hand, the uniform steady-state value of $P_n$ increases as $\kappa_K$ is decreased and eventually the effectiveness of **Loop I** becomes saturated. As the value of $\kappa_K$ is
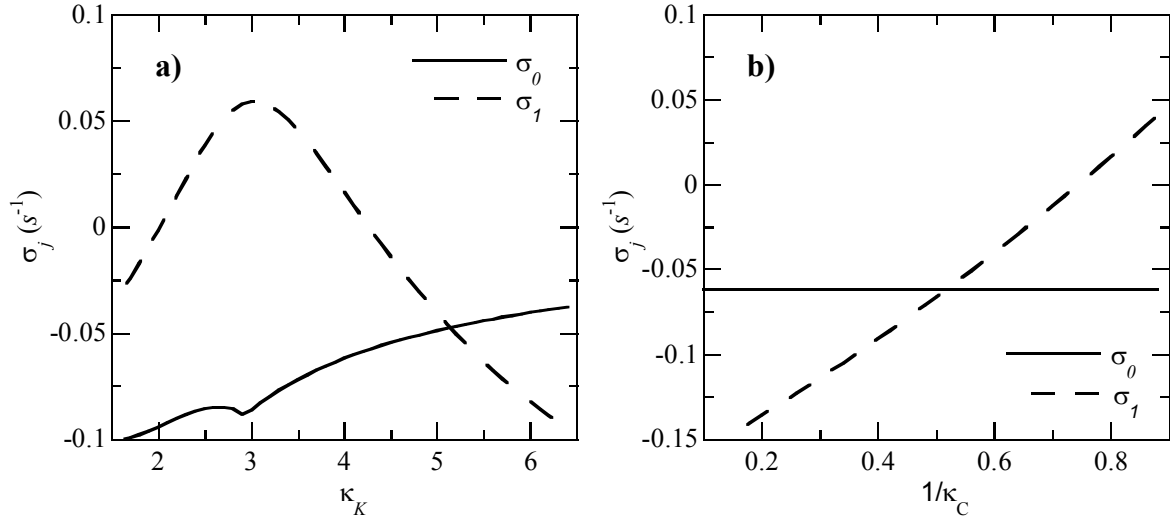
**Figure 3.4. Bifurcation plot.** The largest growth rates for perturbations with $j = 0$ and $j = 1$ about uniform steady-state solutions, are calculated as in Fig. 3.3. Unless otherwise mentioned, the indicated parameter is varied with other parameters fixed at the values used for Case 4. For each parameter choice, the uniform steady-state solution is recalculated before the eigenvalue problem is solved. **a)** $\kappa_K$ is varied. The feedback in **Loop II** becomes more effective for smaller $\kappa_K$ and the uniform steady-state value of $P_n$ increases, though it always remains unique for these combinations of parameters. $\kappa_K = 4$ specifies Case 4. **b)** $1/\kappa_c$ is varied and $1/\kappa_m$ is adjusted such that the relationship $1/\kappa_m + 1/\kappa_c = 1$ is maintained, thus preserving the uniform steady-state solution. Larger $1/\kappa_c$ means that translocating molecules play a more important role in saturating the response of **Loop I**. Their redistribution can lead to highly amplified non-uniform responses. $1/\kappa_c = 0.8$ specifies Case 4.

decreased below approximately 3, the effect of saturation begins to dominate and the growth rate begins to decrease. $\kappa_K = 4$ specifies Case 4.

Increasing $1/\kappa_c$ increases the potential for translocating molecules in **Loop I** to enhance non-uniform responses. As $1/\kappa_c$ is varied in Fig. 3.4, $1/\kappa_m$ is adjusted such that the relationship $1/\kappa_m + 1/\kappa_c = 1$ is preserved (see Table 2.2 and discussion in Appendix A). Thus, the uniform steady-state solution, as well as its response to uniform perturbations ($j = 0$), is unaffected. The growth rate for the fastest growing perturbation at $j = 1$ increases with $1/\kappa_c$, eventually becoming positive. For large $1/\kappa_c$, redistribution

of translocating molecules in response to non-uniform perturbations enhances the

feedback from **Loop I** sufficiently to cause instability. $1/\kappa_c = 0.8$ specifies Case 4.

We note that the bifurcations illustrated in Fig. 3.4 are all supercritical (161). As the

indicated parameters are varied and the uniforms steady-state solution to our model

equations becomes unstable, a stable polarized solution becomes available. The

transition from one stable steady-state response to the other is continuous (not shown). In

contrast, we will find in Chapter 4 that steady-state responses to outside stimuli can vary

discontinuously as outside stimuli are varied.


3.4.5   Stability of polarized solutions

We had found in the previous subsections that the uniform steady-state solution for Case

4 is unstable towards non-uniform perturbations. Thus we might ask if polarized

solutions to our model equations are generally stable, and if there is any characteristic

shape to the fastest growing perturbations about polarized steady-state solutions. To

investigate this, we consider steady-state solutions to our model equations in response to

an externally applied spatially linear gradient of stimulus. Thus, we consider steady-state

solutions in response to a pattern of receptor activation given by

$$\left\{ \mathcal{R} = 0, \ (t < 0); \ \mathcal{R} = S + G\left(1 + S\right)\cos\left(2\pi X\right), \ (t > 0)\right\}, \tag{3.17}$$

where $S = 2$ and $G = 0.05$. This results in a 5% gradient in $\gamma$ with respect to an external

Cartesian coordinate in the direction of the gradient. The forms that $\mathcal{R}$ takes in our

model to reflect different patterns of outside stimuli are discussed further in Sec. 4.2.3 of

Chapter 4. The numerical routine that is used to solve our model equations for steady-

state solutions is discussed in Sec. 4.2.1.

To investigate linear stability of these polarized steady-state solutions, we discretize our model equations in space and use a finite difference approximation in place of the diffusion terms. Trial solutions for the growth of small perturbations about these polarized solutions are inserted in our equations, as expressed by Eq. 3.6, and the equations are linearized with respect to the applied perturbations. We can no longer assume a harmonic spatial dependence (as in Eq. 3.8) because our steady-state solutions, and hence our linearized equations, are now explicitly spatially dependent.

For each disretized spatial point, we obtain a system similar to Eqs. 3.9 – 3.14, with two important differences. First, the finite difference approximation to the diffusion terms results in a coupling between neighboring spatial points (these coupling terms replace the terms of the form $-D(2\pi j)^2 \hat{\boldsymbol{P}}_{i,j}$ in Eq. 3.9 and 3.10, where $i = n$ or $2$). Second, because we are assuming a general spatial dependence for our perturbations, the integrals in our equations need to be linearized and explicitly calculated (they can no longer be replaced by terms of the form $\delta_{0,j}$, which are appropriate for harmonic spatial dependences). These integrals couple our linearized equations at all spatial points. The final result is a linear system of $4N + 2$ equations, where $N$ is the number of points used to discretize the spatial variable of our model.

We solve this system for the components and growth rate of the fastest linearly growing perturbation by the same iteration used to analyze uniform steady states in Sec. 3.4.3. Our system is not symmetric and we are not guaranteed a set of eigenvectors that spans the entire solution space (this was also true when we considered perturbations about uniform solutions) (162). The size of the system, and potential lack of a basis of eigenvectors, makes the calculation a bit less certain (further calculations, however, seem

to indicate that a set of eigenvactors which span the solution space can always be found). Nevertheless, we find that for all initial guesses, the iteration eventually converges on an eigenvector. In general, however, eigenvalues for the fastest growing modes were closely spaced and different choices for our initial guess converged on a small number of different solutions. A complete basis of initial vectors was investigated and the solution corresponding to the largest growth rate was selected. The normalized $P_n$ distribution for this fastest growing eigemode is plotted in Fig. 3.5, together with the normalized $P_n$ distribution of the steady-state solution about which the perturbation was applied.

The growth rate of the fastest growing eigenmode is labeled for each Case in Fig. 3.5, and found to always be negative. Thus, the polarized solutions generated by this particular stimulus are linearly stable to all perturbations. We see in Fig. 3.5 that the $P_n$ distributions for these fastest growing eigenmodes are single peaked. However, the peak of the perturbation is shifted with respect to the steady-state profile[#]. This suggests that polarized solutions are most sensitive to perturbation in the region surrounding their peaks. These kinds of perturbations might cause the axis of polarization to change direction, which is required for a cell to respond to a changing gradient. The depicted eigenmodes have significant components in all of their membrane variables, which are in the qualitative relationship suggested in Secs. 3.4.2 and 3.4.3.

The qualitative features of the above results have been confirmed by explicitly diagonalizing the matrix for our linearized equations, though several details are still

---

[#] This shift is on the order of 20% of the cell circumference (corresponding to an angle of order $\pi/2$ *rad*) for Cases 2-4. For Cases 1 and 3, a solution with a similar shape to those depicted for Cases 2 and 4 was also obtained with a slightly faster decay rate by our iteration. Further investigation by explicitly diagonalizing our linear matrix, however, suggests that the most slowly decaying perturbations for Cases 1 and 3 in fact have the same shape as those depicted for Case 2 and 4.
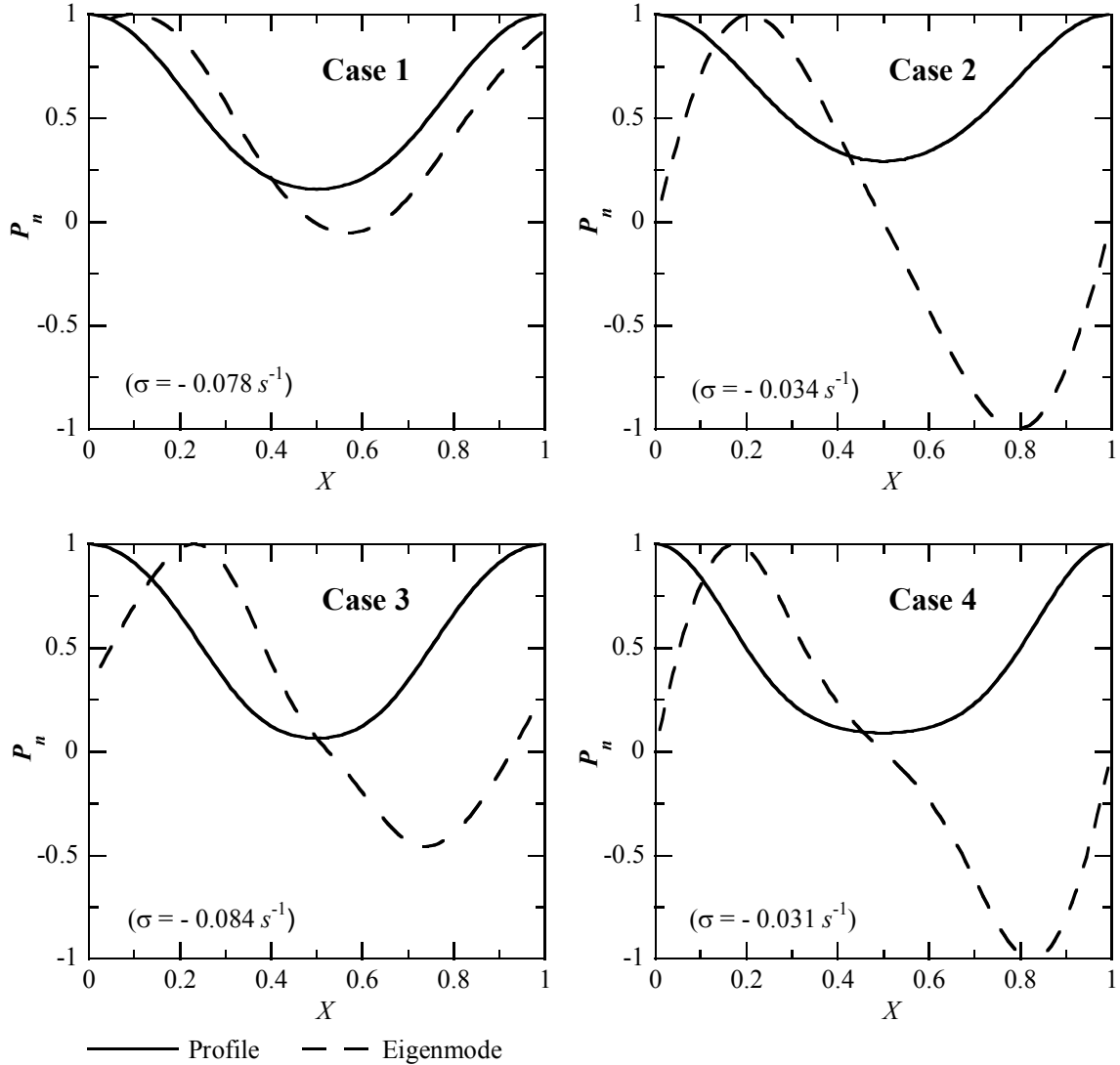
**Figure 3.5. Perturbations about polarized steady-state solutions.** Our system is evolved to steady-state in response to a spatially linear gradient of outside stimulus, defined by Eq. 3.16. The fastest growing eigenmode is calculated by the iterative method of Sec. 3.4.3. The steady-state $P_n$ distribution is given by the solid curve, and the $P_n$ distribution for the eigenmode is given by the dashed curve. Both are normalized by their peak value. The growth rate of the eigenmode, $\sigma$, is indicated for each Case.

under investigation. Stability of other polarized solutions was not investigated, but is

expected to have similar features.

**3.5    Restrictions on parameters for efficient gradient sensing**

Our model variants have been defined to illustrate the different qualitative behaviors that depend on the role of coupled positive feedbacks and translocating molecules in response amplification (see Sec. 2.7 of Chapter 2). These qualitative behaviors exist for a range of parameters, as will be seen in Sec. 4.5 of Chapter 4, when we characterize our model's behaviors over several surfaces in its parameter space. Within the range of parameters that are consistent with a given qualitative behavior, we further expect that different combinations of parameters will result in different efficiencies of gradient sensing. Here we investigate our model's polarized response to a small static gradient of stimulus as several parameters are systematically varied about the values used to define our model variant (parameter values can be found in Tables 2.4 and 2.5 of Chapter 2). In particular, we vary the parameter, $\gamma_0$, which sets the baseline state of the cell (defined in Eq. M.6a of Table 2.3 and discussed in Secs. 2.5.3d and 2.5.5), and the value of the scaled coefficient of lipid diffusion, $D$. For each model variant, we will find different restrictions on these parameters for efficient gradient sensing.

3.5.1    Restrictions on the baseline parameter

The features of the various responses of our model's amplification module (depicted in Fig. 3.2) suggest that in order for each variant to reproduce the characteristic gradient sensing behaviors (enumerated in Sec. 1.2.6), there must be different constraints on the baseline state of the cell, as determined by $\gamma_0$ (defined in Eq. M.6a). If the cell is to adapt to all uniform stimuli, $\gamma_0$ should not be set in the bistable regime of the uniform response of the amplification module (solid curves in Fig. 3.2) since the uniform baseline state of

the cell would then no longer be unique. Additionally, if there is to be a sharp cellular

response to small gradients in $\mathcal{R}$, $\gamma_0$ should be set to a value where responses to non-

uniform $\boldsymbol{\gamma}$, approximated by the '1st mode' response of the amplification module (short-

dashed curves in Fig. 3.2), is sharp.

To investigate constraints on $\gamma_0$, we simulate cellular response to a small static

spatially linear gradient in $\mathcal{R}$, as described by Eq. 3.16. $\gamma_0$ is varied by appropriately

adjusting $\lambda_{K*}$ (see Eqs. M.6 and M.6a); the parameter $\chi_K$ (see Eq. M.3) was adjusted as

well, such that $A_{cell}\boldsymbol{K_c} = 0.5$ was maintained in the unstimulated cell (i.e. 50% of total

PI3K was phosphorylated in the unstimulated cell). In Fig. 3.6, we plot a measure of the

normalized polarization in the 3'PI ($\boldsymbol{P_n}$) distribution that results, as a function of the

normalized baseline parameter, $\tilde{\gamma}_0 \equiv \gamma_0 / \gamma_i$. Here, $i \in \{1, 2, 3, 4\}$ and $\gamma_i$ is the fixed value

of $\gamma_0$ for variant $i$ which is used in subsequent simulations (see Table 2.5). Notice that the

values of $\gamma_i$ have been chosen such that for each curve the polarized response at $\tilde{\gamma}_0 = 1$ is

nearly optimal.

We further see in Fig. 3.6 that for efficient gradient detection in Cases 1 and 3, $\gamma_0$ must

be restricted to a narrow range of values. This range corresponds to the range of $\boldsymbol{\gamma}$ in Fig.

3.2 where the 'uniform' response of the amplification module becomes sharp. Thus, for

these Cases, $\gamma_0$ must be set very near an amplification threshold for the uniform response

of the amplification module if a highly polarized response to a relatively weak gradient is

to result[#] (characteristic behavior ii in Sec. 1.2.6). Thus, Cases 1 and 3 seem to respond

---

[#] The authors of the LI model, which was discussed in Sec. 1.5.3 of Chapter 1, have also found responses to gradients
to be sensitive to variations in parameters which set the baseline state of the cell but robust to perturbations in many
other model parameters (122).

110
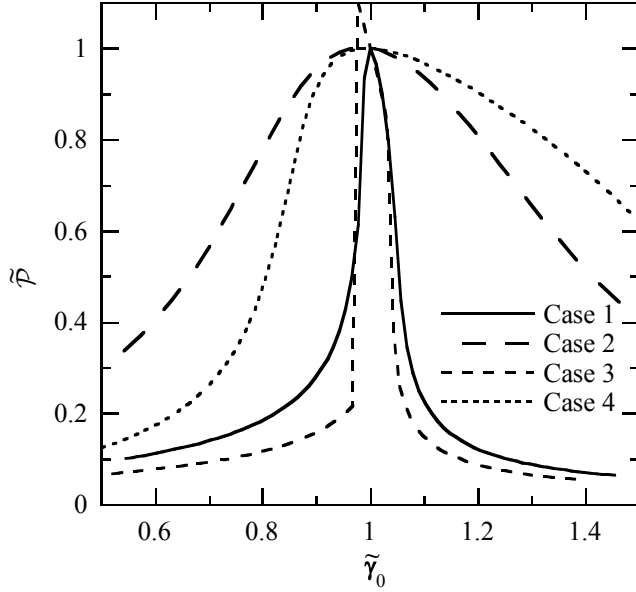
**Figure 3.6. Restrictions on the baseline state of the cell.** The parameter, $\gamma_0$ (see Eq. M.6a of Table 2.3 and Secs. 2.5.3d and 2.5.5 for discussion), is varied with respect to the value used to define our model variants; $\tilde{\gamma}_0 \equiv \gamma_0 / \gamma_i$ is varied, where $i \in \{1,2,3,4\}$ and $\gamma_i$ is the fixed value of $\gamma_0$ for variant $i$, given in Table 2.6. The steady-state cellular response to a small static gradient of external stimulus is calculated as described in the text. The response of the cell is quantified by the normalized polarization of the 3'PI distribution, $\tilde{\mathcal{P}}$, which is proportional to the first Fourier component of the distribution divided by its average value (see Eq. 4.1 of Sec. 4.2.2 for a complete definition), normalized by the value at $\tilde{\gamma}_0 = 1$. The sharp rise in the response of Case 3 is a discontinuity; steady state solutions that might be obtained by a different time course of the applied stimulus are not depicted.

seem to respond to gradients and uniform stimuli by similar mechanisms. The restriction of $\gamma_0$ to a narrow range of values suggests that in the development of cells which sense gradients by these mechanisms, there must exist homeostatic mechanisms that maintain the baseline state near such a threshold. Cases 2 and 4, on the other hand, rely on redistribution of translocating molecules between the front and back of the cell to amplify responses to gradients. These Cases merely require that $\gamma_0$ be high enough for a large fraction of these molecules to be on the membrane in the unstimulated cell, such that their redistribution will have a significant effect[#] (this fraction increases with $\int_0^1 P_n dX = \langle P_n \rangle_X$, which appears in Eqs. M.1/1a; see also Appendix A for a derivation). Note that for Case 3, the depicted jump in response represents a discontinuity, corresponding to a

---

[#] The authors of the PvH model (discussed in Sec. 1.5.3) have also demonstrated enhanced responses to gradients with a high baseline concentration of translocating molecule on the membrane (97).

bifurcation. For this Case, a less polarized solution would result for a different time course of the applied stimulus (not depicted; discussed further in Sec. 4.3.2 of Chapter 4). Multiple steady-states exist for Case 4 as well, though the steady-state response here varies continuously for the depicted range of parameters.

## 3.5.2    Restrictions on the membrane diffusion length

In analyzing the response of our model's amplification module (depicted in Fig. 3.2,) we noted that the 'fixed average' response doubles back on its self, suggesting the possibility of multiple steady-state solutions in responses to some patterns of outside stimuli. However, consideration of the '1st mode' response suggested that this possibility may no longer exist when diffusion is considered, under some conditions. Thus, we expect that cellular response might depend sharply on the relative value of the coefficient of lipid diffusion in our equations ($D$). More specifically, steady-state profiles depend on the ratio $\mathcal{L}^2 \equiv D/\lambda$, where $\lambda$ is a degradation rate constant and $\mathcal{L}^2$ can be thought of as the squared length which a lipid may diffuse before being degraded, per unit concentration of degrading enzyme[#].

In Fig. 3.7 we vary $D$, thereby varying the normalized diffusion length, $\tilde{\mathcal{L}}^2 \equiv \mathcal{L}^2 / \mathcal{L}^2_0$; $\mathcal{L}^2_0$ is the value of $\mathcal{L}^2$ used in subsequent simulations, which was the same for all variants (corresponding to of order 5% of the cell's circumference). As in Sec. 3.5.1, we plot the normalized polarization of the 3'PI distribution in response to a static gradient.

---

[#] The authors of the PvH model (discussed in Sec. 1.5.3) have also investigated the role of diffusion length in gradient sensing, though their model does not include multiple steady states (97).
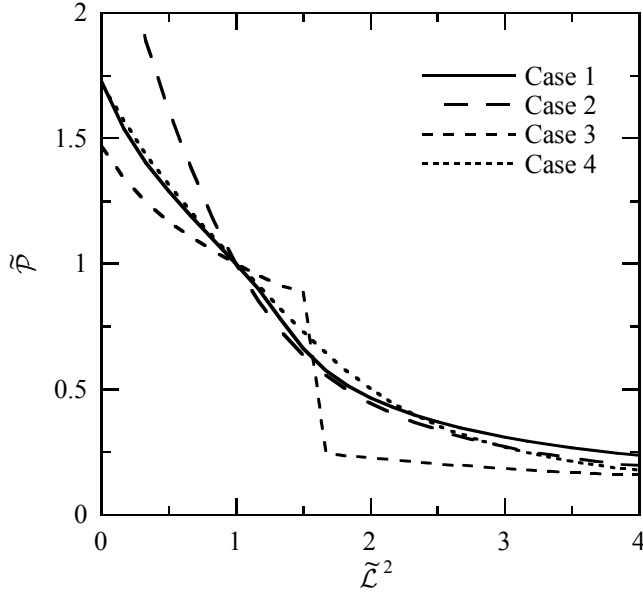
**Figure 3.7. Restrictions on diffusion length.** $\tilde{\mathcal{L}}^2 \equiv \mathcal{L}^2 / \mathcal{L}_0^2$ is varied (see text) and the relative steady-state polarization ($\tilde{\mathcal{P}}$, see Fig. 3.6) is calculated in response to a small static gradient. $\tilde{\mathcal{P}}$ is normalized by its value at $\tilde{\mathcal{L}}^2 = 1$. The depicted drop in the response of Case 3 as $\tilde{\mathcal{L}}^2$ is increased is a discontinuity; other steady-state solutions are not depicted.

Notice that $\tilde{\mathcal{L}}^2 = 1$ is in the regime where, for each variant, diffusion has a similarly significant affect on the polarized response of the cell.

For Case 3, multiple steady-states exist for small $\tilde{\mathcal{L}}^2$, and the sharp drop in polarized response as $\tilde{\mathcal{L}}^2$ is increased is a discontinuity, representing a bifurcation in steady-state response as the diffusion coefficient is varied. As in Fig. 3.6, only the more polarized steady-state solution is plotted, which results from the specified time course of the applied stimulus. While multiple steady-states exist for Case 4, the solution in response to this particular application of stimulus varies continuously.

## 3.5    Summary

In this chapter, we analyzed the structure of our model and its features that lead to the suggested differences in the behaviors of our model variants (Table 2.7). We began by analyzing the phase space dynamics of our model in the $P_n$, $\gamma$ plane, assuming that profiles remained uniform (Sec. 3.2). Our analysis suggested that the uniforms steady-state solutions of our model equations act as attractors in the space of our model

113

variables, provided that the system remains uniform. Our analysis further suggested that many features of our model may be understood based on the behaviors of the variables $P_n$ and $\gamma$, and that the steady-state response of our model's amplification module (represented by $P_n$) a fixed values of its driving parameter ($\gamma$), might contain important information. Because our model includes six variables, four of which are spatially dependent, any analysis that depends on the behavior of two variables is considerably more intuitive.

In Sec. 3.3, we analyzed the steady-state response of our model's amplification module at fixed values of its driving parameter. Simplifying assumptions were made concerning its spatial couplings, highlighting the roles that they play in our equations. We first considered the 'uniform' response of the amplification module. This was found to be considerably steeper for Cases 1 and 3 than for Cases 2 and 4; Cases 2 and 4 significantly deplete the cytosol of molecules that are necessary for response amplification, quickly saturating uniform responses. Next, we analyzed the response of the amplification module, assuming that cytosolic concentrations are fixed (i.e. they do not become depleted in cellular response). Under these conditions, all of the model variants demonstrated steep responses. Thus, under non-uniform conditions, where translocating molecules can be redistributed rather than depleted, Cases 2 and 4 can also demonstrate high gain in their responses. Finally, we analyzed a '1st mode' response, where the effects of diffusion are included, assuming the spatial profile of a 1st mode harmonic perturbation. The responses remained sharp for each model variant. However, where the 'fixed average' responses for all Cases had doubled back on themselves, suggesting the possibility of multiple steady-state responses to non-uniform stimuli, only

114

the responses of Cases 3 and 4 doubled back on themselves for the '1st mode' response. This suggests that diffusion plays an important role in affecting the stability of steady-state solutions for our model.

In Sec. 3.4, we analyzed the linear stability properties of steady-state solutions to our model equations. We began by suggesting that stability properties of uniform steady-state solutions might be understood intuitively based on a 'reduced' model, where all model variables are set to steady-state values with respect to $\gamma$ and $P_n$ and appropriate assumptions made concerning spatial couplings (Sec. 3.4.2). This analysis relied on the shape of the nullcline of the equation describing $P_n$ dynamics in the 'reduced model'. This nullcline is given by the steady-state response of our model's amplification module at fixed $\gamma$, with appropriate assumptions made concerning spatial couplings. Stability conditions in the 'reduced' model have been formally shown to be equivalent to stability conditions in the full model, and were used in practice to more intuitively understand the stability properties of our model as parameters were varied.

In Sec. 3.4.3, we confirmed that the uniform steady-state solutions to our model equations are linearly stable to all perturbations for Cases 1-3, but Case 4 is unstable to '1st mode' perturbations. Indeed, any gradient in external stimulus results in a highly polarized response for Case 4 (discussed further in Chapter 4). Stability properties of uniform steady-state solutions were also investigated as several parameters that had been adjusted to define our model variants were systematically varied (Sec. 3.4.4).

The stability propertied of a set of polarized steady-state solution were examined as well (Sec. 3.4.5). We found that these polarized solutions were linearly stable to all perturbations. The slowest decaying perturbations had a similar profile to the polarized

115

steady-state response under examination, but the peak was shifted. This suggested that polarized solutions to our model equations are most sensitive to perturbations in the transition region, approximately perpendicular to the axis of polarization.

Finally, we analyzed constraints on several model parameters for efficient gradient detection. We found that for Cases 1 and 3, the parameter that fixes that baseline state of the cell ($\gamma_0$) must be restricted to a narrow range to generate a highly polarized response to a small gradient. This corresponded to the range of $\boldsymbol{\gamma}$ where these variants demonstrated steep responses of their amplification modules (Sec. 3.3). Cases 2 and 4 merely required that a large fraction of translocating molecule be on the membrane in the unstimulated cell, such that their redistribution would have a substantial effect.

The value of the lipid diffusion coefficient also had a significant effect on polarized responses to a small gradient. In particular, Case 3, which demonstrates multiple steady states in response to a range of gradients (discussed further in Sec. 4.3.2), no longer does so at sufficient large values of the diffusion coefficient.

We might conclude from the analysis in Sec. 3.5 (as well as 3.4) that homeostatic mechanisms are required in gradient sensing cells to maintain combinations of parameters within appropriate ranges, and that transitions in response can result from small changes in model parameters. These possibilities are examined further in Sec. 4.5.

# Chapter 4: Distinguishing modes of gradient sensing

## 4.1    Overview

How well does each model variant account for characteristic gradient sensing behaviors and how might the variants be distinguished?  To investigate this, we simulate cellular response to uniform stimuli, to static gradients, and to rotating gradients (Sec. 4.3). Differences between the model variants are seen most clearly in simulated dose-response curves which highlight transitions in cellular response.  We use these results to define criteria which distinguish between the Modes of gradient sensing that are illustrated by our model variants (Sec. 4.4).

In applications to real cells, many biochemical parameters and regulatory details will be unknown.  To further investigate how the qualitative behaviors of our model variants depend on suggested biochemical mechanisms and parameters, we systematically vary several of our model's parameters.  For each combination of parameters, we simulate characteristic responses and apply our suggested criteria to determine which Mode of gradient sensing best describes the results (Sec. 4.5).  In this way, we characterize several surfaces in the parameter space of our model.

The results that we emphasize in this chapter are quite general and depend on qualitative features of gradient sensing mechanisms.  Thus, while the details of our model development, as well as the specific molecules whose dynamics it captures, depend on experimental observations in Dictyostelium and Neutrophils, we expect many of our results to be applicable to a wide range of gradient sensing cells that demonstrate

characteristic behaviors. We summarize the conclusions that might be drawn from our results, and discuss their implications for real cells, in Sec. 4.6.

## 4.2    Computation

### 4.2.1    Numerical techniques

Our system of PDEs is converted to a system of ODEs by discretizing the spatial coordinate, *X*, with equally spaced points; a central difference approximation is used for diffusion terms. We solve the system using a partially implicit Euler method; that is, our algorithm is first order in time, diffusion terms are treated implicitly for stability, and reaction terms (which are generally non-linear) are treated explicitly (162). This type of algorithm has the virtues of both speed and stability, and should generalize well to include stochastic terms in extensions of our model.

The accuracy of our results was checked by varying the time step (*h*) and number of spatial points (*N*) by a factor of 2. For all the patterns of stimuli that were tested, deviations between simulations with different *h* and *N* were always less than 0.2% (generally significantly less). Additionally, many of our results have been confirmed using a PDE solver called FiPy, based on a finite volume approach, developed by Jonathan Guyer, Daniel Wheeler, and James Warren at the National Institute of Standards and Technology (163).

### 4.2.2    Characterizing membrane distributions

In order to analyze our simulation results, we will have to define quantities that characterize distributions of molecules on our model membrane. If we assume a linear

relationship between the concentration of external stimulus and our model variable, $\mathcal{R}$,
then a spatially linear gradient of chemotactic stimulus will lead to a pattern of receptor
activation on the membrane of the form $\mathcal{R} \sim A\cos(2\pi X - \varphi)$; here, our spatial variable,
$X$, is defined on the perimeter of the cell and $\varphi$ specifies the direction of the gradient with
respect to the $X = 0$ direction. Under these conditions, we might quantify the polarized
response of the cell based on the magnitude of the component of the resulting distribution
of molecules on the membrane with the same spatial dependence as the stimulus. That is,
we define the polarization of a distribution of signaling molecules on the membrane, such
as 3'PIs ($P_n$), as

$$\mathcal{P}\{P_n\} = 2\sqrt{(C\{P_n\})^2 + (S\{P_n\})^2} / \langle P_n \rangle_X, \tag{4.1}$$

where $C\{P_n\} \equiv \int_0^1 P_n \cos(2\pi X)dX$, $S\{P_n\} \equiv \int_0^1 P_n \sin(2\pi X)dX$, and $\langle P_n \rangle_X \equiv \int_0^1 P_n dX$.
With this definition, if $P_n = A\cos(2\pi X - \theta) + B$ for some arbitrary $\theta$ and constants
$A'$ and $B$, then Eq. 4.1 gives $\mathcal{P}\{P_n\} = A / B$.

Gradient sensing cells seem to adapt their response to the average value of the external
stimulus. This suggests that cells respond to the relative value of a gradient of external
stimulus, rather than its absolute value (6, 124). Similarly, it is likely that the relevant
measure of cellular response is the relative redistribution of signaling molecules on the
membrane, rather than its absolute value[#]. Thus, in Eq. 4.1, we have normalized by the
spatial average of $P_n$.

---

[#] We might imagine that a protein relevant to nucleation of the actin-based structures at the leading edge of
a chemotaxing cell (see Sec. 1.3.4), $\mathcal{N}$, translocates from the cytosol to the membrane, binding linearly to
3'PIs. We might then write an equation for its concentration on the membrane as follows:
$\frac{\partial \mathcal{N}_m}{\partial t} = \chi_\mathcal{N} \cdot \mathcal{N}_c P_n - \lambda_\mathcal{N} \cdot \mathcal{N}_m$; $\mathcal{N}_m$ represents the local concentration of the nucleating protein,

We will also be concerned with whether the direction of the polarized response of the cell accurately reflects the direction of the gradient of stimulus. We thus define the direction of polarization of the distribution as

$$\theta\{P_n\} = \tan^{-1}\left(S\{P_n\}/C\{P_n\}\right); \tag{4.2}$$

$n\pi$ ($n$ = integer) is added or subtracted appropriately, so that $\theta$ changes continuously during the course of a simulation (unless the distribution depolarizes and repolarizes in a new direction). Equation 4.2 was chosen to specify a polarization direction for membrane distributions because it maximizes $\int_0^1 P_n \cos(2\pi X - \varphi')dX$ with respect to $\varphi'$ – if $P_n = A\cos(2\pi X - \varphi)$, then Eq. 4.2 specifies a polarization direction at the peak of the distribution, given by $\theta = \varphi$.

Finally, we can define an angular velocity of rotation of the distribution as

$$\mathcal{V}\{P_n\} = \frac{\partial \theta\{P_n\}}{\partial t}. \tag{4.3}$$

4.2.3   Defining outside stimuli

In analyzing our model, we will measure outside stimuli by their effects on the driving parameter, $\gamma$, which includes both the outside stimuli and basal activation (defined in Eq. M.3a of Table 2.3 of Chapter 2). This seems a natural choice to investigate the network

---

$\mathcal{N}_c = \mathcal{N}_0 - \int_0^1 \mathcal{N}_m dX / A_{cell}$ is the concentration of cytosolic nucleating protein that can be recruited to the membrane, and $\mathcal{N}_0$ is the total concentration of the nucleating protein in the cell. At steady-state, if we assume that most of the nucleating protein is depleted from the cytosol ($\mathcal{N}_c/\mathcal{N}_0$, and thus $\kappa_\mathcal{N} = \lambda_\mathcal{N}/\chi_\mathcal{N}$, are small), we find $\mathcal{N}_m = \dfrac{\mathcal{N}_0 P_n}{\kappa_\mathcal{N} + \langle P_n \rangle_X / A_{cell}} \sim \dfrac{\mathcal{N}_0 A_{cell} P_n}{\langle P_n \rangle_X}$; i.e., the fractional concentration of nucleating protein on the membrane is proportional to the local 3'PI concentration, normalized by its average over the membrane.

of interactions that regulate 3'PI dynamics in gradient sensing, based on our modular interpretation (see Fig. 2.4 of Sec. 2.3.1 and discussion in Secs. 2.5.4 – 2.5.5). Further, as mentioned, the details leading from ligand binding to PI3K recruitment are still not well understood (see Sec. 2.2.3).

The kinds of stimuli that we will investigate in this chapter will be combinations of spatially linear gradients and uniform stimuli, and rotating gradients. These types of stimuli can be written in general form as,

$$\mathcal{R} = S + G(1+S)\cos\big(2\pi\big(X - t/T\big)\big). \tag{4.4}$$

If our simulations are initialized with $\mathcal{R} = 0$ and the outside stimulus is expressed as in Eq. 4.4, then $S$ measures the fractional increase in $\gamma$ above baseline due to ligand-mediate receptor activation. Likewise, $G$ measures the relative strength of a spatially linear gradient in $\gamma$. Specifically, $G = r_c\big(\partial\gamma/\partial Z\big)/\langle\gamma\rangle_X$, where $Z = r_c\cos\big(2\pi X\big)$ is the Cartesian coordinate across the cell in the direction of the gradient and $r_c$ is the radius of the cell. $T$ is the period of gradient rotation.

We note that in applications of our model to any particular cell type, the experimental stimuli will need to be calibrated to relate patterns of ligand in solution to patterns of $\mathcal{R}$ in our model – a linear relationship is only likely to hold over a narrow range of conditions.


## 4.3    Simulations of characteristic behaviors

In this section, we simulate responses of our model variants to stimuli that illustrate characteristic gradient sensing behaviors (enumerated in Sec. 1.2.6). Single simulations of individual responses are discussed first. The results of groups of simulations are then

summarized in dose-response curves.  These highlight the differences between our model variants and will be used to define criteria that distinguish them in the next section.

### 4.3.1   Responses to uniform stimuli

Responses to spatially uniform step stimuli (characteristic behavior 'i' of Sec. 1.2.6) are often used to demonstrate adaptation in gradient sensing cells.  To simulate this type of response, we initialize our model cell by setting its variables to uniform steady-state values with $\mathcal{R} = 0$ (given in Table 2.6).  At time $t = 0$, $\mathcal{R}$ is increased to a new value, $S$, at all points on the membrane.  The driving parameter, $\gamma$, is thus increased, and our model's amplification module is driven.  The concentrations of 3'PIs and of PI3K on the membrane increase (represented by the scaled variables $\boldsymbol{P_n}$ and $\boldsymbol{K_m}$), while the concentration of membrane bound PTEN decreases ($\boldsymbol{T_m}$).  The response is transient. Within tens of seconds, $\gamma$ returns to baseline, as do the values of all our model variables. A typical time course for such a simulation is illustrated in Fig. 4.1.  Here, Case 4 is depicted with $S = 2$.  Other Cases demonstrated qualitatively similar behavior[#].

The simulated response in Fig. 4.1 captures the qualitative features observed experimentally in Dictyostelium cells responding a uniform step stimulus (see Fig. 2.2 for sample experimental data) (79, 132, 137, 164).  To our knowledge, however, the available experimental data is insufficient to resolve finer details of cellular responses than those summarized in the previous paragraph.  For example, the early features of the

---

[#] A different representation of a similar simulated response was depicted in the projected phase space of Fig. 3.1.

response, the absolute value of its maximum, as well as any possible lags between the responses of our three model components, have not been quantified experimentally.

In our simulations, we found that the peak response, represented by $(P_n)_{max}$, increases as the size of the step in $\mathcal{R}$ increases. This qualitative feature has been observed experimentally for non-saturating stimuli, though it has not been quantified in single cells (79). In our model, the peak response occurs on a similar time scale to adaptation of $\gamma$ (in Fig. 4.1, $\gamma$ has nearly returned to its baseline value within ~10 $s$). This timescale increases as the step size decreases, the effect being more pronounced for Cases 1 and 3 than for Cases 2 and 4 (data not shown)[#]. A slower response to weaker stimuli has also been recently noted in Dictyostelium (165). In our model, this occurs because the relative increase in the rate of PI3K recruitment to the membrane, and hence the
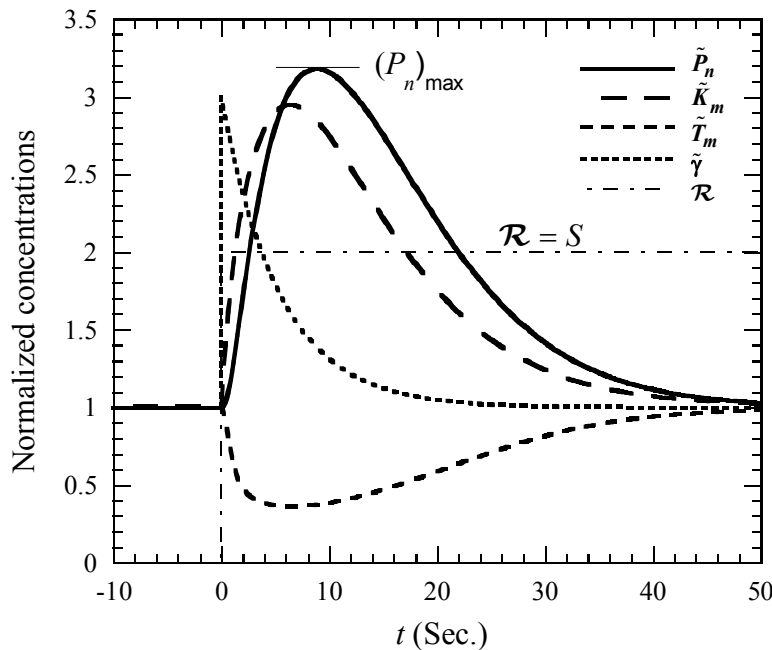


**Fig. 4.1. Response to a uniform step stimulus** applied at $t = 0$:
$\{\mathcal{R} = 0, (t < 0);$
$\mathcal{R} = S, (t > 0)\}$. A sample time course is depicted for Case 4, $S = 2$. Time courses for other Cases were qualitatively similar. Quantities marked by a tilde are normalized by their values prior to $t = 0$. $(P_n)_{max}$ marks the normalized peak 3'PI concentration during the transient response.

---

[#] For our chosen parameter values, response adaptation is generally slower for Cases 1 and 3. For these Cases, $\gamma$ passes near a bifurcation in the uniform response of the amplification module during adaptation. We could have diminished this effect if the values of several kinetic parameters were increased for these Cases. However, as the qualitative features of the time courses for these variants were still in agreement with the noted experimental data, we preferred to keep as many model parameters the same between the variants as possible.

123

subsequent relative increase in its rate of phosphorylation, is proportional to the increase in $\mathcal{R}$.  The fraction of PI3K that needs to be phosphorylated in order for adaptation to occur, however, increases more slowly (never exceeding 1) when larger stimuli are investigated.

To quantify the response of our model to uniform stimuli of different magnitudes, we recorded the peak relative value of $P_n$ ($(P_n)_{max}$, as labeled in Fig. 4.1), in response to uniform stimuli, over a range of $S$.  Time courses for these simulations were always qualitatively similar to Fig. 4.1, with the state of the cell returning to baseline within tens of seconds.  The results are summarized by the dose-response curves in Fig. 4.2.

We find that responses to uniform stimuli are weaker for Cases 2 and 4 than for Cases 1 and 3, due to depletion of cytosolic molecules.  This is consistent with the weaker uniform response of their amplification modules, as noted in Sec. 3.3 (Fig. 3.2). However, while all of the curves show quantitative differences, they are qualitatively similar – continuous and monotonically increasing.  Thus, experiments of this sort alone
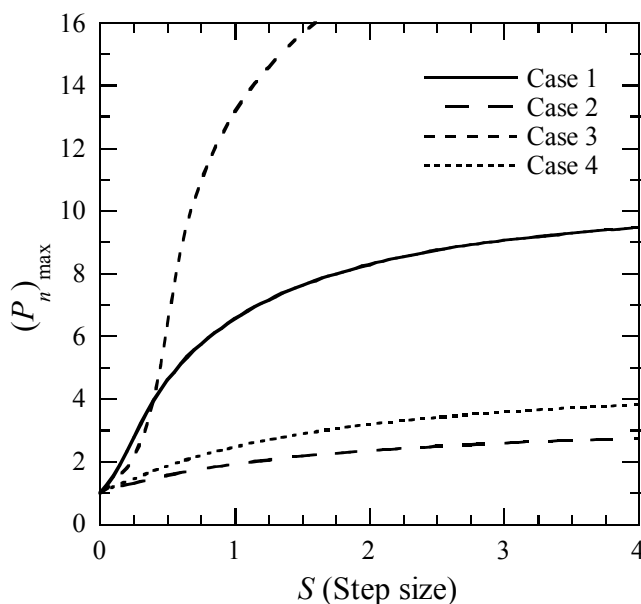


**Fig. 4.2.  Dose-response curves for uniform step stimuli**. The normalized peak 3'PI concentration, $(P_n)_{max}$, is recorded for each variant as a function of the stimulus step size, $S$.  Simulations were as described in Fig. 4.1.

124

are insufficient to distinguish between the qualitative behaviors illustrated by our model variants.

### 4.3.2    Responses to static gradients

Steady-state responses to static gradients are often used to illustrate high gain in the spatial sensing responses (characteristic behavior ii in Sec. 1.2.6). To simulate this behavior, we initialize our model by setting its variables to their uniform steady-state values, this time with $\mathcal{R} = S_i$. Because our model demonstrates perfect adaptation to the average stimulus, the initial steady-state profile is independent of the value of $S_i$ and is still given by the values in Table 2.6 for $S = 0$. At time $t = 0$, a spatially linear gradient is applied, possibly together with a uniform stimulus. The stimulus for $t > 0$ is thus given by $\mathcal{R} = S_f + G\left(1 + S_f\right)\cos\left(2\pi X\right)$. The parameter, $G$, measures the relative strength of the resulting gradient in $\gamma$ (see Sec. 4.2.3). If $S_f = S_i$, then the gradient was applied after equilibration to a uniform stimulus. Alternately, $S_f > S_i$ represents a gradient applied together with a uniform stimulus.

   Figure 4.3 illustrates the simulated steady-state profile of a cell in a 5% spatially linear gradient of stimulus (Case 4 is depicted with $G = 0.05$, though all of the Cases show qualitatively similar profiles). A highly polarized distribution of signaling molecules results on the membrane, though the gradient in stimulus is relatively small. The results are in qualitative agreement with experimental observation in Dictyostelium – 3'PIs are produced and PI3K is recruited to the up-gradient side of the cell, while PTEN becomes localized to the opposite side of the cell (132, 137, 164). The magnitude of this polarized
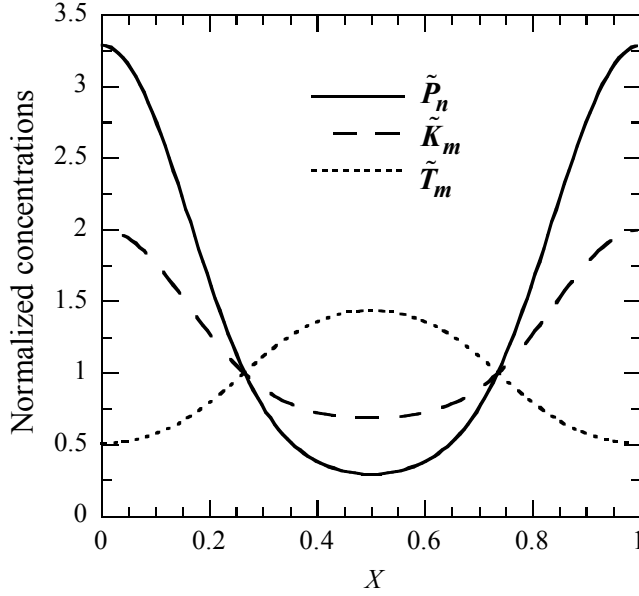
**Fig. 4.3. Steady-state response to a static, spatially linear gradient**. The stimulus is defined by: $\{\mathcal{R} = S_i, \ (t < 0);$ $\mathcal{R} = S_f + G\left(1 + S_f\right)\cos\left(2\pi X\right),$ $(t > 0)\}$. The steady-state profile for Case 4 is depicted in a 5% relative gradient ($G = 0.05$), applied after equilibration to a uniform stimulus ($S_i = S_f = 2.0$). Quantities are normalized by their steady-state values before application of the gradient ($t < 0$). $X = 0$ and 1 mark the up-gradient side of the cell.

response is not well agreed upon experimentally. However, recent data suggests that in rounded and immobile cells, the response may not be as steep as suggested by our simulations, though the spatial distributions in crawling cells may be quite steep (124).

To investigate how our model's response depends on the strength of the applied gradient, simulations were run for each model variant as described above, for a range of strengths of the relative gradient (specified by $G$). $S_f = 2$ was always used, and $S_i = 0$ or 2 was used respectively, depending on if the gradient was applied together with or after equilibration to a uniform stimulus. In practice, this only affected the response for Case 3 (discussed below). For each value of $G$ and combination of $S_f$ and $S_i$, the system was evolved to steady state. The response was quantified by calculating the relative polarization of the 3'PI distribution, $\mathcal{P}\{P_n\}$, as described by Eq. 4.1. The results are summarized by the dose-response curves in Fig. 4.4.

126
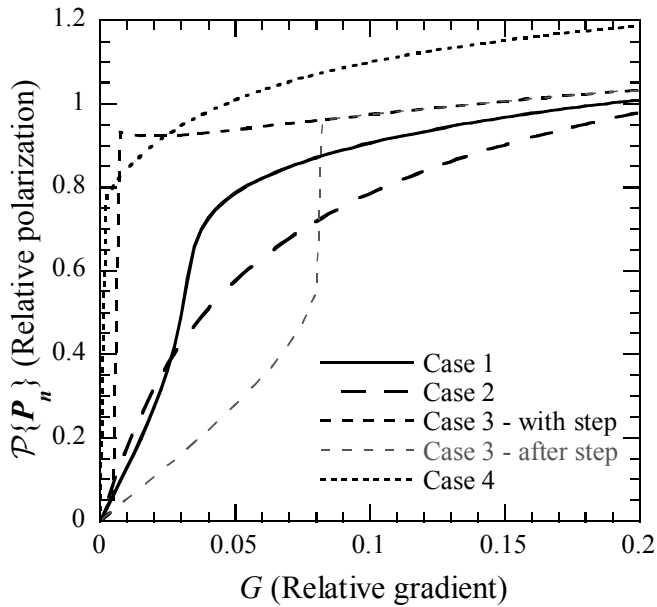
**Fig. 4.4. Responses to static gradients – Dose-response curves**. Simulations were as described in Fig. 4.3. The steady-state relative polarization of the 3'PI distribution was calculated for each variant in response to gradients of relative strength, $G$. The grey curve for Case 3 marks the range of gradient strengths for which the steady-state polarization depends on whether the gradient was applied together with, or after equilibration to, a uniform stimulus; responses for other Cases demonstrate no such dependence. The jumps in steady-state response for Cases 3 and 4 are discontinuities; they indicate bifurcations in steady-state response to gradients, as discussed in the text.

All of the variants show a strong relative polarization in response to relatively weak gradients. For Cases 3 and 4, a discontinuity in the dose-response curve indicates the existence of multiple steady states, highlighting the effects of coupled positive feedbacks and distinguishing these Cases qualitatively from Cases 1 and 2.

For Case 3, a threshold in stimulus must be overcome to induce a highly polarized response to small gradients. This is achieved if the gradient is applied together with a sufficient uniform stimulus (dark curve). Otherwise, the response at small gradients remains weakly polarized (grey curve). If one were to continuously increase the gradient from $G = 0$, the response would follow the grey curve (the gradient would not be applied together with a sufficient uniform stimulus). At $G \sim 0.08$, a weakly polarized state no longer exists, and the steady-state response would jump discontinuously to the black curve. If the gradient was then decreased continuously, the steady-state response would

127

then follow the black curve until $G \sim 0.005$. At this point, a highly polarized solution no longer exists and the steady-state response would drop discontinuously. Thus, the steady-state response of Case 3 to gradients is hysteretic and demonstrates a subcritical bifurcation (161).

For Case 4, the uniform state is unstable to arbitrarily small gradients, and no threshold needs to be crossed to elicit a highly polarized response. The dose-response response is thus discontinuous at zero-gradient. However, because the system was initialized in an unstable uniform steady state, this discontinuity does not clearly demonstrate the response bifurcation that exists.

A more proper discontinuous/hysteretic dose-response curve could be generated for Case 4 by considering reverse polarized states. That is, if Case 4 were initialized in a polarized state (which is stable at zero-gradient) and then a steady gradient applied in opposition to the polarization direction, the initial polarization direction would persists provided that the new gradient wass sufficiently small (data not shown). Thus, a hysteretic response could be demonstrated for Case 4 by increasing and then decreasing the strength of a gradient, if the range of $G$ was extended to include negative values and polarizations were recorded as negative when in opposition to the applied gradient.

### 4.3.3 Responses to rotating gradients

Investigation of responses to rotating gradients may provide insight into the functioning of each variant in natural settings, where stimuli vary in both space and time. To simulate such responses, we first apply a static linear gradient, together with a uniform step stimulus, and allow the polarized distribution of signaling molecules to equilibrate.

We then begin to rotate the gradient at $t = 0$ with different Periods of rotation, $T$. The space/time plots in Fig. 4.5 record $P_n$ as a grey scale value in sample time courses. The initial gradient is in the direction marked by $X = 0$ and 1 (the normalized spatial variable, $X$, is periodic); time is measured relative to $T$ (in gradient revolutions); $P_n$ values are normalized by the peak $P_n$ value before gradient rotation.
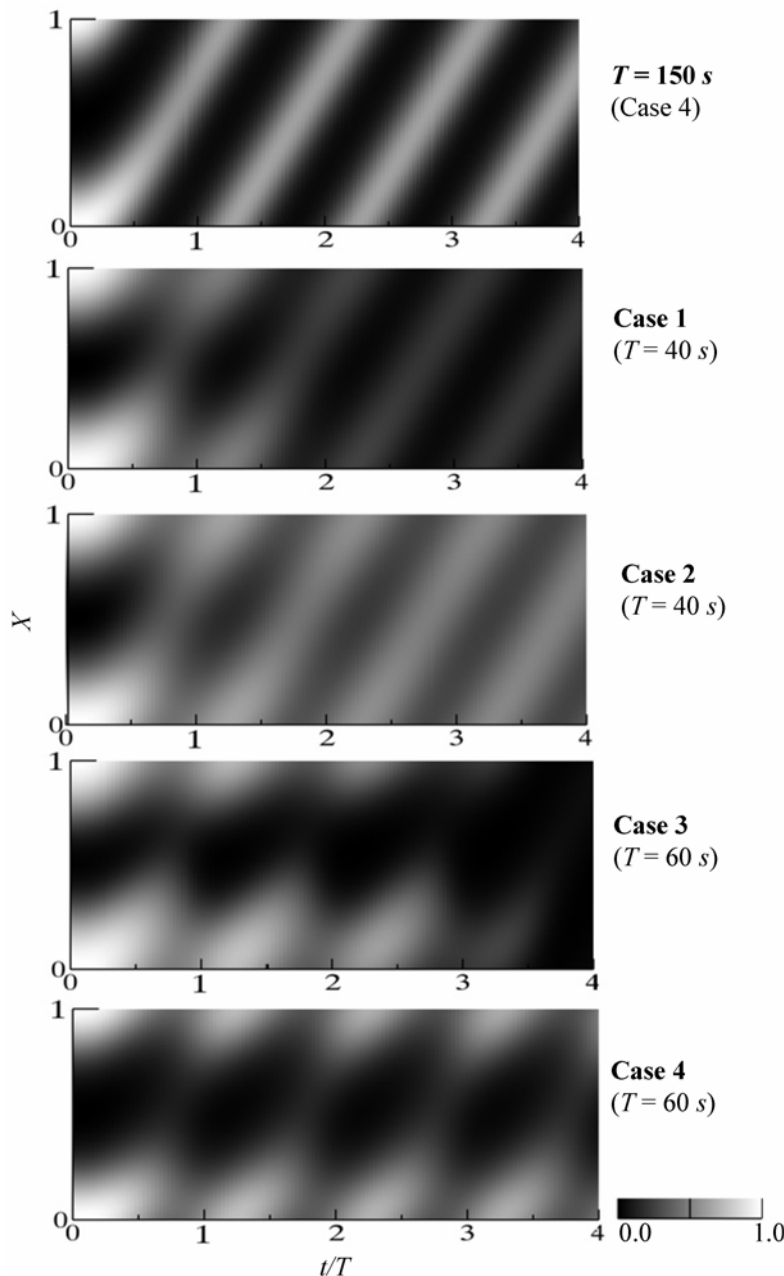


**Fig. 4.5. Responses to rotating gradients**. Unstimulated cells are first polarized in a static gradient ($G = 0.075$, $S = 2$, see Eq. 4.4). After cellular equilibration occurs, the gradient begins to rotate (at $t = 0$) with period, $T$. The $P_n$ value around the membrane is plotted as a gray-scale value, normalized by its peak value before gradient rotation begins. The spatial variable $X$, is periodic, and the initial gradient is in the $X = 0$ and 1 direction. $t/T$ measures time in gradient rotations. The first plot, marked $T = 150\ s$, illustrates efficient following of a slowly rotating gradient. The remaining time courses illustrate the different failings of each of our model variants to follow more quickly rotating gradients.

The first time course in Fig. 4.5, labeled $T = 150\ s$, represents cellular response under conditions of slow gradient rotation.  The shape of the $\boldsymbol{P_n}$ distribution remains relatively steady and its direction follows that of the gradient with a slight lag (the gray scale pattern keeps its shape and is translated diagonally with a period of 1).  Case 4 is depicted, though time courses are qualitatively similar for all Cases, for slow gradient rotation.  The results are consistent with the qualitative observations of experimental responses to changing gradients in rounder Dictyosetelium cells (81).  Further, during aggregation, Dictyostelium generate and respond to waves of cAMP with a period of order 5 min. (166, 167), suggesting that efficient gradient sensing in these cells implies the ability to follow gradients that change on time scales of order 1 min.

Figure 4.5 also illustrates sample time courses from simulations with shorter $T$, where our model variants demonstrate different kinds of failure in gradient following.  For Cases 1 and 2, the polarized distribution becomes gradually washed out, and the weakly polarized steady-state distribution that results eventually follows the direction of gradient rotation.  Case 3 suddenly becomes depolarized when gradient rotation becomes too fast to follow.  Case 4 remains polarized near its initial direction, turning towards the direction of the gradient whenever it is close to the direction of polarization; an oscillatory steady-state behavior results.  To our knowledge, cellular responses under conditions where gradient sensing fails have not yet been systematically investigated.

The above simulations were repeated for a range of $T$ in order to analyze the transition in each variant's behavior when gradient rotation becomes too fast to follow.  For each simulation, we calculated the polarization of the 3'PI distribution at each time point (Eq. 4.1) and normalized by its value prior to gradient rotation (at $t = 0$); we will refer to this

130

time course as $\tilde{\mathcal{P}}(t)$. The angular velocity of rotation of the distribution (Eq. 4.3) was also calculated at each time point and normalized by the angular velocity of gradient rotation; we will refer to this time course as $\tilde{\mathcal{V}}(t)$. $\tilde{\mathcal{P}} = 1$ indicates that the polarized distribution remains stable during the gradient rotation and $\tilde{\mathcal{V}} = 1$ indicates that the direction of polarization follows the gradient perfectly (with a slight lag).

For each $T$, we characterized the cellular response by recording the steady-state quantities, $\tilde{\mathcal{P}}_s$ and $\tilde{\mathcal{V}}_s$, which are long time averages of $\tilde{\mathcal{P}}(t)$ and $\tilde{\mathcal{V}}(t)$, respectively. If no significant oscillations in the polarization direction occurred, we also recorded the long time value of the lag in the direction of polarization behind that of the gradient ($\theta_L$, measured in revolutions for Cases 1-3). When steady oscillations in $\tilde{\mathcal{P}}(t)$ and $\tilde{\mathcal{V}}(t)$ did occur, the long-time value of the amplitude of the oscillations in polarization direction about the average motion was recorded (denoted $\theta_o$, measured in revolutions for Case 4). The dose-response curves thus generated are depicted in Figs. 4.6 – 4.8 below, which summarize the responses of our model variants to simulated gradients rotating with different Periods.

For Cases 1 and 2, at shorter $T$, the $\boldsymbol{P_n}$ distribution becomes increasingly depolarized during an initial transient, after which following becomes perfect ($\tilde{\mathcal{V}}_s = 1$). Thus, we see in Fig. 4.6 that $\tilde{\mathcal{V}}_s = 1$ for all $T$, but $\tilde{\mathcal{P}}_s$ goes smoothly to 0 at shorter $T$. When gradient rotation becomes too fast to follow without significant depolarization, the lag angle, $\theta_L$, begins to increase. For both Cases 1 and 2, $\theta_L$ plateaus at $\sim 0.2$ rotations ($\sim \pi/2$ *rad.*) for a small range of $T$ beginning at $T \sim 50$ *s*. This is consistent with our stability analysis of responses to static gradients, which suggested that polarized distributions in our model
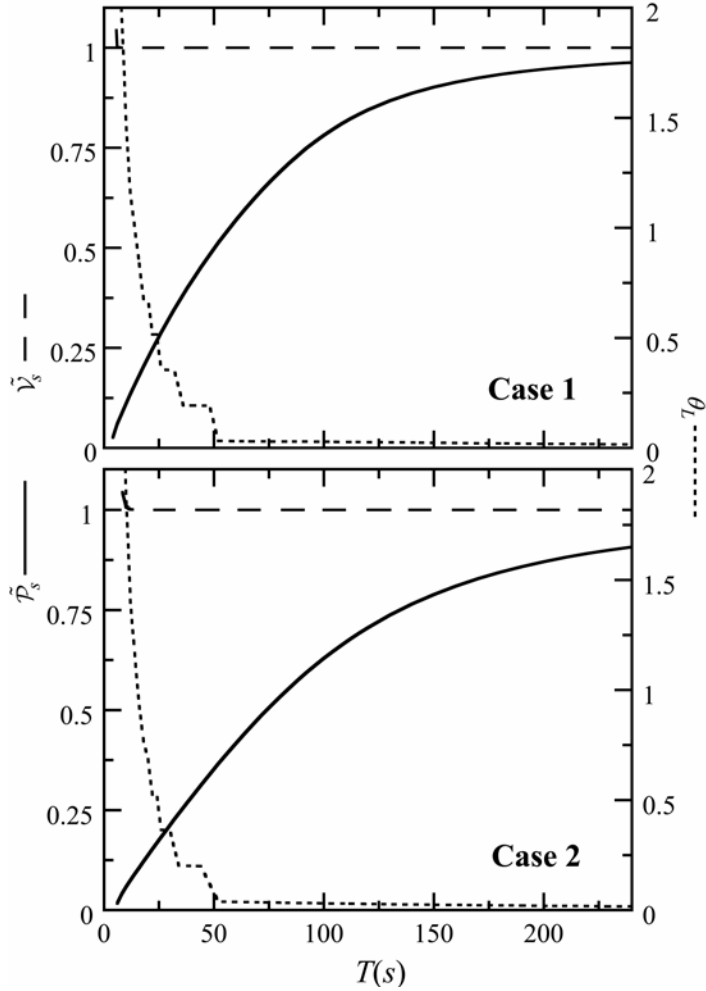
**Fig. 4.6. Rotating gradients – Dose-response curves for Cases 1 and 2**. The simulations of Fig. 4.5 were carried out for a range of periods of gradient rotation ($T$). Quantities that characterize the response were recorded for each $T$. $\tilde{\mathcal{P}}_s$ and $\tilde{\mathcal{V}}_s$ are long time averages of $\tilde{\mathcal{P}}(t) = \mathcal{P}\{P_n(t)\} / \mathcal{P}\{P_n(0)\}$ and $\tilde{\mathcal{V}}(t) = \mathcal{V}\{P_n(t)\}(T / 2\pi)$, which represent normalized polarizations and angular velocities of the 3'PI distribution, respectively (see text and Eqs. 4.1 – 4.3). $\theta_L$ is the long time value of $\theta\{P_n(t)\} / 2\pi - t / T$, and measures the lag of the polarization angle behind that of the gradient, in rotations; $\theta\{P_n(t)\}$ measures the polarization direction of the $P_n$ distribution (in radians, see Eq. 4.2).

are most sensitive to perturbations whose profile is shifted by on the order of 0.2 rotations from the direction of cellular polarization (see Sec. 3.4.5 and Fig. 3.5).

For Case 3, the highly polarized distribution becomes destabilized if it is not sufficiently aligned with the direction of the gradient, as occurs when the rotation becomes too fast to follow. Thus, we see in Fig. 4.7 that $\tilde{\mathcal{P}}_s$ drops sharply at $T \sim 140$ $s$. This drop is a discontinuity and indicates a response bifurcation where the highly polarized distribution can no longer rotate stably at the frequency of gradient rotation. If the simulation had been initialized in the weakly polarized state (that is, the gradient was
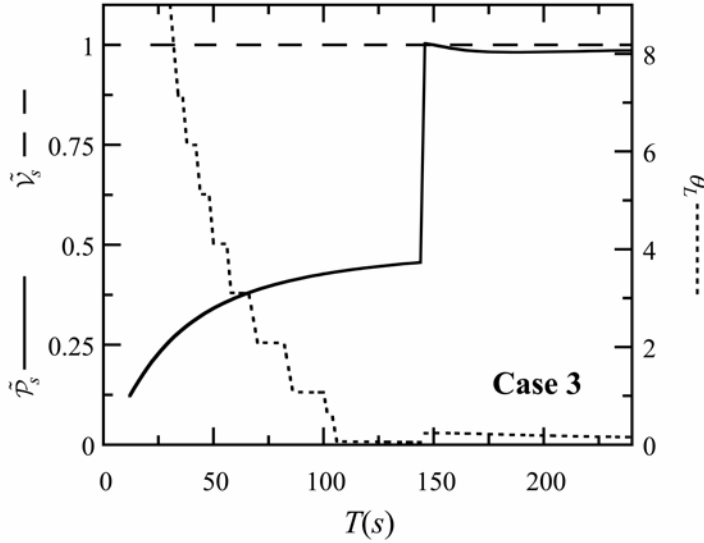
**Fig. 4.7. Rotating gradients – Dose-response curve for Case 3**. Simulations and notation are as in Fig. 4.6. The sharp drop in $\tilde{\mathcal{P}}_s$ at $T \sim 140\ s$ is a discontinuity and indicates a bifurcation in the steady response of Case 3 to rotating gradients.

applied without a sufficient uniform stimulus; see Sec. 3.4.2), there would be no sharp transition in response at short $T$. A hysteretic response would thus be observed if the simulation was initialized in the highly polarized state, as was done for the depicted simulations, and gradient rotation was initialed slowly. If the period of rotation was gradually shortened, the highly polarized state would eventually become destabilized at $T \sim 140\ s$. If the period of gradient rotation was then lengthened, the highly polarized state would not return, as this would require overcoming a threshold in stimulus (not shown).

Applying a weaker gradient for Case 3 results in destabilization of the highly polarized steady state at longer $T$, while a stronger gradient results in a highly polarized state that remains stable at shorter $T$. If a sufficiently strong gradient is applied, Case 3 no longer demonstrates a bistable response to static gradients (see Fig. 4.4), and responses to rotating gradients become similar to Cases 1 and 2 (not shown).

We see in Fig. 4.7 that for Case 3, before depolarization occurs at $T \sim 140\ s$, the lag angle, $\theta_L$, has increased to approximately $\sim 0.2$ rotations. Aagain, this is consistent with our analysis of stability of polarized solutions. At even shorter $T$, the lag angle increases

133

steadily by approximately complete rotations, as illustrated by the distinct plateaus in $\theta_L$. This indicates that for shorter $T$, the polarization direction of Case 3 remains approximately fixed in its initial direction for several gradient rotations before depolarization occurs. The weakly depolarized distribution then follows the rotating gradient, lagging behind it by an amount of order 0.2 revolutions at shorter $T$ (similar to the behaviors of Cases 1 and 2).

For Case 4, the polarized distribution remains fairly stable when gradient rotation becomes too fast to follow. An oscillatory motion ensues, where the polarization direction of the distribution turns towards that of the gradient whenever they are closely aligned. When the gradient has rotated such that there is no longer sufficient alignment, the polarization direction remains approximately fixed until the gradient has rotated such that alignment is again sufficient.

The transition from gradient-following to oscillatory behavior for Case 4 occurs discontinuously in the dose-response curve and is indicated in Fig. 4.8 by the sharp drop in $\tilde{\mathcal{V}}_s$ at shorter $T$. The amplitude of the oscillations in the polarization direction, $\theta_O$,
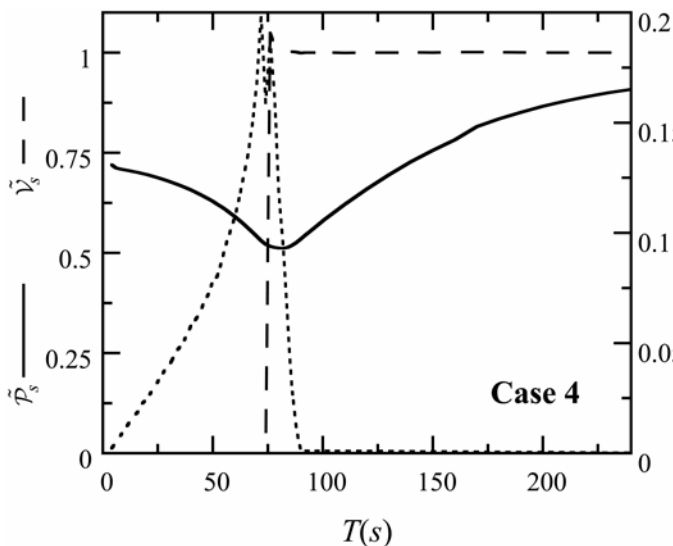


**Fig. 4.8. Rotating gradients – Dose-response curve for Case 4**. Simulations and notation are as in Fig. 4.6. $\theta_o$ measures half the range of $\theta\{P_n(t)\}/2\pi - \tilde{\mathcal{V}}_s t / T$ during the time after oscillations become steady. The sharp drop in $\tilde{\mathcal{V}}_s$ at $T \sim 75$ s, where oscillations begin, is a discontinuity. However, we were not able to find a hysteretic response for Case 4.

134

peaks near this transitions, and is of order of 0.2 revolutions. For shorter $T$, the polarized response has less time to turn towards the direction of the gradient before the gradient is lost, and the amplitude of the oscillations shrinks. Efficient gradient following for Case 4 does continue at shorter $T$ if a stronger gradient is used, similar to Case 3 (not shown). We could not identify a clear hysteretic response to rotating gradients for Case 4 (which was noted for Case 3).

The above simulations indicate that differences between our model variants are most apparent in the characteristics of transitions in response that occur when gradient rotation becomes too fast to follow. The observed differences do not imply that one variant functions more efficiently than the others. Rather, each might have a different utility to the cell types that may use them. In particular, these simulations demonstrate that under conditions where a bistable response is possible, and the polarized response could potentially 'get stuck' in an initial direction (as in Cases 3 and 4), the direction of polarization can still turn to follow a slowly rotating gradient. The simulated responses thus demonstrate sufficient plasticity to account for characteristic gradient sensing behaviors.

The simulations analyzed thus far are designed to probe the roles of coupled positive feedbacks and translocation in gradient sensing behaviors. Experiments and simulations that investigate responses to dynamic stimuli, such as rotating gradients, could also be used to investigate possible lags in the dynamics of the various molecules included in our model. This type of information might further elucidate the structure of the network of interactions that regulates their dynamics. However, to our knowledge, these types of experiments have not yet been done. Other types of dynamic simulations and

experiments could be useful as well to further analyze our model and to investigate other

relevant biochemical/biophysical mechanisms (see, for example, 49, 127, 168).

**4.4    Defining criteria that distinguish modes of gradient sensing**

The behaviors of our model variants are representative of the qualitatively different

modes of gradient sensing that depend on the roles of coupled positive feedbacks and

translocation in our model.  We expect the illustrated behaviors to exist for a range of

parameter values.  Further, we expect that these behaviors will be demonstrated in the

responses of real cells and of other models of gradient sensing.  Thus, we develop criteria

that might be applied to distinguish between the illustrated modes of gradient sensing.

4.4.1    Criteria relating to coupled positive feedbacks

We have seen in Fig. 4.4 that Cases 3 and 4 can be distinguished from the others based on

discontinuities in their dose-response curves to gradients, with possible dependence on

application of a uniform stimulus (differences are also clear in dose-response curves to

rotating gradients, as seen in Figs. 4.6 – 4.8).  The distinct behaviors illustrated reflect the

different roles played by coupled positive feedbacks in signal amplification (which lead

to response bifurcations).

4.4.2    Criteria relating to translocation

Comparison of the data in Figs. 4.2 and 4.4 suggests that in Cases where redistribution of

translocating molecules plays a significant role in amplifying responses to gradients, a

measure of the slope of the dose-response curve for gradients will be significantly greater

than the slope for responses to uniform stimuli. If, on the other hand, translocation does not play a significant role in response amplification, we then expect responses to uniform stimuli and gradients to be comparable.

Any comparison of responses to uniform stimuli and to gradients is necessarily empirical and model dependent, as it requires accounting for the dynamic nature of responses to step stimuli and for diffusive dissipation in responses to gradients. We have found the following criteria, based on the dose-response curves in Figs. 4.2 and 4.4, to be effective in distinguishing between the responses of our model variants where translocating molecules play differing roles, using the notation of Figs. 4.2 and 4.4: If

$$\left[\frac{\partial}{\partial S}(P_n)_{\max}\right]_{\max} > 0.4\mathcal{P}\{G\}/G^{\#}$$ for some $G$ to be specified, then we consider responses to

uniform stimuli and gradients to be comparable; under these conditions, redistribution of translocating molecules does not play a significant role in response amplification. If, on

the other hand, $\left[\frac{\partial}{\partial S}(P_n)_{\max}\right]_{\max} < 0.2\mathcal{P}\{G\}/G$, then we consider responses to uniform

stimuli and gradients to not be comparable; we might then conclude that redistribution of translocating molecules does play a significant role in response amplification. If neither of the above criteria is met, then the response is ambiguous and we can make no conclusion concerning the role of translocating molecules in response amplification.

In the above discussion, $S$ specifies a uniform stimulus and $(P_n)_{\max}$ quantifies the peak response, as in Fig. 4.2. $G$ specifies a gradient stimulus and $\mathcal{P}\{G\}$ quantifies the polarized response, as in Fig. 4.4. $G = 0.05$ was used for all applications that follow.

---

[#] In our model, for the range of stimuli considered, responses to gradients were always steeper than the corresponding responses to uniform stimuli, and $\left[\frac{\partial}{\partial S}(P_n)_{\max}\right]_{\max} > 1.0\mathcal{P}\{G\}/G$ never occurred.

### 4.4.3   Criteria for efficient gradient sensing

We only wish to apply our criteria to distinguish between Modes of gradient sensing in systems that demonstrate characteristic behaviors and respond efficiently to gradients. Thus, we expect perfect adaptation in response to uniform stimuli. We further expect a highly polarized response to a relatively weak static gradient, and that the polarized response follows a slowly changing gradient. Thus, we specify the following criteria for efficient gradient sensing: If the relative polarization in response to a gradient defined by $G = 0.05$ is greater than 0.4 (about half the average value calculated for our model variants, see Fig. 4.4), then we consider the system to demonstrate a strong response to relatively weak gradients; otherwise, we consider the response to be 'weakly polarized'. If either the steady normalized polarization or angular velocity in response to a rotating gradient with a period of 150 $s$ remains above 0.6 at steady state (see Figs. 4.6 – 4.8), then we consider the system to successfully follow a slowly rotating gradient; otherwise we consider the response to be 'poorly following'. In the analysis that follows, we only consider situations where perfect adaptation to uniform stimuli is achieved.

### 4.4.4   Criteria summary

The criteria discussed in Secs. 4.1 – 4.3 are sufficient to distinguish between our model variants. They are summarized in Table 4.1. In Sec. 4.5, we will apply these criteria to determine if the responses of our model for different parameter values share qualitative features with any of our model variants.

**Table 4.1. Criteria for distinguishing Modes of gradient sensing**

| | Mode 1 | Mode 2 | Mode 3 | Mode 4 |
|---|---|---|---|---|
| **Relating to coupled positive feedbacks** | | | | |
| Discontinuity in dose-response to gradients. | No | No | Yes | Yes |
| Dependence of gradient dose-response on simultaneous application of a uniform stimulus. | No | No | Yes | No |
| **Relating to translocation** | | | | |
| Responses to uniform stimuli comparable to responses to gradients. | Yes | No | Yes | No |

**Criteria for efficient gradient sensing**
Strong polarization in response to a static 5% relative gradient.
Successful following of a gradient rotating with a period of 150 $s$.

## 4.5 Parameter space structure

In applications to real cells, many of the interactions that regulate gradient sensing responses will be unknown, as will most of the biochemical parameters. Thus, we wish to investigate how the qualitative features of our model's responses depend on its parameters and suggested regulatory mechanisms. To accomplish this, we systematically varied several model parameters. For each combination of parameters, we simulated responses to uniforms stimuli, to static gradients, and to rotating gradients. The criteria discussed in Sec. 4.4 (summarized in Table 4.1) were then applied to determine if the results demonstrated efficient gradient sensing, and if they further demonstrated the qualitative features of one of the Modes of gradient sensing illustrated by our model variants. We thus characterized several surfaces in the parameter space of our model.

### 4.5.1 Parameters that define the model variants

We began by systematically varying the parameters that were used to specify our model variants. We varied the parameter $\kappa_K$, which adjusts the effectiveness of **Loop II** in

response amplification (see Eq. M.3 of Table 2.3) – decreased $\kappa_K$ means that the feedback in **Loop II** is more effective. We simultaneously varied $1/\kappa_c$, which determines the degree to which depletion of translocating molecules saturates the response of **Loop I** (see Eq. M.1 and M1a) – increased $1/\kappa_c$ means greater cytosolic depletion upon cellular stimulation, and hence a greater potential for redistribution of translocating molecules to amplify responses to gradients[#]. Because our analysis in Fig. 3.6 had suggested that gradient sensing responses might be very sensitive to the value of the base line parameter of our model (defined in Eq. M.6a), for each combination of $\kappa_K$ and $\kappa_c$, $\gamma_0$ was chosen to optimize the polarization of the 3'PI distribution in response to a small static gradient ($G = 0.05$). Only values of $\gamma_0$ for which the uniform steady state of our model was unique were considered – this uniqueness is required for perfect adaptation in our model (see discussion in Sec. 3.3). All other parameters were set as in previous simulations, according to the procedure outlined in Appendix B. Model responses were simulated and the criteria of Sec. 4.4 were applied. The results are illustrated in Fig. 4.9.

Decreasing $\kappa_K$ increases the effectiveness of **Loop II**. We see in Fig. 4.9 that this leads to transitions to Modes of gradient sensing with successively higher gain in response. For example, decreasing $\kappa_K$ at $1/\kappa_c = 0.5$ results in the sequence of transitions: 'Weakly polarized' $\rightarrow$ Mode 2 $\rightarrow$ Mode 4 $\rightarrow$ Mode 4' $\rightarrow$ Mode 3' $\rightarrow$ 'Poorly following'. On the other hand, increasing $1/\kappa_c$ leads to transition to Modes where redistribution of translocating molecules makes coupled positive feedbacks more effective in responses amplification. For example, decreasing $1/\kappa_c$ at $\kappa_K = 3$ results in the sequence of transitions: 'Weakly polarized' $\rightarrow$ Mode 1'/2' $\rightarrow$ Mode 2 $\rightarrow$ Mode 4 in Fig. 4.9.

---

[#] As mentioned in Sec. 2.5.3a, $1/\kappa_m$, which controls the degree to which depletion of membrane-bound molecules saturates **Loop I**, was adjusted such that the relationship $1/\kappa_c + 1/\kappa_m = 1$ was preserved.
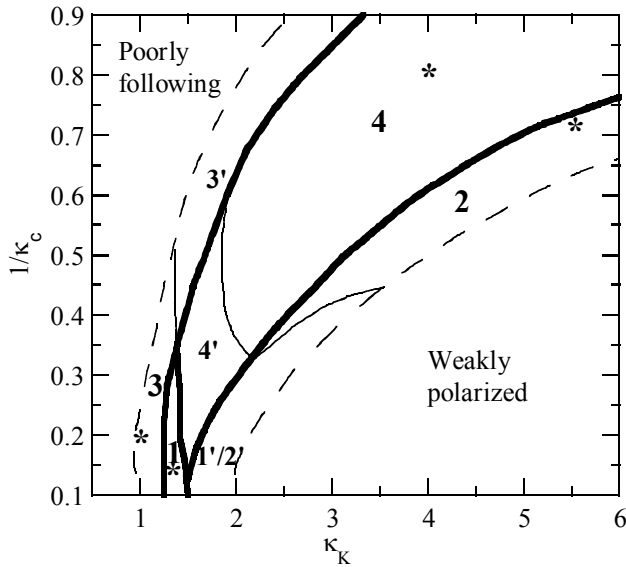
**Fig. 4.9. Parameters that specify the model variants** are systematically varied, model responses are simulated, and the criteria of Sec. 4.4 (summarized in Table 4.1) are applied to the results. Decreased $\kappa_K$ means that feedback in **Loop II** is more effective; increased $1/\kappa_c$ means that translocation is more significant in amplifying responses to gradients. Solid lines separate regions of qualitatively distinct model behaviors; bold lines indicate response bifurcations; regions of inefficient gradient sensing are demarcated by dashed lines and labeled 'Poorly following' or 'weakly polarized. Numbers specify the 'Mode' of gradient sensing that best describes simulation results in a given region. A '*' in a region marks the combination of parameters that was used to specify the corresponding model variant. Regions which gave ambiguous results with respect to translocation were labeled 3' or 4' if they met criteria for Modes 3 or 4 with respect to coupled positive feedbacks, and 1'/2' otherwise.

In general, transitions between Modes which differ in the roles played by coupled positive feedbacks are sharp and represent response bifurcations; these are indicated by bold lines in Fig. 4.9. Gradient sensing responses were often found to be most efficient close to these boundaries. For example, Modes 1 and 2 showed enhanced responses to small gradients; Modes 3 and 4 followed rotating gradients more efficiently (data not shown). On the other hand, transitions between Modes which differ in the importance of translocating molecules pass through regions of parameter space whose qualitative behavior is ambiguous with respect to our criteria (labeled 1'/2', 3' or 4'). Further, we note that regions where each variant functions efficiently might be narrow in some directions, suggesting constraints on parameters. Several such constraints on parameters were discussed in Sec. 3.5.

### 4.5.2 Parameters relating to specific biochemical mechanisms

To investigate the dependence of the qualitative behaviors of our model on the proposed biochemical mechanisms from which it was developed, we systematically varied several other model parameters and applied the analysis of Sec. 4.5.1 to characterize several more surfaces in our parameter space.

In our model, we have interpreted PTEN translocation from the membrane in response to outside stimuli as enhancing the effectiveness of **Loop II**. To our knowledge, however, a significant translocation of PTEN has only been observed experimentally in Dictyostelium. Thus, we wished to investigate the significance of this translocation for our model's response. To do this, we systematically varied the parameter $\zeta_T$ in Eq. M.4 (Table 2.3), which adjusts the importance of constitutive removal of PTEN from the membrane in our model. Larger $\zeta_T$ means a less significant inverse translocation of PTEN from the membrane in response to external stimuli, making **Loop II** less effective. We simultaneously varied $1/\kappa_c$, as in Sec. 4.5.1. For each combination of $\zeta_T$ and $1/\kappa_c$, $\lambda_T$ was adjusted such that $\lambda_T \left( K_{m1} + \zeta_T \right) =$ constant, where $K_{m1}$ is the value of $K_m$ in the unstimulated cell for Case 1. This condition kept the rate of removal of PTEN from the membrane in the unstimulated cell approximately constant, thus maintaining a similar baseline value of $T_m$ as $\zeta_T$ was varied. As in Sec. 4.5.1, $\gamma_0$ was then adjusted to optimize the polarized response to a small, static relative gradient. Other parameters were set to the values used for Case 1 in our previous simulations, according to the procedure of Appendix B. Model responses were simulated and the criteria of Sec. 4.4 were applied.

The results, depicted in Fig. 4.10, demonstrate qualitatively similar features to those noted concerning Fig. 4.9. For example, decreasing $\zeta_T$ (which increase the effectiveness

142

of **Loop II**) results in transitions to Modes of gradient sensing that involve stronger positive feedbacks;. Regions that demonstrate a given behavior are again narrow in some directions, indicating constraints on parameters.

In developing our model, we had proposed that the feedback in **Loop I** operates by enhancing production of PI(4,5)P$_2$ bound to a PITP (PI transfer protein), rather than enhancing the production of free PI(4,5)P$_2$. The particular feature in our model equations that results from including a PITP is the possibility of saturating **Loop I** at high concentrations of PI3K on the membrane if PITP availability is limiting. We would not expect such a saturation to result if the primary 3'PI production were via PI3K acting on free PI(4,5)P$_2$, which is relatively abundant. The value of $P_n$ at which this saturation occurs in our model is determined by the value of the parameter $\kappa_3$ in Eq. M.1[#]. Larger $\kappa_3$ means that binding of PI3K to the PITP does not saturate until a higher fraction of
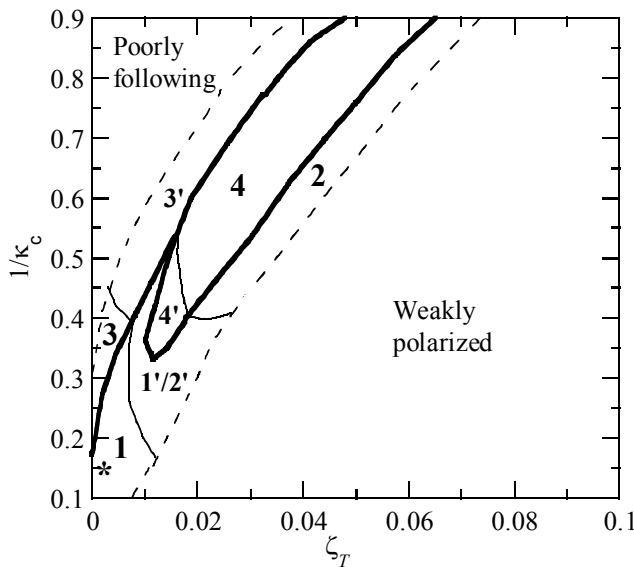


**Fig. 4.10. The role of PTEN translocation** in our model is investigated by systematically varying the parameter, $\zeta_T$, as described in the text. Decreased $\zeta_T$ means a more substantial inverse PTEN translocation in response to external stimuli; this enhances the effectiveness of **Loop II** in our model. Notation and simulations are as in Fig. 4.9. The '*' represents the combination of parameters that was used to define Case 1.

---

[#] One might imagine that the presence of a PITP would also enhance passage of PI(4,5)P$_2$ to PI3K. Thus, the parameter $\chi_3$ of Eq. M.1 would be affected as well. Because increasing $\chi_3$ strengthens the feedback in **Loop I**, we found that its variation had a similar effect to variation of $\kappa_3$, and that simultaneous variations in both parameters could compensate for each other under some conditions. Response dependence on the value of the ratio $\chi_3/\lambda_3$ was examined and this ratio was set empirically. Its value was very significant in determining if clearly distinct variants of our model could be generated with robust gradient sensing responses through variations of $\kappa_K$, $\kappa_c$, and $\gamma_0$.

143

PI3K is on the membrane (saturation becomes significant when $K_m \sim \kappa_3$), making **Loop I** of our amplification module more effective. Thus, to investigate the significance of including a PITP in our model, we systematically varied $\kappa_3$ together with $\kappa_c$ to generate another plot analogous to Fig. 4.9. The results are represented in Fig. 4.11, which again demonstrate qualitatively similar features to those in Fig. 4.9.

### 4.5.3 Compensating parameters

The differences between the Modes of gradient sensing that we have investigated with our model variants derive from the differing roles played by coupled positive feedbacks and translocating molecules in response amplification. Thus, we expect that variations of parameters that affect these model elements similarly will lead to similar transitions in the qualitative features of our model's response. Indeed, we have noted that similar transitions result, for example, if the effectiveness of our model's positive feedbacks is
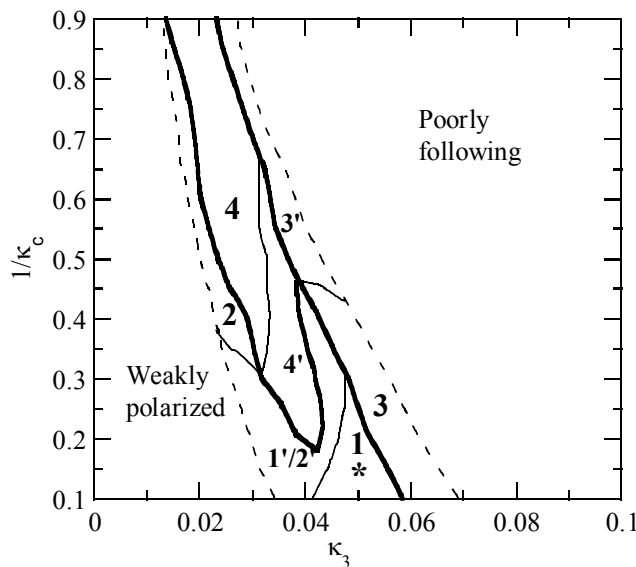


**Fig. 4.11. The significance of including a PITP** in our model is investigated by systematically varying the parameter, $\kappa_3$, as described in the text. Increased $\kappa_3$ means that PI3K binding to the PITP does not occur until higher values of $K_m$, thus enhances the effects of **Loop I** in our model. Increased $\kappa_3$ may reflect conditions where PI3K acts of free PI(4,5)P$_2$, which is abundant (this would eliminate the possibility of saturated binding in our treatment). Notation and simulations are as in Fig. 4.9. The '*' represents the combination of parameters that was used to define Case 1.

144

increased by decreasing $\kappa_K$ (see Fig. 4.9), by decreasing $\zeta_T$ (Fig. 4.10), or by increasing $\kappa_3$ (Fig. 4.11). Thus, we might expect that simultaneous variations of several of these parameters might compensate for each other.

To investigate the manner in which simultaneous variations of parameters might compensate for each other, we simultaneously varied the parameters $\zeta_T$ and $\kappa_K$. Decreasing the value of either of these parameters increases the effectiveness of **Loop II**, resulting in Modes of gradient sensing with stronger coupled positive feedbacks, as discussed in the previous subsection. Parameters were varied and responses simulated as in Secs. 4.5.1 and 4.5.2, though this time model parameters not varied were set to the values used for Case 4 in previous simulations. The resulting parameter space structure is depicted in Fig. 4.12. As expected, we see that decreasing $\kappa_K$ while appropriately increasing $\zeta_T$ often results in the same Mode of gradient sensing. This is indicated by the
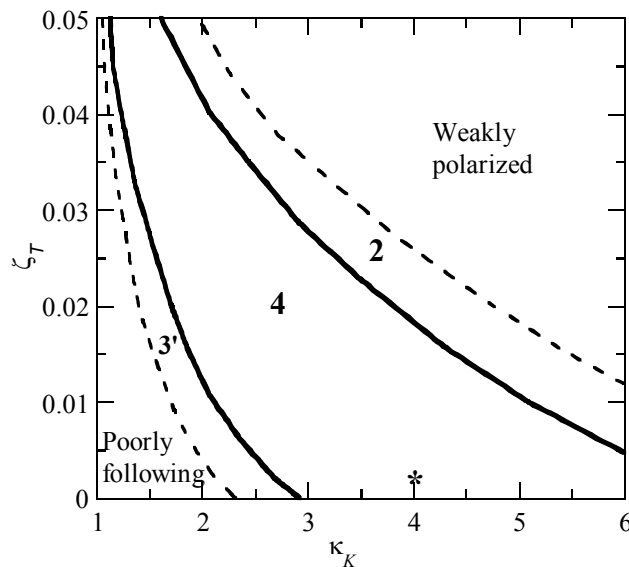


**Fig. 4.12. Compensating parameters**. Increasing $\kappa_K$ strengthens **Loop II** by enhancing 3'PI-mediated stabilization of PI3K on the membrane; increasing $\zeta_T$ strengthens **Loop II** by enhancing PI3K-mediated removal of PTEN from the membrane. Their simultaneous variation has a compensatory effect on the qualitative features of our model's response, as indicated by the hyperbolic boundaries in the depicted parameter space. Notation and simulations are as in Fig. 4.9. The '*' represents the combination of parameters used to define Case 4.

hyperbolic shape of the depicted boundaries on this surface in our model's parameter space[#]. Similar results were found for simultaneous variations of $\kappa_3$ and $\kappa_K$ as well (not shown).

## 4.6    Conclusions and implications for real cells

In presenting the results of this chapter, we have focused on qualitative features of cellular response that depend on the roles of coupled positive feedbacks and redistribution of translocating molecules in gradient sensing responses – these do not depend on the specific details of our model. We thus expect many of our results to apply to a range of cells that demonstrate characteristic gradient sensing behaviors. In this section, we summarize our conclusions from the above simulations and discuss their application to real cells, where many relevant biochemical mechanisms and parameters remain unknown.

4.6.1    Multiple modes of gradient sensing are consistent with available data

Our model reproduces the discussed dynamics of 3'PIs in gradient sensing cells, and is based on a proposed network of biochemical interaction for 3'PI regulation (see Sec. 2.3). The general features of this network suggest that qualitatively different gradient sensing mechanisms might result, depending on the roles of coupled positive feedbacks and redistribution of translocating molecules in response amplification. We varied these

---

[#] Efficient gradient sensing was not found for values of $\zeta_T$ much grater than those depicted in Fig. 4.12. Though decreasing $\kappa_K$ can partially compensate for an increase in $\zeta$T, in practice, for parameter values out of the plotted range, it was not possible to satisfy all of the conditions for efficient gradient sensing without simultaneously varying other model parameters.

elements by adjusting several parameters of our model. We thereby generated four model variants that demonstrate the qualitatively different Modes of gradient sensing which result. Each variant accounts for the characteristic gradient sensing behaviors (as enumerated in Sec. 1.2.6) and biochemical observations (Sec. 2.3.1). We thus conclude that current experimental data is consistent with multiple Modes of gradient sensing.

### 4.6.2 Transitions between efficient gradient sensing and failure highlight differences between Modes of gradient sensing

Experiments that investigate characteristic gradient sensing behaviors generally employ stimuli that give a clear result, such as a saturating uniform stimulus or a strong static gradient. The need to reproduce characteristic gradient sensing behaviors under these idealized conditions greatly constrained our model and motivated the modular framework by which is was developed (Secs. 1.5.1, 1.5.2, 2.4, 2.5.4 and 2.5.5). Further, restrictions on parameters were necessary for efficient gradient sensing, some of which were analyzed in Sec. 3.5. Nevertheless, the behaviors of our model under conditions where gradient sensing begins to fail are not constrained by current observations. Examples of conditions when gradient sensing responses fail include: when a uniform stimulus becomes too small to elicit an observable response; when a gradient is too small to produce a highly polarized response; or when the pipette in a rotating gradient experiment begins to move too quickly for the cell to follow.

Our simulations suggest that it is precisely in the nature of transitions in response from efficient gradient sensing to failure that our model variants can be distinguished. These transitions are highlighted by dose-response experiments, such as those that were simulated in Sec. 4.3. Based on these differences, we were able to suggest criteria that

distinguish between the modes of gradient sensing that were illustrated by our model variants (Sec. 4.4).

### 4.6.3 Multiple measurements of single-cell responses are necessary to distinguish between Modes of gradient sensing

The criteria that we have proposed to distinguish between different Modes of gradient sensing depend on comparisons of cellular responses to several types of stimuli, rather than the results of isolated experiments. For example, Fig. 4.4 indicates that Cases 1-3 all demonstrate weak polarization when very small gradients are applied;. A comparison of transitions in response to gradients of increasing magnitude, applied together with and after equilibration to a uniform stimulus, is necessary to identify the bifurcations in steady-state response that characterize Cases 3 and 4 (Fig. 4.4). Similarly, Cases 1 and 2 cannot be distinguished based on responses solely to uniform stimuli or to gradients (Figs. 4.2 and 4.4);. Rather, a comparison of the two responses is necessary. Further, this comparison must be done empirically, with reference to a suggested model, in order to account for the dynamic nature of responses to uniform stimuli and for diffusive dissipation that shapes responses to gradients (see Sec. 4.4.2). Thus, we conclude that it is necessary to perform multiple experiments on single cells to determine if they demonstrate the qualitative features of one of our model variants.

In addition, variability will exist in any population of cells. For example, each cell will contain a different amount of each of the molecules considered in our model. Responses to any given stimulus will thus vary from one cell to the next, and transitions in a given cell will occur at different stimuli. As a result, the response of each individual cell will be characterized by a different set of dose-response curves. Thus, we further

conclude that multiple single-cell experiments must be repeated, using multiple cells, in order to analyze the distribution of behaviors in a given population.

Performing multiple experiments on single cells is not an easy task and may require development of new experimental tools such as microfluidic devices (169-172) and caged compounds (173-177). The need for quantitative measurements on single cells to observe transitions in behavior has been emphasized in connection to other cellular systems (see, for example 178, 179). Such measurements are only recently being done in connection to gradient sensing (see, for example, 52, 124, 180, 181).

### 4.6.4 Responses to simple stimuli have implications for responses to more complex stimuli

The criteria that we have suggested to distinguish between the Modes of gradient sensing rely on differences in dose-response curves to uniform stimuli and to static gradients (Figs. 4.2 and 4.4). These differences derive directly from the roles played by coupled positive feedbacks and translocating molecules in our model variants. Our analysis of cellular responses to rotating gradients suggests that the differences that define our model variants have consequences for cellular responses to more complex stimuli (Sec. 4.3.3). For example, we found that Cases 1 and 2 always follow a rotating gradient perfectly, their polarization gradually weakening for fast rotations. The polarized response for Case 3 can be turned on and off by strong stimuli that change quickly. Case 4 remains persistently polarized in an initial direction when the gradient changes quickly. Each type of behavior might have a different utility for the cells that use them.

These observations suggest that the differences that define our model variants might further have non-trivial consequences for the behavior of cells in natural settings, where

149

chemotactic stimuli vary in space and time. Examples of behaviors that might be thus affected include the aggregation of Dictyostelium cells during starvation and the population dynamics of neutrophils migrating to a source of infection.

4.6.5 Identifying important parameters in real cells

Our analysis suggests that application of the criteria in Sec. 4.4 to real cells might guide the identification of important positive feedbacks and scarce translocating molecules. For example, if a cell is found to demonstrate a Mode 3 or Mode 4 type of behavior, we might conclude that coupled positive feedbacks play an important role in response amplification; if the results indicate a Mode 2 or Mode 4 type of behavior, we might conclude that redistribution of translocating molecules plays an important role.

The cellular concentrations and activities of many of the molecules known to be involved in gradient sensing can be perturbed externally, either by genetic or pharmacological manipulation. Our analysis of Sec. 4.5 suggests that the qualitative results of such perturbations will depend on their effects on the strengths of positive feedbacks and on depletion of translocating molecules. Thus, investigating transitions in cellular behavior as a particular biochemical interaction is perturbed might further characterize its role in the network of interactions that regulates cellular gradient sensing.

4.6.6 Homeostasis, population distributions and transitions during development

The qualitative features of our model variants exist for a range of parameter values, as illustrated by our analysis of the parameter-space surfaces of Sec. 4.5. In this way, we might think of the different Modes of gradient sensing represented by our model variants

150

as existing within volumes of parameter space and functioning efficiently within sub-volumes. These sub-volumes might have sharp boundaries and may be narrow with respect to variations of some combinations of parameters (the dependence of gradient sensing response on specific combinations of parameters was addressed in Sec. 3.5 as well). Any given cell is continuously regulating its biochemical parameters. Thus, a cell that makes use of a particular Mode of gradient sensing requires homeostatic mechanisms to maintain combinations of biochemical parameters within specific ranges.

As noted, the cells in a given population will have a distribution of biochemical parameters. Further, transitions between qualitative behaviors in the parameter space of our model might depend on small changes in biochemical parameters. Thus, we may further conclude that cells in a given population will demonstrate a range of qualitative behaviors.

Finally, cellular biochemical parameters change during development to accommodate changing needs. For example, in response to starvation, Dictyostelium cells initiate changes in gene expression, that among other things, increase the concentration of receptors for cAMP on their surface, the concentration of Adenylyl Cyclase A (ACA, which is the protein that generates cAMP), and the concentrations of several PI3K isoforms that are relevant for 3'PI signaling in gradient sensing (36-38, 48). Thus, observing transitions over time in the qualitative features of cellular gradient sensing responses could lead to deeper understanding of the roles played by the regulatory molecules that are involved.

### 4.6.7  Motivating new approaches to studying cellular behaviors

In this dissertation, we have developed a quantitative model to analyze the potential function of 3'PI signaling in eukaryotic gradient sensing. We have used this model to investigate a range of qualitative possibilities that are suggested by the generic features of PI signaling in cells. The kinds of results that we have emphasized include: that qualitative differences in behavior can arise in systems that demonstrate different bifurcation in steady-state responses and that rely differently on spatial couplings; that comparisons of cellular behaviors near a threshold in the applied stimulus to elicit a given behavior can yield important information about the qualitative features of that behavior; that sharp transitions in qualitative behaviors can result as particular parameters are varied. While the ideas that motivate these kinds of suggestions are commonplace in the physical sciences, their application is still in it infancy in the biological sciences. Thus, there is tremendous opportunity for the development of new theoretical and experimental approaches for understanding the integrated functions of biological system.

# Appendix A: Derivation of scaled model equation

Here we present a complete set of unscaled equations representing the processes depicted in the biochemical scheme upon which our model is based. This scheme, represented in Fig. 2.8 of the main text, is reproduced below in Fig. A.1. Processes are numbered for easier correspondence with terms in the unscaled equations. In deriving the scaled equations of the main text from unscaled equations, we make the following simplifications: concentrations of molecules whose spatio-temporal dynamics are not well characterized, but which are integral to the signaling network, are set to steady-state values with respect to our model variables (as discussed in Sec. 2.2.5 of the main text); concentrations whose dynamics do not directly concern us are held fixed. This procedure simplifies our system of equations while capturing the structure of the biochemical scheme. The connection between our unscaled and scaled equations could serve as a starting point for extending our analysis to include processes not explicitly modeled.

In our equations, linear kinetics have generally been assumed. We first derive a set of six unscaled equations corresponding to the six scaled equations of the main text (Eqs. M1-M6 of Table 2.3). A generalized notation, which we use to translate our biochemical scheme into differential equations, is discussed with our explanation of the first unscaled equation; this notation was introduced as well in Sec. 2.5.2a. Equations representing the processes in **Loop I** of the biochemical scheme, which are set to steady state in our model, are given next. We use the derived steady-state equations to write the concentrations of these molecules in terms of our model variables. We then use these expressions to rewrite the first six unscaled equation, which correspond to our six scaled model equations, in terms of our model variables. Parameters are grouped in
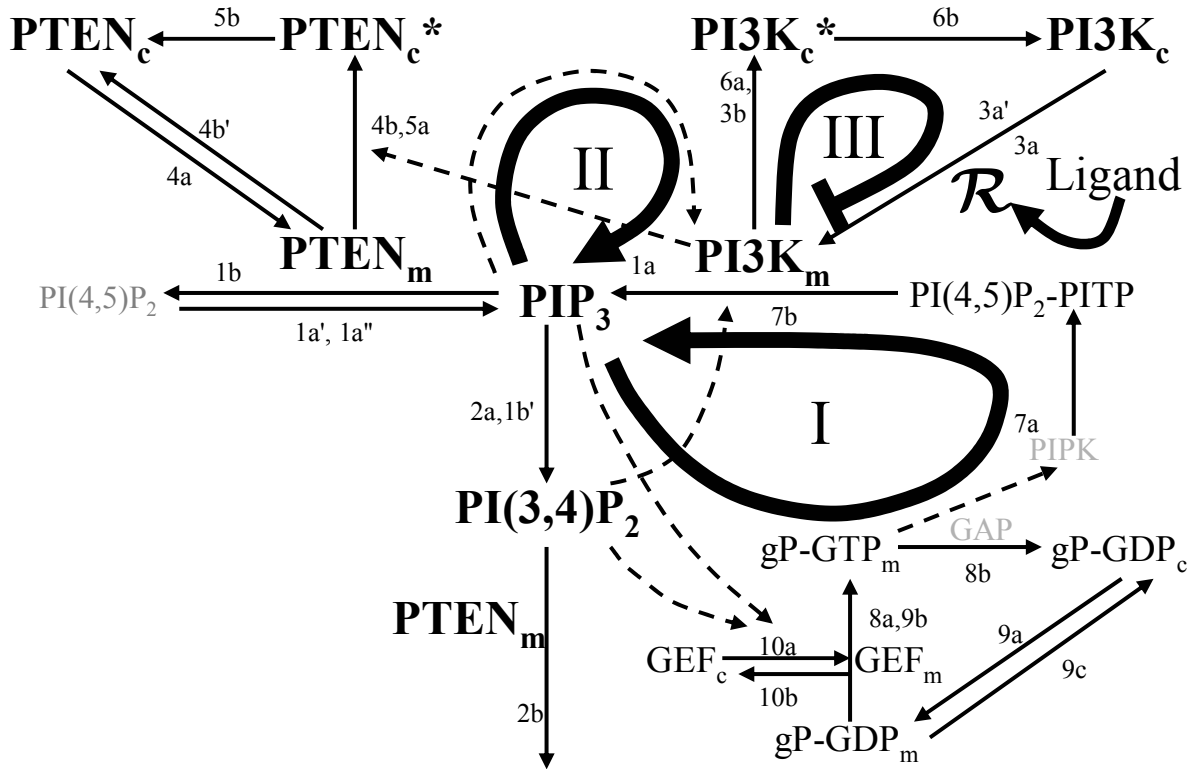
**Fig. A.1. Biochemical scheme.** Notation is as in Fig. 2.8 of the main text. Reactions are numbered in correspondence to the process labels in the unscaled equations below.

correspondence with the scaled model parameters of the main text. Relationships

between scaled and unscaled *variables* are given below in Table A.1, and relationships

between scaled and unscaled *parameters* are given in Table A.2. Discussions of the

proposed biochemical mechanisms have been given in the main text (Sec. 2.3).

*Unscaled equations corresponding to the scaled equations of the main text*

We begin by writing unscaled equations corresponding to the six scaled equations in the

main text (Eqs. 1-6 in Table 2.3 of Sec. 2.5.4). To represent the processes regulating

PI(3,4,5)P$_3$ dynamics on the membrane (abbreviated below, without ambiguity, as PIP$_3$), we write following equation:

$$\frac{\partial[\text{PIP}_3]}{\partial t} = \mathcal{P}_3\Big\{\underbrace{\big([\text{PI3K}_\text{m}]\big\|[\text{PI(4,5)P}_2\bullet\text{PITP}]\big)}_{1a}, \underbrace{\big([\text{PI3K}_\text{m}]\big\|\xi^+_{PI(4,5)P_2}\big)}_{1a'}, \underbrace{\big(\xi^+_{PI3K/PI(4,5)P_2}\big)}_{1a''}\Big\}$$
$$- \mathcal{D}_3\Big\{\underbrace{\big([\text{PTEN}_\text{m}]\big\|[\text{PIP}_3]\big)}_{1b}, \underbrace{\big(\xi^-_{SHIP}\big\|[\text{PIP}_3]\big)}_{1b'}\Big\} + D\frac{\partial^2[\text{PIP}_3]}{\partial X^2}. \tag{A.1}$$

The function $\mathcal{P}_3\{\ \}$ represents biochemical processes that generate PIP$_3$, and the function $\mathcal{D}_3\{\ \}$ represents processes that degrade PIP$_3$. Each biochemical process is represented in parentheses and labeled below the equation in correspondence with Fig. A.1. Concentrations are denoted by strait brackets ('[ ]'). To represent an enzyme, $E_X$, acting on molecule, $Y$, we use the notation, $\big([E_X]\big\|[Y]\big)$. Processes involving molecules whose dynamics are not calculated in our model (i.e. those whose concentrations are treated as fixed) are generally represented by the symbol $\xi$. They are labeled with a prime (e.g. $1a'$), but only included in Fig. A.1 if they do not make it more difficult to read. In the main text, we have generally referred to these processes as constitutive (see Sec. 2.3.3d; their regulation is not included in our model. They often occur in parallel with processes whose regulation is modeled (the corresponding unprimed processes).

Based on the above notation, we interpret the processes in Eq. A.1 that produce PIP$_3$ as follows: $1a$ - PI3K acting on PI(4,5)P$_2$ bound to a transfer protein ( PI(4,5)P$_2\bullet$PITP ); $1a'$ - PI3K acting of free PI(4,5)P$_2$; $1a''$ - the constitutive action on PI(4,5)P$_2$ of other PI3K isoforms that do not display the modeled translocation dynamics. The processes that degrade PIP$_3$ are interpreted as: $1b$ - dephosphorylation of PIP$_3$ in the 3' position by PTEN (making it no longer a 3'PI); $1b'$ - conversion of PIP$_3$ to PI(3,4)P$_2$, through

155

dephosphorylation at the 5' position by a phosphatase such as SHIP (138). Regulation of free PI(4,5)P$_2$, of other PI3K isoforms, and of other phosphatases (such as SHIP), are not included in our model. Thus, we have used the symbols $\xi^+_{PI(4,5)P_2}$, $\xi^+_{PI3K/PI(4,5)P_2}$ and $\xi^-_{SHIP}$ above in representing the processes involving these molecules. PIP$_3$ diffusion on the membrane is also included in Eq. A.1, and the spatial variable ($X$) is normalized so that the circumference of the cell is 1 (as in the main text).

To write a differential equation corresponding to Eq. A.1, we must choose an appropriate model to represent the chemical kinetics included in $\mathcal{P}_3\{\ \}$ and $\mathcal{D}_3\{\ \}$. For simplicity, we have assumed linear kinetics (see Sec. 2.5.1). That is, the concentration of each molecule involved appears linearly in our rate equation. Thus, Eq. A.1 becomes:

$$\frac{\partial [PIP_3]}{\partial t} = \kappa_3^+ [PI3K_m] (\underbrace{[PI(4,5)P_2 \bullet PITP]}_{1a} + \underbrace{\xi^+_{PIP(4,5)P_2}}_{1a'}) + \underbrace{\xi^+_{PI3K/PIP(4,5)P}}_{1a''}$$

$$- \kappa_3^- [PIP_3] (\underbrace{[PTEN_m]}_{1b} + \underbrace{\xi^-_{SHIP}}_{1b'}) + D\frac{\partial^2 [PIP_3]}{\partial X^2}.$$

(A.1')

We generally use the parameter $\kappa^+$ to represent forward rate constants and $\kappa^-$ to represent backwards rate constants. For simplicity, the same symbols used to represent constitutive processes in Eq. A.1 ($\xi$) appear as parameters relating to those processes in Eq. A.1'. The parameters $\xi$ in Eq. A.1' can be considered combinations of rate constants and concentrations of molecules whose regulation we have not modeled. For example, we might think of $\xi^+_{PI(4,5)P_2}$ as being proportional to [PI(4,5)P$_2$], $\xi^+_{PI3K/PI(4,5)P_2}$ as proportional to the concentrations of other PI3K isoforms and to [PI(4,5)P$_2$], and $\xi^-_{SHIP}$ as proportional to [SHIP].

To represent the processes regulating PI(3,4)P$_2$ dynamics on the membrane, we write following equation:

$$\frac{\partial\left[\text{PI(3,4)P}_2\right]}{\partial t} = \mathcal{P}_2\left\{\underbrace{\left(\xi_{SHIP}^-\left\|\left[\text{PI(3,4)P}_2\right]\right)\right.}_{2a},\underbrace{\left(\xi_{2-other}^+\right)}_{2a'}\right\}$$
$$-\mathcal{D}_2\left\{\underbrace{\left(\left[\text{PTEN}_m\right]\left\|\left[\text{PIP}_3\right]\right)\right.}_{2b},\underbrace{\left(\xi_{4'\,phosphatase}^-\left\|\left[\text{PI(3,4)P}_2\right]\right)\right.}_{2b'}\right\}+D\frac{\partial^2\left[\text{PI(3,4)P}_2\right]}{\partial X^2}. \tag{A.2}$$

The notation used is as in Eq. A.1. The represented processes that produce PI(3,4)P$_2$ are: *2a* - conversion of PIP$_3$ to PI(3,4)P$_2$ by a phosphatase such as SHIP (an analogous degradation process appears in Eq. A.1); *2a'* - constitutive production by other biochemical pathways. Processes that degrade PI(3,4)P$_2$ are; *2b* - dephosphorylation at the 3' position by PTEN; *2b'* - constitutive dephosphorylated at the 4' position by other phosphatases. We assume that the scaled diffusion coefficient is the same for PI(3,4)P$_2$ and PIP$_3$. As with Eq. A.1, we assume linear kinetics to describe the processes in Eq. A.2, and derive the following differential equation:

$$\frac{\partial\left[\text{PI(3,4)P}_2\right]}{\partial t} = \underbrace{\kappa_3^-\xi_{SHIP}^-\left[\text{PIP}_3\right]}_{2a}+\underbrace{\xi_{2-other}^+}_{2a'}$$
$$-\kappa_2^-\left[\text{PI(3,4)P}_2\right]\left(\underbrace{\left[\text{PTEN}_m\right]}_{2b}+\underbrace{\xi_{4'\,phosphatase}^-}_{2b'}\right)+D\frac{\partial^2\left[\text{PI(3,4)P}_2\right]}{\partial X^2}. \tag{A.2'}$$

Unscaled equations for the dynamics of PI3K on the membrane were derived as an example in the main text (Sec. 2.5.2). This example is repeated here. We write following equation to represent the processes regulating PI3K dynamics on the membrane:

$$\frac{\partial\left[\text{PI3K}_m\right]}{\partial t} = \mathcal{P}_K\left\{\underbrace{\left(\boldsymbol{R}\left\|\left[\text{PI3K}_c\right]\right)\right.}_{3a},\underbrace{\left(\xi_R\left\|\left[\text{PI3K}_c\right]\right)\right.}_{3a'}\right\}-\mathcal{D}_K\left\{\underbrace{\left(\left[A\right],\left[\text{PI3K}_m\right]\right)}_{3b}\right\}. \tag{A1.3}$$

As in the main text, subscripts m/c denote membrane bound/cytosolic. Membrane bound PI3K is assumed to be active. The represented processes that recruit cytosolic PI3K (PI3K$_c$) to the membrane are: *3a* - recruitment by ligand-activated receptors and HTGs (**R**); *3a'* - constitutive recruitment. Process *3b* represents removal of PI3K from the membrane by phosphorylation. We assume that PI3K is phosphorylated by an unidentified kinase that is constitutively on the membrane, and that this phosphorylation is regulated by an unidentified molecule *A*, as proposed in the main text (Sec. 2.3.3b). Diffusion of proteins along the membrane is not included.

The following mechanism accounts for a form of $\mathcal{D}_K\{\ \}$ that corresponds to the form in Eq. M.3 of the main text (Table 2.3). We assume that *A* binds to PI3K on the membrane, and prevents PI3K phosphorylation. We further assume that *A* translocates to the membrane in response to 3'PI production. The following equations, assuming linear kinetics, describe the dynamics of molecule *A* on the membrane and its complex with PI3K ($A_m$·PI3K$_m$):

$$\frac{\partial[A_m]}{\partial t} = \underbrace{\kappa_A^+[A_c][3'\text{PI}]}_{\substack{\text{translocation in}\\\text{response to 3'PIs}}} \quad - \quad \underbrace{\kappa_A^-[A_m]}_{\substack{\text{spontaneous}\\\text{return to cytosol}}} \tag{A.3a}$$

$$\frac{\partial[A_m\bullet\text{PI3K}_m]}{\partial t} = \underbrace{\kappa_{AK}^+[A_m]\big([\text{PI3K}_m]-[A_m\bullet\text{PI3K}_m]\big)}_{\text{complex formation}} \quad - \quad \underbrace{\kappa_{AK}^-[A_m\bullet\text{PI3K}_m]}_{\text{spontaneous dissociation}} \tag{A.3b}$$

where $[3'\text{PI}] \equiv [\text{PIP}_3] + [\text{PI(3,4)P}_2]$. $\tag{A.3c}$

In Eq. A.3a, cytosolic *A* ($A_c$) binds to 3'PIs on the membrane (1st term) and spontaneously returns to the cytosol (2nd term). We assume that the interaction of *A* and PI3K is limited by the amount of PI3K on the membrane, rather than the amount of *A*. Thus, the 1st term in Eq. A.3b represents production of the complex $A_m$·PI3K$_m$ due to

158

interaction of $A_m$ with PI3K on the membrane that is not already bound to $A$ (PI3K$_m$ –

$A_m$·PI3K $_m$).  The complex also spontaneously dissociates (2nd term).  Because the

properties of molecule $A$ are unknown, we simplify our analysis by setting the LHS of

Eqs. A.3a and A.3b to zer0 and expressing the concentration of the complex, [$A_m$·PI3K$_m$],

in terms of model variables (see discussion in Sec. 2.2.5).  We find:

$$\left[ A_m \bullet \text{PI3K}_m \right] = \frac{\left[ \text{PI3K}_m \right]\left[ 3'\text{PI} \right]/\kappa_{AK}}{\left[ 3'\text{PI} \right]/\kappa_{AK} + 1} \tag{A.3d}$$

where $\kappa_{AK} = \dfrac{\kappa_A^- \kappa_{AK}^-}{\kappa_A^+ \left[ A_c \right] \kappa_{AK}^+}$,  and we have further assumed that only a small fraction of $A$

translocates to the membrane ($A_c \sim$ constant).  Thus, the fraction of PI3K on the

membrane, which is not bound to molecule $A$ and is free to return to the cytosol, is given

by:

$$1 - \frac{\left[ A_m \bullet \text{PI3K}_m \right]}{\left[ \text{PI3K}_m \right]} = \frac{1}{\left[ 3'\text{PI} \right]/\kappa_{AK} + 1}. \tag{A.3e}$$

Thus, if we assume linear kinetics to describe the processes represented in Eq. S1.3, and

use Eqs. S1.3e, the following differential equation results:

$$\frac{\partial \left[ \text{PI3K}_m \right]}{\partial t} = \kappa_K^+ \left[ \text{PI3K}_c \right] \underbrace{(\underline{R}}_{3a} + \underbrace{\xi_R}_{3a'}) - \underbrace{\kappa_K^- \left[ \text{PI3K}_m \right] \frac{1}{\left[ 3'\text{PI} \right]/\kappa_{AK} + 1}}_{3b}. \tag{A.3'}$$

The form obtained for process 3b describes PI3K phosphorylation with rate constant, $\kappa_K^-$,

of the fraction of PI3K on the membrane not bound to molecule $A$.  The concentration of

the unidentified kinase that phosphorylates PI3K, which is assumed to be constant on the

membrane, has been absorbed in the rate constant, $\kappa_K^-$.  This form captures the feedback

represented by **Loop II**, as discussed in the main text.

The following equation represents conservation of total PI3K, and is used to eliminate $[\text{PI3K}_c]$ from Eq. A.3':

$$[\text{PI3K}_0] A_{cell} = [\text{PI3K}_c] A_{cell} + [\text{PI3K}_c*] A_{cell} + \int_0^1 [\text{PI3K}_m] dX . \qquad (\text{A.3''})$$

[PI3K$_0$] is the total PI3K in our assumed 2-d cell, divided by the area of the cell, ($A_{cell}$) where we have assumed that cytosolic molecules are uniformly distributed (e.g. $[PI3K_c*]A_{cell}$ is the total PI3K that is cytosolic and phosphorylated). In units where the circumference is of the cell is 1, $A_{cell} = 1/4\pi$.

We represent the processes that regulate the PTEN phosphatase on the membrane with the following equation:

$$\frac{\partial [\text{PTEN}_m]}{\partial t} = \mathcal{P}_T \Big\{ \underbrace{([\text{PTEN}_c])}_{4a} \Big\} - \mathcal{D}_T \Big\{ \underbrace{([\text{PI3K}_m][\text{PTEN}_m])}_{4b}, \underbrace{([\text{PTEN}_m])}_{4b'} \Big\} . \qquad (\text{A.4})$$

Cytosolic PTEN (PTEN$_c$) is spontaneously recruited to the membrane (*4a*). PTEN is removed from the membrane through PI3K mediated phosphorylation (*4b*), as well as spontaneously (*4b'*). These processes lead to the following differential equation for PTEN on the membrane:

$$\frac{\partial [\text{PTEN}_m]}{\partial t} = \kappa_T^+ \underbrace{[\text{PTEN}_c]}_{4a} - \kappa_T^- [\text{PTEN}_m] (\underbrace{[\text{PI3K}_m]}_{4b} + \underbrace{\xi_T}_{4b'}) . \qquad (\text{A.4'})$$

The parameter, $\xi_T$, is the ratio of the rate constant for spontaneous PTEN return to the cytosol to the rate constant for PI3K-mediated phosphorylation. Possible PTEN anchoring to the membrane by PI(4,5)P$_2$ (182) is not included, though we might imagine, for example, that the rate constants in Eq. A.4' depend on [PI(4,5)P$_2$]. In this way, our

model could be extended to include this regulation. The following relationship expresses conservation of total PTEN, and is used to eliminate [PTEN$_c$] from Eq. A.4':

$$[\text{PTEN}_0]A_{cell} = [\text{PTEN}_c]A_{cell} + [\text{PTEN}_c{}^*]A_{cell} + \int_0^1 [\text{PTEN}_m]dX . \qquad (A.4")$$

As in Eq. A3", [PTEN$_0$] is the total PTEN in our 2-d cell, divided by its area.

To represent the processes that regulate the concentration of phosphorylated inactive PTEN in the cytosol (a '*' denotes a catalytically inactive phosphorylated state in our equations), we write the following equation:

$$\frac{\partial[\text{PTEN}_c{}^*]}{\partial t} = \mathcal{P}_{T*}\left\{\underbrace{\int_0^1 ([\text{PI3K}_m][\text{PTEN}_m])dX}_{5a}\right\} - \mathcal{D}_{T*}\left\{\underbrace{([\text{PTEN}_c{}^*])}_{5b}\right\} . \qquad (A.5)$$

We have assumed that the cytosol is uniform and exchanges material with the entire membrane (that is, cytosolic diffusion effectively occurs infinitely quickly in our model). Thus, process *5a* represents PI3K-mediated phosphorylation of PTEN over the entire membrane. An analogous degradation process appears in Eq. A.4. Process *5b* represents unregulated dephosphorylation of PTEN in the cytosol by unspecified phosphatases. Equation A.5 gives rise to the following differential equation:

$$\frac{\partial[\text{PTEN}_c{}^*]}{\partial t} = \underbrace{\kappa_T^- \int_0^1 [\text{PTEN}_m][\text{PI3K}_m]dX / A_{cell}}_{5a} - \underbrace{\kappa_{T*}^- [\text{PTEN}_c{}^*]}_{5b} . \qquad (A.5')$$

A loss term analogous to *5a* appears in Eq. A.4'. If another phosphatase is required for PTEN dephosphorylation (process *5b*), its concentration is included in the rate constant, $\kappa_{T*}^-$. Eq. A.5' does not depend on *X*.

The following equation represents the processes regulating cytosolic phosphorylated PI3K, which is catalytically inactive and uniformly distributed in our model:

$$\frac{\partial[\text{PI3K}_c*]}{\partial t} = \mathcal{P}_{K*}\left\{\underbrace{\int_0^1([A],[\text{PI3K}_m])dX}_{6a}\right\} - \mathcal{D}_{K*}\left\{\underbrace{\left(\frac{[\text{PI3K}_c*]}{[\text{PI3K}_c*]+a_{K*}}\right)}_{6b}\right\}. \tag{A.6}$$

Process *6a* represents PI3K phosphorylation over the entire membrane, and is analogous to process *3b* in Eq. A.3. Process *6b* represents PI3K dephosphorylation in the cytosol by an unspecified phosphatase, with Michalis-Menten kinetics. The constant, $a_{K*}$, is assumed small, such that this reaction is saturated. This condition leads to perfect adaptation in our model, as discussed in the main text (Secs. 2.5.3d and 2.5.5). Equation A.6 leads to the following differential equation:

$$\frac{\partial[\text{PI3K}_c*]}{\partial t} = \kappa_K^-\underbrace{\int_0^1\frac{[\text{PI3K}_m]}{[3'\text{PI}]/\kappa_{AK}+1}dX/A_{cell}}_{6a} - \kappa_{K*}^-\underbrace{\frac{[\text{PI3K}_c*]}{[\text{PI3K}_c*]+a_{K*}}}_{6b}. \tag{A.6'}$$

Term *6a* is analogous to term 3b in Eq. A.3'. The rate constant, $\kappa_{K*}^-$, includes the concentration of the relevant phosphatase that dephosphorylated PI3K.

Equations A.1' – A.6' are unscaled versions of the six scaled equations that comprise our model (Eqs. M.1-M.6 of Table 2.3). Below we give equations for the elements of **Loop I** (Fig. A.1), which are set to steady-state in deriving our scaled equations.

*Unscaled equations for processes in **Loop I** that are set to steady-state.*

To describe the processes in **Loop I** that are set to steady-state in our model, we directly write differential equations, assuming linear kinetics, rather than first representing production and degradation processes symbolically. Terms are still labeled in correspondence to the processes in Fig. A.1.

For the concentration of PI(4,5)P$_2$ that is bound to a transfer protein ($\left[\text{PI(4,5)P}_2\bullet\text{PITP}\right]$) we write the following differential equation:

$$\frac{\partial\left[\text{PI(4,5)P}_2\bullet\text{PITP}\right]}{\partial t} =$$

$$\underbrace{\kappa^+_{PITP}\left[\text{PITP}\bullet\text{PIP}\right]\left[\text{PIPK}_\text{m}\right]\left(\left[\text{PA}\right]+\xi_{non-PA}\right)\left(\left[\text{gP}\bullet\text{GTP}_\text{m}\right]+\xi_{non-gP}\right)}_{7a} \qquad (A.7)$$

$$\underbrace{-\kappa^+_3\left[\text{PI3K}_\text{m}\right]\left[\text{PI(4,5)P}_2\bullet\text{PITP}\right]}_{7b}\underbrace{-\xi_{competitive}\left[\text{PI(4,5)P}_2\bullet\text{PITP}\right]}_{7b'}.$$

In Eq. A.7, the first term (*7a*) represents small GTPase-regulated production of PI(4,5)P$_2$ bound to a PI transfer protein (PITP). We assume that PI(4')P is already bound to the PITP on the membrane ( PITP•PIP ). A PI(4)P 5'kinase (PIPK) acts on this PI(4)P to produce PI(4,5)P$_2$•PITP . Phosphatidic acid (PA) and small GTPases of the Arf and Rho families (in the GTP state, denoted gP•GTP$_\text{m}$, which is membrane-bound), are known to enhance this reaction (183, 184). The parameters, $\xi_{non-PA}$ and $\xi_{non-gP}$ represent activity which is independent of PA and gP, respectively. Regulation by small GTPases is the most essential feature of **Loop I**, while regulation of the other molecules involved does not play as clear a role. Thus we simplify our system by setting:

$\left[\text{PITP}\bullet\text{PIP}\right]$ = constant
$\left[\text{PIPK}\right]$ = constant  $\qquad\qquad$ (A.7')
$\left[\text{PA}\right]$ = constant.

Terms *7b* and *7b'* in Eq. A.7 represent loss of PI(4,5)P$_2$•PITP due to action of PI3K and to other competitive processes that make use of PI(4,5)P$_2$, respectively.

The dynamics of membrane-bound, activated small GTPase, are described by the following equation:

$$\frac{\partial\left[\text{gP}\bullet\text{GTP}_\text{m}\right]}{\partial t} = \underbrace{\kappa^+_{gP\bullet T}\left[\text{gP}\bullet\text{GDP}_\text{m}\right]\left[\text{GEF}_\text{m}\right]}_{8a} - \underbrace{\kappa^-_{gP\bullet T}\left[\text{GAP}\right]\left[\text{gP}\bullet\text{GTP}_\text{m}\right]}_{8b}. \tag{A.8}$$

The first term in Eq. A.8 (*8a*) corresponds to a GTP exchange factor (GEF) catalyzing the exchange of GDP for GTP in the GTPase, stabilizing its association with the membrane. Term *8b* corresponds to hydrolysis of GTP by the GTPase, catalyzed by a GTPase activating protein (GAP). This destabilizes the GTPase's association with the membrane. We do not model GAP dynamics, which often depends on PIP(4,5)P$_2$ (150). Thus, we set:

$$\left[\text{GAP}\right] = \text{constant} . \tag{A.8'}$$

We assume that the GTPase weakly associates with the membrane in the GDP state, before nucleotide exchange is achieved. This is described by the following equation:

$$\frac{\partial\left[\text{gP}\bullet\text{GDP}_\text{m}\right]}{\partial t} = \underbrace{\kappa^+_{gP\bullet D}\left[\text{gP}\bullet\text{GDP}_\text{c}\right]}_{9a} - \underbrace{\kappa^+_{gP\bullet T}\left[\text{gP}\bullet\text{GDP}_\text{m}\right]\left[\text{GEF}_\text{m}\right]}_{9b} - \underbrace{\kappa^-_{gP\bullet D}\left[\text{gP}\bullet\text{GDP}_\text{m}\right]}_{9c}. \tag{A.9}$$

The production term in Eq. A.9 (*9a*) represents unregulated translocation of cytosolic GTPase (in the GDP state) to the membrane. Term *9b* represents nucleotide exchange in the GTPase (which was included as term *8a* in Eq. A.8); term *9c* represents unregulated return of the GTPase to the cytosol. If only a small fraction of the GTPase associates with the membrane, we have the relationship:

$$\left[\text{gP}\bullet\text{GDP}_\text{c}\right] = \text{constant} . \tag{A.9'}$$

The dynamics of the exchange factor (GEF), required for nucleotide exchange in the GTPase, are described by the following equation:

$$\frac{\partial[GEF_m]}{\partial t} = \underbrace{\kappa_{GEF}^+[GEF_c][3'PI]}_{10a} - \underbrace{\kappa_{GEF}^-[GEF_m]}_{10b}, \qquad \backprime \qquad (A.10)$$

where $[GEF_c] = ([GEF_0]A_{cell} - \int_0^1 [GEF_m]dX)/A_{cell}$. $\qquad$ (A.10')

The first term in Eq. A.10 (*10a*) represents 3'PI-induced translocation of cytosolic GEF to the membrane. Return to the cytosol is unregulated (*10b*). Total GEF (GEF$_0$) is conserved, and this is used to eliminate GEF$_c$ from our equations (Eq. A.10'). This completes the set of unscaled equations for our model.


*Steady-state solutions*

Here we present steady-state solutions to Eqs. A.7 – A.10. The LHS of these equations are set to zero and the represented concentrations are expressed in terms of our model variables.

If we set Eq. A.10 to steady state, and use relationship A.10', we find:

$$[GEF_m] = [GEF_0]A_{cell}\frac{[3'PI]/\kappa_{GEF}}{\int_0^1 [3'PI]dX/\kappa_{GEF}+1}, \qquad (A.11)$$

where $\kappa_{GEF} \equiv A_{cell}\kappa_{GEF}^-/\kappa_{GEF}^+$.

Setting Eq. A.9 to steady state, we find:

$$[gP\bullet GDP_m] = \frac{V_{gP\bullet D}[gP\bullet GDP_c]}{[GEF_m]/\kappa_{gP\bullet D}+1},$$

where $V_{gP\bullet D} \equiv \kappa_{gP\bullet D}^+/\kappa_{gP\bullet D}^- \qquad (A.12)$

and $\kappa_{gP\bullet D} \equiv \kappa_{gP\bullet D}^-/\kappa_{gP\bullet T}^+$.

Setting Eq. A.8 to steady state, and using Eqs. A.11 and A.12, we find:

$$[\text{gP·GTP}_m] = \frac{V_{gP·T}[3'\text{PI}]}{[3'\text{PI}]/\kappa_{gP·T} + \int_0^1 [3'\text{PI}]dX/\kappa_{GEF} + 1},$$

$$\text{where } V_{gP·T} \equiv \left(\kappa_{gP·T}^+ / \kappa_{gP·T}^- [\text{GAP}]\right)\left(V_{gP·D}[\text{gP·GDP}_c]\right)\left([\text{GEF}_0]A_{cell}/\kappa_{GEF}\right) \qquad \text{(A.13)}$$

$$\text{and } \kappa_{gP·T} \equiv \kappa_{gP·D} / \left([\text{GEF}_0]A_{cell}/\kappa_{GEF}\right).$$

Finally, setting Eq. A.7 to steady state, and using Eq. A.13:

$$[\text{PI(4,5)P}_2\text{·PITP}] = \frac{\dfrac{V_{PITP}[3'\text{PI}]}{[3'\text{PI}]/\kappa_{gP·T} + \int_0^1 [3'\text{PI}]dX/\kappa_{GEF} + 1} + V_{PITP}\xi_{non-gP}}{[\text{PI3K}_m]/\kappa_{PITP} + 1},$$

$$\text{where } V_{PITP} \equiv \kappa_{PITP}^+ [\text{PITP·PIP}][\text{PIPK}]([\text{PA}] + \xi_{non-PA})V_{gP·T}/\xi_{competitive} \qquad \text{(A.14)}$$

$$\text{and } \kappa_{PITP} \equiv \xi_{competitive}/\kappa_3^+.$$

Eq. A.14 effectively includes the feedback in **Loop I** without explicitly including many of the molecules involved, whose dynamics are not well characterized.

*Correspondence to scaled equations*:

Now, we insert Eq. A.14 into Eq. A.1', and rewrite Eqs. A.1' – A.6' in terms of our model variables (see Table A.1). Parameters are grouped to correspond with the presentation of the scaled equations in the main text.

$$\frac{\partial \boldsymbol{P_3}}{\partial t} = \left(\kappa_3^+ V_{PITP}A_{cell}[\text{PI3K}_0]\right)\boldsymbol{K_m}\left(\frac{\tilde{\Xi} + \left(\xi_{non-gP}/[3'\text{PI}_0]\right)}{\boldsymbol{K_m}/\left(\kappa_{PITP}/A_{cell}[\text{PI3K}_0]\right) + 1} + \frac{\xi_{PIP(4,5)P_2}^+}{V_{PITP}[3'\text{PI}_0]}\right)$$

$$+ \frac{\xi_{PI3K/PIP(4,5)P}^+}{[3'\text{PI}_0]} - \left(\kappa_3^- A_{cell}[\text{PTEN}_0]\right)\boldsymbol{P_3}\left(\boldsymbol{T_m} + \frac{\xi_{SHIP}^-}{A_{cell}[\text{PTEN}_0]}\right) + D\frac{\partial^2 \boldsymbol{P_3}}{\partial X^2} \qquad \text{(A.15)}$$

$$\text{where } \tilde{\Xi} \equiv \frac{\boldsymbol{P_n}}{[3'\text{PI}_0]\left(\boldsymbol{P_n}/\kappa_{gP·T} + \int_0^1 [3'\text{PI}]dX/\kappa_{GEF}\right) + 1}$$

$$\text{and } [3'\text{PI}_0] \equiv \kappa_{gP·T} + \kappa_{GEF}$$

$$\frac{\partial \boldsymbol{P_2}}{\partial t} = \left(\kappa_3^- \xi_{SHIP}^-\right)\boldsymbol{P_3} + \frac{\xi_{2-other}^+}{[3'\text{PI}_0]} - \left(\kappa_2^- A_{cell}[\text{PTEN}_0]\right)\boldsymbol{P_2}\left(\boldsymbol{T_m} + \frac{\xi_{4'\,phosphatase}^-}{A_{cell}[\text{PTEN}_0]}\right) + D\frac{\partial^2 \boldsymbol{P_2}}{\partial X^2} \quad \text{(A.16)}$$

166

$$\frac{\partial \boldsymbol{K_m}}{\partial t} = \kappa_K^- \left( \gamma - \frac{\boldsymbol{K_m}}{\boldsymbol{P_n} / \left( \kappa_{AK} / [3'\mathrm{PI}_0] \right) + 1} \right)$$

$$\text{where } \gamma = \left( \frac{\xi_R \kappa_K^+}{\kappa_K^-} \right) \boldsymbol{K_c} \left( \mathcal{R} + 1 \right) \tag{A.17}$$

$$1 = \boldsymbol{K_c} A_{cell} - \boldsymbol{K_c} {}^* A_{cell} + \int_0^1 \boldsymbol{K_m} dX \tag{A.17'}$$

$$\frac{\partial \boldsymbol{T_m}}{\partial t} = \kappa_T^+ \boldsymbol{T_c} - \left( \kappa_T^- A_{cell} [\mathrm{PI3K}_0] \right) \boldsymbol{T_m} \left( \boldsymbol{K_m} + \frac{\xi_T}{A_{cell} [\mathrm{PI3K}_0]} \right) \tag{A.18}$$

$$1 = \boldsymbol{T_c} A_{cell} + \boldsymbol{T_c} {}^* A_{cell} + \int_0^1 \boldsymbol{T_m} dX \tag{A.18'}$$

$$\frac{\partial \boldsymbol{T_c}{}^*}{\partial t} = \left( \kappa_T^- A_{cell} [\mathrm{PI3K}_0] \right) \int_0^1 \boldsymbol{T_m} \boldsymbol{K_m} dX / A_{cell} - \kappa_{T*}^- \boldsymbol{T_m} \tag{A.19}$$

$$\frac{\partial \boldsymbol{K_c}{}^*}{\partial t} = \kappa_K^- \int_0^1 \frac{\boldsymbol{K_m}}{\boldsymbol{P_n} / \left( \kappa_{AK} / [3'\mathrm{PI}_0] \right) + 1} dX / A_{cell}$$

$$- \left( \frac{\kappa_{K*}^-}{A_{cell} [\mathrm{PI3K}_0]} \right) \frac{\boldsymbol{K_c}{}^*}{\boldsymbol{K_c}{}^* + \left( a_{K*} / A_{cell} [\mathrm{PI3K}_0] \right)} \tag{A.20}$$

Substituting the scaled parameters of Table A.2 below into Eqs. A.15-A.20, one obtains

the scaled model equations of the main text (Eqs. M.1-M.6 of table 2.3).  Note, that the

expressions for the scaled parameters in Table A.2 make use of the definitions in Eqs.

A.11-A.15.

**Table A.1: Definitions of scaled variables**

| Scaled variable | Definition |
| --- | --- |
| $P_3$ | $[\text{PIP}_3]/(\kappa_{gP \cdot T} + \kappa_{GEF})$ |
| $P_2$ | $[\text{PI(3,4)P}_2]/(\kappa_{gP \cdot T} + \kappa_{GEF})$ |
| $P_n$ | $P_3 + P_2$ |
| $K_m$ | $[\text{PI3K}_m]/A_{cell}[\text{PI3K}_0]$ |
| $K_c{*}$ | $[\text{PI3K}_c{*}]/A_{cell}[\text{PI3K}_0]$ |
| $T_m$ | $[\text{PTEN}_m]/A_{cell}[\text{PTEN}_0]$ |
| $T_c$ | $[\text{PTEN}_c{*}]/A_{cell}[\text{PTEN}_0]$ |

**Table A.2: Definitions of scaled parameters**

| Parameters | Definition |
| --- | --- |
| $\chi_3$ | $\kappa_3^+ V_{PITP} A_{cell} \left[ \text{PI3K}_0 \right]$ |
| $\kappa_3$ | $\kappa_{PITP} / A_{cell} \left[ \text{PI3K}_0 \right]$ |
| $\kappa_m$ | $\kappa_{gP \cdot T} / \left[ 3'\text{PI}_0 \right]$ |
| $\kappa_c$ | $\kappa_{GEF} / \left[ 3'\text{PI}_0 \right]$ |
| $\zeta_{PITP}$ | $\xi_{non-gP} / \left[ 3'\text{PI}_0 \right]$ |
| $\zeta_{3/PITP}$ | $\xi_{PIP(4,5)P_2}^+ / V_{PITP} \left[ 3'\text{PI}_0 \right]$ |
| $\zeta_3$ | $\xi_{PI3K/PIP(4,5)P_2}^+ / \left[ 3'\text{PI}_0 \right]$ |
| $\lambda_3$ | $\kappa_3^- A_{cell} \left[ \text{PTEN}_0 \right]$ |
| $\zeta_{3/T}$ | $\xi_{SHIP}^- / A_{cell} \left[ \text{PTEN}_0 \right]$ |
| $\zeta_2$ | $\xi_{2-other}^+ / \left[ 3'\text{PI}_0 \right]$ |
| $\lambda_2$ | $\kappa_2^- A_{cell} \left[ \text{PTEN}_0 \right]$ |
| $\zeta_{2/T}$ | $\xi_{4'phosphatase}^- / A_{cell} \left[ \text{PTEN}_0 \right]$ |
| $\chi_K$ | $\kappa_K^+ \xi_R$ |
| $\mathcal{R}$ | $R/\xi_R$ |
| $\lambda_K$ | $\kappa_K^-$ |
| $\kappa_K$ | $\kappa_{AK} / \left[ 3'\text{PI}_0 \right]$ |
| $\chi_T$ | $\kappa_T^+$ |
| $\lambda_T$ | $\kappa_T^- A_{cell} \left[ \text{PI3K}_0 \right]$ |
| $\zeta_T$ | $\xi_T / A_{cell} \left[ \text{PI3K}_0 \right]$ |
| $\lambda_{T*}$ | $\kappa_{T*}^-$ |
| $\lambda_{K*}$ | $\kappa_{K*}^- / A_{cell} \left[ \text{PI3K}_0 \right]$ |
| $\kappa_{K*}$ | $a_{K*} / A_{cell} \left[ \text{PI3K}_0 \right]$ |

# Appendix B: Setting parameters

Most of the parameters used in our model have not been measured directly. Further, it is not clear how to quantitatively relate in-vitro data to processes occurring inside of cells, where multiple interactions and complex geometries exist. For these reasons, most of our parameters have been set empirically, principally to give characteristic responses seen in Dictyostelium (see Sec. 2.6 of the main text). Values of most parameters are the same for all of our model variants, but, as discussed in the main text, several were adjusted separately to generate the qualitative differences which distinguish our model variants (see Sec. 2.7). Below we give the values of our model parameters, together with the procedure that we followed in setting them, indicating relevant data from the literature where ever possible. The resulting uniform initial condition for each variant, before stimulation, is also given.

Combinations of parameters which determine the uniform steady-state response of the amplification module at fixed $\gamma$ (Eqs. M1-M5 of Table 2.3), as depicted by the solid curves in Fig. 3.2 of Sec. 3.3, were set first. Here we list them, together with considerations that suggest their approximate values. Their specific values are given in the tables below. The meanings of individual parameters are given in Table 2.4 of the main text.

$\zeta_{PITP}$, $\zeta_{3/PITP}$, $\zeta_3/\chi_3\kappa_3$ ($\ll 1$): These are ratios of unregulated to regulated $PIP_3$ production. They are set to be small so that a large increase in $PIP_3$ production occurs upon cellular stimulation (139). The following observations suggest that constitutive production plays a role secondary to that regulated by the molecules considered in our model: in permeabilized neutrophils there is a ~10X increase in stimulated $PIP_3$ production when PITP and PI3K$\gamma$ are added (153); in HL60 cells treated with the Rho GTPase inhibitor, *Clostridium difficile* toxin B, translocation of 3'PI specific PH domains is not observed (102).

$\zeta_2/\lambda_2\zeta_{2/T}$ ($\ll 1$): This ratio determines the concentration of $PI(3,4)P_2$ on the membrane in the absence of $PIP_3$ and PTEN. As above, this is set to be small so that there is only a low level of $PI(3,4)P_2$ generated by unregulated processes, allowing for a large increase upon cellular stimulation (139).

$\zeta_T + \chi_T/A_{cell}\lambda_T$ (~0.01): This is the scaled concentration at which PI3K begins to affect PTEN concentration on the membrane. For PI3K-mediated inactivation of PTEN to contribute to feedback-enhanced $PIP_3$ production upon cellular stimulation, this quantity should be set equal to or smaller than the scaled concentration of membrane-associated PI3K in the unstimulated cell. The baseline fraction of PI3K on the membrane was set to be a few percent, as most PI3K$\gamma$ is cytosolic in resting neutrophils (153).

$\kappa_3$ (~0.05 - 0.1): Amount/fraction of PI3K on the membrane that begins to saturate available PITP. This should be of the same order, or greater than, the scaled PI3K concentration on the membrane in a stimulated cell, if the feedback in **Loop I** is to be effective. Since PI3K translocation seems to parallel $PIP_3$ production upon cellular stimulation, we expect the peak membrane-bound fraction PI3K to be on the order of 5-10X baseline, or on the order of 10% of the total PI3K (132, 140).

$(1 - A_{cell}\boldsymbol{T^*}_{t=0})\chi_T/A_{cell}\lambda_T\zeta_{3/T}$, $(1 - A_{cell}\boldsymbol{T^*}_{t=0})\chi_T/A_{cell}\lambda_T\zeta_{2/T}$ (~0.03 - 0.1): Scaled PI3K concentrations at which action of PTEN on $PIP_3$ and $PI(3,4)P_2$ is substantially inhibited,

respectively. These quantities should be greater than the scaled baseline PI3K concentration on the membrane for PI3K inactivation of PTEN to enhance the effects of **Loop II**. $(1-A_{cell}\boldsymbol{T^*}_{t=0})\chi_T/A_{cell}\lambda_T\zeta_{2/T}$ should be greater than $(1-A_{cell}\boldsymbol{T^*}_{t=0})\chi_T/A_{cell}\lambda_T\zeta_{3/T}$, as well. This means that in our model, PI3K affects the action of PTEN on PI(3,4)P$_2$ over a larger range of concentration than on PIP$_3$; indeed, there is evidence to suggest that PTEN action on PI(3,4)P$_2$ might be more important than on PIP$_3$ (140).

$\lambda_3\zeta_{3/T}/\lambda_2\zeta_{2/T}$ (~5 - 10): Ratio of rates of PTEN independent dephosphorylation of PIP$_3$ to PTEN independent dephosphorylation of PI(3,4)P$_2$. This quantity should be large to account for the observation that in Dictyostelium, if PTEN is knocked out, PIP$_3$ is degraded almost normally while PH domains translocation is prolonged upon uniform stimulation. This suggests that degradation of another 3'PI besides PIP$_3$ (probably PI(3,4)P$_2$) has been perturbed in these cells, and that PTEN is essential for degradation of PI(3,4)P$_2$ (140); i.e. that the actions of phosphatases other than PTEN on PIP$_3$ are more important than they are on PI(3,4)P$_2$.

$\chi_3\kappa_3/\lambda_3\zeta_{3/T}$ (>1): Sets the strength of **Loop I**. This quantity can be interpreted as the ratio of rates of PIP$_3$ production to degradation in the stimulated cell. It should be set such that the feedback in **Loop I** becomes activated at scaled PI3K concentrations a little above the baseline state of the cell.

$\kappa_K$ (~1-5): $\boldsymbol{P_n}$ at which 3'PI inhibition of PI3K return to the cytosol becomes significant. This quantity controls the effectiveness of **Loop II** and should be of order 1 if **Loops I** and **II** are to be activated simultaneously upon cellular stimulation. This was adjusted to control the amount of non-linearity in response amplification in defining our model variants. Smaller $\kappa_K$ means more non-linearity in amplification.

$\gamma_0$ (~0.01): This quantity is equal to $\boldsymbol{K_m}/\left(1+\boldsymbol{P_n}/\kappa_K\right)$ in the uniform, unstimulated cell, and sets the baseline state. It should be of order 0.01 if only a few percent of total PI3K is to be membrane bound in the resting cell. Larger $\gamma_0$ means more PI3K, and hence more 3'PI, on the membrane in the unstimulated cell.

To analyze the 'fixed average' response of the amplification module (long-dashed curves in Fig. 3.2 of the main text), we further specified the following quantities:

$A_{cell}\boldsymbol{K^*}_{t=0}$ (~0.5): A higher fraction of phosphorylated PI3K results in faster adaptation dynamics for a given set of values for other parameters. $\boldsymbol{K_c^*}$ increases as the cell adapts to a uniform stimulus. We were not able to find good estimates of the faction of PI3K that is phosphorylated in resting cells of the types considered, and chose a value intermediate between 0 and 1 for our simulations. This quantity was not chosen too close to 1, so that depletion of cytoplasmic PI3K would not be very significant upon cellular stimulation.

$A_{cell}\boldsymbol{T^*}_{t=0}$ (~0.5): The fraction of phosphorylated PTEN in resting cells could not be set too high, in order to achieve ~5-10% of PTEN on the membrane (137) for the chosen values of other parameters. As with PI3K, we could not find good estimates of the fraction of phosphorylated PTEN in resting cells of the types considered, and chose a value intermediate between 0 and 1 for our simulations.

$\left(\chi_T/A_{cell}\lambda_T\right)/\left(\chi_T/A_{cell}\lambda_T+\zeta_T\right)$ (~0.5 - 1.0): This is the fraction of unphosphorylated PTEN that would be on the membrane in the absence of PI3K. Since other parameters are set such that PI3K already inhibits a substantial amount of PTEN from binding to the membrane, this quantity should be set close to 1.

$\kappa_c$ (~1 - 10): This parameter sets the scaled 3'PI concentration at which cytosolic depletion begins to saturate the amplification that results from activating **Loop I** upon cellular stimulation. We adjusted $\kappa_c$, in defining our model variants, to control the importance of translocating molecules in amplifying responses to gradients. Larger $\kappa_c$ (smaller $1/\kappa_c$) means that translocating molecules are less important in response amplification for typical $P_n$ values.

Based on the above considerations, we chose values for the above mentioned quantities, as given in Tables B.1 and B.2, below.

**Table B.1. Quantities that are the same for all model variants**

| Quantity | Value | Quantity | Value |
|---|---|---|---|
| $\zeta_{PITP}$ | 0.025 | $(1 - A_{cell}T^*_{t=0})\chi_T/A_{cell}\lambda_T\zeta_{3/T}$ | 0.03 |
| $\zeta_{3/PITP}$ | 0.025 | $(1 - A_{cell}T^*_{t=0})\chi_T/A_{cell}\lambda_T\zeta_{2/T}$ | 0.08 |
| $\zeta_3/\chi_3\kappa_3$ | 0.05 | $\lambda_3\zeta_{3/T}/\lambda_2\zeta_{2/T}$ | 5.0 |
| $\zeta_2/\lambda_2\zeta_{2/T}$ | 0.05 | $\chi_3\kappa_3/\lambda_3\zeta_{3/T}$ | 3.0 |
| $\zeta_T + \chi_T/A_{cell}\lambda_T$ | 0.01 | $A_{cell}K_c^*_{t=0}$ | 0.5 |
| $\kappa_3$ | 0.05 | $A_{cell}T_c^*_{t=0}$ | 0.5 |
| | | $(\chi_T/A_{cell}\lambda_T)/(\chi_T/A_{cell}\lambda_T + \zeta_T)$ | 0.8 |

**Table B.2. Parameters which define the model variants**

| Parameter | Case 1 | Case 2 | Case 3 | Case 4 |
|---|---|---|---|---|
| $\kappa_K$ | 1.3 | 5.5 | 0.95 | 4.0 |
| $\kappa_c$ | 6.7 | 1.38 | 5.0 | 1.25 |
| $\gamma_0$ | 0.014 | 0.037 | 0.011 | 0.028 |

Specifying the quantities in Tables B.1 and B.2 sets the initial values for our model variables in the uniform, unstimulated cell. These are given in Table B.3.

**Table B.3. Steady-state, uniform profile for each variant before stimulation**

| Variable | Case 1 | Case 2 | Case 3 | Case 4 |
|---|---|---|---|---|
| $P_3$ | 0.38 | 1.16 | 0.19 | 0.85 |
| $P_2$ | 0.60 | 2.82 | 0.25 | 1.78 |
| $P_n$ ($=P_3+P_2$) | 0.98 | 4.0 | 0.44 | 2.63 |
| $K_m$ | 0.025 | 0.064 | 0.016 | 0.046 |
| $T_m$ | 0.1 | 0.054 | 0.15 | 0.071 |
| $A_{cell}K_c^*$ | 0.50 | 0.50 | 0.50 | 0.50 |
| $A_{cell}T_c^*$ | 0.50 | 0.50 | 0.50 | 0.50 |

Tables B.2 and B.3 were given in the main text as Tables 2.6 and 2.6 respectively.

Finally, several dynamic parameters were set. These parameters were set to the same value for all model variants, and are given in Table B.4, together with considerations in setting them.

**Table B.4. Remaining dynamic parameters**

| Parameter | Value | Considerations in setting |
|---|---|---|
| $\lambda_3$ | 15.0 | $\lambda_3(T_m + \zeta_{3/T})$ gives the rate constant for PIP$_3$ degradation, which should be > 1 $s^{-1}$ so that transient PIP$_3$ production and PI3K translocation to the membrane happen almost simultaneously in response to uniform stimuli (132), and in order to stabilize polarized responses against diffusion. $\lambda_3$ adjusts the diffusion length in our model (see 'Model Characterization' in the main text). |
| $\lambda_K \kappa_K$ | 4.0 | $\lambda_K$ sets the adaptation time in response to uniform step stimuli. This was set empirically (as our system is highly non-linear) to give typical time courses seen in Dictyostelium, with adaptation times on the order of ~25 $s$ (132). |
| $\lambda_T$ | 30.0 | $\lambda_T(K_m + \zeta_T)$ gives the rate constant for PTEN removal from the membrane, which should also be > 1 $s^{-1}$ so that transient PTEN translocation from the membrane follows PI3K translocation to the membrane in response to uniform stimuli, with a slight lag (132) |
| $\kappa_{K*}$ | 0.013 | << $K_c*$ for perfect adaptation (see main text). |
| $D$ | 0.003 | This corresponds to a diffusion coefficient of ~2 $\mu m^2/s$ in a cell of radius of ~4 $\mu m$. This is higher than some measured values (52) by a factor of approximately 2, because we have only considered 1-D diffusion rather than 2-D. |

The above quantities specify the complete set of parameter values for our model, which are given in Table B.5.

**Table B.5. Model parameters**

| Parameter | Case 1 | Case 2 | Case 3 | Case 4 |
|---|---|---|---|---|
| $\chi_3$ | 120.0 | 120.0 | 120.0 | 120.0 |
| $\kappa_m$ | 1.18 | 3.64 | 1.25 | 5.0 |
| $\kappa_c$ | 6.7 | 1.38 | 5.0 | 1.25 |
| $\zeta_{PITP}$ | 0.025 | 0.025 | 0.025 | 0.025 |
| $\kappa_3$ | 0.05 | 0.05 | 0.05 | 0.05 |
| $\zeta_{3/PITP}$ | 0.025 | 0.025 | 0.025 | 0.025 |
| $\zeta_3$ | 0.3 | 0.3 | 0.3 | 0.3 |
| $\lambda_3$ | 15.0 | 15.0 | 15.0 | 15.0 |
| $\zeta_{3/T}$ | 0.13 | 0.13 | 0.13 | 0.13 |
| $\zeta_2$ | 0.02 | 0.02 | 0.02 | 0.02 |
| $\lambda_2$ | 8.0 | 8.0 | 8.0 | 8.0 |
| $\zeta_{2/T}$ | 0.05 | 0.05 | 0.05 | 0.05 |
| $\chi_K$ | 0.0074 | 0.0049 | 0.0076 | 0.005 |
| $\lambda_K$ | 3.2 | 0.73 | 4.2 | 1.0 |
| $\kappa_K$ | 1.3 | 5.5 | 0.95 | 4.0 |
| $\chi_T$ | 0.019 | 0.019 | 0.019 | 0.019 |
| $\lambda_T$ | 30.0 | 30.0 | 30.0 | 30.0 |
| $\zeta_T$ | 0.002 | 0.002 | 0.002 | 0.002 |
| $\lambda_{T*}$ | 0.17 | 0.21 | 0.15 | 0.20 |
| $\lambda_{K*}$ | 0.55 | 0.34 | 0.58 | 0.35 |
| $\kappa_{K*}$ | 0.013 | 0.013 | 0.013 | 0.013 |

$D = 0.003$

## Appendix C: Equivalence of stability criteria in the full and 'reduced' models

Here we demonstrate the equivalence of stability conditions for uniforms steady-state solutions to the equations of the 'full' (Eq. M.1-M.6 of Table 2.3) and the equations of the 'reduced' model, where other model variables are set to steady-state values with respect to the variables, $P_n$ and $\gamma$. This appendix makes use of the terms and equations developed in Secs. 3.3.3 and 3.4.2.

The condition for a uniform solution of the 'full' model to be linearly unstable to a perturbation of wave number $j$ is that there exists a solution to Eqs. 3.9' – 3.14' with $\sigma_j > 0$ (see main text, Sec. 3.4.2). The corresponding eigenvector can be used to find a perturbation with positive linear growth in the 'reduced' model, where we replace $\sigma$ by 0 in Eqs. 3.10' – 3.13'. To see this, consider a solution to Eqs. 3.9' – 3.14' with positive growth rate for the full model, which we represent by the vector

$\bar{U}_{j,f} = \left( \hat{P}_{n,j,f}, \hat{P}_{2,j,f}, \hat{K}_{m,j,f}, \hat{T}_{m,j,f}, \delta_{0,j}\hat{T}_{c,f}, \delta_{0,j}\hat{\gamma}_f \right)$, where the subscript, '$f$' denotes the 'full' model. Of course, $\hat{\gamma}_f = 0$ in accordance with Eq. 3.14'. We denote the positive linear growth rate of this solution by $\sigma_{j,f}$. Now, fix $\hat{P}_{n,j,f}$ and solve Eq. 3.10' – 3.13' with $\sigma_j = 0$. We can denote this solution as $\bar{U}_{j,r} = \left( \hat{P}_{n,j,f}, \hat{P}_{2,j,r}, \hat{K}_{m,j,r}, \hat{T}_{m,0,r}, \delta_{0,j}\hat{T}_{c,r}, 0 \right)$ up to normalization; the subscript '$r$' is used because we will see that this is a solution with positive growth rate for the 'reduced' model. From Eqs. 3.10' – 3.13' it is clear that such a solution exists and that the following relationships hold:

$$\hat{P}_{2,j,r} > \hat{P}_{2,j,f}; \ \hat{K}_{m,j,r} > \hat{K}_{m,j,f}; \ \hat{T}_{m,j,r} > \hat{T}_{m,0,f}; \ \hat{T}_{c,r} > \hat{T}_{c,f} \tag{C.1}$$

Thus, the RHS of Eq. 3.9' will be larger for the 'reduced' model solution than for the 'full'

model solution, and $\bar{U}_{j,r}$ is an eigenvector for the 'reduced' system, with $\sigma_{j,r} > \sigma_{j,f}$. Therefore, instability in the 'full' model implies instability in the 'reduced' model.

The procedure outlined above can be inverted to obtain a solution for a growing perturbation in the 'full' model from a solution for a growing perturbation in the 'reduced' model. If such a solution exists, fix $\hat{P}_{n,j,r}$. Now we can continuously increase a trial growth rate, $\sigma_{j,f}*$, from 0 to $\sigma_{j,r}$. For each $\sigma_{j,f}*$, at fixed $\hat{P}_{n,j,r}$, we solve Eqs. 3.10' – 3.13' (replacing $\sigma_j$ by $\sigma_{j,f}*$) for the other components of the perturbation. As above, these are necessarily smaller than the components for the 'reduced' model, though their signs are the same. If we plug these components back Eq. 3.9', the RHS becomes smaller as well, but its sign is maintained. Then we can solve for a new growth rate in Eq. 3.9' ($\hat{P}_{n,j,r}$ is still fixed), which we denote $\sigma_{j,r}*$, and the relationship $\sigma_{j,r}* < \sigma_{j,r}$ must hold. This procedure can be iterated by continuously increasing $\sigma_{j,f}*$, and calculating a new $\sigma_{j,r}*$, which should be smaller than the previous value. The iteration is continued until $\sigma_{j,r}* = \sigma_{j,f}*$. At this point the growth rate, in the 'full' model, of a solution to Eqs. 3.9' – 3.14', has been found as $\sigma_{j,r}* = \sigma_{j,f}* = \sigma_{j,f}$. By construction, $\sigma_{j,f} \in (0, \sigma_{j,r})$ and should exist because solutions of Eqs. 3.9' – 3.14' vary smoothly with $\sigma_j$ over this range, and they maintain their sign. Thus, instability in the 'reduced' model implies instability in the 'full' model, and we conclude that stability conditions for both models are equivalent.

# References

1.  Segall, J. E., Block, S. M. & Berg, H. C. 1986. Temporal comparisons in bacterial chemotaxis. *Proc Natl Acad Sci U S A* 83(23):8987-91.

2.  Block, S. M., Segall, J. E. & Berg, H. C. 1983. Adaptation kinetics in bacterial chemotaxis. *J Bacteriol* 154(1):312-23.

3.  Berg, H. C. 1975. Chemotaxis in bacteria. *Annu Rev Biophys Bioeng* 4(00):119-36.

4.  Iijima, M., Huang, Y. E. & Devreotes, P. 2002. Temporal and spatial regulation of chemotaxis. *Dev Cell* 3(4):469-78.

5.  Devreotes, P. & Janetopoulos, C. 2003. Eukaryotic chemotaxis: distinctions between directional sensing and polarization. *J Biol Chem* 278(23):20445-8.

6.  Parent, C. A. & Devreotes, P. N. 1999. A cell's sense of direction. *Science* 284(5415):765-70.

7.  Sarawar, S. R., Lee, B. J., Anderson, M., Teng, Y. C., Zuberi, R. & Von Gesjen, S. 2002. Chemokine induction and leukocyte trafficking to the lungs during murine gammaherpesvirus 68 (MHV-68) infection. *Virology* 293(1):54-62.

8.  Olson, T. S. & Ley, K. 2002. Chemokines and chemokine receptors in leukocyte trafficking. *Am J Physiol Regul Integr Comp Physiol* 283(1):R7-28.

9.  Wagle, M. A. & Tranquillo, R. T. 2000. A self-consistent cell flux expression for simultaneous chemotaxis and contact guidance in tissues. *J Math Biol* 41(4):315-30.

10. Gillitzer, R. & Goebeler, M. 2001. Chemokines in cutaneous wound healing. *J Leukoc Biol* 69(4):513-21.

11. Giniger, E. 2002. How do Rho family GTPases direct axon growth and guidance? A proposal relating signaling pathways to growth cone mechanics. *Differentiation* 70(8):385-96.

12. Isbister, C. M., Mackenzie, P. J., To, K. C. & O'Connor, T. P. 2003. Gradient steepness influences the pathfinding decisions of neuronal growth cones in vivo. *J Neurosci* 23(1):193-202.

13. Zeller, P. J., Skalak, T. C., Ponce, A. M. & Price, R. J. 2001. In vivo chemotactic properties and spatial expression of PDGF in developing mesenteric microvascular networks. *Am J Physiol Heart Circ Physiol* 280(5):H2116-25.

14.     Yang, X., Dormann, D., Munsterberg, A. E. & Weijer, C. J. 2002. Cell movement patterns during gastrulation in the chick are controlled by positive and negative chemotaxis mediated by FGF4 and FGF8. *Dev Cell* 3(3):425-37.

15.     Firtel, R. A. & Meili, R. 2000. Dictyostelium: a model for regulated cell movement during morphogenesis. *Curr Opin Genet Dev* 10(4):421-7.

16.     Thrasher, A. J. 2002. WASp in immune-system organization and function. *Nat Rev Immunol* 2(9):635-46.

17.     Capogrosso Sansone, B., Scalerandi, M. & Condat, C. A. 2001. Emergence of taxis and synergy in angiogenesis. *Phys Rev Lett* 87(12):128102.

18.     Kassis, J., Lauffenburger, D. A., Turner, T. & Wells, A. 2001. Tumor invasion as dysregulated cell motility. *Semin Cancer Biol* 11(2):105-17.

19.     Wang, W., Wyckoff, J. B., Frohlich, V. C., Oleynikov, Y., Huttelmaier, S., Zavadil, J., Cermak, L., Bottinger, E. P., Singer, R. H., White, J. G., Segall, J. E. & Condeelis, J. S. 2002. Single cell behavior in metastatic primary mammary tumors correlated with gene expression patterns revealed by molecular profiling. *Cancer Res* 62(21):6278-88.

20.     Wang, W., Wyckoff, J. B., Wang, Y., Bottinger, E. P., Segall, J. E. & Condeelis, J. S. 2003. Gene expression analysis on small numbers of invasive cells collected by chemotaxis from primary mammary tumors of the mouse. *BMC Biotechnol* 3(1):13.

21.     Tranquillo, R. T., Lauffenburger, D. A. & Zigmond, S. H. 1988. A stochastic model for leukocyte random motility and chemotaxis based on receptor binding fluctuations. *J Cell Biol* 106(2):303-9.

22.     Alt, W. 1980. Biased random walk models for chemotaxis and related diffusion approximations. *J Math Biol* 9(2):147-77.

23.     Nossal, R. & Zigmond, S. H. 1976. Chemotropism indices for polymorphonuclear leukocytes. *Biophys J* 16(10):1171-82.

24.     Zigmond, S. H., Levitsky, H. I. & Kreel, B. J. 1981. Cell polarity: an examination of its behavioral expression and its consequences for polymorphonuclear leukocyte chemotaxis. *J Cell Biol* 89(3):585-92.

25.     Fisher, P. R., Merkl, R. & Gerisch, G. 1989. Quantitative analysis of cell motility and chemotaxis in Dictyostelium discoideum by using an image processing system and a novel chemotaxis chamber providing stationary chemical gradients. *J Cell Biol* 108(3):973-84.

26. Maheshwari, G. & Lauffenburger, D. A. 1998. Deconstructing (and reconstructing) cell migration. *Microsc Res Tech* 43(5):358-68.

27. Alt, W. & Hoffmann, G. (1990) *Biological motion : proceedings of a workshop held in Königswinter, Germany, March 16-19, 1989* (Springer-Verlag, Berlin ; New York).

28. Alberts, B., Johnson, A., Lewis, J., Raff, M., Roberts, K. & Walter, P. (2002) *Molecular biology of the cell* (Garland Science, New York, NY).

29. Weiner, O. D., Servant, G., Welch, M. D., Mitchison, T. J., Sedat, J. W. & Bourne, H. R. 1999. Spatial control of actin polymerization during neutrophil chemotaxis. *Nat Cell Biol* 1(2):75-81.

30. Zhelev, D. V. & Alteraifi, A. 2002. Signaling in the motility responses of the human neutrophil. *Ann Biomed Eng* 30(3):356-70.

31. Servant, G., Weiner, O. D., Neptune, E. R., Sedat, J. W. & Bourne, H. R. 1999. Dynamics of a chemoattractant receptor in living neutrophils during chemotaxis. *Mol Biol Cell* 10(4):1163-78.

32. Servant, G., Weiner, O. D., Herzmark, P., Balla, T., Sedat, J. W. & Bourne, H. R. 2000. Polarization of chemoattractant receptor signaling during neutrophil chemotaxis. *Science* 287(5455):1037-40.

33. Balla, T., Bondeva, T. & Varnai, P. 2000. How accurately can we image inositol lipids in living cells? *Trends Pharmacol Sci* 21(7):238-41.

34. Meyer, T. & Teruel, M. N. 2003. Fluorescence imaging of signaling networks. *Trends Cell Biol* 13(2):101-6.

35. Kimmel, A. R. & Firtel, R. A. 2004. Breaking symmetries: regulation of Dictyostelium development through chemoattractant and morphogen signal-response. *Curr Opin Genet Dev* 14(5):540-9.

36. Firtel, R. A., van Haastert, P. J., Kimmel, A. R. & Devreotes, P. N. 1989. G protein linked signal transduction pathways in development: dictyostelium as an experimental system. *Cell* 58(2):235-9.

37. Soderbom, F. & Loomis, W. F. 1998. Cell-cell signaling during Dictyostelium development. *Trends Microbiol* 6(10):402-6.

38. Loomis, W. F. 1996. Genetic networks that regulate development in Dictyostelium cells. *Microbiol Rev* 60(1):135-50.

39.     Levine, H., Aranson, I., Tsimring, L. & Truong, T. V. 1996. Positive genetic feedback governs cAMP spiral wave formation in Dictyostelium. *Proc Natl Acad Sci U S A* 93(13):6382-6.

40.     Levine, H. 1994. Modeling spatial patterns in Dictyostelium. *Chaos* 4(3):563-568.

41.     Palsson, E. & Othmer, H. G. 2000. A model for individual and collective cell movement in Dictyostelium discoideum. *Proc Natl Acad Sci U S A* 97(19):10448-53.

42.     Levine, H. & Reynolds, W. 1991. Streaming instability of aggregating slime mold amoebae. *Physical Review Letters* 66(18):2400-2403.

43.     Dallon, J. C. & Othmer, H. G. 1998. A continuum analysis of the chemotactic signal seen by Dictyostelium discoideum. *J Theor Biol* 194(4):461-83.

44.     Falcke, M. & Levine, H. 1998. Pattern selection by gene expression in Dictyostelium discoidium. *Physical Review Letters* 80(17):3875-3878.

45.     Levine, H., Tsimring, L. & Kessler, D. 1997. COmputational modeling of mound development in Dictyostelium. *Physica D* 106:375-388.

46.     Parent, C. A., Johns HOpkins University School of Medicine).

47.     van Es, S. & Devreotes, P. N. 1999. Molecular basis of localized responses during chemotaxis in amoebae and leukocytes. *Cell Mol Life Sci* 55(10):1341-51.

48.     Manahan, C. L., Iglesias, P. A., Long, Y. & Devreotes, P. N. 2004. Chemoattractant signaling in dictyostelium discoideum. *Annu Rev Cell Dev Biol* 20:223-53.

49.     Haugh, J. M., Codazzi, F., Teruel, M. & Meyer, T. 2000. Spatial sensing in fibroblasts mediated by 3' phosphoinositides. *J Cell Biol* 151(6):1269-80.

50.     Rosoff, W. J., Urbach, J. S., Esrick, M. A., McAllister, R. G., Richards, L. J. & Goodhill, G. J. 2004. A new chemotaxis assay shows the extreme sensitivity of axons to molecular gradients. *Nat Neurosci* 7(6):678-82.

51.     Haugh, J. M. & Schneider, I. C. 2004. Spatial analysis of 3' phosphoinositide signaling in living fibroblasts: I. Uniform stimulation model and bounds on dimensionless groups. *Biophys J* 86(1 Pt 1):589-98.

52.     Schneider, I. C. & Haugh, J. M. 2004. Spatial analysis of 3' phosphoinositide signaling in living fibroblasts: II. Parameter estimates for individual cells from experiments. *Biophys J* 86(1 Pt 1):599-608.

53. Pierini, L. M., Lawson, M. A., Eddy, R. J., Hendey, B. & Maxfield, F. R. 2000. Oriented endocytic recycling of alpha5beta1 in motile neutrophils. *Blood* 95(8):2471-80.

54. Eddy, R. J., Pierini, L. M. & Maxfield, F. R. 2002. Microtubule Asymmetry during Neutrophil Polarization and Migration. *Mol Biol Cell* 13(12):4470-83.

55. Bretscher, M. S. & Aguado-Velasco, C. 1998. EGF induces recycling membrane to form ruffles. *Curr Biol* 8(12):721-4.

56. Svitkina, T. M., Bulanova, E. A., Chaga, O. Y., Vignjevic, D. M., Kojima, S., Vasiliev, J. M. & Borisy, G. G. 2003. Mechanism of filopodia initiation by reorganization of a dendritic network. *J Cell Biol* 160(3):409-21.

57. Kaverina, I., Krylyshkina, O., Gimona, M., Beningo, K., Wang, Y. L. & Small, J. V. 2000. Enforced polarisation and locomotion of fibroblasts lacking microtubules. *Curr Biol* 10(12):739-42.

58. Kaverina, I., Krylyshkina, O. & Small, J. V. 2002. Regulation of substrate adhesion dynamics during cell motility. *Int J Biochem Cell Biol* 34(7):746-61.

59. Wiseman, P. W., Brown, C. M., Webb, D. J., Hebert, B., Johnson, N. L., Squier, J. A., Ellisman, M. H. & Horwitz, A. F. 2004. Spatial mapping of integrin interactions and dynamics during cell migration by image correlation microscopy. *J Cell Sci* 117(Pt 23):5521-34.

60. Clow, P. A. & McNally, J. G. 1999. In vivo observations of myosin II dynamics support a role in rear retraction. *Mol Biol Cell* 10(5):1309-23.

61. Chebotareva, N. A., Kurganov, B. I. & Livanova, N. B. 2004. Biochemical effects of molecular crowding. *Biochemistry (Mosc)* 69(11):1239-51.

62. Hall, D. & Minton, A. P. 2003. Macromolecular crowding: qualitative and semiquantitative successes, quantitative challenges. *Biochim Biophys Acta* 1649(2):127-39.

63. Small, J. V., Stradal, T., Vignal, E. & Rottner, K. 2002. The lamellipodium: where motility begins. *Trends Cell Biol* 12(3):112-20.

64. Mogilner, A. & Edelstein-Keshet, L. 2002. Regulation of actin dynamics in rapidly moving cells: a quantitative analysis. *Biophys J* 83(3):1237-58.

65. Mogilner, A. & Oster, G. 2003. Force Generation by Actin Polymerization II: The Elastic Ratchet and Tethered Filaments. *Biophys J* 84(3):1591-605.

66. Chung, C. Y., Funamoto, S. & Firtel, R. A. 2001. Signaling pathways controlling cell polarity and chemotaxis. *Trends Biochem Sci* 26(9):557-66.

67. Xu, J., Wang, F., Van Keymeulen, A., Herzmark, P., Straight, A., Kelly, K., Takuwa, Y., Sugimoto, N., Mitchison, T. & Bourne, H. R. 2003. Divergent signals and cytoskeletal assemblies regulate self-organizing polarity in neutrophils. *Cell* 114(2):201-14.

68. Janmey, P. A. & Weitz, D. A. 2004. Dealing with mechanics: mechanisms of force transduction in cells. *Trends Biochem Sci* 29(7):364-70.

69. Janmey, P. A. 1998. The cytoskeleton and cell signaling: component localization and mechanical coupling. *Physiol Rev* 78(3):763-81.

70. Bretscher, M. S. & Aguado-Velasco, C. 1998. Membrane traffic during cell locomotion. *Curr Opin Cell Biol* 10(4):537-41.

71. Seveau, S., Eddy, R. J., Maxfield, F. R. & Pierini, L. M. 2001. Cytoskeleton-dependent membrane domain segregation during neutrophil polarization. *Mol Biol Cell* 12(11):3550-62.

72. Pierini, L. M., Eddy, R. J., Fuortes, M., Seveau, S., Casulo, C. & Maxfield, F. R. 2003. Membrane lipid organization is critical for human neutrophil polarization. *J Biol Chem*.

73. Aguado-Velasco, C. & Bretscher, M. S. 1999. Circulation of the plasma membrane in Dictyostelium. *Mol Biol Cell* 10(12):4419-27.

74. Wessels, D., Reynolds, J., Johnson, O., Voss, E., Burns, R., Daniels, K., Garrard, E., O'Halloran, T. J. & Soll, D. R. 2000. Clathrin plays a novel role in the regulation of cell polarity, pseudopod formation, uropod stability and motility in Dictyostelium. *J Cell Sci* 113 ( Pt 1):21-36.

75. Small, J. V., Geiger, B., Kaverina, I. & Bershadsky, A. 2002. How do microtubules guide migrating cells? *Nat Rev Mol Cell Biol* 3(12):957-64.

76. Wehrle-Haller, B. & Imhof, B. A. 2003. Actin, microtubules and focal adhesion dynamics during cell migration. *Int J Biochem Cell Biol* 35(1):39-50.

77. Alenghat, F. J. & Ingber, D. E. 2002. Mechanotransduction: all signals point to cytoskeleton, matrix, and integrins. *Sci STKE* 2002(119):PE6.

78. Iglesias, P. A. & Levchenko, A. 2002. Modeling the cell's guidance system. *Sci STKE* 2002(148):RE12.

79. Parent, C. A., Blacklock, B. J., Froehlich, W. M., Murphy, D. B. & Devreotes, P. N. 1998. G protein signaling events are activated at the leading edge of chemotactic cells. *Cell* 95(1):81-91.

80. Bretschneider, T., Jonkman, J., Kohler, J., Medalia, O., Barisic, K., Weber, I., Stelzer, E. H., Baumeister, W. & Gerisch, G. 2002. Dynamic organization of the actin system in the motile cells of Dictyostelium. *J Muscle Res Cell Motil* 23(7-8):639-49.

81. Jin, T., Zhang, N., Long, Y., Parent, C. A. & Devreotes, P. N. 2000. Localization of the G protein betagamma complex in living cells during chemotaxis. *Science* 287(5455):1034-6.

82. Zigmond, S. H. 1977. Ability of polymorphonuclear leukocytes to orient in gradients of chemotactic factors. *J Cell Biol* 75(2 Pt 1):606-16.

83. Moghe, P. V. & Tranquillo, R. T. 1994. Stochastic model of chemoattractant receptor dynamics in leukocyte chemosensory movement. *Bull Math Biol* 56(6):1041-93.

84. Jordan, J. D., Landau, E. M. & Iyengar, R. 2000. Signaling networks: the origins of cellular multitasking. *Cell* 103(2):193-200.

85. Gilman, A. G., Simon, M. I., Bourne, H. R., Harris, B. A., Long, R., Ross, E. M., Stull, J. T., Taussig, R., Arkin, A. P., Cobb, M. H., Cyster, J. G., Devreotes, P. N., Ferrell, J. E., Fruman, D., Gold, M., Weiss, A., Berridge, M. J., Cantley, L. C., Catterall, W. A., Coughlin, S. R., Olson, E. N., Smith, T. F., Brugge, J. S., Botstein, D., Dixon, J. E., Hunter, T., Lefkowitz, R. J., Pawson, A. J., Sternberg, P. W., Varmus, H., Subramaniam, S., Sinkovits, R. S., Li, J., Mock, D., Ning, Y., Saunders, B., Sternweis, P. C., Hilgemann, D., Scheuermann, R. H., DeCamp, D., Hsueh, R., Lin, K. M., Ni, Y., Seaman, W. E., Simpson, P. C., O'Connell, T. D., Roach, T., Choi, S., Eversole-Cire, P., Fraser, I., Mumby, M. C., Zhao, Y., Brekken, D., Shu, H., Meyer, T., Chandy, G., Heo, W. D., Liou, J., O'Rourke, N., Verghese, M., Mumby, S. M., Han, H., Brown, H. A., Forrester, J. S., Ivanova, P., Milne, S. B., Casey, P. J., Harden, T. K., Doyle, J., Gray, M. L., Michnick, S., Schmidt, M. A., Toner, M., Tsien, R. Y., Natarajan, M., Ranganathan, R. & Sambrano, G. R. 2002. Overview of the Alliance for Cellular Signaling. *Nature* 420(6916):703-6.

86. McLaughlin, S., Wang, J., Gambhir, A. & Murray, D. 2002. PIP(2) and proteins: interactions, organization, and information flow. *Annu Rev Biophys Biomol Struct* 31:151-75.

87. Vanhaesebroeck, B., Leevers, S. J., Ahmadi, K., Timms, J., Katso, R., Driscoll, P. C., Woscholski, R., Parker, P. J. & Waterfield, M. D. 2001. Synthesis and function of 3-phosphorylated inositol lipids. *Annu Rev Biochem* 70:535-602.

88.    Gillooly, D. J. & Stenmark, H. 2001. Cell biology. A lipid oils the endocytosis machine. *Science* 291(5506):993-4.

89.    Simonsen, A., Wurmser, A. E., Emr, S. D. & Stenmark, H. 2001. The role of phosphoinositides in membrane transport. *Curr Opin Cell Biol* 13(4):485-92.

90.    Cockcroft, S. & De Matteis, M. A. 2001. Inositol lipids as spatial regulators of membrane traffic. *J Membr Biol* 180(3):187-94.

91.    Martin, T. F. 1998. Phosphoinositide lipids as signaling molecules: common themes for signal transduction, cytoskeletal regulation, and membrane trafficking. *Annu Rev Cell Dev Biol* 14:231-64.

92.    Leevers, S. J., Vanhaesebroeck, B. & Waterfield, M. D. 1999. Signalling through phosphoinositide 3-kinases: the lipids take centre stage. *Curr Opin Cell Biol* 11(2):219-25.

93.    Rameh, L. E. & Cantley, L. C. 1999. The role of phosphoinositide 3-kinase lipid products in cell function. *J Biol Chem* 274(13):8347-50.

94.    Wang, F., Herzmark, P., Weiner, O. D., Srinivasan, S., Servant, G. & Bourne, H. R. 2002. Lipid products of PI(3)Ks maintain persistent cell polarity and directed motility in neutrophils. *Nat Cell Biol* 4(7):513-8.

95.    Hurley, J. H., Tsujishita, Y. & Pearson, M. A. 2000. Floundering about at cell membranes: a structural view of phospholipid signaling. *Curr Opin Struct Biol* 10(6):737-43.

96.    Hurley, J. H. & Meyer, T. 2001. Subcellular targeting by membrane lipids. *Curr Opin Cell Biol* 13(2):146-52.

97.    Postma, M. & Van Haastert, P. J. 2001. A diffusion-translocation model for gradient sensing by chemotactic cells. *Biophys J* 81(3):1314-23.

98.    Yin, H. L. & Janmey, P. A. 2002. Phosphoinositide Regulation of the Actin Cytoskeleton. *Annu Rev Physiol*.

99.    Takei, K. & Haucke, V. 2001. Clathrin-mediated endocytosis: membrane factors pull the trigger. *Trends Cell Biol* 11(9):385-91.

100.   Divecha, N., Roefs, M., Halstead, J. R., D'Andrea, S., Fernandez-Borga, M., Oomen, L., Saqib, K. M., Wakelam, M. J. & D'Santos, C. 2000. Interaction of the type Ialpha PIPkinase with phospholipase D: a role for the local generation of phosphatidylinositol 4, 5-bisphosphate in the regulation of PLD2 activity. *Embo J* 19(20):5440-9.

101.   Kam, J. L., Miura, K., Jackson, T. R., Gruschus, J., Roller, P., Stauffer, S., Clark, J., Aneja, R. & Randazzo, P. A. 2000. Phosphoinositide-dependent activation of the ADP-ribosylation factor GTPase-activating protein ASAP1. Evidence for the pleckstrin homology domain functioning as an allosteric site. *J Biol Chem* 275(13):9653-63.

102.   Weiner, O. D., Neilsen, P. O., Prestwich, G. D., Kirschner, M. W., Cantley, L. C. & Bourne, H. R. 2002. A PtdInsP(3)- and Rho GTPase-mediated positive feedback loop regulates neutrophil polarity. *Nat Cell Biol* 4(7):509-13.

103.   Rickert, P., Weiner, O. D., Wang, F., Bourne, H. R. & Servant, G. 2000. Leukocytes navigate by compass: roles of PI3Kgamma and its lipid products. *Trends Cell Biol* 10(11):466-73.

104.   Weiner, O. D. 2002. Regulation of cell polarity during eukaryotic chemotaxis: the chemotactic compass. *Curr Opin Cell Biol* 14(2):196-202.

105.   Kitano, H. 2002. Computational systems biology. *Nature* 420(6912):206-10.

106.   Csete, M. E. & Doyle, J. C. 2002. Reverse engineering of biological complexity. *Science* 295(5560):1664-9.

107.   Arkin, A. P. 2001. Synthetic cell biology. *Curr Opin Biotechnol* 12(6):638-44.

108.   Lauffenburger, D. A. 2000. Cell signaling pathways as control modules: complexity for simplicity? *Proc Natl Acad Sci U S A* 97(10):5031-3.

109.   Wiley, H. S., Shvartsman, S. Y. & Lauffenburger, D. A. 2003. Computational modeling of the EGF-receptor system: a paradigm for systems biology. *Trends Cell Biol* 13(1):43-50.

110.   Asthagiri, A. R. & Lauffenburger, D. A. 2000. Bioengineering models of cell signaling. *Annu Rev Biomed Eng* 2:31-53.

111.   Niehrs, C. & Meinhardt, H. 2002. Modular feedback. *Nature* 417(6884):35-6.

112.   Hartwell, L. H., Hopfield, J. J., Leibler, S. & Murray, A. W. 1999. From molecular to modular cell biology. *Nature* 402(6761 Suppl):C47-52.

113.   Kussell, E., Kishony, R., Balaban, N. Q. & Leibler, S. 2005. Bacterial persistence: a model of survival in changing environments. *Genetics* 169(4):1807-14.

114.   Segre, D., Deluna, A., Church, G. M. & Kishony, R. 2005. Modular epistasis in yeast metabolism. *Nat Genet* 37(1):77-83.

115. Gierer, A. & Meinhardt, H. 1972. A theory of biological pattern formation. *Kybernetik* 12(1):30-9.

116. Meinhardt, H. & Gierer, A. 2000. Pattern formation by local self-activation and lateral inhibition. *Bioessays* 22(8):753-60.

117. Novak, B. & Tyson, J. J. 2004. A model for restriction point control of the mammalian cell cycle. *J Theor Biol* 230(4):563-79.

118. Sveiczer, A., Tyson, J. J. & Novak, B. 2004. Modelling the fission yeast cell cycle. *Brief Funct Genomic Proteomic* 2(4):298-307.

119. Von Dassow, G. & Odell, G. M. 2002. Design and constraints of the Drosophila segment polarity module: robust spatial patterning emerges from intertwined cell state switches. *J Exp Zool* 294(3):179-215.

120. Devreotes, P. N. & Zigmond, S. H. 1988. Chemotaxis in eukaryotic cells: a focus on leukocytes and Dictyostelium. *Annu Rev Cell Biol* 4:649-86.

121. Yi, T. M., Huang, Y., Simon, M. I. & Doyle, J. 2000. Robust perfect adaptation in bacterial chemotaxis through integral feedback control. *Proc Natl Acad Sci U S A* 97(9):4649-53.

122. Levchenko, A. & Iglesias, P. A. 2002. Models of eukaryotic gradient sensing: application to chemotaxis of amoebae and neutrophils. *Biophys J* 82(1 Pt 1):50-63.

123. Narang, A., Subramanian, K. K. & Lauffenburger, D. A. 2001. A mathematical model for chemoattractant gradient sensing based on receptor-regulated membrane phospholipid signaling dynamics. *Ann Biomed Eng* 29(8):677-91.

124. Janetopoulos, C., Ma, L., Devreotes, P. N. & Iglesias, P. A. 2004. Chemoattractant-induced phosphatidylinositol 3,4,5-trisphosphate accumulation is spatially amplified and adapts, independent of the actin cytoskeleton. *Proc Natl Acad Sci U S A* 101(24):8951-6.

125. Ruchira, Hink, M. A., Bosgraaf, L., van Haastert, P. J. & Visser, A. J. 2004. Pleckstrin homology domain diffusion in Dictyostelium cytoplasm studied using fluorescence correlation spectroscopy. *J Biol Chem* 279(11):10013-9.

126. Ueda, M., Sako, Y., Tanaka, T., Devreotes, P. & Yanagida, T. 2001. Single-molecule analysis of chemotactic signaling in Dictyostelium cells. *Science* 294(5543):864-7.

127. Rappel, W. J., Thomas, P. J., Levine, H. & Loomis, W. F. 2002. Establishing direction during chemotaxis in eukaryotic cells. *Biophys J* 83(3):1361-7.

128. Potma, E. O., de Boeij, W. P., Bosgraaf, L., Roelofs, J., van Haastert, P. J. & Wiersma, D. A. 2001. Reduced protein diffusion rate by cytoskeleton in vegetative and polarized dictyostelium cells. *Biophys J* 81(4):2010-9.

129. Seksek, O., Biwersi, J. & Verkman, A. S. 1997. Translational diffusion of macromolecule-sized solutes in cytoplasm and nucleus. *J Cell Biol* 138(1):131-42.

130. Braga, J., Desterro, J. M. & Carmo-Fonseca, M. 2004. Intracellular macromolecular mobility measured by fluorescence recovery after photobleaching with confocal laser scanning microscopes. *Mol Biol Cell* 15(10):4749-60.

131. Langer, J. S. 1987. Dendritic sidebranching in the three-dimensional symmetric model in the presence of noise. *Physical Review. A* 36(7):3350-3358.

132. Funamoto, S., Meili, R., Lee, S., Parry, L. & Firtel, R. A. 2002. Spatial and temporal regulation of 3-phosphoinositides by PI 3-kinase and PTEN mediates chemotaxis. *Cell* 109(5):611-23.

133. Brock, C., Schaefer, M., Reusch, H. P., Czupalla, C., Michalke, M., Spicher, K., Schultz, G. & Nurnberg, B. 2003. Roles of G beta gamma in membrane recruitment and activation of p110 gamma/p101 phosphoinositide 3-kinase gamma. *J Cell Biol* 160(1):89-99.

134. Ali, H., Richardson, R. M., Tomhave, E. D., Didsbury, J. R. & Snyderman, R. 1993. Differences in phosphorylation of formylpeptide and C5a chemoattractant receptors correlate with differences in desensitization. *J Biol Chem* 268(32):24247-54.

135. Xiao, Z., Yao, Y., Long, Y. & Devreotes, P. 1999. Desensitization of G-protein-coupled receptors. agonist-induced phosphorylation of the chemoattractant receptor cAR1 lowers its intrinsic affinity for cAMP. *J Biol Chem* 274(3):1440-8.

136. Janetopoulos, C., Jin, T. & Devreotes, P. 2001. Receptor-mediated activation of heterotrimeric G-proteins in living cells. *Science* 291(5512):2408-11.

137. Iijima, M. & Devreotes, P. 2002. Tumor suppressor PTEN mediates sensing of chemoattractant gradients. *Cell* 109(5):599-610.

138. Backers, K., Blero, D., Paternotte, N., Zhang, J. & Erneux, C. 2003. The termination of PI3K signalling by SHIP1 and SHIP2 inositol 5-phosphatases. *Adv Enzyme Regul* 43:15-28.

139. Stephens, L. R., Hughes, K. T. & Irvine, R. F. 1991. Pathway of phosphatidylinositol(3,4,5)-trisphosphate synthesis in activated neutrophils. *Nature* 351(6321):33-9.

140. Huang, Y. E., Iijima, M., Parent, C. A., Funamoto, S., Firtel, R. A. & Devreotes, P. 2003. Receptor-mediated regulation of PI3Ks confines PI(3,4,5)P3 to the leading edge of chemotaxing cells. *Mol Biol Cell* 14(5):1913-22.

141. Skippen, A., Jones, D. H., Morgan, C. P., Li, M. & Cockcroft, S. 2002. Mechanism of ADP ribosylation factor-stimulated phosphatidylinositol 4,5-bisphosphate synthesis in HL60 cells. *J Biol Chem* 277(8):5823-31.

142. Weernink, P. A., Meletiadis, K., Hommeltenberg, S., Hinz, M., Ishihara, H., Schmidt, M. & Jakobs, K. H. 2004. Activation of type I phosphatidylinositol 4-phosphate 5-kinase isoforms by the Rho GTPases, RhoA, Rac1, and Cdc42. *J Biol Chem* 279(9):7840-9.

143. Czupalla, C., Culo, M., Muller, E. C., Brock, C., Reusch, H. P., Spicher, K., Krause, E. & Nurnberg, B. 2003. Identification and characterization of the autophosphorylation sites of phosphoinositide 3-kinase isoforms beta and gamma. *J Biol Chem* 278(13):11536-45.

144. Vazquez, F., Ramaswamy, S., Nakamura, N. & Sellers, W. R. 2000. Phosphorylation of the PTEN tail regulates protein stability and function. *Mol Cell Biol* 20(14):5010-8.

145. Jackson, T. R., Kearns, B. G. & Theibert, A. B. 2000. Cytohesins and centaurins: mediators of PI 3-kinase-regulated Arf signaling. *Trends Biochem Sci* 25(10):489-95.

146. Welch, H. C., Coadwell, W. J., Stephens, L. R. & Hawkins, P. T. 2003. Phosphoinositide 3-kinase-dependent activation of Rac. *FEBS Lett* 546(1):93-7.

147. Hawadle, M. A., Folarin, N., Martin, R. & Jackson, T. R. 2002. Cytohesins and centaurins control subcellular trafficking of macromolecular signaling complexes: regulation by phosphoinositides and ADP-ribosylation factors. *Biol Res* 35(2):247-65.

148. Ridley, A. J. 2001. Rho GTPases and cell migration. *J Cell Sci* 114(Pt 15):2713-22.

149. Glogauer, M., Hartwig, J. & Stossel, T. 2000. Two pathways through Cdc42 couple the N-formyl receptor to actin nucleation in permeabilized human neutrophils. *J Cell Biol* 150(4):785-96.

150. Randazzo, P. A. & Hirsch, D. S. 2004. Arf GAPs: multifunctional proteins that regulate membrane traffic and actin remodelling. *Cell Signal* 16(4):401-13.

151. Insall, R. H. & Weiner, O. D. 2001. PIP3, PIP2, and cell movement--similar messages, different meanings? *Dev Cell* 1(6):743-7.

152. Stauffer, T. P., Ahn, S. & Meyer, T. 1998. Receptor-induced transient reduction in plasma membrane PtdIns(4,5)P2 concentration monitored in living cells. *Curr Biol* 8(6):343-6.

153. Kular, G., Loubtchenkov, M., Swigart, P., Whatmore, J., Ball, A., Cockcroft, S. & Wetzker, R. 1997. Co-operation of phosphatidylinositol transfer protein with phosphoinositide 3-kinase gamma in the formylmethionyl-leucylphenylalanine-dependent production of phosphatidylinositol 3,4,5-trisphosphate in human neutrophils. *Biochem J* 325 ( Pt 2):299-301.

154. Li, Z., Jiang, H., Xie, W., Zhang, Z., Smrcka, A. V. & Wu, D. 2000. Roles of PLC-beta2 and -beta3 and PI3Kgamma in chemoattractant-mediated signal transduction. *Science* 287(5455):1046-9.

155. Bondeva, T., Pirola, L., Bulgarelli-Leva, G., Rubio, I., Wetzker, R. & Wymann, M. P. 1998. Bifurcation of lipid and protein kinase signals of PI3Kgamma to the protein kinases PKB and MAPK. *Science* 282(5387):293-6.

156. Czupalla, C., Nurnberg, B. & Krause, E. 2003. Analysis of class I phosphoinositide 3-kinase autophosphorylation sites by mass spectrometry. *Rapid Commun Mass Spectrom* 17(7):690-6.

157. Vanhaesebroeck, B., Higashi, K., Raven, C., Welham, M., Anderson, S., Brennan, P., Ward, S. G. & Waterfield, M. D. 1999. Autophosphorylation of p110delta phosphoinositide 3-kinase: a new paradigm for the regulation of lipid kinases in vitro and in vivo. *Embo J* 18(5):1292-302.

158. Bondev, A., Rubio, I. & Wetzker, R. 1999. Differential regulation of lipid and protein kinase activities of phosphoinositide 3-kinase gamma in vitro. *Biol Chem* 380(11):1337-40.

159. Ma, L., Janetopoulos, C. J., Yang, L., Devreotes, P. N. & Iglesias, P. A. 2004. Two local excitation, global inhibition mechanisms acting complementarily in parallel can explain the chemoattractant-induced PI(3,4,5)P3 response in Dictyostelium. *Biophys J*.

160. Meinhardt, H. 1999. Orientation of chemotactic cells and growth cones: models and mechanisms. *J Cell Sci* 112 ( Pt 17):2867-74.

161. Cross, M. C. & Hohenberg, P. C. 1993. Pattern formation outside of equilibrium. *Rev. Mod. Phys.* 65(3):851-1112.

162. Press, W. H., Teukolsky, S. A., Vettering, W. T. & Flannery, B. P. (2002) *Numerical recipes in C : the art of scientific computing* (Cambridge University Press, Cambridge [Cambridgeshire] ; New York).

163. Guyer, J., Wheeler, D. & Warren, J. *FiPy.* (this computational package is freely available at http://www.ctcms.nist.gov/fipy/).

164. Comer, F. I. & Parent, C. A. 2002. PI 3-kinases and PTEN: how opposites chemoattract. *Cell* 109(5):541-4.

165. Xu, X., Meier-Schellersheim, M., Jiao, X., Nelson, L. E. & Jin, T. 2005. Quantitative imaging of single live cells reveals spatiotemporal dynamics of multistep signaling events of chemoattractant gradient sensing in Dictyostelium. *Mol Biol Cell* 16(2):676-88.

166. Tomchik, K. J. & Devreotes, P. N. 1981. Adenosine 3',5'-monophosphate waves in Dictyostelium discoideum: a demonstration by isotope dilution--fluorography. *Science* 212(4493):443-6.

167. Rietdorf, J., Siegert, F. & Weijer, C. J. 1996. Analysis of optical density wave propagation and cell movement during mound formation in Dictyostelium discoideum. *Dev Biol* 177(2):427-38.

168. Subramanian, K. K. & Narang, A. 2004. A mechanistic model for eukaryotic gradient sensing: spontaneous and induced phosphoinositide polarization. *J Theor Biol* 231(1):49-67.

169. Lin, F., Saadi, W., Rhee, S. W., Wang, S. J., Mittal, S. & Jeon, N. L. 2004. Generation of dynamic temporal and spatial concentration gradients using microfluidic devices. *Lab Chip* 4(3):164-7.

170. Lin, F., Nguyen, C. M., Wang, S. J., Saadi, W., Gross, S. P. & Jeon, N. L. 2005. Neutrophil migration in opposing chemoattractant gradients using microfluidic chemotaxis devices. *Ann Biomed Eng* 33(4):475-82.

171. Li Jeon, N., Baskaran, H., Dertinger, S. K., Whitesides, G. M., Van de Water, L. & Toner, M. 2002. Neutrophil chemotaxis in linear and complex gradients of interleukin-8 formed in a microfabricated device. *Nat Biotechnol* 20(8):826-30.

172. Wang, S. J., Saadi, W., Lin, F., Minh-Canh Nguyen, C. & Li Jeon, N. 2004. Differential effects of EGF gradient profiles on MDA-MB-231 breast cancer cell chemotaxis. *Exp Cell Res* 300(1):180-9.

173. Brown, E. B., Shear, J. B., Adams, S. R., Tsien, R. Y. & Webb, W. W. 1999. Photolysis of caged calcium in femtoliter volumes using two-photon excitation. *Biophys J* 76(1 Pt 1):489-99.

174. Kiskin, N. I., Chillingworth, R., McCray, J. A., Piston, D. & Ogden, D. 2002. The efficiency of two-photon photolysis of a "caged" fluorophore, o-1-(2-nitrophenyl)ethylpyranine, in relation to photodamage of synaptic terminals. *Eur Biophys J* 30(8):588-604.

175. Kiskin, N. I. & Ogden, D. 2002. Two-photon excitation and photolysis by pulsed laser illumination modelled by spatially non-uniform reactions with simultaneous diffusion. *Eur Biophys J* 30(8):571-87.

176. Hagen, V., Bendig, J., Frings, S., Wiesner, B., Schade, B., Helm, S., Lorenz, D. & Kaupp, U. B. 1999. Synthesis, photochemistry and application of (7-methoxycoumarin-4-yl)methyl-caged 8-bromoadenosine cyclic 3',5'-monophosphate and 8-bromoguanosine cyclic 3',5'-monophosphate photolyzed in the nanosecond time region. *J Photochem Photobiol B* 53(1-3):91-102.

177. Hagen, V., Frings, S., Wiesner, B., Helm, S., Kaupp, U. B. & Bendig, J. 2003. [7-(Dialkylamino)coumarin-4-yl]methyl-Caged Compounds as Ultrafast and Effective Long-Wavelength Phototriggers of 8-Bromo-Substituted Cyclic Nucleotides. *Chembiochem* 4(5):434-42.

178. Cluzel, P., Surette, M. & Leibler, S. 2000. An ultrasensitive bacterial motor revealed by monitoring signaling proteins in single cells. *Science* 287(5458):1652-5.

179. Ferrell, J. E., Jr. & Machleder, E. M. 1998. The biochemical basis of an all-or-none cell fate switch in Xenopus oocytes. *Science* 280(5365):895-8.

180. Postma, M., Roelofs, J., Goedhart, J., Loovers, H. M., Visser, A. J. & Van Haastert, P. J. 2004. Sensitization of Dictyostelium chemotaxis by phosphoinositide-3-kinase-mediated self-organizing signalling patches. *J Cell Sci* 117(Pt 14):2925-35.

181. Xu, X., Meier-Schellersheim, M., Jiao, X., Nelson, L. E. & Jin, T. 2004. Quantitative Imaging of Single Live Cells Reveals Spatiotemporal Dynamics of Multi-Step Signaling Events of Chemoattractant Gradient Sensing in Dictyostelium. *Mol Biol Cell*.

182. Iijima, M., Huang, Y. E., Luo, H. R., Vazquez, F. & Devreotes, P. N. 2004. Novel mechanism of PTEN regulation by its phosphatidylinositol 4,5-bisphosphate binding motif is critical for chemotaxis. *J Biol Chem* 279(16):16606-13.

183. Kanaho, Y. & Suzuki, T. 2002. Phosphoinositide kinases as enzymes that produce versatile signaling lipids, phosphoinositides. *J Biochem (Tokyo)* 131(4):503-9.

184. Doughman, R. L., Firestone, A. J. & Anderson, R. A. 2003. Phosphatidylinositol phosphate kinases put PI4,5P(2) in its place. *J Membr Biol* 194(2):77-89.